IDENTIFICATION, CHARACTERISATION AND MODELLING OF DYNAMIC ADHESION FOR OPTIMISED TRANSFER SYSTEM DESIGN

From

The University of Newcastle

Discipline of Mechanical Engineering

By

MICHAEL JOHN CARR

BE (Mech) (Hons) (Newcastle)

Thesis submitted in fulfilment of the requirements for the award of the degree

DOCTOR OF PHILOSOPHY

April 2019

This research was supported by an Australian Government

Research Training Program (RTP) Scholarship

This page is left intentionally blank

STATEMENT OF ORIGINALITY

I hereby certify that the work embodied in the thesis is my own work, conducted under normal supervision. The thesis contains no material which has been accepted, or is being examined, for the award of any other degree or diploma in any university or other tertiary institution and, to the best of my knowledge and belief, contains no material previously published or written by another person, except where due reference has been made. I give consent to the final version of my thesis being made available worldwide when deposited in the University's Digital Repository, subject to the provisions of the Copyright Act 1968 and any approved embargo.

…………………......................................

Michael John Carr

This page is left intentionally blank

ABSTRACT

The depletion of favourable bulk material deposits in relation to their handleability is prompting the industry to consider mining material that may have comparatively less favourable flow properties. Typically found beneath the water-table, less favourable bulk materials frequently exhibit an increased clay and moisture content, leading to Wet and Sticky Material (WSM) and problematic behaviours regarding handleability. WSMs can have a significant impact in the materials handling stream due to the expensive downtime of processing equipment, which is attributed to the complex inter-particle and boundary adhesion mechanisms found within the bulk material. To better understand the characteristics of WSMs, new theoretical models are required and consequently developed within the scope of this research.

For the identification of a WSM, a comprehensive study was undertaken where revised testing methods have been developed to attain quantifiable measurements for the problematic characteristics of bulk materials. The wall adhesion and inter-particle adhesion tests were developed and adapted for iron ore from existing methods that are typically used for fine powders. These tests have been performed in conjunction with a sweep of traditional flow property tests which were conducted on three iron ore samples. The three iron ore samples have been supplied from the Pilbara region of Western Australia and include; Upper Channel Iron Deposit (UCID), Lower Channel Iron Deposit (LCID) and the Denatured Zone (found between the UCID and LCID layers). The threshold moisture content for problematic behaviours were identified, where, Denatured was identified as the most problematic in relation to the adhesive strength it exhibits.

To further understand the adhesive properties of the iron ore samples, a revised methodology for the estimation of bulk material adhesion determined from the extrapolation of the Instantaneous Yield Locus (IYL) produced from Jenike direct shear testing was undertaken. The predicted adhesion values from this methodology are compared to experimental measurements using an inter-particle adhesion tester where good correlation was found. Once the adhesive properties of each iron ore sample were identified, a theoretical model was developed and validated experimentally to define the dynamic adhesion of the bulk material samples. The developed model was able to predict the geometrical constraints where the identification of the effective angle at which the shear failure equates to a zero-bond depth was found for three typical wall liners used in industry.

Following the identification of the dynamic adhesion geometrical constraints, it was observed by the author that the natural agglomeration of the iron ore samples assisted in the flow of the material through transfer systems. Additionally, it was also observed that the formed

agglomerates reduced the amount of dust generated during transportation. An investigation was undertaken on the effects of agglomeration on the materials handling sector where the benefits of reduced build-up and a reduction of dust generation was shown. It was found that for an equivalent Run-of-Mine (ROM) iron ore moisture content, there was a significant reduction for the amount of build-up that commonly leads to potential blockages in industry.

The final aspect of the presented research is the utilisation of numerical simulations for the prediction of problematic behaviours found in industrial systems. The characteristics of WSMs can be computationally expensive to model and with the development of the Discrete Element Method (DEM) in conjunction with the advancement in computational power over the past decade, it is now more feasible to model WSMs in DEM simulations. Three cohesion models capable of replicating WSMs are investigated where the potential to replicate problematic bulk material behaviours and computational solve times are analysed. The models used include; the Simplified Johnson-Kendall-Roberts (SJKR) model, Easo Liquid Bridging model and the Edinburgh Elasto-Plastic Adhesion (EEPA) model.

In this study, the coupling of the SJKR and Easo Liquid Bridging models is proposed and used to predict problematic bulk material behaviour. Additionally, a calibration procedure is developed and undertaken where the parameters for each cohesion model are discussed in detail. A series of calibration simulations with systematic parameter variation was undertaken to define a set of calibration matrices. The developed calibration matrices resulted in the selection of a unique parameter setting, which can be used for the simulation of on-site applications to optimise plant geometry and other operational parameters. Finally, numerical modelling validation was undertaken using a lab scale vertical impact testing facility where good correlation between experimental and simulation results was found.

ACKNOWLEDGEMENTS

I would like to take this opportunity to express my sincerest thanks to my supervisors for their support and guidance over the past four years. Firstly, Professor Craig Wheeler for the advice, encouragement and technical discussions which were critical in producing this thesis. Emeritus Professor Alan Roberts for taking the time to share the invaluable knowledge he has in the field of bulk materials handling and for significantly increasing my knowledge and passion for bulk solids. Thank you. Associate Professor Kenneth Williams for the opportunity to undertake an industrial PhD. Finally, Professor André Katterfeld for the support and guidance with the simulation phase of the research and allowing me to work with your group at Otto-von-Guericke University (OVGU) in Magdeburg. Additionally, I would like to acknowledge the Australian Research Council (ARC) and BHP, with particular thanks to Mr Greg Elphick and Ms Kylie Nettleton, for the financial support and in-kind contributions given during the research.

At this point I would also like to thank my friends and colleagues from TUNRA Bulk Solids (TBS), the Centre for Bulk Solids and Particulate Technologies (CBSPT), the Mechanical Engineering Workshop at the University of Newcastle and the Institute of Logistics and Materials Handling (ILM) at OVGU. The significant amount of people from these groups to name individually is impractical so as a collective group thank-you for the support over the last four years. I hope each of you know how much I appreciate the assistance given. I would, however, like to personally acknowledge Mr Daniel Ausling and Mr Bruce Merrotsy for their input into the technical writing aspects. Mr Hendrik Otto and Mr Thomas Rößler for their assistance given during my visit to Magdeburg, Germany. To Dr Peter Robinson and Dr Ognjen Orozovic for the technical discussions throughout this process. Finally, to Dr Jens Plinke, Mr Brodie Hayter and Mr Jordan Pascoe for their assistance given during the experimental phases.

Lastly, I would like to thank my friends and family. In particular to Ashleigh Alexander, thank you for your patience, support and understanding over the last four years, this would not have been possible without you.

This page is left intentionally blank

TABLE OF CONTENTS

LIST OF FIGURES

LIST OF TABLES

NOMENCLATURE

ROMAN SYMBOLS

A	*contact area of adhesion partners*	m^2
A_a	*area of material stream at exit to "flow-round" zone*	m^2
A_p	*area of material stream at entrance to "flow-round" zone*	m^2
a	*contact radius of particles in contact*	m
A_{cont}	*contact area between two particles*	m^2
a_{JKR}	*contact radius of particles in contact*	m
A_{ws}	*contact area of wall liner sample*	m^2
b	*intersection point on shear stress axis*	Pa
b_w	*bulk material stream width*	m
c	*scaling factor*	-
c_b	*bulk material cohesion*	Pa
C	*resultant force vector for kinetic wall friction tester*	N
C_{JDST}	*cohesion determined using Jenike direct shear tester*	Pa
C_p	*correction factor for hardness indenter shape*	-
d	*scaling factor*	-
D	*inter-particle distance*	m
d_2	*thickness of capillary liquid*	m
d_o	*liquid bridge rupture distance*	m
d_p	*diameter of particle*	m
$d_{sp/sp}$	*interaction of two spheres in contact*	m
e	*coefficient of restitution*	-
E^*	*equivalent particle Young's modulus*	Pa
F_A	*adhesive force*	N
F_{ad}	*adhesive force acting between particles*	N
F_c	*capillary force*	N
F_{CP}	*particle cohesion force*	N
F_D	*frictional drag force*	N
f_{hys}	*sum of hysteretic spring force*	N
F_{IPA}	*inter-particle adhesion force*	N
F_{normal}	*force acting in normal direction*	N
F_n	*external normal force acting on particle*	N
f_n	*normal force acting on particle for EEPA model*	N
f_{nd}	*normal damping force*	N
f_o	*pull-off force*	N
F_{PO}	*pull-off force required to separate two contacting particles*	N
F_{SJKR}	*force required to separate two contacting particles*	N
$F_{sp/pl}$	*capillary force for particle-to-wall contact*	N
$F_{sp/sp}$	*capillary force for particle-to-particle contact*	N
$F_{tangential}$	*force acting in tangential direction*	N
F_{viscN}	*viscous force normal component*	N
F_{viscT}	*viscous force tangential component*	N
F_{WA}	*wall adhesion force*	N
g	*acceleration due to gravity*	m/s^2
h	*adjusted bulk material stream drop height*	m
H	*horizontal force component for kinetic wall friction tester*	N
h_a	*thickness of material stream at exit to "flow-round" zone*	m
h_b	*bulk material burden height*	m

H_b	*build-up height*	m
h_{crit}	*critical build-up height where build-up stops*	m
h_i	*build-up height as defined in Figure 4.10*	m
H_{lb}	*minimum distance of liquid bridge*	m
h_o	*initial bulk material stream drop height*	m
h_p	*thickness of material stream at entrance to "flow-round" zone*	m
h_s	*height of rock-box transfer*	mm
k_1	*initial loading stiffness*	N/m
k_2	*unloading/loading stiffness*	N/m
K_a	*adhesive handleability ranking*	-
k_{adh}	*adhesive stiffness*	N/m
K_c	*cohesive handleability ranking*	-
K_f	*flowability ranking*	-
K_n	*Hertzian normal stiffness*	N/m
k_n	*stiffness in normal direction*	N/m
k_t	*stiffness in tangential direction*	N/m
L	*length of roughness measurement*	mm
L_o	*initial thickness of bulk material stream*	m
L_p	*length of indentation along its axis*	mm
L_s	*thickness of bulk material stream*	m
m	*shear index*	-
$\dot{m}$	*mass flow rate*	kg/s
$\dot{m}_{out}$	*mass flow rate after impact*	kg/s
m^*	*equivalent particle mass*	kg
m_1	*residual mass from dynamic adhesion testing*	kg
m_{after}	*final mass of filter bag and dust*	g
m_{bag}	*initial mass of filter bag*	g
m_{cone}	*mass of empty cone*	g
M_D	*draw down remaining mass*	kg
$m_{drained}$	*final mass of drained sample*	g
m_{full}	*mass of cone filled with sample*	g
M_S	*shear box remaining mass*	kg
m_{sample}	*mass of sample in tumble drum*	g
M_W	*build-up remaining mass*	kg
$mass_{bulk}$	*mass of bulk material sample*	g
$mass_{total}$	*mass of bulk material particle*	g
n	*shear index*	-
N	*normal force*	N
n_p	*power value for force overlap relationship*	-
P_{HK}	*applied load for Knoop hardness measurement*	kgf
R	*radius of particle centre to contact point*	m
R^*	*equivalent particle radii*	m
r_1	*radius of steel surfaces*	m
R_1	*radius of particle*	m
R_2	*radius of particle*	m
R_a	*centre line average roughness*	µm
R_b	*radius of material burden centroid*	m
R_h	*radius of head pulley*	m
R_{OZ}	*mean radius of material stream curvature*	m
R_p	*radius of particle*	m
r_P	*radius of major Mohr stress circle*	Pa

R_t	*centroid radius of element*	m
r_T	*radius of major Mohr stress circle*	Pa
R_q	*root mean square roughness*	µm
S	*separation distance between particles*	m
T	*tensile strength determined using tensile tester*	Pa
t	*element thickness*	m
t_{bc}	*belt carry back element thickness*	m
$\vec{u}$	*normal vector from particle centre to contact point*	-
v	*velocity of mass element*	m/s
v_a	*thickness of material stream at exit to "flow-round" zone*	m/s
v_p	*thickness of material stream at entrance to "flow-round" zone*	m/s
V	*vertical force component for kinetic wall friction tester*	N
V_b	*belt velocity*	m/s
V_{bond}	*volume of liquid bridge*	m^3
V_d	*discharge velocity*	m/s
V_{lb}	*volume of liquid bridge*	m^3
v_n	*particle normal relative velocity*	m/s
$v_{n\overrightarrow{rel}}$	*normal component of relative velocity*	m/s
V_{slc}	*surficial liquid volume to solids volume*	%
V_{sLi}	*particle i surface liquid volume*	m^3
V_{sLj}	*particle j surface liquid volume*	m^3
v_t	*particle tangential relative velocity*	m/s
$volume_{particle}$	*volume of bulk material particle*	m^3
$volume_{total}$	*volume of bulk density testing apparatus*	m^3
v_{out}	*stream velocity off build-up*	m/s
w_d	*width of rock-box transfer dynamic zone*	mm
w_s	*width of rock-box transfer static zone*	mm
W_{Tot}	*total energy of liquid bridge*	J
x	*power value for adhesion branch*	-
x_{c1}	*distance from centre to edge of liquid bridge*	m
x_{c2}	*distance from centre to edge of liquid bridge*	m

GREEK SYMBOLS

α	*stress angle acting on arbitrary plane*	°
α_b	*conveyor inclination angle*	°
α_c	*liquid bridge embracing angle*	°
α_d	*discharge angle*	°
α_i	*angle of impact plate*	°
α_p	*angle of material stream inflow to impact plate*	°
β	*damping coefficient*	-
β_o	*ore surface angle*	°
β_p	*impact plate inclination angle*	°
β_{wall}	*wall liner angle*	°
γ	*liquid surface tension*	N/m
γ_b	*bulk material specific weight*	kN/m^3
γ_d	*dynamic shear angle determined from rock-box transfer*	°
γ_n	*coefficient of critical damping in normal direction*	-
γ_s	*static shear angle determined from rock-box transfer*	°
γ_t	*coefficient of critical damping in tangential direction*	-
ΔA	*element contact area*	m^2
ΔA_h	*stream element contact area*	m^2
ΔA_{IPA}	*element contact area between inter-particle bonds*	m^2
ΔA_{WA}	*element contact area between element and belt surface*	m^2
ΔA_t	*belt carry back element contact area*	m^2
ΔF_c	*centrifugal force*	N
ΔG	*gravitational force*	N
Δh_i	*incremental change in build-up height*	m
Δm	*element mass*	kg
Δr	*change in radius*	m
$\Delta\gamma$	*contact surface energy*	N/m
δ	*effective angle of internal friction*	°
δ_1	*half filling angle*	°
δ_2	*half filling angle*	°
δ_{JKR}	*particle overlap for JKR contact model*	m
δ_{min}	*particle overlap where minimum hysteretic force occurs*	m
δ_n	*particle overlap in normal direction*	m
δ_p	*plastic particle overlap*	m
δ_{po}	*plastic overlap*	m
ε	*voidage acting between particles*	-
ε_c	*admissible relative deviation value*	%
ε_D	*shear angle determined using draw down test*	°
ε_r	*co-efficient of restitution*	-
ε_S	*shear angle determined using shear box test*	°
θ	*total inclination angle*	°
θ_a	*Horizontal angle of material stream inflow to impact plate*	°
θ_c	*liquid bridge contact angle*	°
θ_{eff}	*effective contact angle between particles i and j*	°
μ	*coefficient of friction*	-
μ_f	*viscosity of fluid*	m^2/s
μ_k	*kinematic surface friction*	-
μ_p	*particle-to-particle friction*	-
μ_r	*particle rolling friction*	-

μ_s	*particle sliding friction*	-
μ_{st}	*static surface friction*	-
ρ_{bulk}	*bulk density of bulk material sample*	kg/m^3
$\rho_{particle}$	*particle solids density of bulk material sample*	kg/m^3
σ	*normal stress*	Pa
σ_1	*major principal stress*	Pa
σ_{1c}	*nominated consolidation pressure*	Pa
σ_2	*minor principal stress*	Pa
σ_α	*acting normal stress*	Pa
σ_a	*adhesive stress*	Pa
σ_{ao}	*adhesive strength*	Pa
$\sigma_{a(lin)}$	*adhesive stress linear prediction*	Pa
$\sigma_{a(par)}$	*adhesive stress parabolic prediction*	Pa
σ_{ave}	*average principal stress*	Pa
σ_c	*unconfined yield strength*	Pa
σ_{co}	*cohesive strength*	Pa
σ_{IPA}	*inter-particle adhesion stress*	Pa
σ_n	*normal stress for kinetic wall friction tester*	Pa
σ_P	*pre-consolidation normal stress*	Pa
σ_s	*shear stress for kinetic wall friction tester*	Pa
σ_{ST}	*liquid surface tension*	N/m
σ_t	*tensile adhesive strength*	Pa
σ_T	*normal stress component connecting IYL and major Mohr circle*	Pa
σ_w	*normal stress to the wall*	Pa
σ_{wa}	*tensile strength from wall adhesion tester*	Pa
σ_{WA}	*wall adhesion stress*	Pa
τ	*shear stress*	Pa
τ_α	*acting shear stress*	Pa
τ_k	*kinematic shear stress*	Pa
τ_o	*cohesive stress*	Pa
τ_P	*pre-consolidation shear stress*	Pa
τ_s	*static shear stress*	Pa
τ_T	*shear stress component connecting IYL and major Mohr circle*	Pa
τ_w	*shear stress at the wall*	Pa
τ_{wa}	*cohesive stress at the wall*	Pa
φ	*planing angle for kinetic wall friction tester*	°
φ_f	*angle co-ordinate of flow round zone*	°
φ_{imp}	*impingement angle*	°
φ_t	*angle of internal friction*	°
φ_w	*wall friction angle*	°
Ω_{AED}	*adhesion energy density*	J/m^3
Ω_{CED}	*cohesion energy density*	J/m^3
ω_D	*angle of repose determined using draw down test*	°

This page is left intentionally blank

ABBREVIATIONS

AED	**A**dhesion **E**nergy **D**ensity
AOR	**A**ngle **o**f **R**epose
AR	**A**dhesive Handleability **R**anking
BIF	**B**anded **I**ron-**F**ormation
CED	**C**ohesion **E**nergy **D**ensity
CID	**C**hannel **I**ron **D**eposit
CLA	**C**entre **L**ine **A**verage
COR	**C**oefficient **o**f **R**estitution
CPU	**C**entral **P**rocessing **U**nit
CR	**C**ohesive Handleability **R**anking
DEM	**D**iscrete **E**lement **M**ethod
DEMC	**D**ust **E**xtinction **M**oisture **C**ontent
DMT	**D**erjaguin-**M**uller-**T**oporov
EEPA	**E**dinburgh **E**lasto-**P**lastic **A**dhesion
EYL	**E**ffective **Y**ield **L**ocus
GPU	**G**raphics **P**rocessing **U**nit
HK	**K**noop **H**ardness
IOA	**I**ron **O**re **A**
IOB	**I**ron **O**re **B**
IOC	**I**ron **O**re **C**
IYL	**I**nstantaneous **Y**ield **L**ocus
JKR	**J**ohnson-**K**endall-**R**oberts
LAMMPS	**L**arge-scale **A**tomic/**M**olecular **M**assively **P**arallel **S**imulator
LCID	**L**ower **C**hannel **I**ron **D**eposit
LIGGGHTS	**L**AMMPS **I**mproved for **G**eneral **G**ranular and **G**ranular **H**eat **T**ransfer **S**imulations
MC	**M**oisture **C**ontent
PF	**P**article Sliding **F**riction
PFA	**P**owder **F**low **A**nalyser
PSD	**P**article **S**ize **D**istribution
RF	Particle **R**olling **F**riction
RMS	**R**oot **M**ean **S**quare
ROM	**R**un-**o**f-**M**ine
RSD	**R**otary **S**ample **D**ivider
SDMC	**S**aturated **D**rained **M**oisture **C**ontent
SJKR	**S**implified **J**ohnson-**K**endall-**R**oberts
ST	**S**urface **T**ension
UCID	**U**pper **C**hannel **I**ron **D**eposit
WSBCT	**W**arren **S**pring-**B**radford **C**ohesion **T**ester
WSM	**W**et and **S**ticky **M**aterial
WYL	**W**all **Y**ield **L**ocus
XRF	**X**-**R**ay **F**luorescence

This page is left intentionally blank

PUBLICATIONS

The following publications have been produced during the time of the PhD candidature:

JOURNAL

Carr, M. J., Roberts, A. W. and Wheeler, C. A., 2019. *A Revised Methodology for the Determination of Bulk Material Cohesion and Adhesion.* Advanced Powder Technology, Vol. 30, No. 10, pp. 2110-2116. (doi:10.1016/j.apt.2019.06.025)

CONFERENCE

Carr, M., Roberts, A. and Wheeler, C., 2018. *A Revised Methodology for Cohesion and Adhesion Analysis of Bulk Materials.* In: Proceedings 9th International Conference for Conveying and Handling of Particulate Solids - CHoPS 2018. London, United Kingdom.

Carr, M., Wheeler, C., Williams, K., Katterfeld, A., Elphick, G., Nettleton, K. and Chen, W., 2018. *Discrete Element Modelling of Problematic Bulk Solids onto Impact Plates.* In: Proceedings 9th International Conference for Conveying and Handling of Particulate Solids - CHoPS 2018. London, United Kingdom.

Carr, M., Plinke, J., Williams, K., Roberts, A. and Chen, W. 2017. *Determination of the Handleability Index of Adhesive Bulk Materials.* In: Proceedings AusIMM (6th Ed.), Iron Ore 2017 Conference Proceedings. Australasian Institute of Mining and Metallurgy (AusIMM), Perth, Australia.

Carr, M., Williams, K., Chen, W., Hayter, B., Roberts, A. and Wheeler, C., 2017. *The Dynamic Adhesion of Wet and Sticky Iron Ores onto Impact Plates*. In: Proceedings AusIMM (6th Ed.), Iron Ore 2017 Conference Proceedings. Australasian Institute of Mining and Metallurgy (AusIMM), Perth, Australia.

Carr, M. J., Chen, W., Williams, K. and Katterfeld, A., 2016. *Comparative Investigation on Modelling Wet and Sticky Material Behaviours with a Simplified JKR Cohesion Model and Liquid Bridging Cohesion Model in DEM.* In: Proceedings 12th International Conference on Bulk Solids Material Storage, Handling and Transport (ICBMH), Darwin, Australia.

This page is left intentionally blank

CHAPTER ONE – INTRODUCTION

1.1 PROBLEMATIC MATERIALS AND THE EFFECTS ON THE MINING SECTOR

The production and development of the modern world has seen an ever-increasing demand for the extraction of minerals such as iron ore, coal and bauxite leading to the exploitation of ore bodies that may typically have been disregarded in the past. This demand has called for more efficient systems that can transport these bulk commodities from the mine site where they are usually distributed to processing plants, power stations or export terminals. The depletion of favourable bulk material deposits in relation to their handleability is prompting the industry to consider mining material that may have comparatively less favourable flow properties. Normally found beneath the water-table, less favourable bulk materials frequently exhibit an increased clay and moisture content, leading to Wet and Sticky Material (WSM) and problematic behaviours regarding handleability.

WSMs are prone to cause problems in all phases of the materials handling stream, which is attributed to the inter-particle and boundary cohesion and adhesion forces. Some of the typical problems that arise from WSMs include carry back on belt conveyors, the clogging of screens and chute build-up among others [1, 2]. When transfer chutes are considered, downtimes can be caused from belt runoff events where mistracking of the conveyor belt can cause costly damage to the materials handling operation. These types of events are commonly caused from overloaded belts where a prior blockage has dislodged and fallen onto the conveyor. WSMs lead to additional handling costs which are attributed to sub-optimal running conditions resulting in system downtime. There have been reported cases where systems operating with sub-optimal conditions resulted in downtimes of approximately 7-30 hours per week [3]. This will naturally be an area of concern financially for the mining industry and measures must be set in place to increase the likelihood of these systems performing effectively.

Extensive research has been undertaken regarding the theory of the flow properties of bulk materials. This flow property theory, presented in the work of Jenike [4] and Roberts [1], is necessary to design bulk material handling equipment, where, quantitative measurements are utilised to optimise the design process of bulk handling equipment such as storage bins, feeders and chutes. Although the fundamental flow properties are well documented, the adhesive and cohesive characteristics that WSMs can possess are still yet to be fully understood.

WSMs are seen to be problematic within the materials handling stream, due to the inter-particle and boundary cohesion and adhesion forces. These forces can be determined from the flow properties of the bulk material, however, only a very basic knowledge of how they interact is currently known. The aim of this research is to develop models to predict how WSMs will perform in bulk material handling operations with a great emphasis on the dynamic response to adhesive build-up. Additionally, the parameter sets for the shear failure mechanism and effective angle which equates to zero bond depth, will be identified.

During the initial experimental phase of the research, it was observed by the author that the natural agglomeration of the bulk material assisted in the flow through transfer systems. Additionally, it was observed that the formed agglomerates also reduced the amount of dust generated during transportation. This phenomenon is consequently explored further in this thesis and the effects that agglomeration has on the materials handling stream is also investigated. The fundamentals of agglomeration on the materials handling stream is explored to see the effects of the reduction of adhesive bonds that are present within WSMs, where a methodology for implementation to industrial systems will be proposed.

The current numerical capabilities to model the flow of bulk materials in a simulated domain over the past decade has increased significantly. These capabilities, however, still have a very limited capacity to model the behavioural traits of WSMs. A further aspect of this research is the adaption of existing numerical models that can represent WSMs. These numerical models are simulated into the Discrete Element Method (DEM) and correlated to experimental data.

1.2 MOHR-COULOMB STRENGTH ASSESSMENT AND CURRENT LIMITATIONS

During the transportation of a bulk material, flow is initiated when the bulk material shears on itself and yields. This shear can be further categorised into internal shear and boundary shear, which are influenced by the walls (boundary) of the bulk material handling equipment. Although bulk materials deform and dilate when they flow, they will have similar stresses to those found in solids. The stresses found in bulk materials will have different stresses for different cutting planes, similar to solid materials. Using the well-established Mohr stress circle theory, the following equations can be used to determine the elemental stresses for different planes.

$$\sigma_\alpha = \frac{\sigma_2 + \sigma_1}{2} + \frac{\sigma_2 - \sigma_1}{2}\cos(2\alpha) \tag{1.1}$$

$$\tau_\alpha = \frac{\sigma_2 - \sigma_1}{2}\sin(2\alpha) \tag{1.2}$$

where:

σ_1 is the major principal stress [Pa].

σ_2 is the minor principal stress [Pa].

τ_α is the shear stress acting on the bulk material [Pa].

σ_α is the normal stress acting on the bulk material [Pa].

α is the stress angle acting on an arbitrary plane [°].

Expanding further from the Mohr circle theory, the flow function of a bulk material is defined as the bulk materials unconfined yield strength, σ_c, as a function of the major consolidation stress (major principal stress), σ_1. The flow function provides a measure for the amount of load that is required for the material to internally shear and initiate flow. A well-designed hopper will enable the flow of the bulk material to be initiated purely by gravity once the gate is opened. Conversely, handling equipment that is designed poorly or a bulk material that has poor flow characteristics can cause blockage problems. Estimation of the flow function is therefore of critical importance, as it can provide a quantitative measure for the design of adequate bulk material handling equipment. The unconfined yield stress is defined as the principal stress causing failure in a cutting plane of a bulk material. It will depend on the consolidation stress, σ_1, as well as a number of other factors such as the consolidation time, direction of consolidation, moisture content, particle size, particle size distribution, particle shape and particle shape distribution, among others [1].

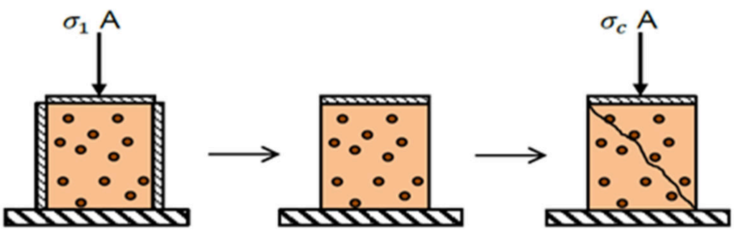

Figure 1.1 – Hypothetical uniaxial compression model (Schulze,2008).

The measurement of the flow function of a bulk material can be demonstrated with a uniaxial compression test, shown in Figure 1.1. A hollow cylinder, where frictionless walls are assumed, is filled with a bulk material sample, which is then compressed until the consolidation stress, σ_1, is reached. As the consolidation stress is applied to the sample in the vertical direction, compression of the sample will occur. This compression of the bulk material sample will result in an increase in bulk density and strength [5]. After consolidation, the bulk material sample is relieved of the consolidation stress and the hollow cylinder is removed. Finally, the consolidated cylindrical sample is loaded with an increasing vertical compressive stress, where the sample will break (fail) at a certain stress level. The stress causing failure is typically called the unconfined yield stress, σ_c. In bulk material handling, the failure of the sample is commonly referred to as "*incipient flow*" because at failure, the consolidated bulk material sample starts to flow. It is appropriate to note that the unconfined compression test is well known and used within soil mechanics.

The most commonly used testing procedure to obtain flow functions is with direct shear testers. A widely accepted method for direct shear testing is undertaken using Jenike direct shear testers which are undertaken in accordance with the procedure outlined in ASTM International [6] and by the Institute of Chemical Engineers [7].

The handleability of a bulk material can be defined as a measure of the cohesive strength of the bulk material where, $K_c = Cohesive\ Handleability\ Ranking$. The higher the cohesive strength, the more difficult the handling becomes. Similarly, the measure of the ability for a bulk material to flow can be referred to as the "*flowability ranking, K_f*". The higher the value of K_f the more easily the material handles and flows. It can be determined further that the flowability is the inverse of the handleability, i.e. $K_f = \frac{1}{K_c}$. When considering WSMs, there is an increased focus on the cohesive strength, hence, handleability must be considered. Numerically the regions of handleability can be determined using:

$$\sigma_c = K_c(\sigma_{co} + c\sigma_{1c}) \qquad (1.3)$$

where:

	σ_{1c}	is the nominated consolidation pressure [Pa].
	σ_c	is the corresponding unconfined yield strength [Pa].
	σ_{co}	is the cohesive strength of the bulk material [Pa].
	K_c	is the cohesive handleability ranking [-] (see Table 1.1).
	c	is a scaling factor [-].

Table 1.1 – Cohesion Handleability Ranking Assessment (Roberts, 1998).

Cohesive Handleability Ranking Assessment	*Cohesive Handleability Ranking (CR)*	*Cohesive Handleability Characteristic*
$\boldsymbol{K_c \geq 1}$	*1*	Extremely Cohesive
$\boldsymbol{0.75 \leq K_c \leq 1}$	*2*	Very Cohesive
$\boldsymbol{0.5 \leq K_c \leq 0.75}$	*3*	Cohesive
$\boldsymbol{0.25 \leq K_c \leq 0.5}$	*4*	Free Flowing – High Cohesive Strength
$\boldsymbol{0.1 \leq K_c \leq 0.25}$	*5*	Free Flowing – Moderate Cohesive Strength
$\boldsymbol{0 \leq K_c \leq 0.1}$	*6*	Free Flowing – Low Cohesive Strength

By way of example, a typical ranking assessment of a flow function, labelled A, produced from direct shear testing procedures is shown in Figure 1.2. Characteristically the bulk material does not usually present the same handleability over the entire consolidation range of σ_1. The cohesive strength of the bulk material is given as $\sigma_{co} = 5kPa$ and the scaling factor is given as $c = 0.5$. Each of the regions, indicated from the five solid lines, are given a ranking depending on the handling characteristics that will be experienced. This ranking is determined from the cohesive handleability ranking, K_c, used in Equation 1.3. The cohesive handleability ranking assessment is summarised in Table 1.1.

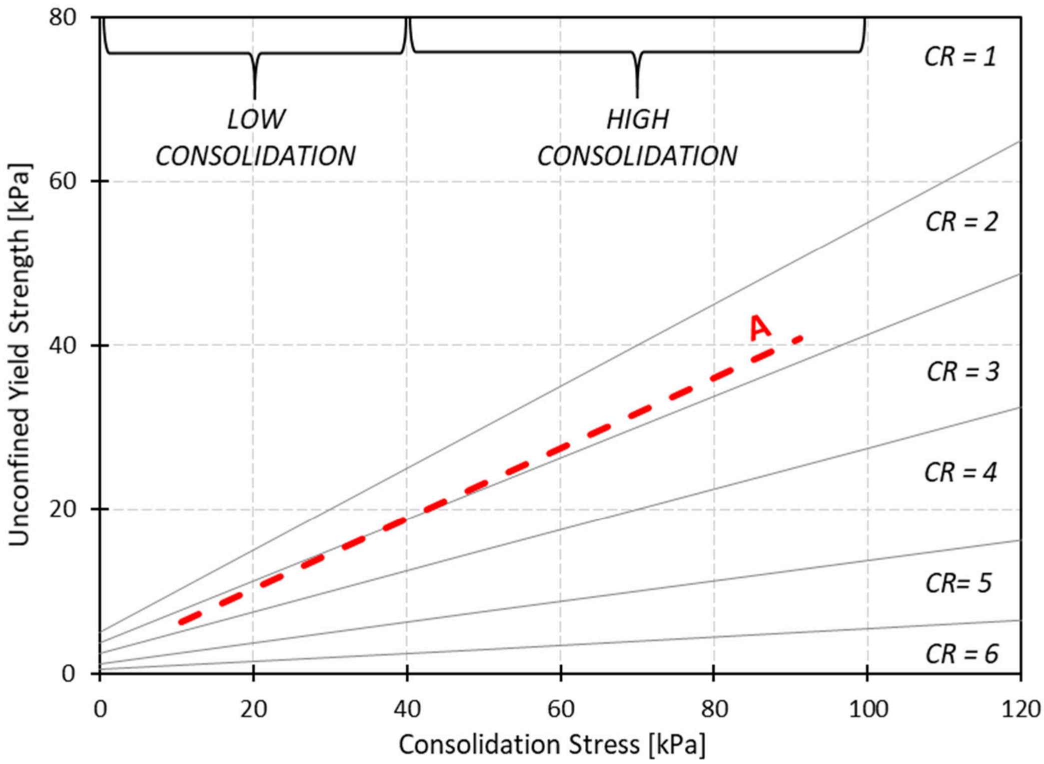

Figure 1.2 – Typical cohesive handleability ranking (CR) with flow function from Jenike direct shear tester.

Flow functions will generally be determined with the use of direct shear testers which will apply loads in two directions [7]. WSMs often show a large plasticity, which causes problems with common practices to determine the flow function. These limitations need to be addressed in order to characterise flowability of wet and sticky material and determine quantifiable levels for adhesive and cohesive behaviour.

The wall friction in bulk material handling will be produced between a bulk material and the surface of the material handling equipment [1]. The wall friction will typically affect the performance of hoppers, feeders and chutes among others where this can also be attributed to the cohesion and adhesion found within the bulk material. For applications such as that of bins and hoppers, the friction will be the governing factor in regards to initiating flow. During the design of hoppers, a great emphasis is put on low wall friction for an effective and reliable performance [1]. A common form to depict the wall friction properties is through the wall friction angle, ϕ_W, determined using:

$$\phi_W = \tan^{-1}\left(\frac{\tau_W}{\sigma_W}\right) \tag{1.4}$$

where: τ_W is the shear stress at the wall [Pa].

σ_W is the normal stress to the wall [Pa].

The wall friction angle is determined from the frictional shear force that is produced from the interaction between wall lining material and bulk material. Typically, this is referred to as the Wall Yield Locus (WYL), which is attributed to the acting normal force. For cohesive bulk materials, the WYL will rarely pass through the origin of the graph, as shown in Figure 1.3. From this, we can determine that there will be a shear force on the boundary surface, even if a normal load is absent. This is attributed to the boundary adhesion forces acting between the wall liner and the bulk material. The determination of these adhesive forces using conventional shear testing techniques is rather difficult due to the small values they possess, and they are found to have negative (tensile) forces which these testers are unable to measure. Inverted wall friction testers do exist which measure the adhesive forces, however, limitations still can exist in determining accurate measurement data.

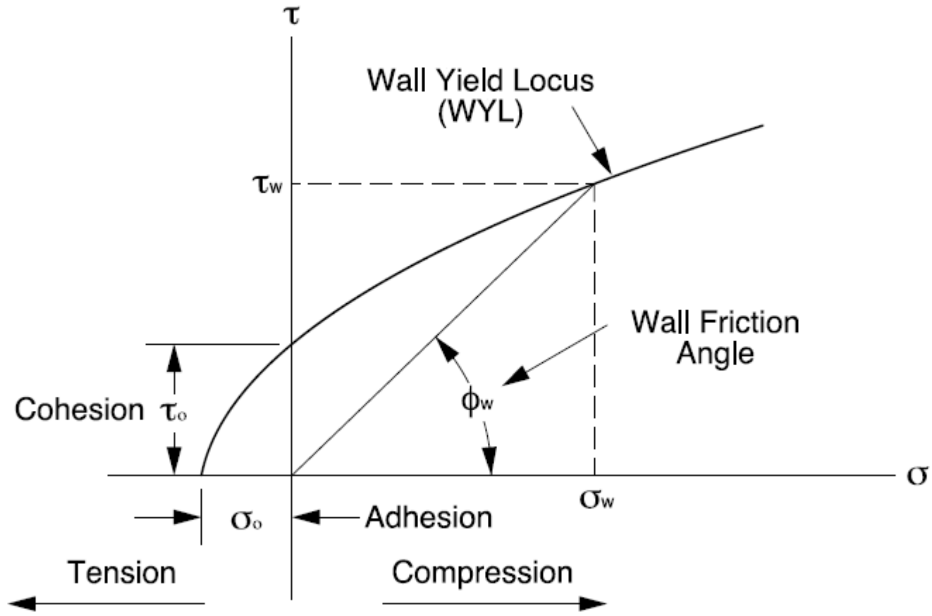

Figure 1.3 – Adhesive stresses determined from WYL (Roberts, 1998).

The shear stress necessary for relative movement at the boundary surface without any normal load, can be described as the adhesive shear stress, τ_o. The intersection of the WYL with the normal stress axis gives an approximate value of the adhesive tensile stress [1]. The further development of the approximate adhesive zone found in the tensile component of Figure 1.3, will be the focal point of this research. Revised testing methods for an accurate determination of these parameters will be proposed within this thesis.

1.3 THESIS OVERVIEW

The primary aim of the research outlined within this thesis is to provide insight into the behavioural traits WSMs exhibit in the materials handling stream. Emphasis will be on transfer systems that typically exhibit rapid induced bulk material blockages. The main areas of research are:

1. The determination of a methodology to explain the dynamic adhesion of problematic bulk materials in transfer systems.
2. To investigate methods for the reduction of adhesive bonds which can allow for the continuation of flow, reducing the likelihood of blockages caused by problematic bulk materials.
3. Adaption, development and validation of numerical models to be used for the prediction of blockage events prior to entry into the materials handling stream.

Chapter 2 outlines the iron ore samples supplied by the industry partner and their origin. The characterisation of these samples and the testing procedures used will also be discussed. The development of a modified inter-particle adhesion tester will also be outlined where the results are used for the theoretical model developed in Chapter 3. In addition, the wall lining properties are also determined to give an insight into the influence that equipment handling surfaces have on rapid induced bulk material blockages.

Chapter 3 will provide an overview of the current theoretical models that describe the strength of bulk materials. As explained in Section 1.2, the cohesive elements of the Mohr-Coulomb strength model are well defined. For the adhesive (tensile) elements however, there are no real measurement or modelling procedures defined. This chapter will build on existing methods to define a measurement and modelling procedure to capture the adhesive behaviour of bulk materials.

To expand further on the adhesion modelling proposed above, Chapter 4 will incorporate the effects of dynamic conditions and the way this alters the flow of the bulk material through transfer systems. An in-depth verification of the dynamic adhesion modelling will be undertaken, where a comparison between experimental results (outlined in Chapter 6) to predicted dynamic adhesion behaviour will also be included.

Chapter 5 presents methodologies for the reduction of adhesive bonds which can be used on an industrial basis. The results presented in Chapter 4 will be used, where the critical release angles that are found impractical to assist in the flow of the bulk material will be investigated further. To assist in the flow of the bulk material, this chapter will consider the effects of the agglomeration of Run-Of-Mine (ROM) ores on the bulk material handling industry and the methods available to produce the agglomerates. The fundamentals of agglomeration on the materials handling stream will be explored and the industrial systems suitable for implementation to the materials handling sector are proposed.

Chapter 6 provides a summary of the experimental measurement apparatus and results which will be used for validation of the proposed modelling above. The dynamic adhesion of bulk material to wall liner type will be defined, where the shear failure mechanisms and critical release angle will also be found. In addition, the classification and ranking of the severity of dynamic adhesion for the critical release angle will be determined, and protocols will be proposed to reduce the effects of dynamic adhesion.

Numerical modelling for the prediction of problematic bulk material behaviour will be presented in Chapter 7. This chapter will include an overview of the Discrete Element Method (DEM) and the numerical contact models used for the DEM simulations. The coupling of two existing models is proposed and used to predict problematic bulk material behaviour. Additionally, a calibration procedure is proposed where the discussion of parameters and calibration matrices will be included. Numerical modelling validation will also be undertaken using a lab scale vertical impact testing facility.

Concluding remarks from the work contained within this thesis, including the applications to industry, a summary of important results obtained and correlation to theoretical modelling of dynamic adhesion are presented in Chapter 8. A summary of the numerical modelling undertaken is also presented. Additionally, a section on the reduction of adhesive bonds with the effect on the materials handling stream is contained within. Finally, a concise indication of further work that should be undertaken will also be included.

This page is left intentionally blank

CHAPTER TWO – BULK MATERIAL PROPERTIES & WALL LINER CHARACTERISATION

The following chapter builds on the existing testing methods available for the characterisation of the iron ore samples where the corresponding results are also presented. This process is critical to distinguish between the samples and allow for the theoretical models developed in the proceeding chapters to be robust and allow for the adaption to other bulk commodities.

2.1 INTRODUCTION

The recent demand of mineral resources has seen the use of ore bodies which are referred to as being *"problematic"* being disregarded and, in most cases, avoided completely during the exploration phases of any mining operation. These bulk commodities are problematic when negotiating the materials handling stream due to the adhesive and cohesive properties they possess [8]. These properties of the bulk materials are due to the excessive inherent moisture found within the bulk material itself, as they are typically mined from beneath the water-table [9]. Another source of excessive moisture can be caused by heavy rainfall and tropical storms which can lead to a reasonably free flowing ore to turn problematic relatively quickly leading to handling problems.

The physical properties, or flow properties as they are commonly termed, of bulk materials, can give an insight into the behaviour they may exhibit when negotiating the materials handling stream. The following chapter explains the procedures that have been used during the course of the research for the characterisation of the bulk material samples and wall lining materials, where a summary of the testing results is also included. In addition, a brief section on the geology and origin of the iron ore samples will be included to give a background and context to why the samples may exhibit certain properties.

2.2 IRON ORE SAMPLES

The iron ore samples that were used for this research have been sourced from the Pilbara region in Western Australia. More specifically, the ores have been sourced from the Hammersley province where the BHP Iron Ore Yandi operation is located [10]. Predominantly, the main ore that is mined in this region are Channel Iron Deposits (CID) which infill paleochannels incised into Proterozoic basement rocks [11] and began to form during the Oligocene to Miocene periods some 30 million years ago [12]. CIDs in this region are found to range from <1m up to 100m thick and the channel width of the deposit is typically around 1 km, but in some areas, can be up to several kilometres [13].

The composition of the CIDs can be split into three main members which are shown in the schematic of Figure 2.1. These members can be categorised into the following: Munjina Member, Barimunya Member and the Iowa Eastern Member [10]. Much research has been conducted into the formation and composition of these members and a brief overview is included below where further explanations are in the cited literature [10 - 14].

The current mineralogy and the approximate thickness of each layer component from the respective members of the Marillana Formation has been discussed in detail in the work of Kneeshaw [10]. A summary for each of the respective layers is as follows:

MUNJINA MEMBER

BASAL CONGLOMERATE

The Basal Conglomerate zone is usually 0-20 m thick which will vary considerably across and along the length. Generally, it contains a grey-black siltstone-clay horizon that appears in the mid-section of the channel layer [10]. Rare clasts of CID and maghemite have been discovered in the channel layer [15]. The Basal Conglomerate typically adjoins to the Basal Clay channel layer, however, in higher regions it may directly underlie the Barimunya Member [10].

BASAL CLAY

The Basal Clay zone is usually 0-20 m thick and contains a yellow coloured kaolinitic clay with some pockets containing ocherous goethitic clay. The Basal Clay layer adjoins to the Lower CID of the Barimunya Member as shown in Figure 2.1. It can be common to also find some small sporadic deposits of ocherous CID, which will typically be red-brown in appearance, in the centre portion of the channel [10].

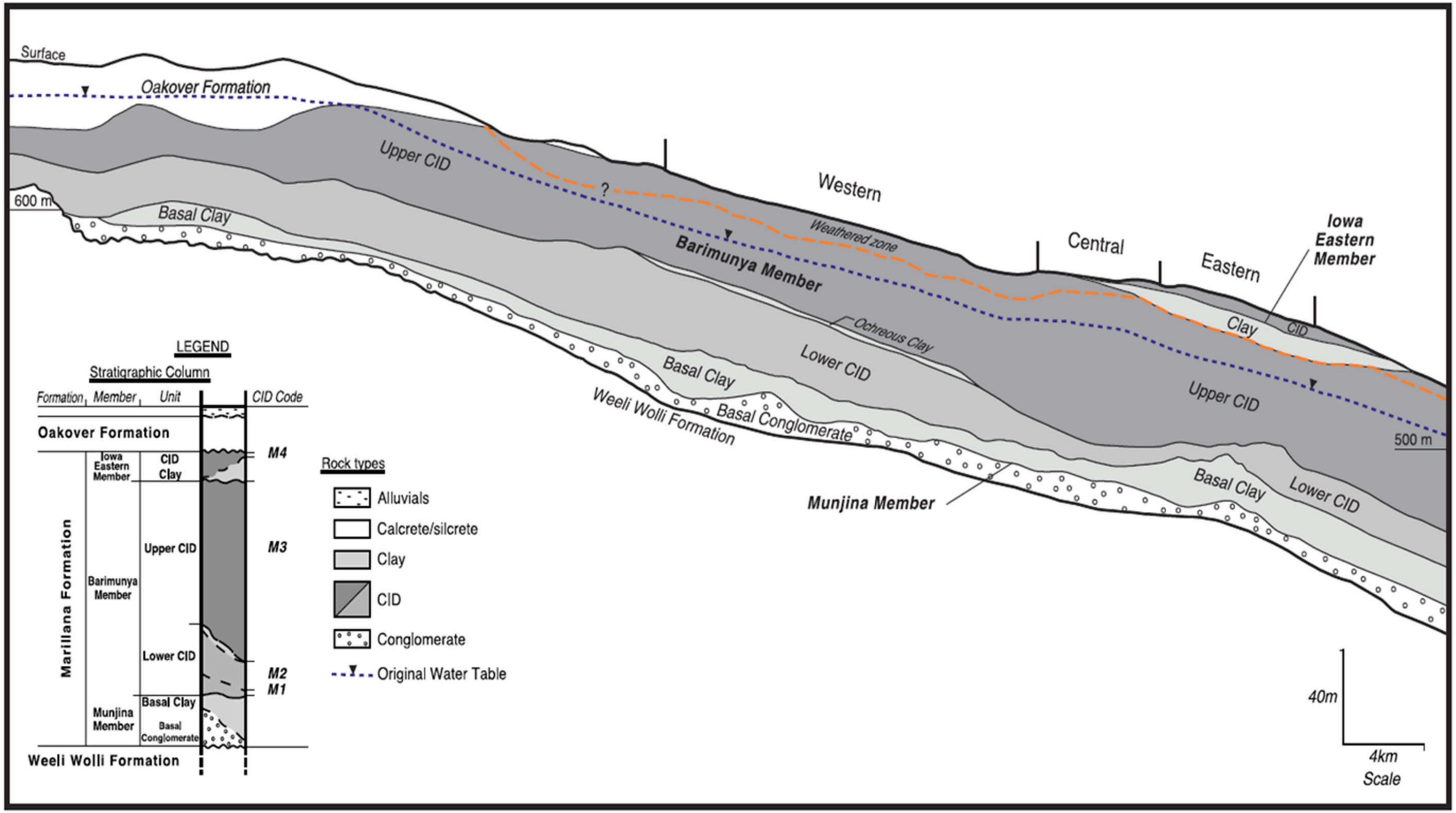

Figure 2.1 – Schematic cross-section of the Marillana Formation channel iron deposits and the corresponding constituent layers (Kneeshaw, 2003).

BARIMUNYA MEMBER

LOWER CHANNEL IRON DEPOSIT (LCID)

The lower CID is typically 10-30 m thick in the lower segment of the Barimunya Member shown in Figure 2.1. It is comprised of yellow-brown goethite granules which were caused by the oxidation of the original red-brown hematite-goethite granules. It is thought that this occurred due to the water-table, where solution-reprecipitation processes occurred [10].

UPPER CHANNEL IRON DEPOSIT (UCID)

The upper CID will vary from 25-45 m in thickness and will generally be exposed due to the weathered zone shown in Figure 2.1. It will typically be comprised of red-brown hematite-goethite granules [10].

DENATURED ZONES

During the formation of the Barimunya Member, it is thought that the emergence and lowering of the water-table resulted in the development of ores which had reduced quality. These denatured zones have increased contents of goethite, silica and/or alumina and be quite friable [12]. The Denatured Zone is found in the lower part of the Upper CID and the upper part of the Lower CID adjoining with the Ochreous Clay Pod zone as shown in Figure 2.1.

OCHREOUS CLAY PODS

The Ochreous Clay Pods are found in voids throughout the Barimunya Member of both the upper and lower CID. The pods are generally small, however, there have been cases where examples of 10 m wide by 1.5 m high clay pods have been found [10]. The mineralogy of the Ochreous Clay Pods will generally be ochreous goethite with yellow clay or kaolinite with white clay.

IOWA EASTERN MEMBER

IOWA EASTERN CHANNEL IRON DEPOSIT

The Iowa Eastern CID is the youngest preserved CID in the Marillana Formation and has a maximum thickness of approximately 12 m. It occurs as an extensively weathered capping due to its location at the top on the CID [10] as shown in Figure 2.1.

IOWA EASTERN CLAY

The Iowa Eastern Clay zone ranges from 0-12 m thick and lies directly on top of the main CID as shown in Figure 2.1. It is commonly comprised of a white-brown kaolinitic clay to yellow goethitic clay [10]. Clasts of Banded Iron-Formation (BIF), chert (silica) and maghemite have been discovered in the base of the Iowa Eastern Clay zone [15].

The supplied samples originate from the Barimunya Member where the BHP Yandi operation mines CIDs [10]. The three iron ore samples, more specifically, are from the Upper CID (UCID), Lower CID (LCID) and from the Denatured Zone and are of -11.2 mm size fraction. Table 2.1 gives the identification name for each respective sample which will be used beyond this point for the remainder of the thesis. Additionally, the as supplied Moisture Content (MC) and corresponding Saturated Drained Moisture Content (SDMC) of each sample, and the typical geology, has also been included. It is important to note the moisture content measurements have been undertaken on a wet basis method.

Table 2.1 – Iron Ore Sample Details

Bulk Material Identification Name	*Ore Body*	*As Supplied Moisture Content*	*Typical Geology*
IOA	UCID	6.3% MC (~40% SDMC)	Goethite (~75 Wt.%), Hematite (~24 Wt.%), Magnetite and Quartz.
IOB	Denatured	13.4% MC (~50% SDMC)	Goethite (~98 Wt.%), Magnetite, Quartz and Kaolinite.
IOC	LCID	11.5% MC (~50% SDMC)	Goethite (~97 Wt.%), Magnetite, Quartz and Kaolinite.

The moisture content of the iron ore samples is critical in the determination of problematic behaviours that may be exhibited when negotiating the materials handling stream. The differences seen between the as supplied moisture contents, seen in Table 2.1, can be explained by the amount of ore that is mined beneath the water-table. A study completed by Golder Associates [16], found that at the Yandi operation of BHP, 75% of the CIDs are below the water-table where the maximum saturated thickness was found to be 80m deep. It was also determined that the typical mining water-table level is found around the denatured zone layer of the Barimunya Member [16].

Not only does mining CIDs below the water-table pose an immediate problem to the Yandi operation in relation to materials handling problems, the BHP Munjina operation, as an example, is in the exploration and mine planning phases and it was found that 100% of the CIDs are below the water-table, where the maximum saturated thickness was found to be 50m deep [16]. This exploitation of unattractive ore bodies, due to supply and demand of iron ore shows the importance for an understanding in the way problematic bulk materials can be handled. In addition to the moisture content of the iron ore samples, the mineralogical composition can also give an indication into the handling characteristics that may be experienced as the ore negotiates through the materials handling stream. The presence of goethite and kaolinite (white clay) in both IOB and IOC samples, as indicated in Table 2.1, can lead to the potential for problematic behaviour, which is explored in more detail in the subsequent section and chapters of this thesis.

2.3 DEFINITION OF WET AND STICKY BULK MATERIALS

The adhesion and cohesion of so-called problematic bulk materials is commonly caused by either the excessive moisture or increasing clay content that is found from mining ore bodies that are typically disregarded. These types of problematic bulk materials are referred to as Wet and Sticky Material (WSM) due to the nature of their physical properties and the mechanisms that are present when they negotiate the materials handling stream.

Within the materials handling stream, WSMs cause significant downtimes due to events such as blockages of bins, hoppers and transfer chutes, remains left in train wagons and dump trucks, as well as conveyor belt carry back [1, 2]. In addition, downtimes can also be caused from belt runoff events where mistracking of the conveyor belt can cause costly damage to the materials handling operation, whether it’s from damage to the structure and idler rolls or the conveyor belt itself. These types of events are typically caused from overloaded belts where a prior blockage has dislodged and fallen onto the conveyor. The cost that WSMs can add to the price of bulk materials due to sub-optimal running conditions outlined above is attributed to system downtime where some cases have reported downtimes of approximately 7-30 hours per week [3].

2.3.1 TESTING METHODS FOR WET AND STICKY BULK MATERIALS

The economic consequences that WSMs can have on the mining industry are of critical concern and require extensive thought and research to understand the mechanisms that cause their problematic behaviours. Conventional testing methods that are used for the design of bulk material handling systems are extremely effective when dealing with free-flowing bulk materials. These testing methods have been developed from the flow property theory which is presented in the work of Jenike [4], Roberts [1], Arnold et al. [17] and Johanson [18].

The conventional testing methods utilise quantitative measurements to optimise the design process of bulk handling equipment such as storage bins, feeders and chutes. Although the fundamental flow properties are well documented, the adhesive and cohesive characteristics that WSMs can possess are still yet to be fully understood. From this, it is necessary to develop testing methods that are capable to quantify the amount of adhesion and cohesion within a bulk material sample.

For the measurement of the interaction between the wall lining material and the adhesion present in a bulk material sample, a wall adhesion tester has been used. The wall adhesion tester, as indicated in Figure 2.2, was further developed from the initial work of Plinke et al. [8] to gain a quantifiable measure for the tensile force that would be acting between a wall liner and the bulk material sample. The adhesive tensile stress can be defined as:

$$\sigma_{\mathrm{WA}} = \frac{F_{WA}}{A} \tag{2.1}$$

where: F_{WA} is the separating force of the bulk material from the surface [N].
A is the contact area of the adhesion partners [m^2].

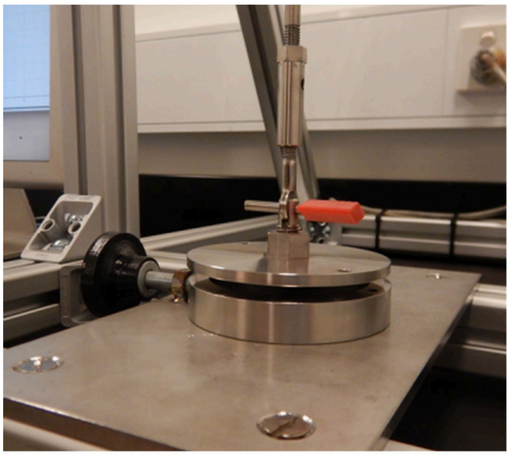

Figure 2.2 – Wall adhesion tester.

For the measurement of the interaction between the inter-particle adhesion present within a bulk material sample, an inter-particle adhesion tester has been used. The inter-particle adhesion tester, as indicated in Figure 2.3, was further developed by the author from the initial work of Ashton et al. [19]. Similar to the wall adhesion tester, the inter-particle adhesion tester is used to gain a quantifiable measure for the tensile force that would be present between the particles of the bulk material. The base of the cell has a ribbed pattern to assist the cell in holding the sample while the experiment is being conducted. The inter-particle adhesive tensile stress can be defined as:

$$\sigma_{\mathrm{IPA}} = \frac{F_{IPA}}{A} \tag{2.2}$$

where: F_{IPA} is the force to internally fail the bulk material sample [N].
A is the contact area of the adhesion partners [m^2].

Figure 2.3 – Inter-Particle adhesion tester.

The two methods presented above are by no means fully developed in relation to the way adhesion and cohesion can be measured in the most accurate way. They do, however, allow for a quantifiable measure for the adhesion present within the samples that are used in this research, to be identified. Section 2.4.9.1 and 2.4.9.2 describes the testing procedures used and the corresponding results are also presented. In addition, the values obtained from the wall adhesion and inter-particle adhesion testing will also be used to validate the theoretical models presented in Section 3.3 and Section 4.3.

2.4 BULK MATERIAL FLOW PROPERTY TESTING METHODS AND RESULTS

The physical properties and characteristics (flow properties) of the bulk material samples need to be quantified for the determination of parameters to be used in the theoretical modelling and Discrete Element Method (DEM) phases of the research. The following section outlines the procedures used for the determination of the flow properties of the three iron ore samples and the corresponding results are also presented. The flow property testing has been undertaken by the author in conjunction with the staff at TUNRA Bulk Solids from the University of Newcastle.

2.4.1 IRON ORE SAMPLE PREPARATION

The iron ore samples were supplied from the processing stream directly after the primary crusher, from site, resulting in the top size of the material to have approximately a 300 mm size lump in each of the samples. This was deemed to be excessively large for the lab scale testing that needed to be conducted. To create a representative product that would be found on site further down the processing stream, the samples needed to be prepared accordingly. The sample preparation was conducted in accordance with the flow sheet shown in Figure 2.4. It is appropriate to identify that the top size material required to be crushed to create a representative sample that would be found in industry. Simply screening the samples and disposing of the top size material would have resulted in behaviours that were much more problematic than what would be found on site. This is due to the increased clay ridden fines component that would have resulted if the top size iron dominant lump was not blended (after crushing) through each of the supplied samples.

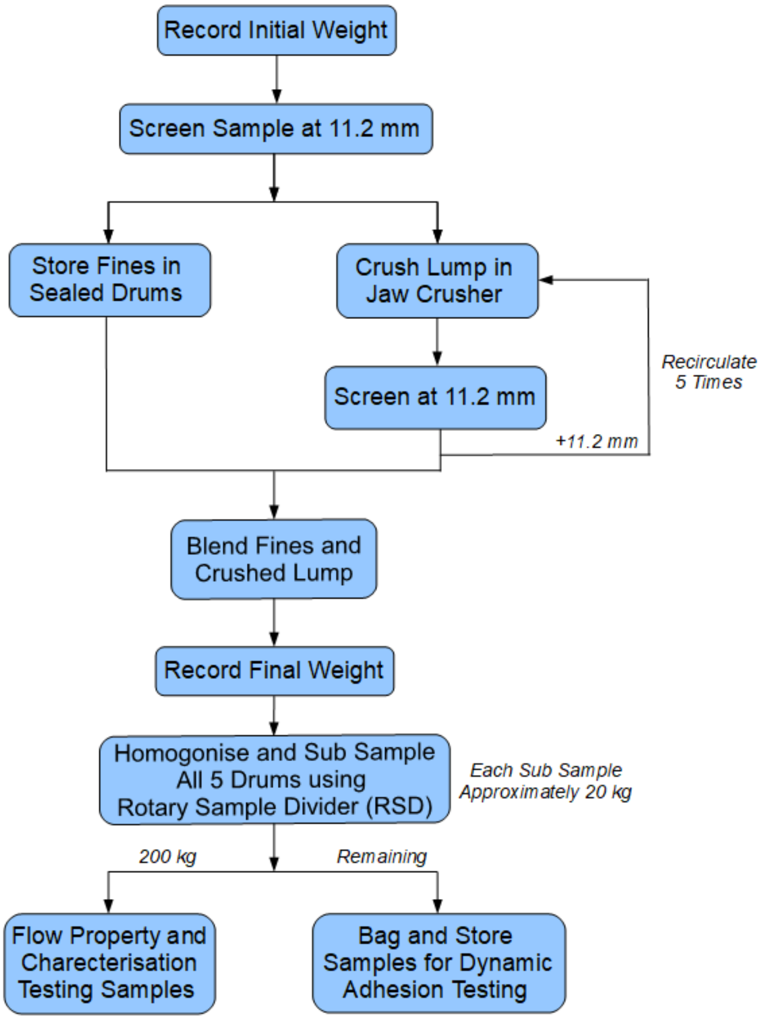

Figure 2.4 – Sample preparation flow sheet.

Once the sample preparation was complete using the procedure outlined in Figure 2.4, the characterisation of the iron ore samples could be undertaken. Furthermore, upon completion of these characterisation tests, the determination of the moisture contents to be used for the recirculating system experiments (as outlined in Section 6.2) was undertaken.

2.4.2 SATURATED MOISTURE CONTENT

The Saturated Drained Moisture Content (SDMC) of a bulk material sample is used for the determination of the *"worst-case"* moisture content when designing bulk material handling equipment [20]. This worst-case moisture is where the peak strength of the bulk material is found, and the corresponding materials handling issues will typically begin to occur. As a guide, the worst-case moisture for a generic bulk material sample is around 60% of the SDMC [20]. This will be of particular relevance as a WSM is generally found to correspond to, or in some cases be beyond, the worst-case moisture content.

There is no specific standard for the determination of the SDMC, however, a procedure has been put forth in Appendix B of AS 3880 [20] to be used as an informative guide in the calculation of the SDMC. The SDMC is determined using the following:

$$SDMC = \frac{(m_{drained} - m_{cone}) - (m_{full} - m_{cone})}{m_{drained} - m_{cone}} \times 100 \tag{2.3}$$

where:
- $m_{drained}$ is the final mass of the drained sample [g].
- m_{cone} is the mass of the empty cone [g].
- m_{full} is the mass of the cone filled with bulk material [g].

The SDMC for the three iron ore samples are presented in Table 2.2. The sample size fractions tested were -11.2 mm Run-of-Mine (ROM) samples to be used for the dynamic adhesion testing in Section 6.2 and -4 mm samples used for the characterisation testing in Section 2.4.8 and Section 2.4.9.

Table 2.2 – Saturated Drained Moisture Content of Samples

SDMC [%]	**IOA**		**IOB**		**IOC**	
	-11.2 mm Fraction	*-4 mm Fraction*	*-11.2 mm Fraction*	*-4 mm Fraction*	*-11.2 mm Fraction*	*-4 mm Fraction*
10	1.5	2.6	2.7	3.5	2.3	3.6
20	3.1	5.2	5.4	7.1	4.5	7.3
30	4.6	7.8	8.0	10.6	6.8	10.9
40	6.2	10.4	10.7	14.2	9.1	14.6
50	7.7	13.1	13.4	17.7	11.3	18.2
60	9.3	15.7	16.1	21.3	13.6	21.9
70	10.8	18.3	18.8	24.8	15.9	25.5
80	12.4	20.9	21.4	28.4	18.1	29.2
90	13.9	23.5	24.1	31.9	20.4	32.8
100	15.5	26.1	26.8	35.5	22.7	36.5

2.4.3 DUST EXTINCTION MOISTURE CONTENT

During the transportation of a bulk material, the generation of dust particulates can occur when insufficient moisture is present. The moisture content where the suppression of dust particles occurs is typically referred to as the Dust Extinction Moisture Content (DEMC). There is a fine balance for the amount of moisture required for the suppression of dust, where excess moisture may cause material handling problems. With this in mind, it is necessary to gain an understanding for the minimum moisture requirement for the three iron ore samples.

The determination of the DEMC is undertaken in accordance with AS 4156.6 [21] which uses a dustiness tumble drum test to determine the dust to moisture relationship for a particular bulk material where a sample size fraction of -6.3 mm was used. AS 4156.6 [21] has been developed for the determination of the DEMC of coal, where the modification of the amount of *"charge"* material into the tumble drum has been increased from 1 kg to 2.5 kg to account for the higher bulk density of iron ore. The laboratory testing conditions must lie within the limits of $20°C \pm 2°C$ for temperature and $63\% \pm 2\%$ for the relative humidity. The Dust Number is determined using the following:

$$Dust\ Number = \frac{(m_{after} - m_{bag})}{m_{sample}} \times 100{,}000 \tag{2.4}$$

where: m_{after} is the final mass of the filter bag and dust [g].

m_{bag} is the initial mass of the filter bag [g].

m_{sample} is the mass of the sample in the tumble drum [g].

The DEMC of a bulk material is found when a dust number of ten is achieved. The DEMC for the three iron ore samples are presented in Table 2.3.

Table 2.3 – Dust Extinction Moisture Content of Samples

Bulk Material Sample	*Dust Extinction Moisture Content [% MC]*
IOA	5.1
IOB	10.6
IOC	9.0

2.4.4 PARTICLE SIZE DISTRIBUTION

The determination of the Particle Size Distribution (PSD) of a bulk material can give an indication into the potential moisture retention of a sample due to a higher fines component. Highly friable *"soft"* ores will tend to breakdown at a much higher rate when compared to *"harder"* ores [22].

PSDs on the three iron ore samples have been undertaken in accordance with ISO 4701:2008(E) [23] on a dry sieving basis, where the distribution curves are found in Figure 2.5. A summary of the d10 and d50 percent finer values are also outlined in Table 2.4. This allows for a more convenient comparison of the key size fraction components of the three iron ore samples.

Table 2.4 – Percent Finer Comparison of Samples

Bulk Material Sample	*Percent Finer [%]*	
	d10 [mm]	*d50 [mm]*
IOA	0.304	4.096
IOB	0.215	2.679
IOC	0.142	1.640

The usual procedure that is undertaken for the determination of a PSD test includes a sample that is placed into the top of a series of sieves which are shaken for a standardised time (20 minutes) and at a standard frequency (40 Hz). After this, each sieve is weighed, and the retained mass recorded for each particle size fraction. The percentage of material retained for each particle size is then used to produce the distribution curves which are presented in Figure 2.5, for the supplied iron ore samples. The lower particle size limit of the PSD testing procedure is 45 µm which is collected in a base tin. This sub 45 µm sample is generally used for the classification of clays found in the sample, which will be explained in Section 2.4.5.

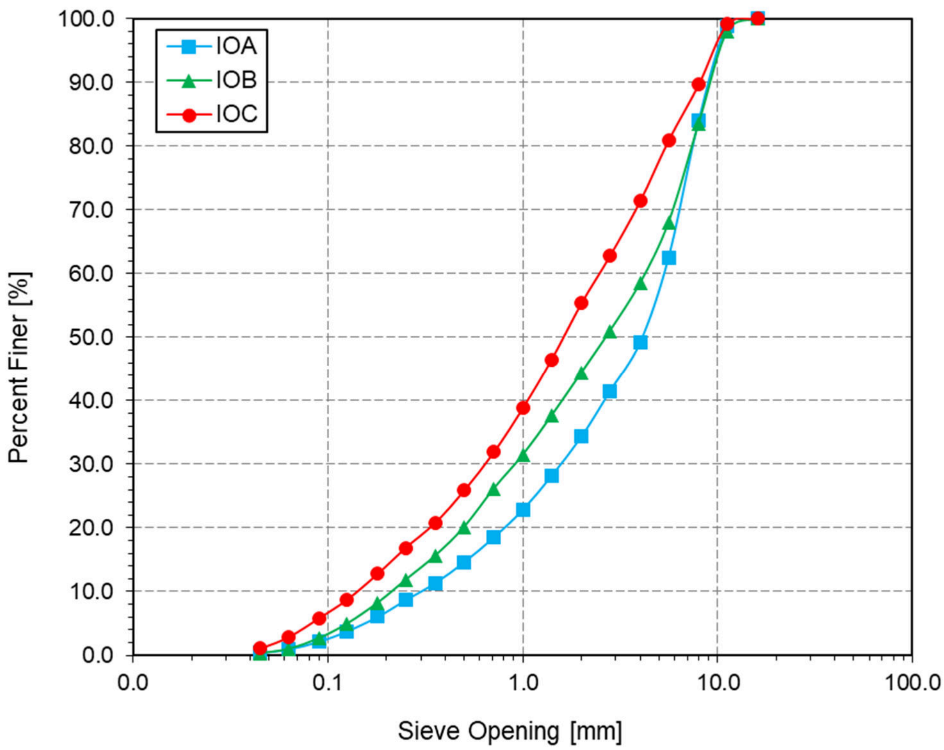

Figure 2.5 – Particle size distribution of iron ore samples.

2.4.5 CLAY CLASSIFICATION

By way of background, the United States Department of Agriculture [24] breaks down the classification of soil texture into the following categories of sand (2000 – 50 µm), silt (50 – 2 µm) and clays (<2 µm). The clay category is regarded as the finest inorganic fraction and is typically formed by the weathering of the larger particle size fractions [25]. This definition varies from that of the Clay Mineral Society, which considers clay particles to be < 74 µm [26 - 27]. Research by Ranville and Schmiermund [28] believe that the range of 2 µm to 5 µm describes the hydro-dynamic behaviour of large colloids better, which coincides with the slit-clay boundary in soils [28]. The relative proportions of the separates determine the texture of the soil sample. Fine textured soils are plastic when wet and harden when dry. The United States Department of Agriculture recognises 12 different soil textures as shown in Figure 2.6:

1. Sands, which are all soils characterised by a sand content of > 75 % [25]. This group includes sand and loamy sand.
2. Loams, which are all the soils characterised by loam, sandy loam and silt loam textures [25]. The soil classes include loams, sandy loam soils and silt loam soils.
3. Clay loams, which are all the soils characterised by clay loam, sandy clay loam, and silt textures [25]. This group includes the clay loam soils, sandy clay loam soils and silty clay loam soils.
4. Clays, which are all the soils containing 35 % clay [25]. The soil classes in the group include the clay soils, sandy clay soils, and silty clay soils.

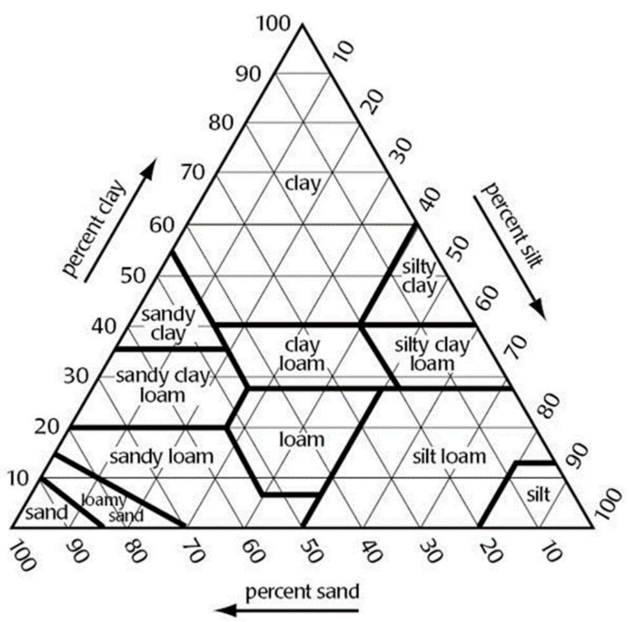

Figure 2.6 – United States Department of Agriculture guide for soil textural classification (Soil Survey Staff, 1951).

The determination of the texture of the iron ore samples has been undertaken using a Malvern Mastersizer 2000E Optical Bench [29]. The Malvern unit can analyse the particle size of the sample from 0.1 µm to 1000 µm. The sample is analysed using a laser beam, where the sample is distributed via circulating water and a central detector measures the light reflectance for the determination of the particle sizing. A summary of the texture of the three iron ore samples is presented in Table 2.5.

Table 2.5 – Texture of Samples

Bulk Material Sample	*Sand [%]*	*Silt [%]*	*Clay [%]*	*Classification*
IOA	29.76	65.73	4.51	Silt Loam
IOB	20.80	72.45	6.75	Silt Loam
IOC	23.57	68.51	7.92	Silt Loam

2.4.6 BULK DENSITY

The bulk density of a bulk material is the mass of the sample per unit volume and is determined using:

$$\rho_{bulk} = \frac{mass_{bulk}}{volume_{total}} \tag{2.5}$$

There are two forms of bulk density measurements that are of importance and of interest within the bulk material handling field, and are explained in the following sections.

2.4.6.1 LOOSE POURED

The loose poured bulk density is determined by carefully pouring the sample into a graduated cylinder of known volume, without introducing any form of consolidation or compaction to the testing specimen. For the case of this research the cylinder volume was 0.0073 m^3. The loose poured bulk density of the three iron ore samples are presented in Table 2.6,Table 2.7 and Table 2.8 respectively and show each of the corresponding moisture contents that have been tested. It is important to note that an -11.2 mm size fraction of each sample was tested.

Table 2.6 – Loose Poured Bulk Density of IOA

Sample Moisture Content	*Loose Poured Bulk Density [kg/m³]*
6.3% MC (~40% SDMC)	1651
7.8% MC (~50% SDMC)	1583
9.3% MC (~60% SDMC)	1573
10.7% MC (~70% SDMC)	1668
11.5% MC (~75% SDMC)	1680

Table 2.7 – Loose Poured Bulk Density of IOB

Sample Moisture Content	*Loose Poured Bulk Density [kg/m^3]*
13.4% MC (~50% SDMC)	1485
14.6% MC (~55% SDMC)	1385
15.9% MC (~60% SDMC)	1333
17.3% MC (~65% SDMC)	1342
18.5% MC (~70% SDMC)	1467

Table 2.8 – Loose Poured Bulk Density of IOC

Sample Moisture Content	*Loose Poured Bulk Density [kg/m^3]*
11.5% MC (~50% SDMC)	1500
13.6% MC (~60% SDMC)	1459
14.8% MC (~65% SDMC)	1468
16.0% MC (~70% SDMC)	1703
18.2% MC (~80% SDMC)	1822

2.4.6.2 COMPRESSIBILITY

The determination of the compressibility of the bulk material samples has been conducted using the large bulk density (compressibility) tester. This test is a modified version of the test outlined in AS 3880: 2017 [20] and is used to measure the bulk density of the sample as a function of the major consolidation pressure. The tester consists of a 305 mm diameter and 100 mm deep cell, which is typically filled with -11.2 mm Run-of-Mine (ROM) product. Variable normal loads are applied to the sample by means of a consolidation lid and hydraulic cylinder, and the compression of the sample is measured with a displacement transducer. A schematic of the testing apparatus is shown in Figure 2.7.

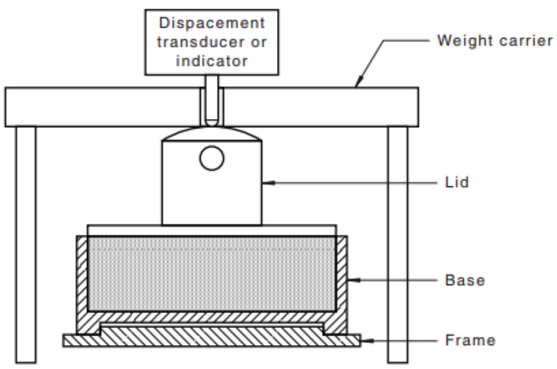

Figure 2.7 – Schematic of bulk density (compressibility) tester (AS 3880, 2017).

By using Equation 2.5 and the loading applied during testing, a relationship between bulk density and the consolidation pressure can be established. Figure 2.8, Figure 2.9 and Figure 2.10 show the bulk density results for each of the respective iron ore samples. This testing has been undertaken in accordance with an adapted version of AS 3880:2017 [20] which allows for the testing of ROM bulk materials.

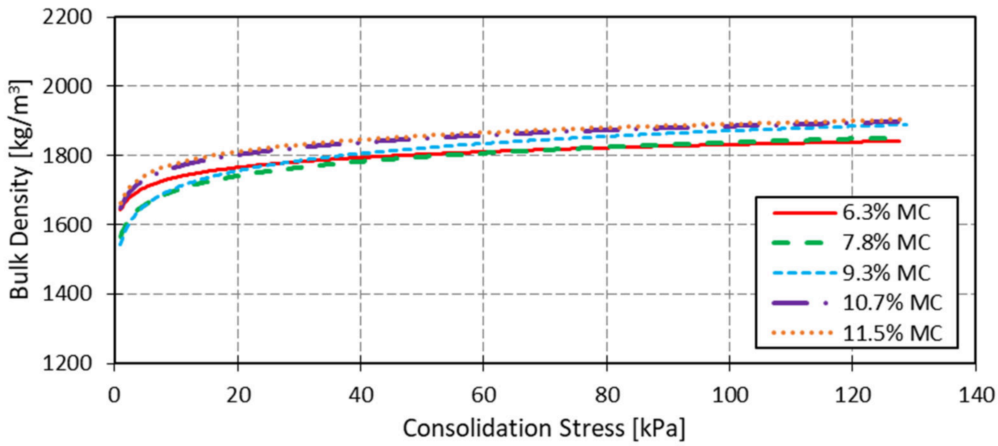

Figure 2.8 – Compressibility bulk density testing results for IOA.

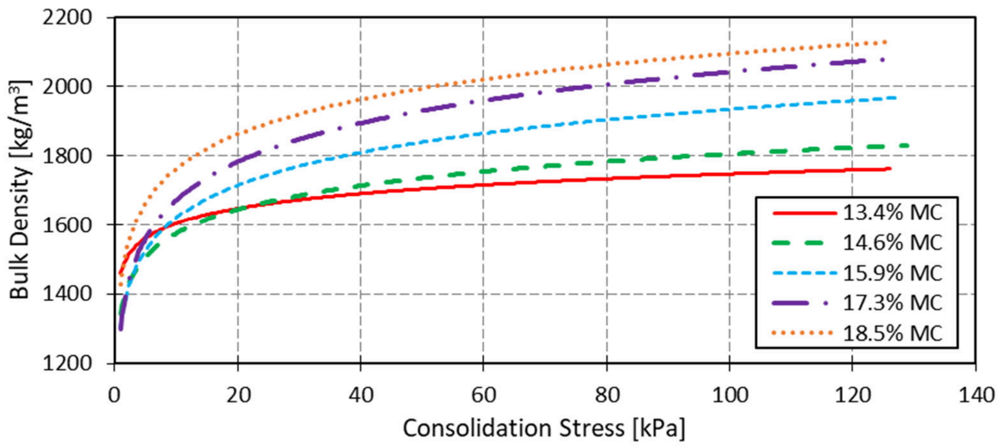

Figure 2.9 – Compressibility bulk density testing results for IOB.

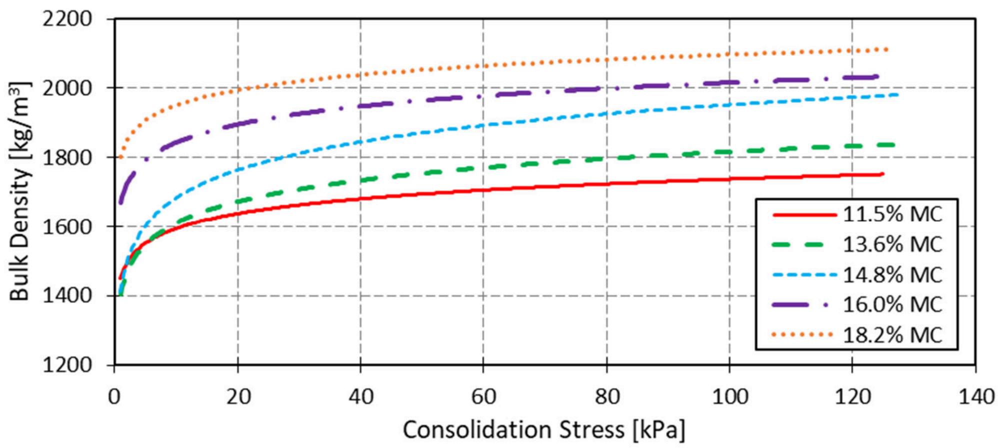

Figure 2.10 – Compressibility bulk density testing results for IOC.

2.4.7 PARTICLE SOLIDS DENSITY

The determination of the particle density of a bulk material sample is typically achieved using a nitrogen displacement pycnometer solids density tester. The particle solids density of a bulk material is the mass of the particle per unit of its true volume and can be determined using:

$$\rho_{particle} = \frac{mass_{total}}{volume_{particle}} \tag{2.6}$$

The particle solids density of the samples was conducted in accordance with AS1289.3.5.1-2006 [30] where the particle density of the three iron ore samples are presented in Table 2.9.

Table 2.9 – Particle Solids Density of Samples

Bulk Material Sample	*Particle Density [kg/m³]*
IOA	3497
IOB	4271
IOC	4091

2.4.8 SHEAR TESTING (FLOW FUNCTION DETERMINATION)

The internal strength of bulk materials is commonly measured using direct shear testing procedures, where the most notable measurement technique is the Jenike shear test apparatus [4]. The determination of the shear strength of a bulk material depends on a multitude of factors, including, moisture content, particle size distribution, temperature, consolidation pressure, time of consolidation and particle shape [1].

Roberts [1] conducted studies to see the influence of particle size on the shear strength of Pyrophyllite, where the reduction of particle size corresponded to the increase in shear strength, as shown in Figure 2.11. It was also shown that when the particle size fractions of the bulk material were mixed together, the shear strength of the material was similar to the minus 425 µm. For this reason, it can be determined that for a ROM sample, the typical size fraction that is tested in the Jenike shear tester will be -4 mm.

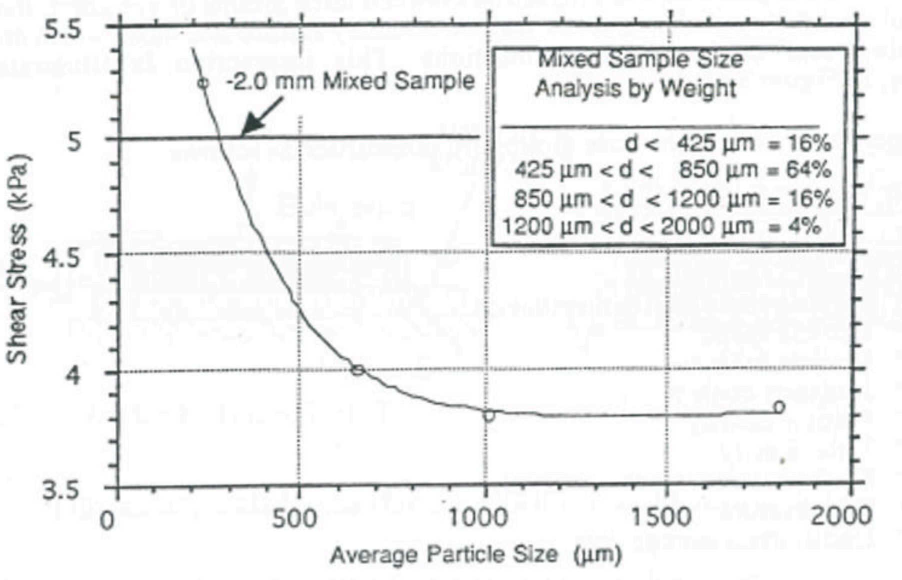

Figure 2.11 – Effect of particle size on the shear strength of pyrophyllite (Roberts, 1998).

The Jenike shear cell consists of a circular cross section, a gravity vertical loading system and an automated shear loading device, which operates at 2.5 mm/min. A schematic is shown in Figure 2.12 below. Typically, the internal diameter of the shear ring is 95 mm, which will give an approximate area of the shear plane as 7000 mm^2. The application of the shearing load is applied and measured for a range of normal loading conditions, where the resulting major and minor Mohr circles are recorded. From this, a series of yield loci are generated, as shown in Figure 2.13.

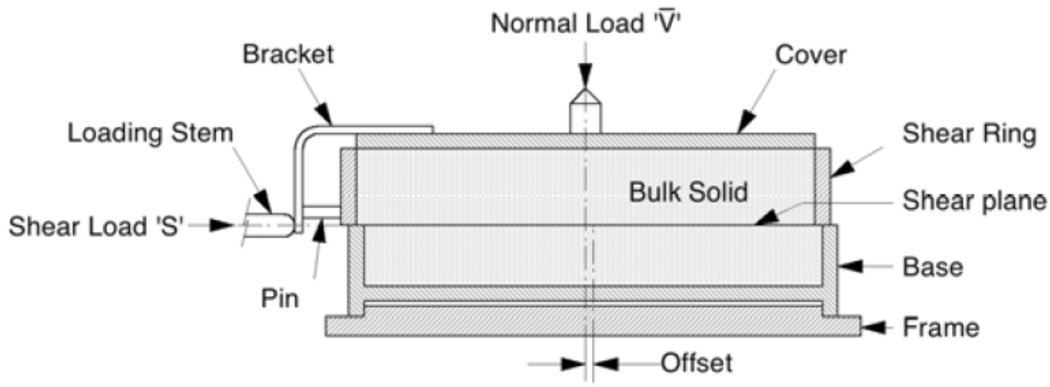

Figure 2.12 – Schematic of Jenike direct shear cell testing apparatus (Roberts, 1998).

From the yield loci, the following properties of the bulk material can be determined:

1. Flow Function which is a measurement of the bulk material's unconfined yield strength as a function of the major consolidation pressure (as described in Section 1.2);
2. Effective Angle of Internal Friction, δ, which is the angle of the line from the origin and lies tangent to the major Mohr circle. This forms the Effective Yield Locus (EYL);
3. Angle of Internal Friction, φ_t, which is the angle of the line at the point of tangency of the Instantaneous Yield Locus (IYL) and the major Mohr circle;
4. The measurement of cohesion is determined by the extrapolation of the IYL to the shear stress axis, where the corresponding normal (consolidation) stress would be zero.

This allows the Flow Function of a bulk material to be classified according to its level of internal strength, as described in Section 1.2. Typically, the Flow Function of a non-cohesive bulk material will coincide with the horizontal axis at zero and show a very low strength across a range of consolidation loads. Additionally, for non-cohesive bulk materials, such as dry sand or gravel, the internal angles of friction, δ and φ_t will be equal.

The Flow Function of a cohesive bulk material and/or WSM will typically show strength of some description across all consolidation loading conditions. In addition, it can be quite common for a cohesive bulk material to have high strength at low consolidation loads, which is the cause of why they tend to hold their shape, even when not stressed.

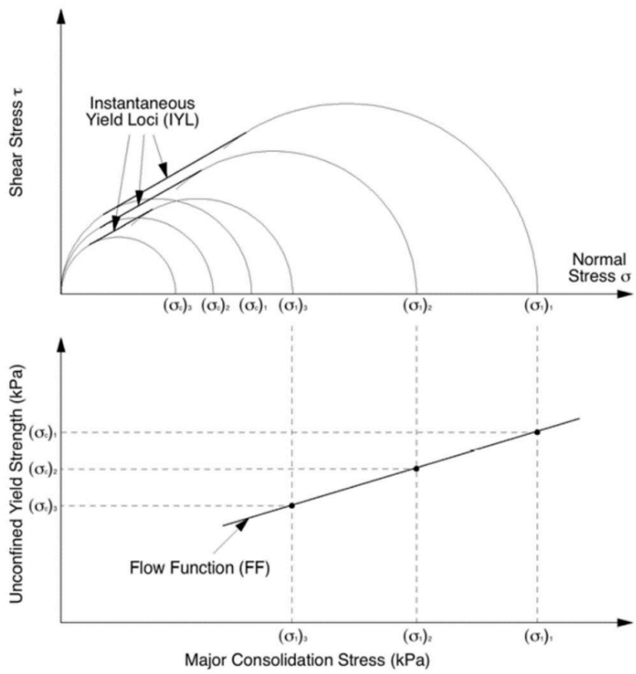

Figure 2.13 – Determination of the Yield Locus and corresponding flow function using direct shear test (Roberts,1998).

The iron ore samples that have been tested are in two size fractions as previously discussed; namely -11.2 mm and -4 mm. For the correlation of the theoretical models in the following chapters it is necessary to undertake the characterisation testing (-4 mm samples) in Section 2.4.8 and Section 2.4.9 and the dynamic adhesion testing (-11.2 mm ROM sample) in Section 6.2, at equivalent moisture contents. This was achieved by using the SDMC presented in Section 2.4.2.

Table 2.10 shows the corresponding moisture contents used for the characterisation testing of each iron ore sample. It is appropriate to identify that moisture contents lower than those used in the dynamic adhesion testing have been undertaken and included to give an insight into the possible handleability of these samples. Furthermore, by drying out these particular samples, it should be noted that the structure of the clays potentially break down. This may cause different material behaviours than those experienced by the same bulk materials, which are at an equivalent moisture content, without the need for drying.

Table 2.10 – Characterisation Testing Moisture Content of -4 mm Samples

IOA	***IOB***	***IOC***
7.8% MC (~30% SDMC)	10.6% MC (~30% SDMC)	10.0% MC (~30% SDMC)
10.5% MC (~40% SDMC)	14.2% MC (~40% SDMC)	14.6% MC (~40% SDMC)
13.1% MC (~50% SDMC)	17.8% MC (~50% SDMC)	18.2% MC (~50% SDMC)
15.7% MC (~60% SDMC)	21.3% MC (~60% SDMC)	21.9% MC (~60% SDMC)
18.3% MC (~70% SDMC)	24.9% MC (~70% SDMC)	25.6% MC (~70% SDMC)

The flow functions for the three iron ore samples have been undertaken in accordance with AS 3880 [20], where the results are presented in Figure 2.14, Figure 2.15 and Figure 2.16 for each of the respective samples. It is appropriate to identify that the limitations of the Jenike direct shear test resulted in plastic characteristics (unable to obtain a defined shear plane) being shown for IOA at 15.7% MC, IOB at 24.9% MC and IOC at 25.6% MC. Testing above these moistures for each sample was not undertaken as it has been experienced previously by the author, that the same plastic characteristics would result.

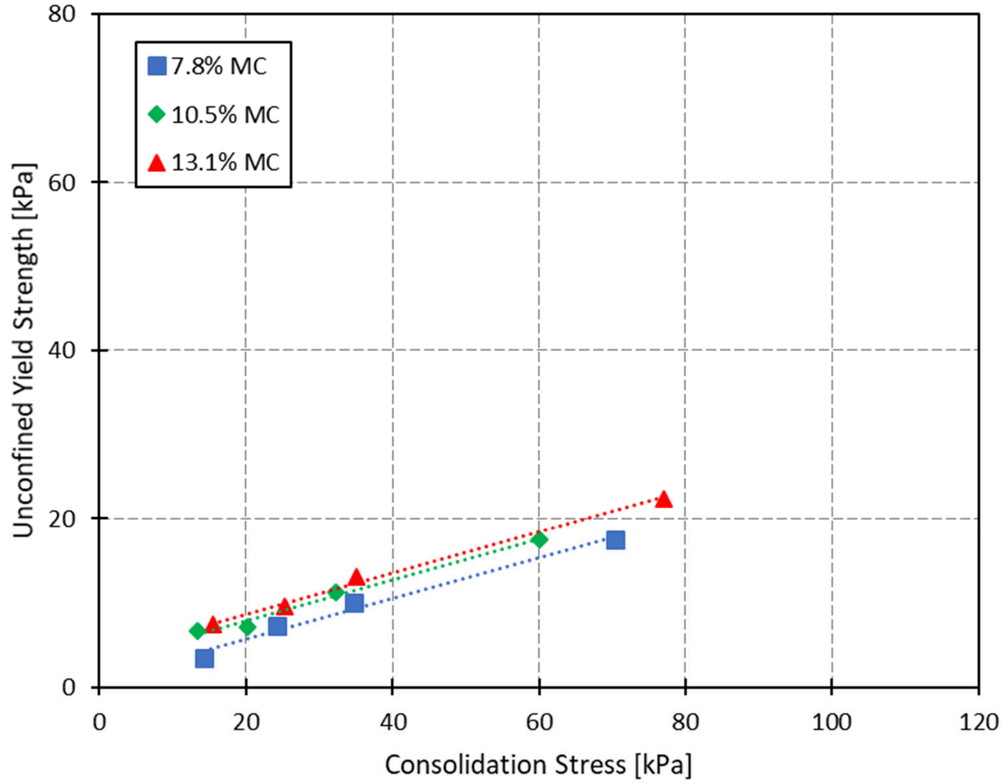

Figure 2.14 – Flow functions for IOA.

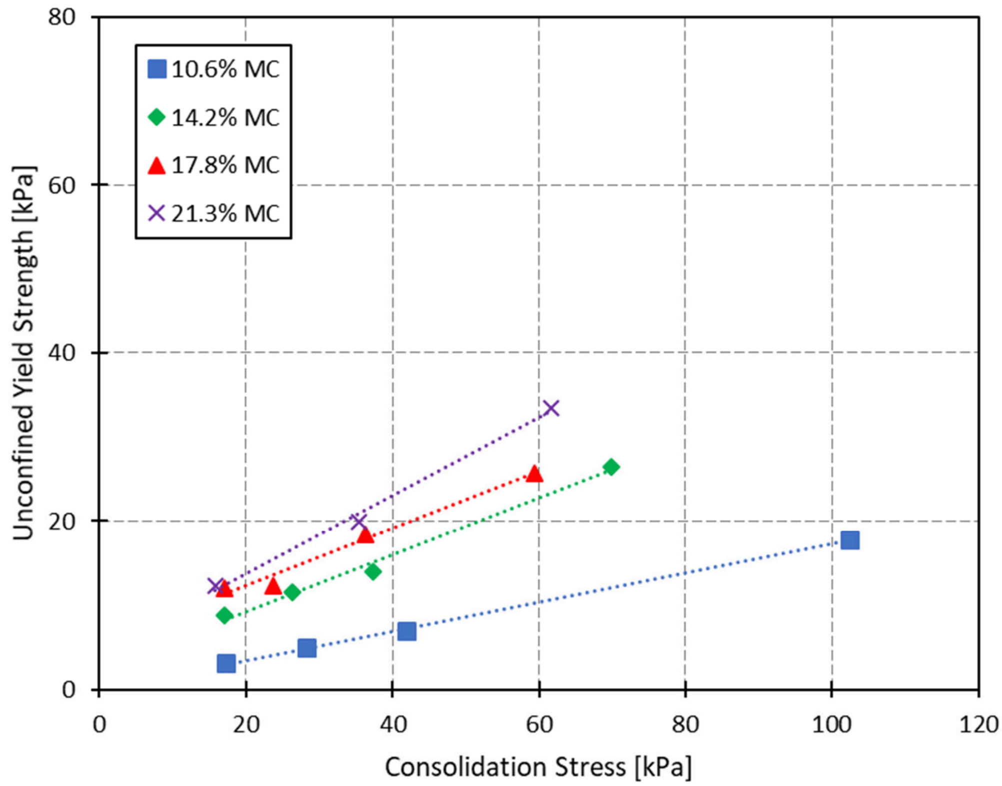

Figure 2.15 – Flow functions for IOB.

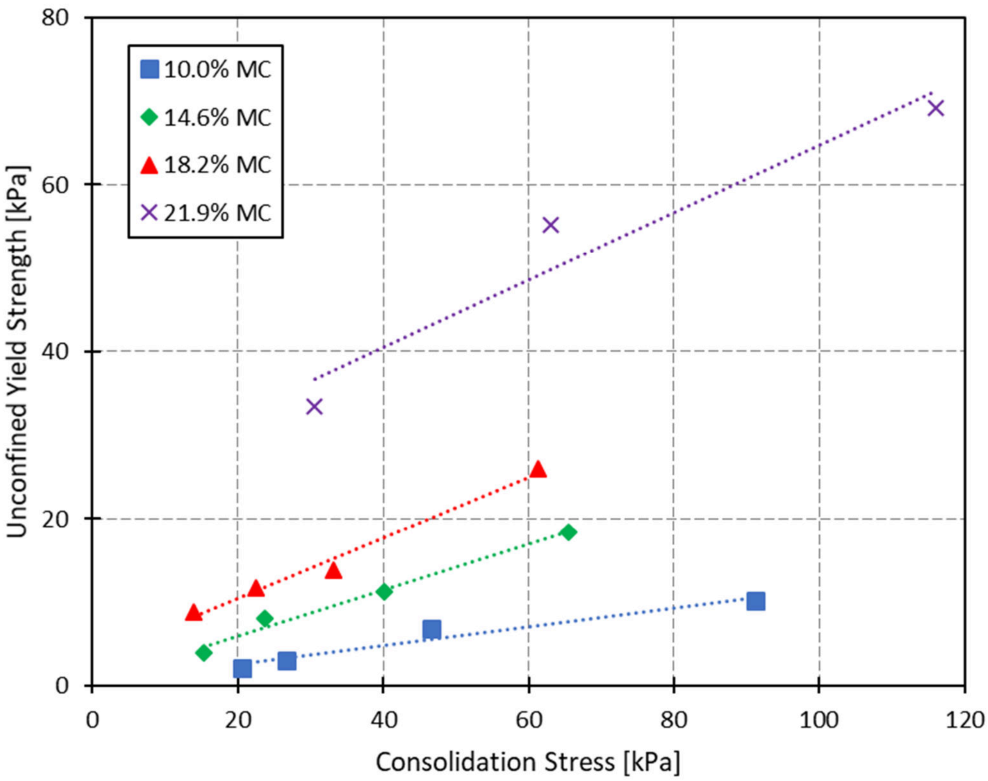

Figure 2.16 – Flow functions for IOC.

When the flow functions for IOA are considered, very little variation can be seen for the three tested moisture contents (shown in Figure 2.14). Additionally, when IOA (shown in Figure 2.14), IOB (shown in Figure 2.15) and IOC (shown in Figure 2.16) are considered for approximately 30% SDMC, similar unconfined yield strengths result which do not exceed 10 kPa for low consolidation conditions (approximately 30 kPa). This is not the case when the higher tested moisture contents for IOB and IOC are considered. For IOB (shown in Figure 2.15) the peak strength was exhibited for 21.3% MC (60% SDMC). Additionally, for IOC (shown in Figure 2.16) the peak strength was exhibited for 21.9% MC (60% SDMC). It is also appropriate to note that IOC at 21.9% MC showed the highest unconfined yield strength. This was observed to be approximately double the internal strength for the peak values of IOB (shown in Figure 2.15) and approximately three times the values of IOA (shown in Figure 2.14). One of the interesting observations which arose from the current testing program, was the peak unconfined yield strength for each of the respective samples containing clays (such as IOB and IOC) was achieved at approximately 60% SDMC. When materials which did not have clays present (such as IOA) are considered, the peak unconfined yield strength was experienced at approximately 50% SDMC. Furthermore, testing above these peak strength moisture content values for each sample was conducted however limitations of the Jenike direct shear test resulted in plastic characteristics.

2.4.9 TESTING MEASUREMENTS FOR WET AND STICKY BULK MATERIALS

The determination of adhesive force that is present between a bulk material and material handling surface can be quantified using a wall adhesion tester. Additionally, the determination of adhesive force that is present within a bulk material can be quantified using an inter-particle adhesion tester. Both of these testers were presented in Section 2.3.1 and the following section outlines the testing procedures and a summary of the results obtained for the three iron ore samples.

2.4.9.1 WALL ADHESION TESTING

The adhesive force that is present between a bulk material and material handling surface can be quantified using a wall adhesion tester. For a repeatable set of experiments two clearly defined steps were established. The first step is the consolidation of the sample, where a pre-determined pressure is applied with use of weights on the consolidation lid. Once this is achieved the sample is rotated and a loading stem is attached where the force response is recorded. A schematic of the procedure is shown in Figure 2.17.

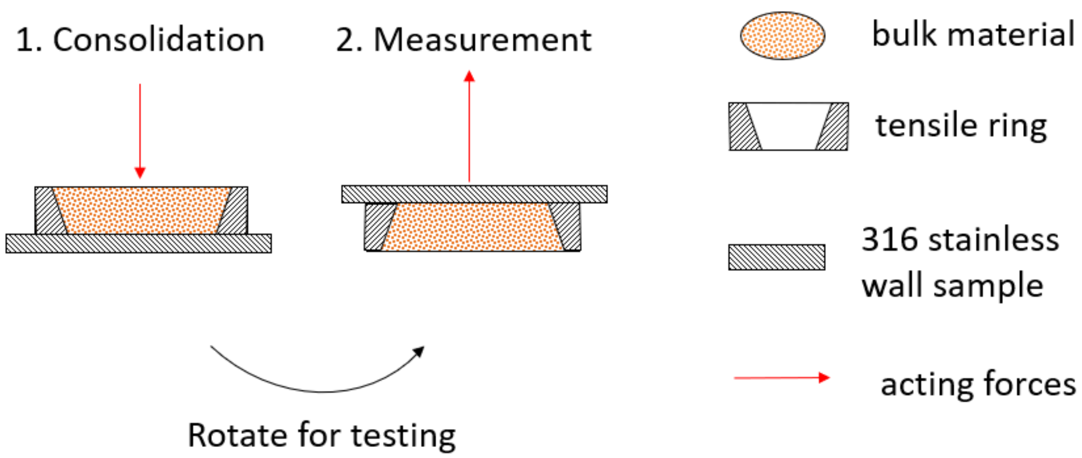

Figure 2.17 – Schematic of wall adhesion testing procedure.

These tests are typically repeated for a range of consolidation pressures and moisture contents, to gain an understanding of the wall adhesion threshold of a problematic material. The consolidation process follows the standard wall friction testing technique, as described in 'Standard Shear Testing Technique for Particulate Solids Using the Jenike Shear Cell' [7]. A typical measurement of adhesive tensile strength can be divided into four sections:

1. Constant datum value resulting from the weight of the tensile mechanism;
2. The tensile force increases until failure occurs at a peak force;
3. The tensile force decreases until all adhesive bonds are broken;
4. The remaining tensile force results from the material's bodyweight and the weight of the tensile mechanism.

A schematic of a typical testing measurement from the wall adhesion tester can be found in Figure 2.18, where σ_{a0} will be the adhesive tensile force.

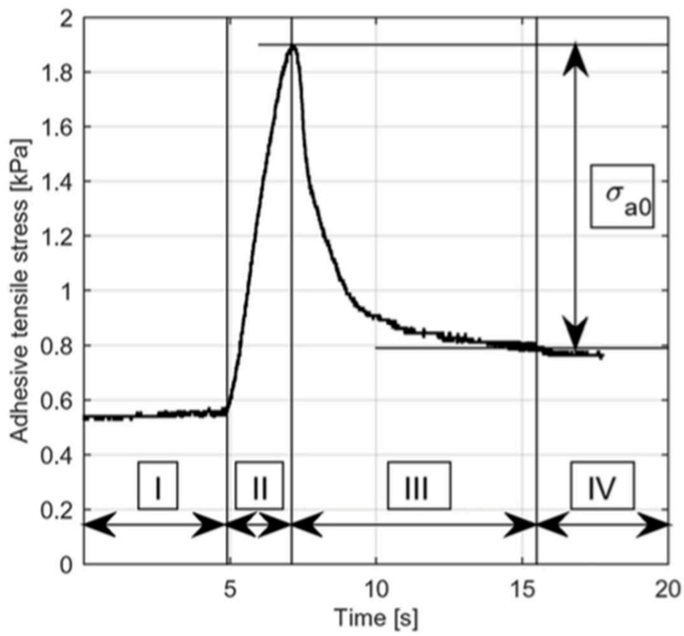

Figure 2.18 – Typical force measurement of a wall adhesion test (Plinke et al., 2016).

A summary of the wall adhesion results are presented in Figure 2.19, Figure 2.20 and Figure 2.21 for each of the respective iron ore samples. It is appropriate to identify that materials that did not exhibit adhesive characteristics were shown for IOA at 7.8% MC, IOB at 10.6% MC and IOC at 10.0% MC. Testing below these moistures was not undertaken as it has been experienced previously by the author, that the same characteristics would result.

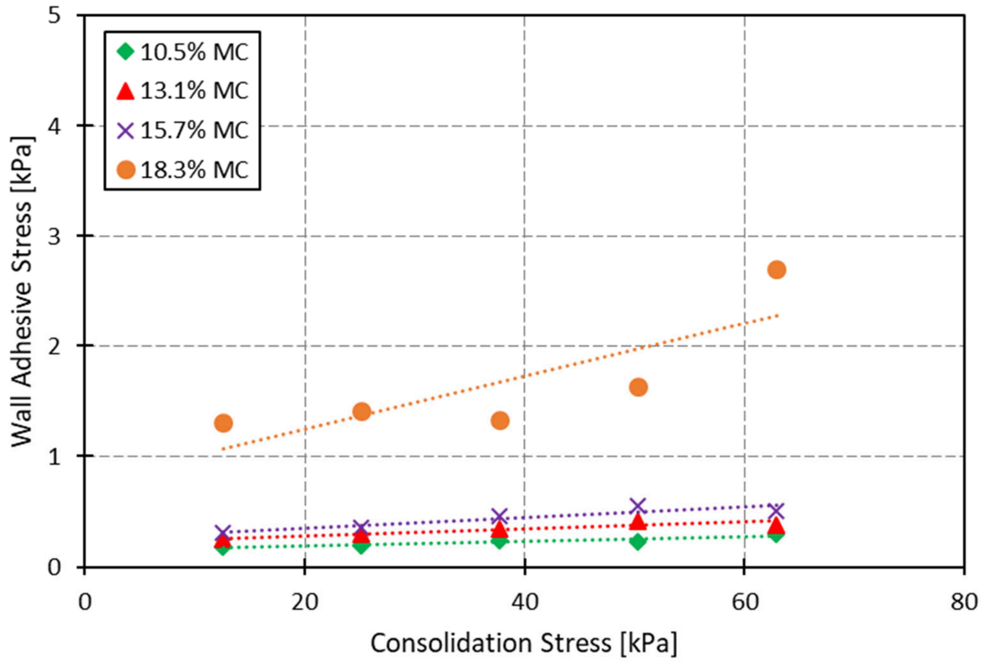

Figure 2.19 – Wall adhesion testing results for IOA.

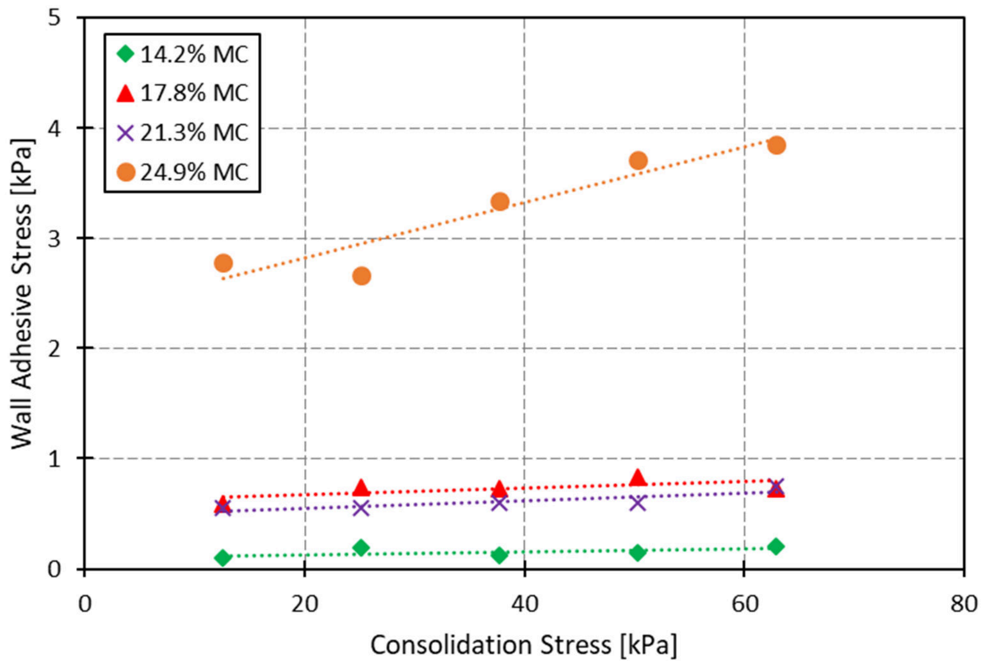

Figure 2.20 – Wall adhesion testing results for IOB.

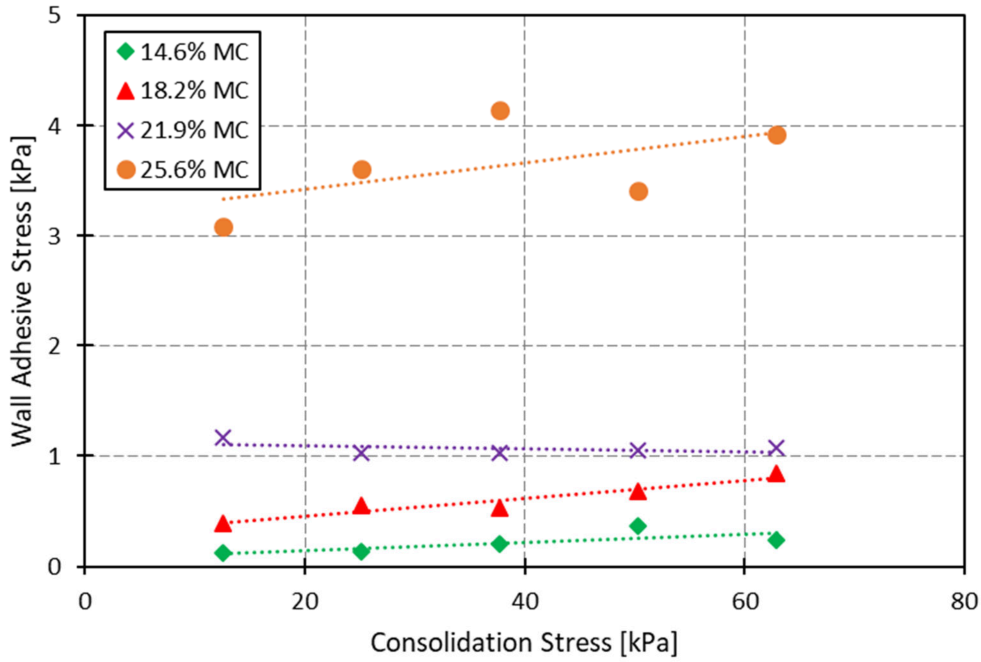

Figure 2.21 – Wall adhesion testing results for IOC.

When the wall adhesion testing results for IOA are considered, very little variation can be seen for the lower three tested moisture contents (shown in Figure 2.19). Unlike the flow function results for IOA (shown in Figure 2.14), results were able to be obtained for both 15.7% MC and 18.3% MC, where the peak strength occurred at approximately 70% SDMC which was significantly higher than the flow function equivalent which resulted in plastic characteristics for the same moisture content. Additionally, when IOA (shown in Figure 2.19), IOB (shown in Figure 2.20) and IOC (shown in Figure 2.21) are considered for approximately 40 - 60% SDMC, the wall adhesion test results do not exceed 1 kPa for the full range of tested consolidation conditions (approximately 10 - 60 kPa). This is not the case when the higher tested moisture contents (approximately 70% SDMC) for all tested samples are considered. For IOA (shown in Figure 2.19) the peak strength was exhibited for 18.3% MC (70% SDMC). Furthermore, for IOB (shown in Figure 2.20) the peak strength was exhibited for 24.9% MC (70% SDMC) where this was approximately double the peak strength of IOA. Finally, for IOC (shown in Figure 2.21) the peak strength was exhibited for 25.6% MC (70% SDMC) where this was slightly greater than the peak strength of IOB. One of the interesting observations which arose from the current testing program, was the peak wall adhesive strength for each of the respective samples was achieved at approximately 70% SDMC. It is important to note the variation of data points from the line fit for the 70% SDMC testing results can be attributed to the capillary suction effects acting between the bulk material and wall liner interface.

2.4.9.2 INTER-PARTICLE ADHESION TESTING

The adhesive force that is present within a bulk material can be quantified using an inter-particle adhesion tester. Similar to the wall adhesion tester, for a repeatable set of experiments, there are two clearly defined steps. The first step is the consolidation of the sample, where a pre-determined pressure is applied with use of weights on the consolidation lid. The sample is then split with the use of a loading stem which is attached to one side of the testing apparatus, while the other side remains fixed. The force response is recorded via an S-type load cell. A schematic of the procedure is shown in Figure 2.22, which is described in detail from the work of Plinke et al. [8].

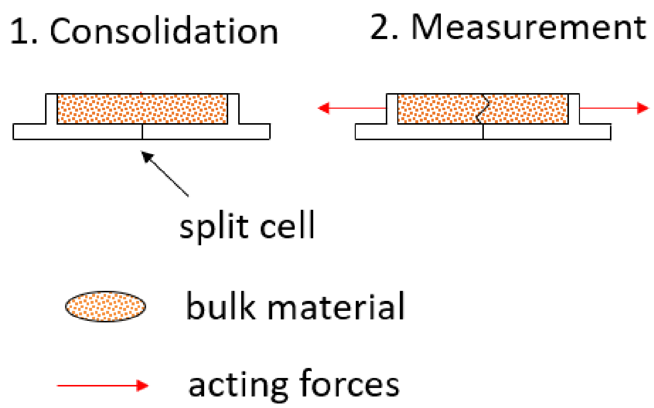

Figure 2.22 – Schematic of inter-particle adhesion testing procedure.

These tests are generally repeated for a range of consolidation pressures and moisture contents, to gain an understanding of the threshold of a problematic material in relation to the adhesion characteristics for particle-to-particle contact. The typical testing measurement from the inter-particle adhesion tester is similar to the wall adhesion testing regime described above.

A summary of the inter-particle adhesion results are found in Figure 2.23, Figure 2.24 and Figure 2.25. It is appropriate to identify that materials that did not exhibit adhesive characteristics were shown for IOB at 10.6% MC and IOC at 10.0% MC. Testing below these moistures was not undertaken as it has been experienced previously by the author, that the same characteristics would result. Another limitation which was encountered is when the material was *"too sticky"* and would pull away from the tester, failing to internally break. This occurred for IOA at 18.3% MC, IOB at 24.9% MC and IOC at 25.6% MC.

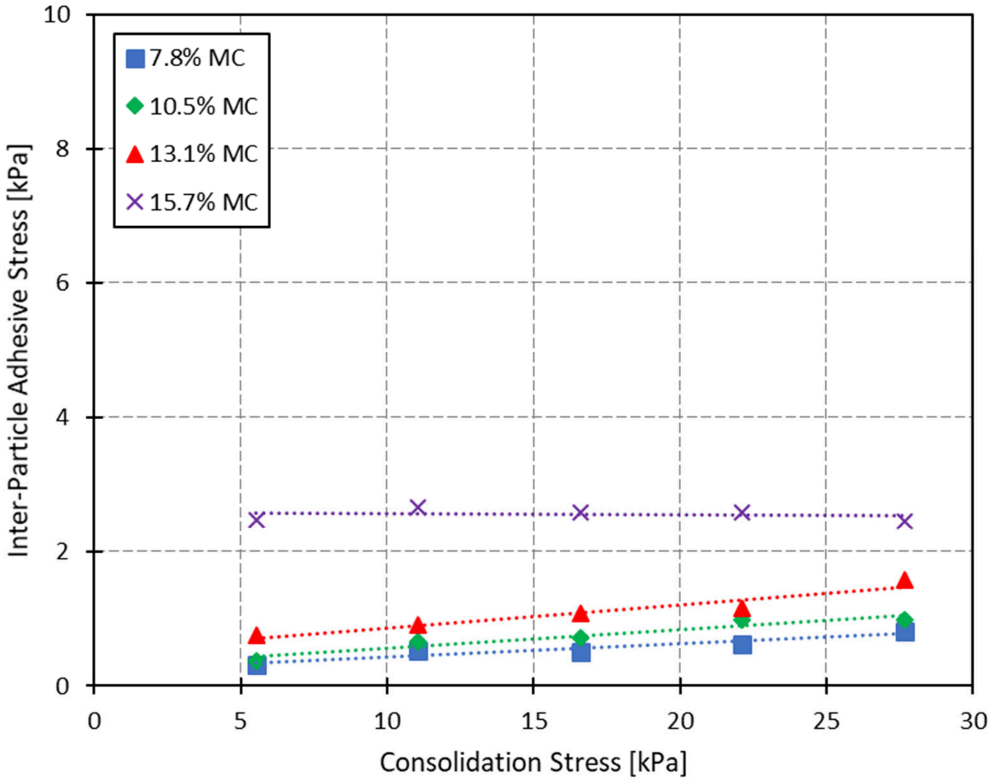

Figure 2.23 – Inter-Particle adhesion testing results for IOA.

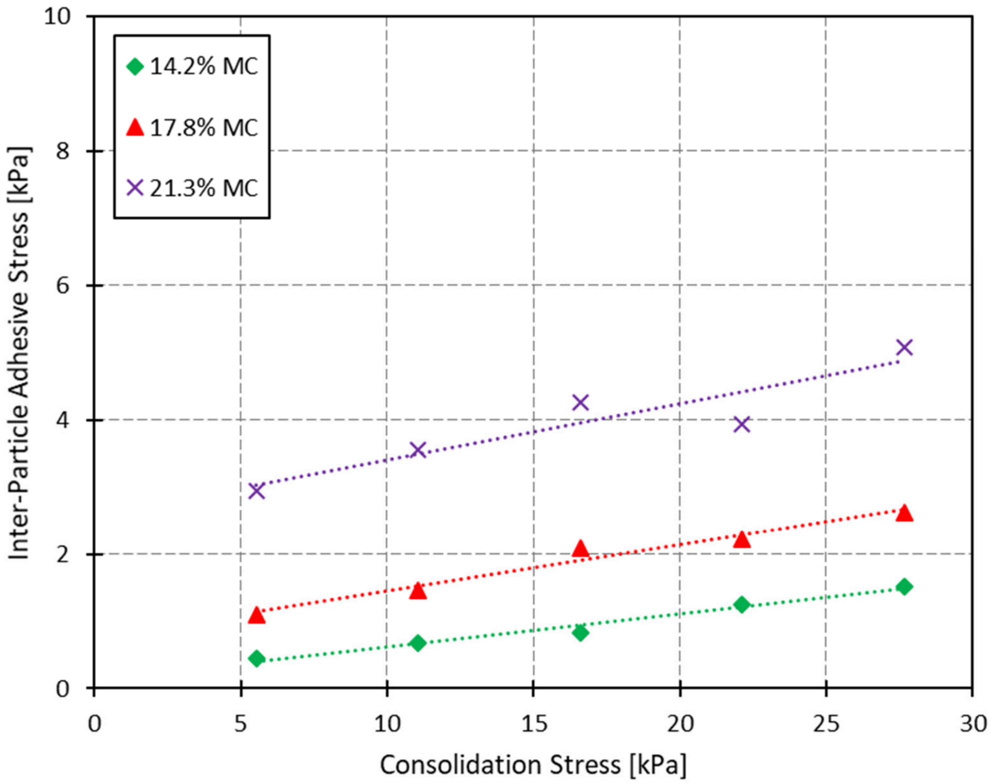

Figure 2.24 – Inter-Particle adhesion testing results for IOB.

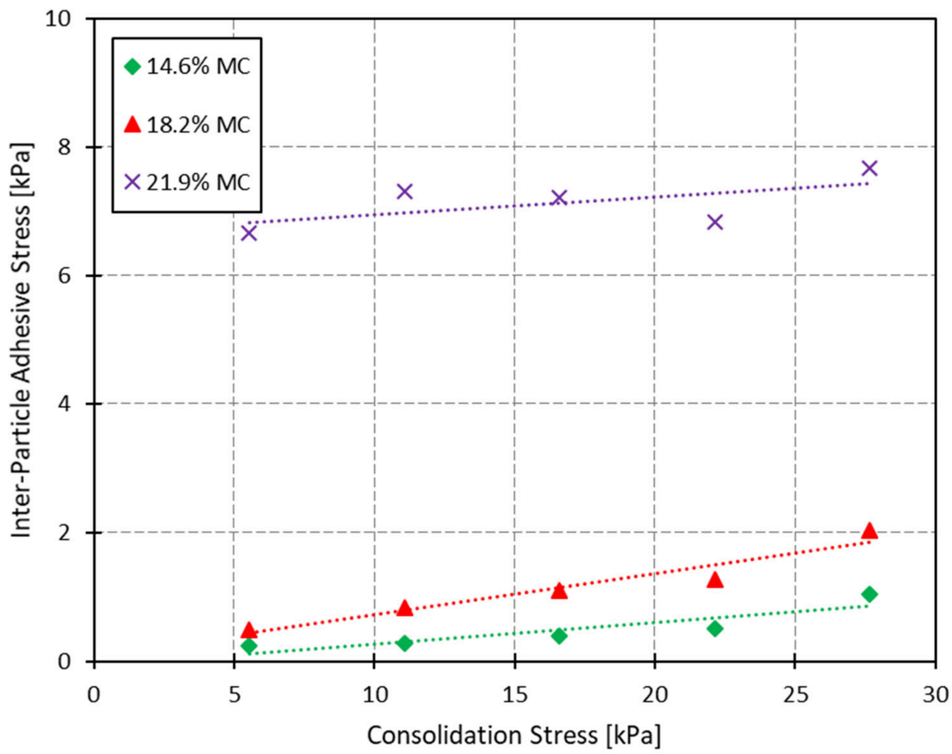

Figure 2.25 – Inter-Particle adhesion testing results for IOC.

When the inter-particle adhesion testing results for IOA are considered, an increase in strength can be associated with an increase in moisture content (shown in Figure 2.23). Unlike the flow function results for IOA (shown in Figure 2.14), results were able to be obtained for 15.7% MC, where the peak strength occurred at approximately 60% SDMC which was significantly higher than the flow function equivalent which resulted in plastic characteristics for the same moisture content. Additionally, when IOA (shown in Figure 2.23), IOB (shown in Figure 2.24) and IOC (shown in Figure 2.25) are considered for approximately 40 - 50% SDMC, the inter-particle adhesion test results do not exceed 2 kPa for the full range of tested consolidation conditions (approximately 5 - 30 kPa). This is not the case when the higher tested moisture contents (approximately 60% SDMC) for all tested samples are considered. For IOA (shown in Figure 2.23) the peak strength was exhibited for 15.7% MC (60% SDMC). Additionally, for IOB (shown in Figure 2.24) the peak strength was exhibited for 21.3% MC (60% SDMC) where this was approximately double the peak strength of IOA. Finally, for IOC (shown in Figure 2.25) the peak strength was exhibited for 21.9% MC (60% SDMC) where this was approximately double the peak strength of IOB. The increase in strength for IOB and IOC can be attributed to the presence of clays in each sample (outlined in Table 2.1). One of the interesting observations which arose from the current testing program, was the peak inter-particle adhesive strength for each of the respective samples was achieved at approximately 60% SDMC.

2.5 WALL FRICTION TESTING AND WALL LINER PROPERTIES

The properties of the wall liner material and their associated characteristics are of critical importance as they dictate the friction parameters that are produced between the bulk material handling equipment and the bulk material itself. The main contributors to the friction interaction described above is the surface roughness and hardness of the wall lining material [1]. The following section outlines the testing procedures used for the determination of the wall liner properties, and a summary of results obtained for three wall liner samples are included. Additionally, a summary of the wall friction testing results for each wall liner conducted for all three iron ore samples is also included.

2.5.1 WALL LINER PROPERTIES

The determination of the wall liner properties can give an insight into the influence that the friction produced between the bulk material and equipment handling surface have on the potential for bulk material build-up to occur. The corresponding relationship of the adhesive characteristics of the bulk material can also dictate the potential for this build-up to occur. For instance, a rough surface can assist in the build-up of a bulk material when compared to a smoother surface. However, if the bulk material shows low inter-particle adhesion properties, the potential for build-up is lower. The following section explains the measurement procedures used to determine both the surface roughness and hardness parameters, where the results of the measured wall liners are also included. Additionally, the chemical composition of the wall liners will be included for completeness of the thesis.

The three wall liners analysed in this research are commonly used internal wall liners found in the iron ore industry. More specifically, the wall liners are Ceramic Tiles, Rough Welded Overlay and a White Cast Iron Alloy. Table 2.11 gives the identification name for each respective wall liner sample and the density has also been included for completeness.

Table 2.11 – Wall Liner Sample Details

Wall Liner Identification Name	*Material Type*	*Density [kg/m^3]*
WLA	Ceramic Tile	3835
WLB	Rough Welded Overlay	7518
WLC	White Cast Iron Alloy	7592

2.5.1.1 SURFACE ROUGHNESS

It can be argued that the surface roughness of bulk material handling systems is the most crucial of parameters when designing any bulk handling plant, from bins and hoppers through to transfer chutes. The influence that the surface roughness plays on the wall friction produced between the bulk material and the handling system to be designed is quite complex and needs detailed consideration [1].

Much research has been undertaken on the topic of surface roughness regarding the measurement and analysis of surfaces, where notable work has been conducted by Thomas [31], Nowicki [32], Ooms [33] and Roberts [1]. It is beyond the scope of this research and not feasible to discuss all the parameters of surface roughness in detail. However, the common measurement parameters are discussed and used for the determination of the differences of the wall lining materials used in relation to surface roughness.

For the measurement of the surface roughness for the wall lining materials considered, two common height measurements are typically used, namely, R_a, a Centre Line Average (CLA) roughness and R_q, the Root Mean Square (RMS) roughness. A schematic of the method used for the determination of height measurements is found in Figure 2.26.

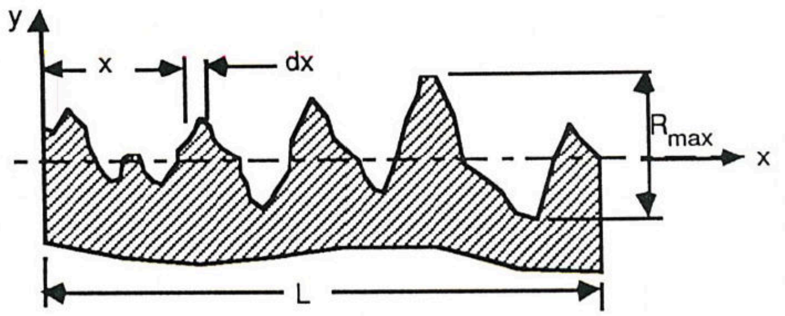

Figure 2.26 – Schematic of roughness surface profile (Roberts, 1998).

The CLA roughness is the most common measurement method used and is determined by:

$$R_a = \frac{1}{L}\int_0^L |y(x)|\, dx \qquad (2.7)$$

where: $|y(x)|$ is the absolute value of the coordinate height from the mean centreline.

The RMS roughness is a more accurate measure for surface roughness as it weighs the deviation from the centreline, greater than that of the value determined using the CLA method. The RMS roughness is determined using:

$$R_q = \sqrt{\frac{1}{L}\int_0^L [y(x)]^2\,dx} \tag{2.8}$$

The calculated surface roughness for the wall liners used in this research is summarised in Table 2.12. The surface roughness has been determined in accordance with ASTM D7127 – 17 [34] using a stylus probe.

Table 2.12 – Surface Roughness Values for Wall Lining Materials

Wall Liner Sample	*CLA Roughness [μm]*	*RMS Roughness [μm]*
WLA	1.12	1.46
WLB	3.83	4.89
WLC	7.90	9.79

2.5.1.2 HARDNESS

The influence that the hardness of a wall lining material has on the flow or build-up of a bulk material can be regarded as only having very minimal effect, in comparison to the surface roughness. Although the hardness of a wall liner may only contribute in a small manner to the way bulk materials flow or build-up, it is still critical into how a bulk material handling system performs. If a wall lining material is *"soft"* it may wear quicker than a system with *"hard"* wall lining material.

Wear that is evident in bulk materials handling, is a topic where extensive literature and research is available (see references [35 - 46]) due to the adverse effects it can have on any materials handling system. Although the research presented in this thesis is predominantly on the build-up of WSMs, the influence that hardness has on the wear of wall lining materials must be acknowledged. This relationship should be recognised as the wear of a wall lining material that will effectively change the surface properties and wall friction, which can significantly change the way a bulk material will either flow or build-up.

There are numerous methods and standards available for the determination of the hardness of a material. The method used to determine the hardness of the wall liners used in this research was undertaken with a Knoop Hardness (HK) test, where a pyramid shaped diamond indenter is pressed into the material with a known load (typically 100 grams) for a specific dwell time. This load is set before the testing begins [47]. The Knoop hardness is determined using:

$$HK = \frac{P_{HK}}{C_p {L_p}^2} \tag{2.9}$$

where: P_{HK} is the applied load [kgf].

C_p is the correction factor for the indenter shape (ideally, 0.070279).

L_p is the length of indentation along its axis [mm].

The measured hardness for the wall liners used in this research is summarised in Table 2.13. The hardness testing has been undertaken in accordance with ASTM E384 [48]. The results presented in this section are merely for reference and completeness of this thesis, where future investigations should be undertaken on the influence that the hardness will have on surface roughness and the associated relationship on wall friction.

Table 2.13 – Knoop Hardness Values for Wall Lining Materials

Wall Liner Sample	*Knoop Hardness (HK)*
WLA	890
WLB	624
WLC	338

2.5.1.3 X-RAY FLUORESCENCE (XRF) SPECTROMETRY MEASUREMENTS

The chemical composition of a wall liner can give an indication into the potential hardness that may be present. Within the mining sector, the need for *"harder"* wall liners can be associated with the wear of a wall lining material. Wall lining materials which portray higher hardness values typically demonstrate lower surface roughness values. This is shown when the values of the surface roughness and hardness of each wall liner are analysed in Table 2.12 and Table 2.13 respectively. Furthermore, the addition of elements to steel alloys can increase the overall strength and hardness of the material for enhanced performance.

X-Ray Fluorescence (XRF) spectrometry is an elemental analysis technique used for the quantitative measure of the chemical elemental composition of materials. The method of XRF measurements is based on the fundamental principle that individual atoms are excited with an external energy source and emit X-Ray photons which can be analysed via different wavelengths. The analysis of a sample is undertaken by counting the number of photons present for each wavelength where the elements present can be identified and then quantified [49]. The measured XRF results of each respective wall liner sample can be found in Table 2.14.

Table 2.14 – Chemical Elemental Analysis for Wall Lining Materials using XRF

Wall Liner Sample	*Chemical Elements Composition and Percentage*										
	Mg	*Al*	*Si*	*P*	*S*	*K*	*Cr*	*Mn*	*Fe*	*Zr*	*LE*
WLA		54.0	3.3							0.7	42.0
WLB	6.2	4.2	3.9	0.1		0.3	28.3	1.2	55.8		
WLC		2.2	17.9	7.7	0.7	0.2	20.5	2.8	39.9	8.1	

Among the three wall liners analysed, the presence of Chromium (Cr) for WLB and WLC would result in materials with higher hardness which are more resilient to wear when compared to untreated mild steel. In XRF analysis, the element component Light Elements (LE) for WLA refers to elements in various compositions that have low atomic numbers. The elements in this category include: Magnesium (Mg), Aluminium (Al), Silicon (Si), Phosphorus (P), Sulfur (S) and Chlorine (Cl). The results presented in this section, similar to wall liner hardness, are merely for reference and completeness of this thesis. Future investigations should be undertaken to determine the influence of the chemical composition on the surface properties of the wall liner. Additionally, the influence of these properties should be related to the associated build-up and wear that may be present.

2.5.2 WALL FRICTION TESTING

The friction that is produced between a wall liner and bulk material is of critical importance and needs careful consideration in the design of any bulk material handling equipment. The following section outlines the procedures used for the determination of the wall friction for both low and high-speed conditions.

2.5.2.1 KINEMATIC WALL FRICTION (SLOW-SPEED)

The kinematic wall friction refers to slow moving friction which would be experienced in hoppers, silos or bins. The kinematic wall friction can be measured using an adaption of the Jenike direct shear tester. The base of the cell is replaced by a wall lining material as shown in Figure 2.27. As the shear load is applied to the shear ring, the normal load is reduced at regular intervals and a shear plane is established between the wall liner to bulk material interface. The Wall Yield Locus (WYL), as explained in Section 1.2, is then determined by measuring the normal stress against the shear stress.

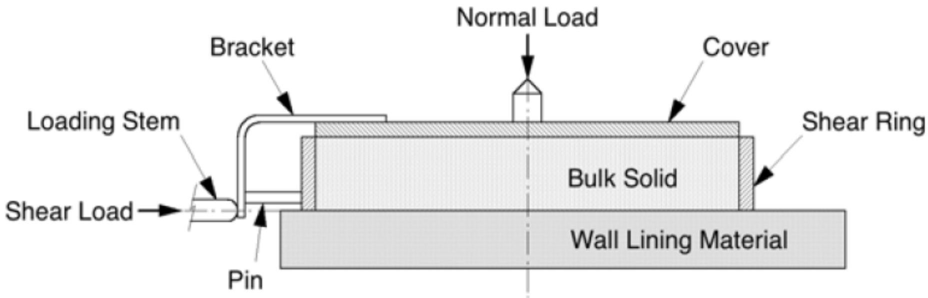

Figure 2.27 – Schematic of wall friction testing apparatus (Roberts, 1998).

Once the WYL is defined, a common form to depict the wall friction angle, ϕ_W, determined using:

$$\phi_W = \tan^{-1}\left(\frac{\tau_W}{\sigma_W}\right) \tag{2.10}$$

where: τ_W is the shear stress at the wall [Pa].

σ_W is the normal stress to the wall [Pa].

For lower consolidation pressures, the wall friction angle is limited by the effective angle of internal friction, δ, which is defined as the upper bound limit for the wall friction angle, ϕ_W [1]. It can be quite common at low normal pressures for the bulk material to fail internally by shear, rather than by sliding along the wall boundary. The wall friction testing for the three iron ore samples have been undertaken in accordance with AS 3880 [20], where the measurements have been undertaken on the three different wall lining materials identified above.

A summary of the WYL plots which consider the influence of the moisture content on the wall friction undertaken for Wall Liner A are found in Figure 2.28, Figure 2.29 and Figure 2.30 for each respective iron ore sample. Additionally, a summary of the WYL plots which consider the influence of the wall liner material for the worst case moisture content are found in Figure 2.31, Figure 2.32 and Figure 2.33 for IOA (13.1% MC), IOB (14.2% MC) and IOC (14.6% MC) respectively. The corresponding wall friction angle plots which consider the influence of the moisture content undertaken for Wall Liner A are found in Figure 2.34, Figure 2.35 and Figure 2.36 for each respective iron ore sample. Additionally, the corresponding wall friction angle plots which consider the influence of the wall liner material for the worst case moisture content are found in Figure 2.37, Figure 2.38 and Figure 2.39 for IOA (13.1% MC), IOB (14.2% MC) and IOC (14.6% MC) respectively. It is important to note that comparisons regarding MC have been undertaken for all wall lining materials, however, only WLA has been included due to the significant variability shown in the WYL plots with increasing MC. Some variability was shown for WLB and WLC, but these did not change as significantly in comparison to WLA.

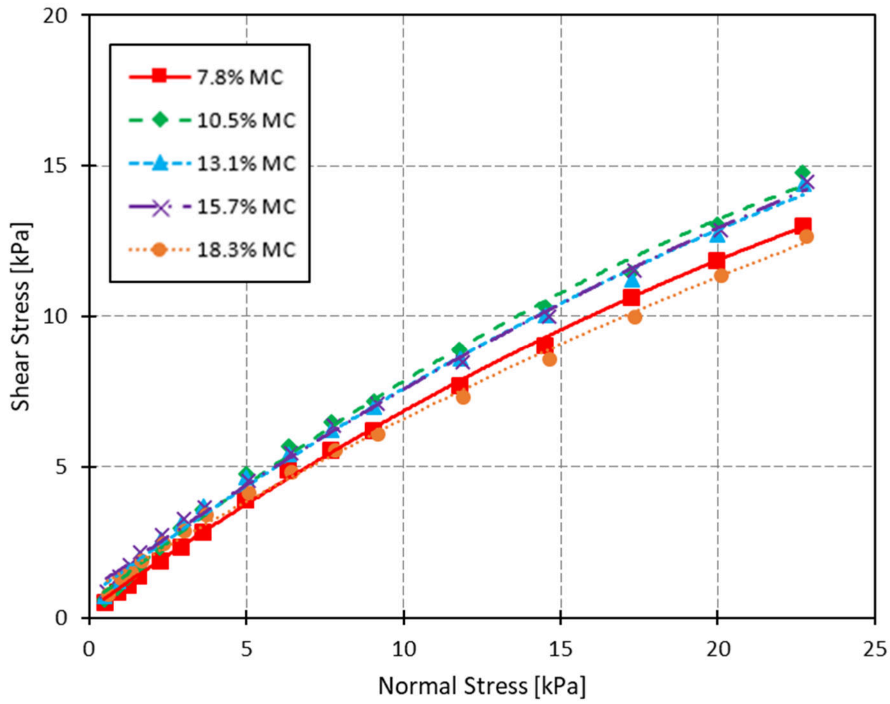

Figure 2.28 – Wall Yield Locus of IOA for Ceramic Tile Liner at different moisture contents.

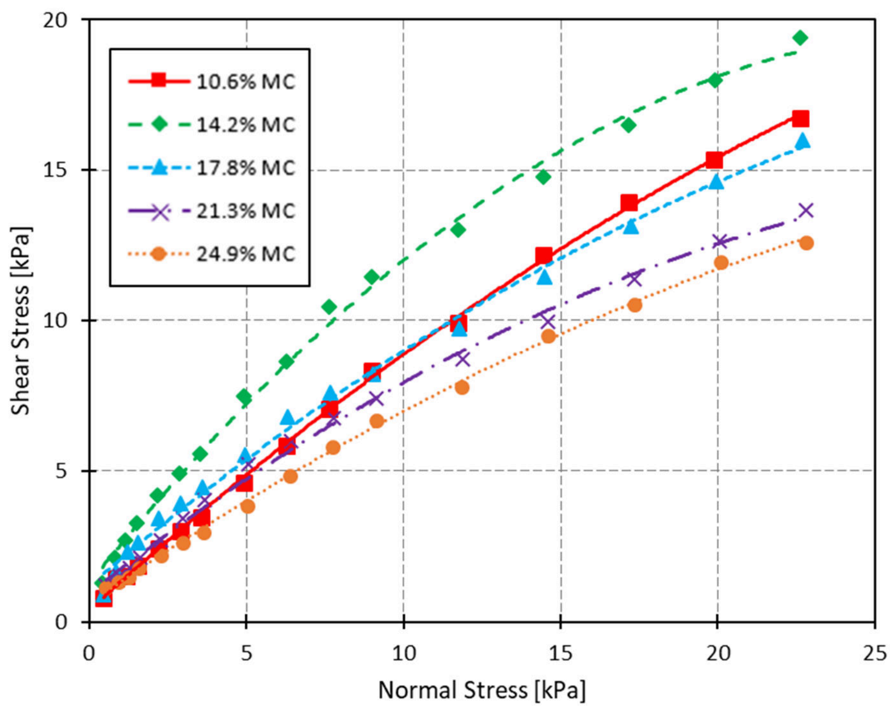

Figure 2.29 – Wall Yield Locus of IOB for Ceramic Tile Liner at different moisture contents.

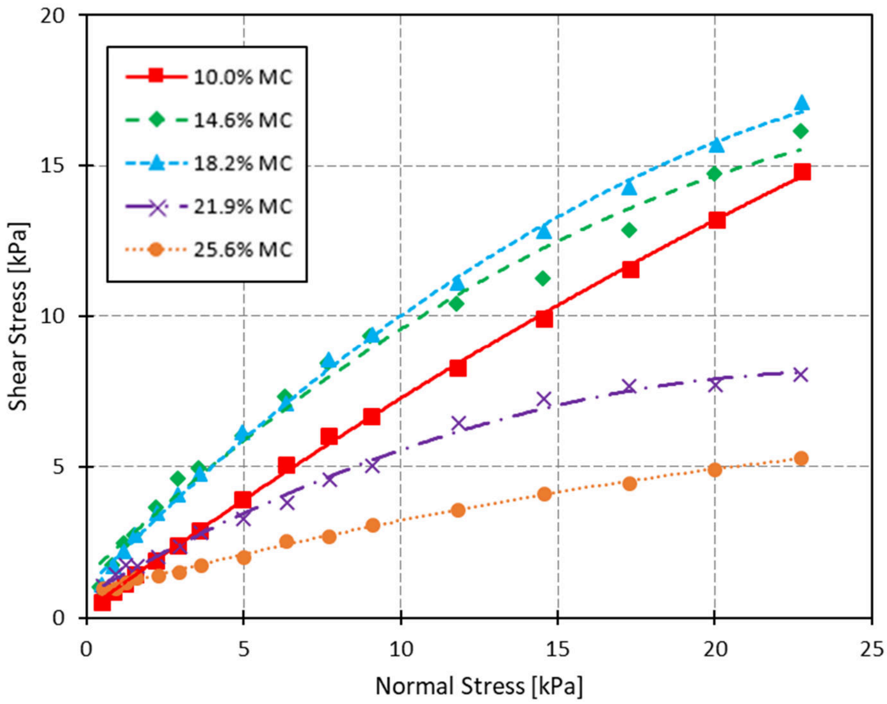

Figure 2.30 – Wall Yield Locus of IOC for Ceramic Tile Liner at different moisture contents.

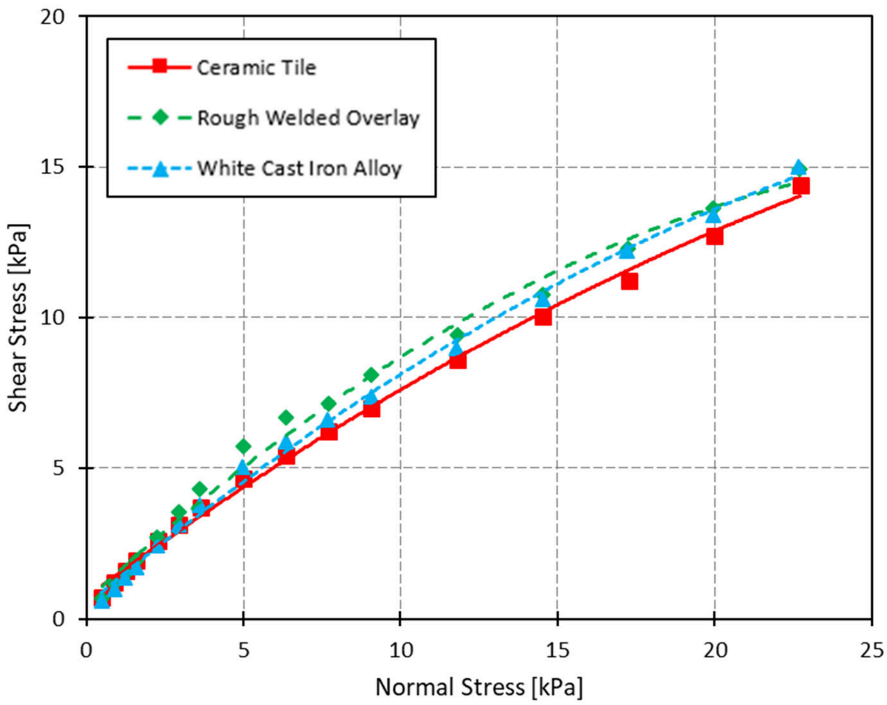

Figure 2.31 – Wall Yield Locus of IOA (13.1% MC) for different wall lining materials.

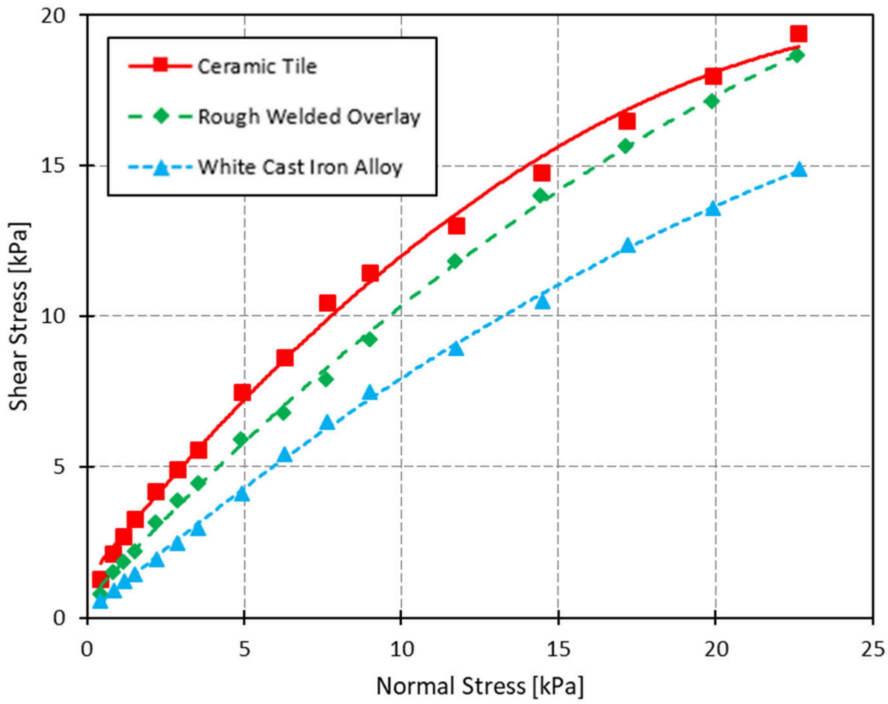

Figure 2.32 – Wall Yield Locus of IOB (14.2% MC) for different wall lining materials.

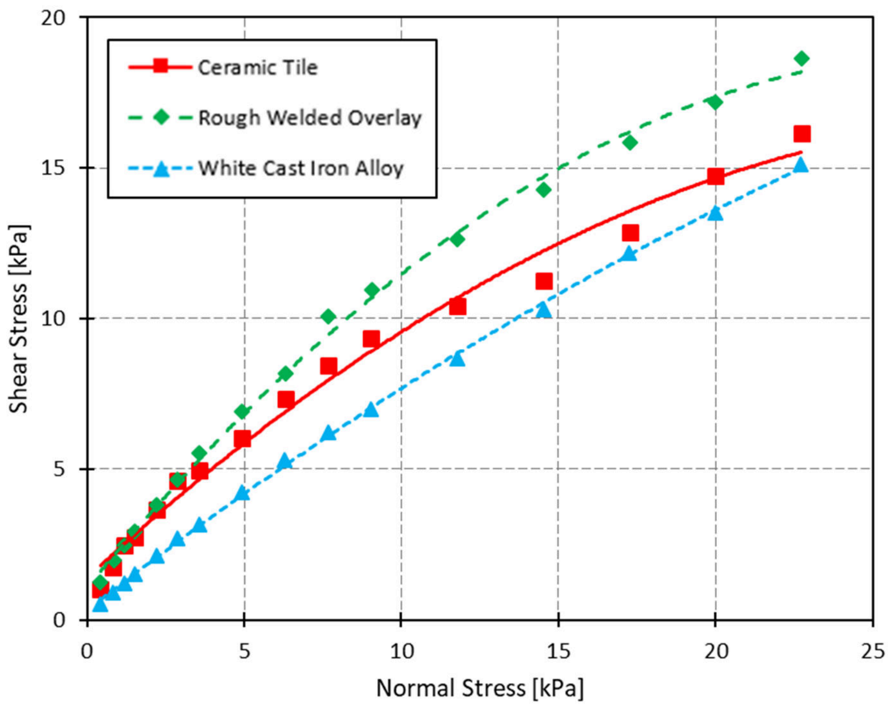

Figure 2.33 – Wall Yield Locus of IOC (14.6% MC) for different wall lining materials.

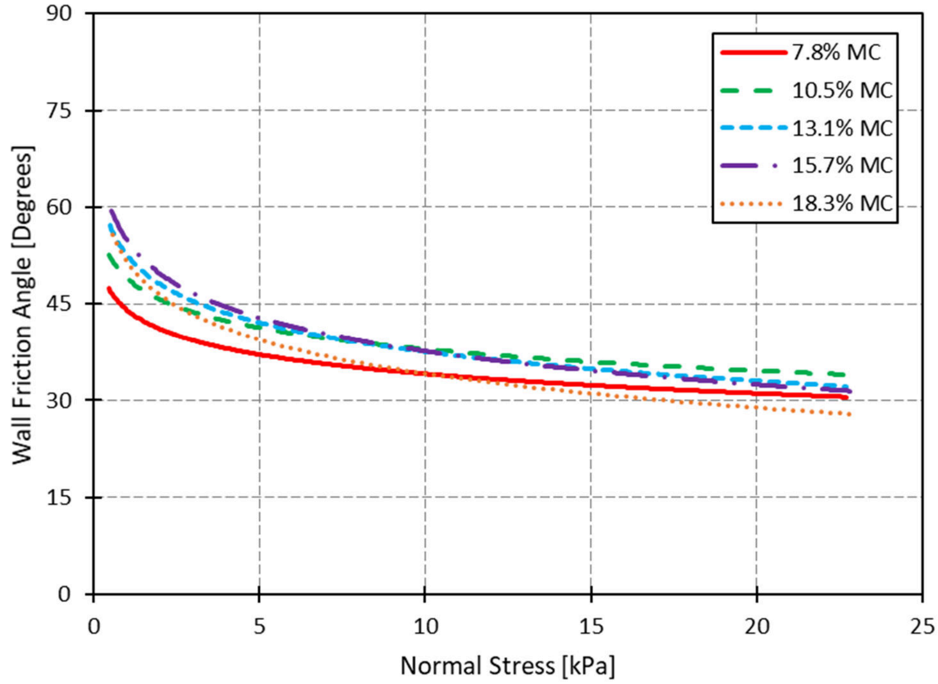

Figure 2.34 – Wall friction angles of IOA for Ceramic Tile Liner at different moisture contents.

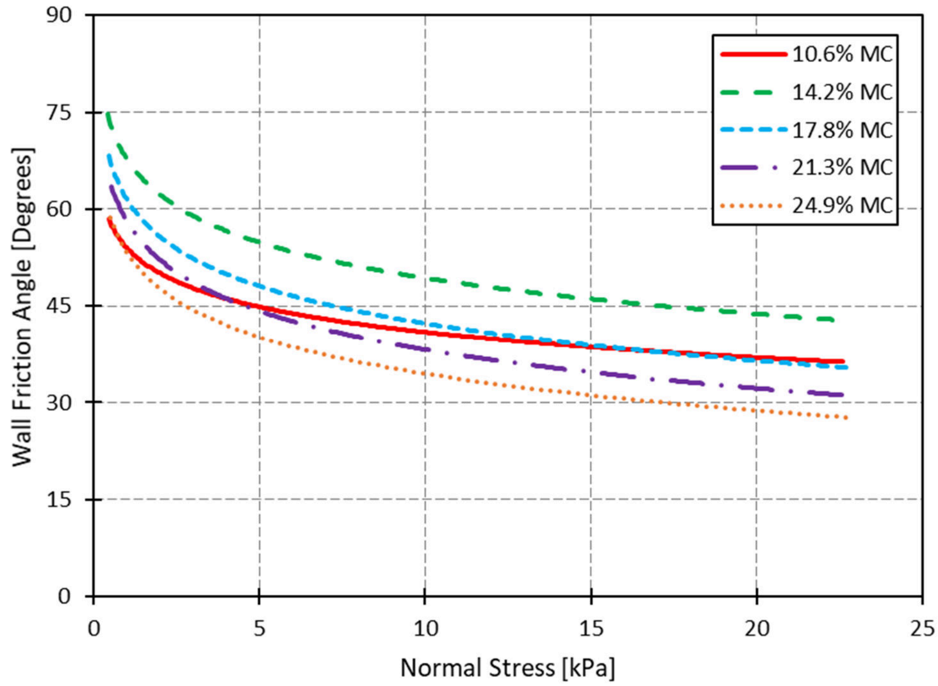

Figure 2.35 – Wall friction angles of IOB for Ceramic Tile Liner at different moisture contents.

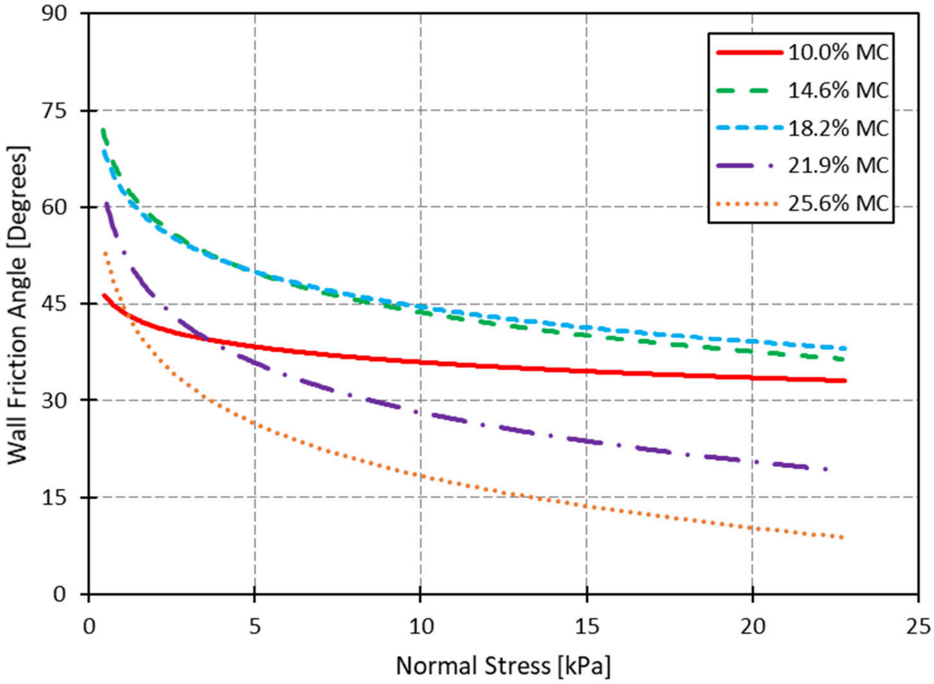

Figure 2.36 – Wall friction angles of IOC for Ceramic Tile Liner at different moisture contents.

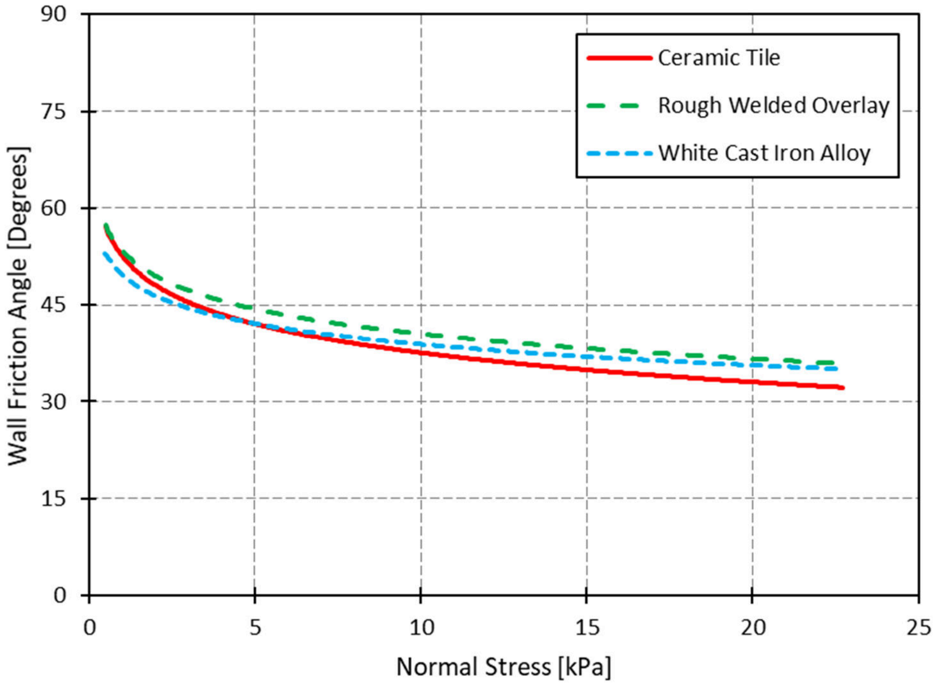

Figure 2.37 – Wall friction angles of IOA (13.1% MC) for different wall lining materials.

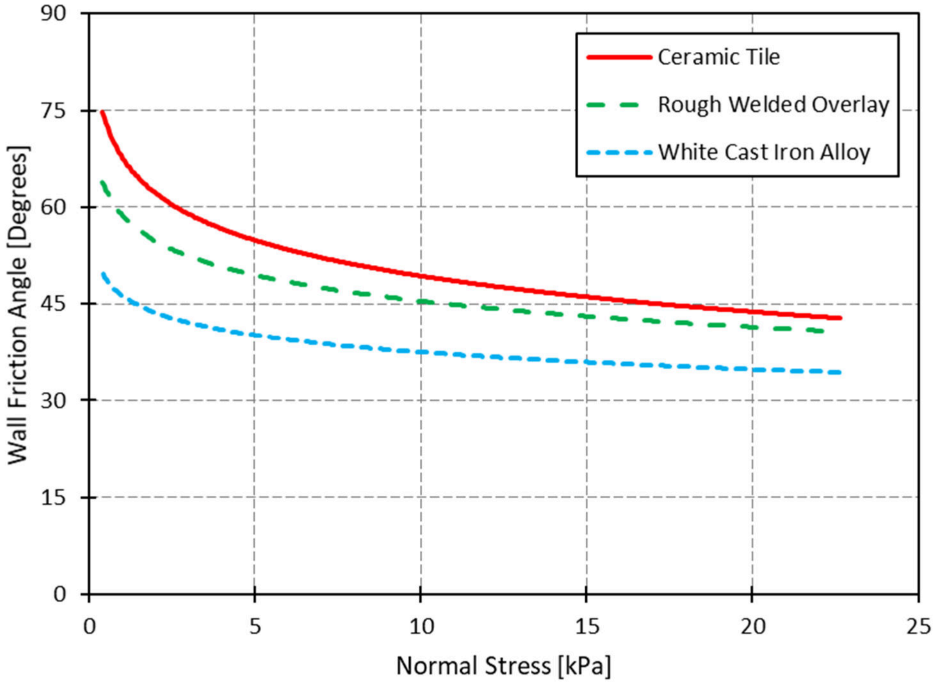

Figure 2.38 – Wall friction angles of IOB (14.2% MC) for different wall lining materials.

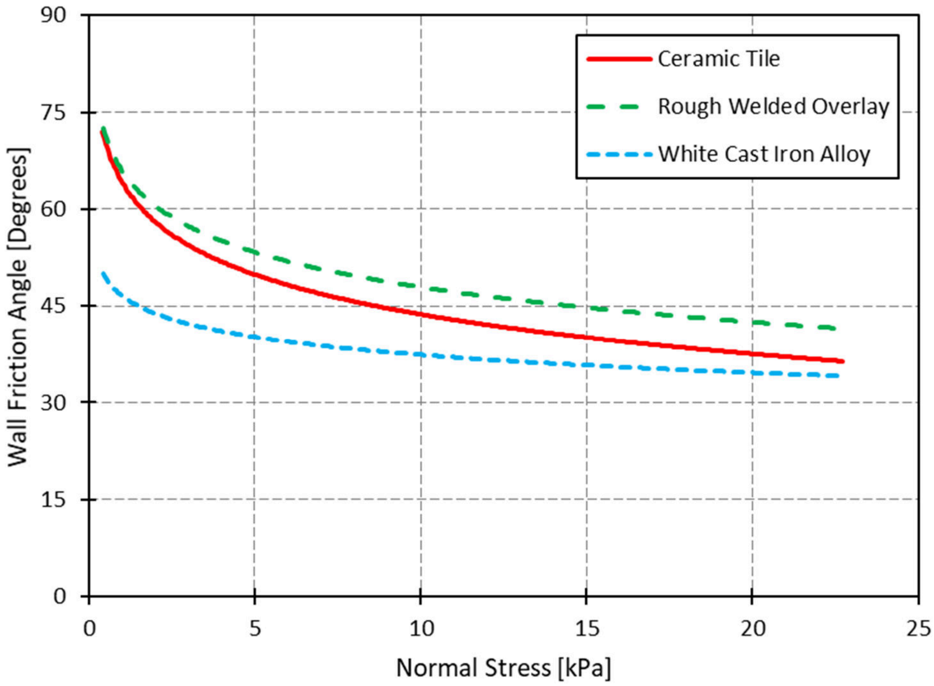

Figure 2.39 – Wall friction angles of IOC (14.6% MC) for different wall lining materials.

From the presented results, it can be observed that the bulk materials which contain clays such as IOB and IOC will have a much greater variance in wall friction depending on the moisture content present. This is best explained when Figure 2.29 and Figure 2.30 are considered, where the maximum shear stress acting at the wall is experienced when the moisture content of the sample is approximately 40% of the SDMC. These values are significantly higher than the WYL of IOA, outlined in Figure 2.28, which can be attributed to the additional adhesion due to the presence of clays (as outlined in Table 2.1). Conversely, when the moisture content of IOB and IOC is increased further, a reduction of the WYL is experienced as outlined in Figure 2.29 and Figure 2.30 respectively. This effect can be attributed to the additional moisture which allow the present clays to act more as a slurry allowing the material to slide at the bulk material to wall liner interface.

The variance due to a different wall lining material is also evident, however, this is not as pronounced in comparison to changes in the moisture content of the bulk material. The WYL of IOA was less susceptible to change when the above variables were altered, as outlined in Figure 2.28 and Figure 2.31. This can be attributed to the absence of clays in IOA (as outlined in Table 2.1). It is appropriate to identify that the change in wall friction angle for all three wall liners showed similar characteristics when the moisture content was altered for each respective sample. The values presented in Figure 2.37, Figure 2.38 and Figure 2.39 will be used in conjunction with the obtained results from the following section for the determination of the dynamic adhesion of the supplied samples, which is evaluated in Section 4.3.

2.5.2.2 KINETIC WALL FRICTION

The kinetic (dynamic) wall friction refers to fast moving friction which would be typically experienced in transfer chutes and considers the slip that is evident at the bulk material to wall liner interface. The kinetic wall friction can be measured using a circular bed wear tester developed by Wiche et al. [50] where a schematic is shown in Figure 2.40.

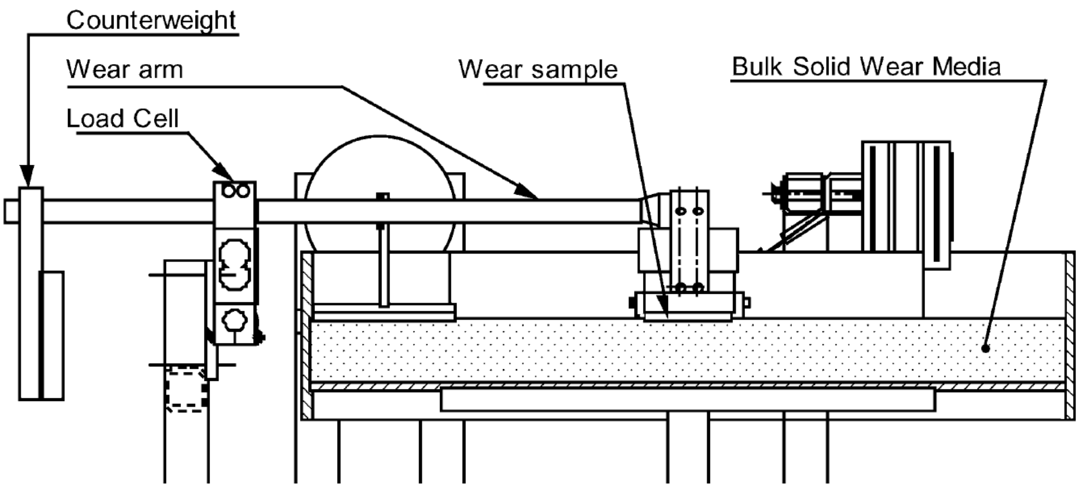

Figure 2.40 – Circular bed wear and wall friction tester (Wiche et al., 2004).

The kinetic wall friction is determined by measuring the drag force via a loadcell attached to the wear arm shown in Figure 2.40. The kinetic wall friction can be determined for a range of consolidation loads and linear velocities. One of the major limitations of the circular bed wear tester is the formation of a *"bow wave"* of bulk material at the leading edge of the wall liner sample in the direction of travel (as shown in Figure 2.41a). This bow wave is produced when the liner *"digs"* into the bulk material sample, where the problem becomes much more significant with increasing linear velocity and increasing normal load. To prevent the formation of a bow wave, the plane angle of the wall liner must be adjusted until the leading edge of the wall liner is in line with the approaching bulk material bed surface (as shown in Figure 2.41b). It is appropriate to identify that when the sample planes below the bed surface, the angle is too small. Additionally, if only the rear half of the sample planes on the bed surface, the angle is too large [50, 51]. This adjustment is critical to accurately measure the drag force.

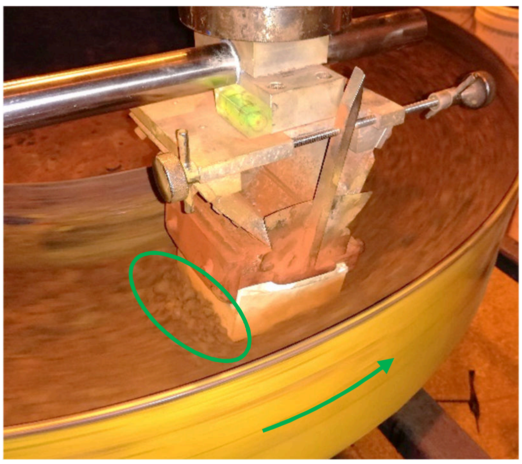

a) Bow wave

b) No bow wave

Figure 2.41 – Bow wave determination at leading edge of wall liner sample in direction of travel.

When measuring the kinetic wall friction, the formation of a bow wave can introduce additional drag forces which result in significantly higher values than those without an evident bow wave. It was determined above, that the planing angle of the wall liner is critical for the accurate determination of the drag force. During the development of the circular wear tester this problem was identified, where the resulting reaction forces for different planing angles were determined [50, 51]. Figure 2.42 shows the reaction forces due to the frictional drag caused by the planing wall liner on the bulk material bed.

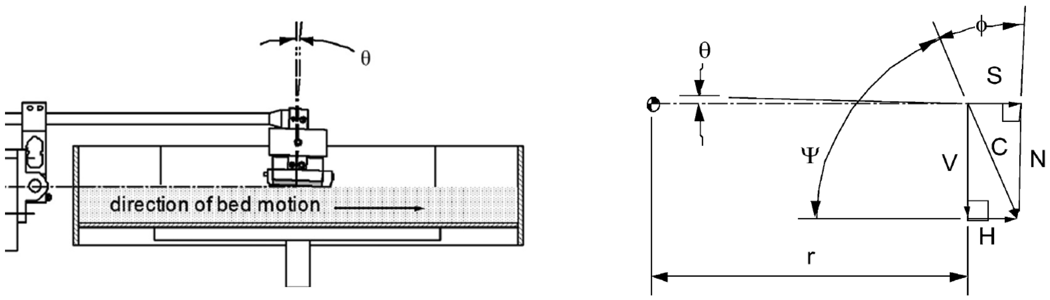

a) Wall liner location *b) Wall liner drag geometry*

Figure 2.42 – Reaction forces acting on wall liner sample due to frictional drag (Wiche et al., 2004).

After some simple analysis of the resulting forces, the stresses acting on the wall liner are determined by:

$$\sigma_s = \frac{C \sin \varphi}{A_{ws}} \tag{2.11}$$

$$\sigma_n = \frac{C \cos \varphi}{A_{ws}} \tag{2.12}$$

where: $\varphi = 90 - \psi + \theta; C = \sqrt{H^2 + V^2}$ and $\psi = \tan^{-1}(V/H)$.

The planing angles that were required to prevent the formation of a bow wave during testing ranged from 0.5° up to 5° depending on the linear velocity and applied normal load. Additionally, the required planing angle would also be dependent on the surface texture of the wall liner specimen, the bulk material sample and moisture content of the bulk material. Furthermore, it was found that a limiting load of 3.5 kilograms (~3.4 kPa normal pressure) and limiting linear velocity of 0.512 m/s were found. Any values greater than these resulted in a consistent bow wave, where accurate testing could not be completed. It is appropriate to identify that the planing angle will ultimately have very little effect on the applied normal stress in the vertical direction, where inclination angles of up to 5° only reduce the equivalent normal (vertical) load by approximately 0.4%. The corresponding horizontal component, however, needs much more consideration in the kinetic wall friction analysis, where an additional 8.7% increase in the force results from a 5° planing angle.

The kinetic wall friction results for the three iron ore samples yielded similar results. This testing was conducted at the as supplied moisture content for each respective sample where a -11.2 mm size fraction was used. The general trend identified exhibited a linear increase in the drag force for an increasing normal load. It is appropriate to identify that testing has been conducted on the as supplied moisture contents only due to the agglomeration of the samples. The agglomeration of the samples occurred when additional moisture was added to the sample prior to testing. It was observed that the properties of the bulk material changed significantly whilst conducting these tests. A summary of the results for IOA (6.3% MC) for the ceramic wall liner material is shown in Figure 2.43. The overall trend for the friction coefficient was seen to be quite close for each sample, however, as the linear velocity is increased above 0.5 m/s the measured friction deviates away from the observed trend with increasing normal load. This deviation for higher linear velocity can be attributed to the introduction of the bow wave during these tests adding additional drag force to the measurement.

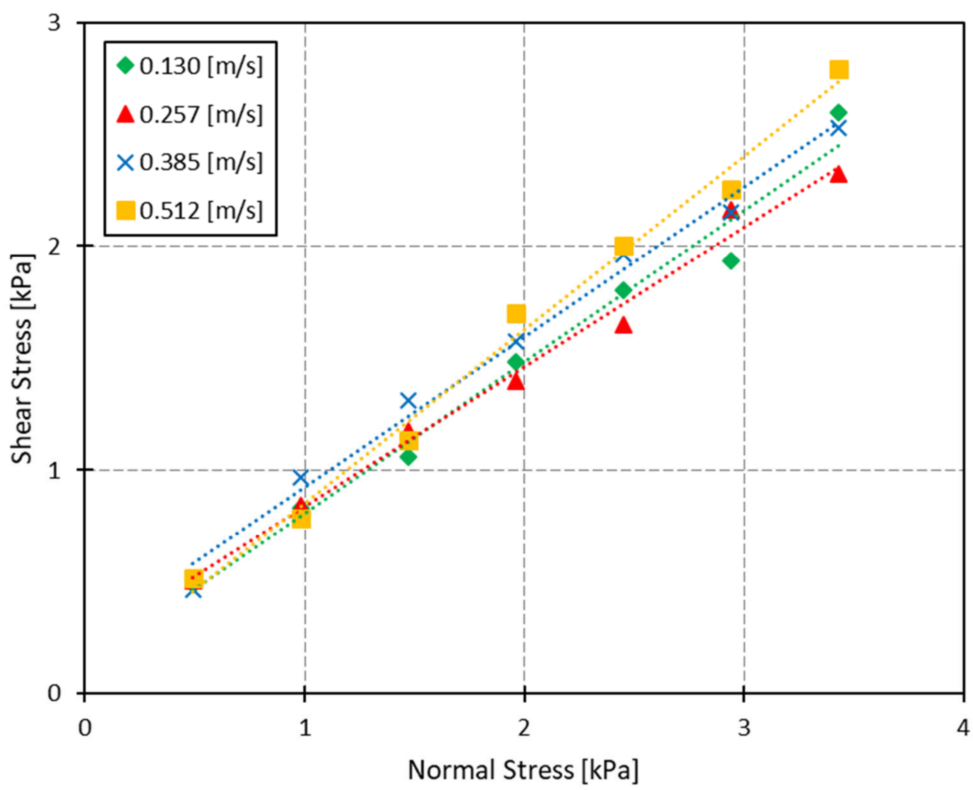

Figure 2.43 – Kinetic wall friction measurements of IOA (6.3% MC) for ceramic wall lining material.

To investigate the influence of the wall lining material on the kinetic wall friction, a comparison can be made with the kinetic friction coefficient for each tested linear velocity. A summary of the results for IOC (11.5% MC) for all three wall lining materials is shown in Figure 2.44. It can be assumed to some extent from these testing results, that the influence of the wall lining material on the kinetic wall friction can have minimal effect. However, the limitations and significant reduction in successful testing parameters undertaken would make this assumption to be quite untimely. The potential modification of the testing apparatus to overcome the current limitations would enable for an increase in scope for the parameters that could be successfully tested. Unfortunately, the accurate measurement of the kinetic wall friction is an extremely complex problem where the potential solutions have merely been identified to outline the current limitations of the testing apparatus.

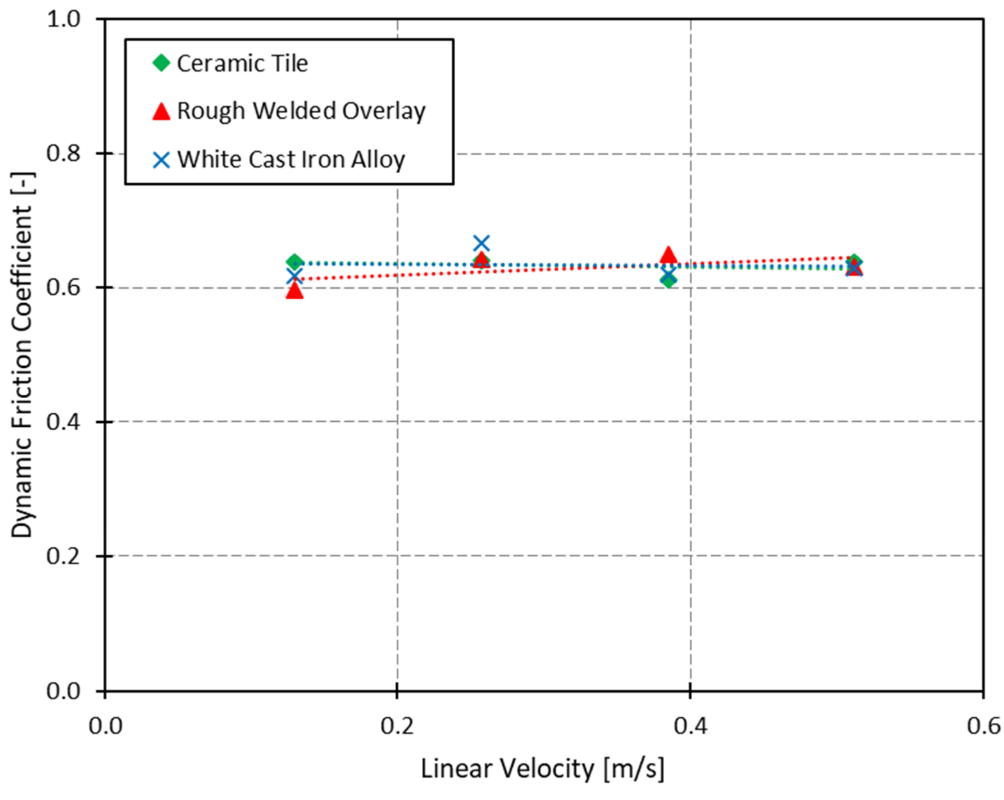

Figure 2.44 – Comparison of kinetic friction coefficient of IOC (11.5% MC) for different wall lining materials.

To investigate the influence of the bulk material on the kinetic wall friction, a similar comparison can be made when the friction coefficient for each tested linear velocity is considered. A summary of the results for the ceramic tile wall liner for all three iron ore samples is shown in Figure 2.45. Unlike the comparison made above, a much greater variance is shown when the kinetic friction coefficient of different bulk materials are compared on the same wall lining material. The influence that the bulk material has on the kinetic wall friction can be further examined when the potential for bulk material build-up is considered. The further investigation of this relationship between bulk material sample and wall lining material will be undertaken in Section 6.3.

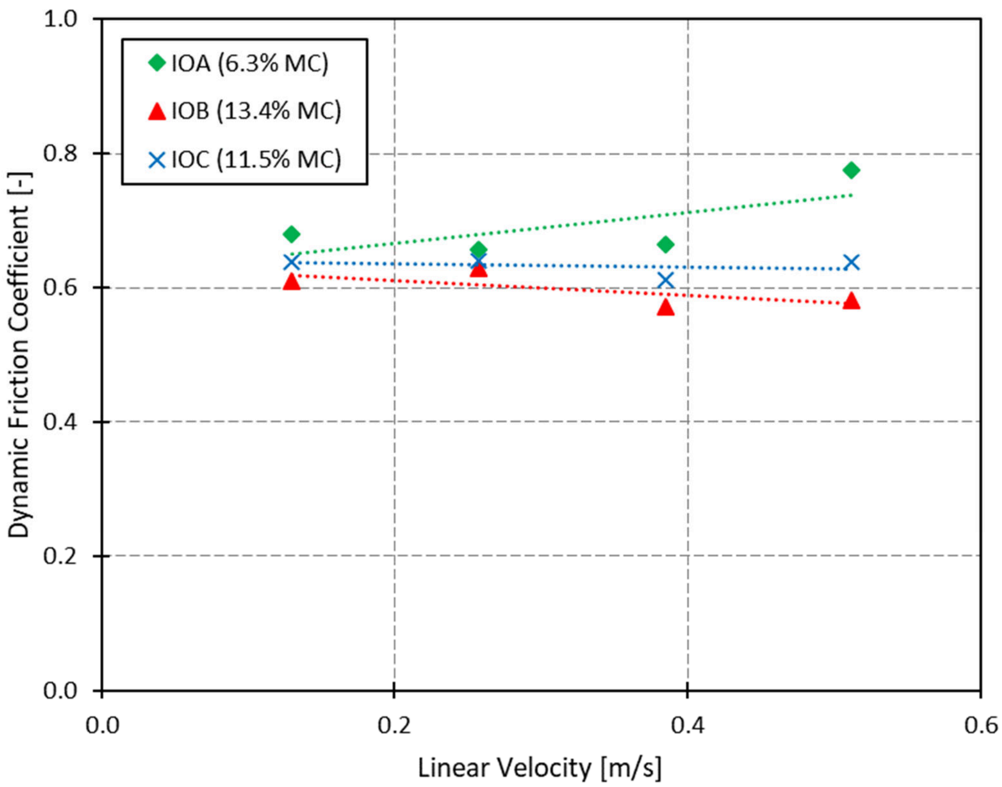

Figure 2.45 – Comparison of kinetic friction coefficient of ceramic tile for IOA, IOB and IOC.

2.6 DISCUSSION

During the characterisation experimental measurements a minimum of three successful repeat measurements are typically undertaken for each consolidation pressure where visual checks of the experiment are recorded with each measurement. This was undertaken to analyse if any moisture of the sample was *"pushed"* out of the sample where a reduction in moisture content and therefore strength of the sample would result. In the case where a significant difference in the measured force was observed, this measurement was deemed to be an *"outlier"* where these data were neglected and a further measurement was undertaken. When the Jenike direct shear testing measurements are considered, the reproducibility of the results are considered within the AS 3880 [20] standard. The standard clearly indicates that the pre-shear of the sample should reach a steady state value for critical compaction where the under or over consolidation are clearly defined. In the case where the sample wasn't compacted to the critical state, the measurement was abandoned and an additional measurement was undertaken. It is important to note that a similar procedure has been used for the bulk density, wall adhesion, inter-particle adhesion and wall friction measurements.

To analyse the properties of each respective iron ore sample in more detail, it was deemed appropriate to summarise the moisture contents where the peak strength occurred. Table 2.15 shows the peak strength moisture contents which were experienced for each iron ore sample. This analysis has been undertaken for the bulk density, Jenike direct shear, wall adhesion, inter-particle adhesion and wall friction measurements. When the Jenike direct shear and inter-particle adhesion characterisation measurements are considered, the peak strength occurred at approximately 60% SDMC. It is important to note that the peak strength for IOA occurred at approximately 50% SDMC for the Jenike direct shear test. This can be attributed to the absence of clays which would result in a reduction of cohesive strength for IOA. When the peak strength for the interface between the bulk material and wall lining surfaces is considered, the peak strength occurred at approximately 70% SDMC for the wall adhesion measurements and approximately 40% SDMC for the wall friction measurements. It is important to note that the peak strength for IOC occurred at approximately 50% SDMC for the wall friction measurements. This can be attributed to the presence of clays which would result in additional adhesive bonds at the bulk material to wall liner interface.

Table 2.15 – Summary of Flow Property Peak Strength for Iron Ore Samples

Testing Procedure	*Size Fraction [mm]*	*Moisture Content [% MC]*		
		IOA	*IOB*	*IOC*
Bulk Density	-11.2	11.5 (~75% SDMC)	18.5 (~70% SDMC)	18.2 (~80% SDMC)
Jenike Direct Shear	-4	13.1 (~50% SDMC)	21.3 (~60% SDMC)	21.9 (~60% SDMC)
Wall Adhesion	-4	18.3 (~70% SDMC)	24.9 (~70% SDMC)	25.6 (~70% SDMC)
Inter-Particle Adhesion	-4	15.7 (~60% SDMC)	21.3 (~60% SDMC)	21.9 (~60% SDMC)
Wall Friction	-4	10.5 (~40% SDMC)	14.2 (~40% SDMC)	18.2 (~50% SDMC)

The internal strength of the iron ore samples can be analysed using the cohesive handleability ranking assessment outlined in Section 1.2. Table 2.16 shows the cohesive handleability ranking for each of the respective iron ore samples. This analysis has been considered for low consolidation conditions which would be experienced within transfer chutes.

When IOC at 21.9% MC is considered, a classification of extremely cohesive results. Additionally, when IOC at 18.2% MC and IOB at 17.8% MC and 21.3% MC are considered a classification of very cohesive results. These classifications can be attributed to the presence of clays (outlined in Table 2.1) which would result in additional cohesive bonds increasing the strength of the samples at these particular moisture contents. When the flow of these materials within transfer chute systems are considered, the internal strength of the bulk material may lead to blockages. This will be dependent on the transfer chute lining material and the overarching geometry.

Table 2.16 – Cohesive Handleability Ranking (CR) Assessment for Iron Ore Samples (Low Consolidation)

Bulk Material Sample	*Moisture Content [% MC]*	*Cohesive Handleability Ranking (CR)*
IOA	*7.8* (~30% SDMC)	4 (Free Flowing – High Cohesive Strength)
	10.5 (~40% SDMC)	3 (Cohesive)
	13.1 (~50% SDMC)	3 (Cohesive)
IOB	10.6 (~30% SDMC)	4 (Free Flowing – High Cohesive Strength)
	14.2 (~40% SDMC)	3 (Cohesive)
	17.8 (~50% SDMC)	2 (Very Cohesive)
	21.3 (~60% SDMC)	2 (Very Cohesive)
IOC	10.0 (~30% SDMC)	4 (Free Flowing – High Cohesive Strength)
	14.6 (~40% SDMC)	3 (Cohesive)
	18.2 (~50% SDMC)	2 (Very Cohesive)
	21.9 (~60% SDMC)	1 (Extremely Cohesive)

The inter-particle adhesive strength of the iron ore samples can be analysed using the adhesive handleability ranking assessment, outlined in Section 3.4. Similar to the cohesive handleability ranking assessment above, this analysis has been considered for low consolidation conditions which would be experienced within transfer chutes. Table 2.17 shows the adhesive handleability ranking for each of the respective iron ore samples. When IOC at 21.9% MC is considered, a classification of extremely adhesive results. Additionally, when IOB at 21.3% MC is considered a classification of very adhesive results. These classifications can be attributed to the presence of clays (outlined in Table 2.1) which would result in additional inter-particle adhesive bonds increasing the strength of the samples at these particular moisture contents. When the flow of these materials within transfer chute systems are considered, the inter-particle adhesive strength of the bulk material can lead to blockages. These blockages lead to downtimes which are caused from belt runoff events where mistracking of the conveyor belt can cause costly damage to the materials handling operation. These types of events are commonly caused from overloaded belts where a prior blockage has dislodged and fallen onto the conveyor.

Table 2.17 – Adhesive Handleability Ranking (AR) Assessment for Iron Ore Samples (Low Consolidation)

Bulk Material Sample	*Moisture Content [% MC]*	*Adhesive Handleability Ranking (AR)*
IOA	*7.8* (~30% SDMC)	4 (Free Flowing – High Adhesive Strength)
	10.5 (~40% SDMC)	4 (Free Flowing – High Adhesive Strength)
	13.1 (~50% SDMC)	4 (Free Flowing – High Adhesive Strength)
	15.7 (~60% SDMC)	3 (Adhesive)
IOB	14.2 (~40% SDMC)	4 (Free Flowing – High Adhesive Strength)
	17.8 (~50% SDMC)	3 (Adhesive)
	21.3 (~60% SDMC)	2 (Very Adhesive)
IOC	14.6 (~40% SDMC)	4 (Free Flowing – High Adhesive Strength)
	18.2 (~50% SDMC)	4 (Free Flowing – High Adhesive Strength)
	21.9 (~60% SDMC)	1 (Extremely Adhesive)

When all three iron ore samples are considered, Figure 2.29 shows that worst case wall friction occurs for IOB at 14.2% MC. When the internal cohesion from the Jenike direct shear measurements is considered, Figure 2.16 shows highest internal strength occurs at 21.9% MC for IOC. This was also observed to be the case for the inter-particle adhesion measurements, as shown in Figure 2.25. It is important to note the worst case moisture content can be different when the particle-to-particle and particle-to-wall failure envelopes, outlined in Section 3.4, are considered. This can be shown when different interactions and properties of the iron ore samples are analysed. In the case of IOB, Figure 2.29 shows the worst case wall friction angle on the ceramic tile liner occurs at 14.2% MC, however, Figure 2.20 shows the maximum wall adhesive strength occurs at 24.9% MC. This is attributed to the suction effects which are present for the wall adhesion test which occurs for higher moisture contents. When the internal strength from the Jenike direct shear measurements is considered, Figure 2.15 shows highest internal strength occurs at 21.3% MC. Additionally, the inter-particle adhesion measurements show the peak strength also occurs at 21.3% MC for the full range of consolidation stresses.

2.7 CONCLUSION

This chapter has presented some insight into the problems that WSMs pose to the materials handling stream. It was determined that the existing methods used to determine the physical flow properties of bulk materials lack any direct quantitative measurement technique to the amount of cohesion or adhesion present. To overcome this, wall adhesion and inter-particle adhesion tests were developed and undertaken. Additionally, the geology and origin of the iron ore samples was included to give a background and context as to why the samples may exhibit certain properties. Finally, the flow property and wall lining characterisation tests that were undertaken have been outlined and a summary of key results were also presented.

CHAPTER THREE – METHODOLOGY FOR COHESION & ADHESION ANALYSIS OF BULK MATERIALS

The following chapter builds on the existing methodology available for the determination of the cohesion and adhesion of bulk materials. This revised methodology for the estimation of cohesion and adhesion is presented and verified with experimentally measured adhesion values. To complement the revised adhesion prediction methodology, a new yielding strength model is also proposed.

3.1 INTRODUCTION

The determination of the wall liner properties and more importantly the flow properties of a bulk material (as outlined in Chapter Two) are critical for the design of any bulk material handling system. The design of such materials handling systems are most effective when handling bulk materials at the physical properties they were designed to handle. Due to the fast-paced nature of expansion in the mining industry and demand of mineral resources, it is quite common for materials handling systems to handle bulk materials that were not intended for the system. WSMs are problematic within the materials handling stream due to the inter-particle, boundary cohesion and adhesion forces. WSMs cause significant downtimes within the materials handling stream due to events such as blockages of bins, hoppers and transfer chutes, remains left in train wagons and dump trucks, as well as conveyor belt carry back [1, 2].

The current measurement techniques for WSMs have limitations where new methods must be considered (as outlined in Section 2.3.1). The development and measurement of the wall adhesion and inter-particle adhesion testers can give a quantitative value for the adhesion present in a bulk material sample. The following chapter outlines the current state of knowledge in relation to the adhesion and cohesion of bulk materials and the associated strength that can be present. Additionally, a revised methodology for the estimation of cohesion and adhesion is presented and validated with experimentally determined adhesion values using an inter-particle adhesion tester. To complement the revised adhesion prediction methodology, a new yielding strength model is also proposed and explained in Section 3.4.

3.2 COHESION AND ADHESION OF BULK MATERIALS

In the field of bulk material handling, adhesion can be defined as the tensile force for particle-to-particle and particle-to-wall contacts of the bulk material, whilst cohesion is the shear resistance for particle-to-particle and particle-to-wall contact under zero normal stress [52]. Hering et al. [52] states that the adherence of the bulk material to equipment surfaces typically shows only microscopic effects. This adherence layer only becomes problematic when cohesion and adhesion are present within the bulk material [53]. The combination of these effects will typically cause blockages [53].

The bonding mechanisms of adhesion and cohesion of bulk materials can be distinguished by the occurrence of material bridges between the attracting partners [54]. These bonding mechanisms, however, can occur with or without material bridges. The material bridges described by Rumpf [54] can have the form of a liquid, solid or solidified liquid. Commonly identified mechanisms of cohesion and adhesion are indicated in Table 3.1. It should also be noted that the solid bridges identified in Table 3.1 are rendered insignificant for the mechanisms of adhesion within the material handling sector as these typically only have effect with the addition of heat or relatively long contact times.

Table 3.1 – Mechanisms of Adhesion (Rumpf, 1958)

Without Material Bridges	**With Material Bridges**	
	Liquid Bridges	**Solid Bridges**

• Electrostatic Attraction
• Van-der-Waals Forces
• Valence Bond
	• Freely movable liquid surface
	    • Capillary forces
	    • Interfacial forces
	• Non-moveable binder bridges
	    • Binder
	    • Glue
	    • Adsorption layer
		• Sintering
		• Recrystallization
		• Chemical reaction of primary particle
		• Grain growth
		• Crystallisation of solids in the contact liquid between particles

Within the materials handling sector, WSMs commonly exhibit higher moisture contents in comparison to free-flowing ores. This higher moisture leads to an adsorption layer of water which surround the particles of the bulk material [55]. Adsorption is a result from the accumulation of a dissolved substance at the interface of a solid and the solution phase [55]. When an aqueous solution is present, water in most cases for bulk materials, the contact with mineral surfaces results in a residual electric charge to be found [56]. In the case where clays are present within the mineral surface, the charge will be permanent. The electric surface charge is most prominent for oxides and hydroxides of Iron (Fe), Aluminium (Al), Titanium (Ti), Silicon (Si) and Manganese (Mn) [56].

The adsorption layer of water that is found to surround the particles cause the formation of a liquid bridge, where this formation will be assisted by the residual electric charge [56]. The governing adhesion forces from the formation of a liquid bridge can be attributed to both the capillary and interfacial forces. Additionally, the surface roughness of both the particles and wall surfaces add to the adhesion forces present within the liquid bridge. Burbaum [53] was able to measure the adhesive tensile stress between two stainless steel surfaces connected by a liquid bridge as shown in Figure 3.1.

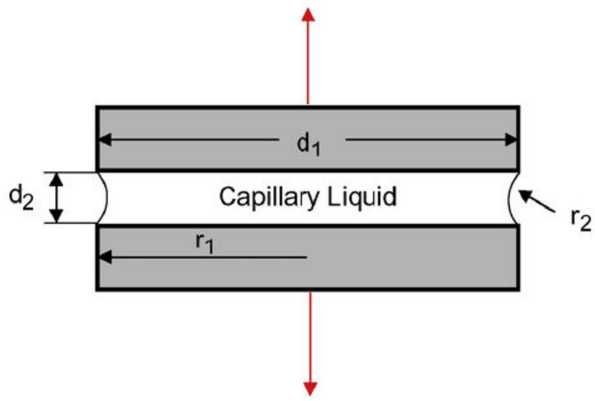

Figure 3.1 – Capillary model for solid surfaces (Plinke et al., 2016).

By solving the Young-Laplace equation, Habenicht [57], used a mathematical approach to prove that the determination of the capillary force could be calculated using:

$$F_c = \gamma \left(\frac{1}{r_1} + \frac{2}{d_2}\right) \pi {r_1}^2 \tag{3.1}$$

where: F_c is the capillary force [N].

γ is the surface tension [N/m].

r_1 is the radius of the steel surfaces [m].

d_2 is the thickness of the capillary liquid [m].

Burbaum [53] undertook experiments which validated Habenicht's [57] mathematical approach. Additionally, Burbaum [53] could apply the model to a similar adhesion test between a cohesive soil sample and stainless-steel surface. It was determined during this particular study that the capillary forces were the main cause of adhesion, while boundary effects from surface tension and surface roughness were much smaller than the present capillary forces. The subsequent sections give an overview into the stresses evident in bulk materials under different loading conditions. This forms the basis of how the cohesion and adhesion will be present for WSMs and the analysis undertaken in Section 3.3.

3.2.1 MOHR-COULOMB STRENGTH MODEL

During the transportation of a bulk material, stresses are induced throughout the material that are not the same in all directions. Bulk materials are quite similar to solid materials in the way that different stresses can be found in different cutting planes [5]. The flow of a bulk material is generally initiated by shearing, where the bulk material deforms and fails. To describe the stresses that act on a bulk material, Section 1.2 gave a brief outline on the well-established Mohr stress circle theory, where Equations 1.1 and 1.2 can be used to determine the elemental stresses for different planes.

The use of the Mohr stress circle gives a graphical representation into the theory for bulk materials, which was initially used in the work of Jenike [4, 58, 59] and then further developed by Nedderman [60], where a failure analysis was used to analytically determine the stress states of granular bulk material samples under different loading conditions. Nedderman [60], assumed an ideal Coulomb material which enabled for the formation of a yielding criterion to describe the way a granular material fails. This analysis incorporated the work undertaken by Rankine [61] in 1857, which described the stress conditions in soils at a state of plastic equilibrium. This body of work is typically referred to as Rankine's theory of earth pressure, which describes the stress conditions in a soil element where failure of the soil occurs once plastic equilibrium has been reached.

To further establish the stress conditions found in both non-cohesive and cohesive bulk materials, these stress values are typically plotted on a normal stress and shear stress diagram, as shown in Figure 3.2. The principal stresses, σ_1 the major principal stress and σ_2 the minor principal stress occur when no shear stresses are present. When both principal stresses are given, the Mohr stress circle is well defined [5]. In the case of a simple uniaxial compression test, both the horizontal and vertical planes have no shear stresses present. For this particular case, the vertical stress is the major principal stress, σ_1, as this will be much greater than the horizontal stress which is the minor principal stress, σ_2, which occurs at an active stress state.

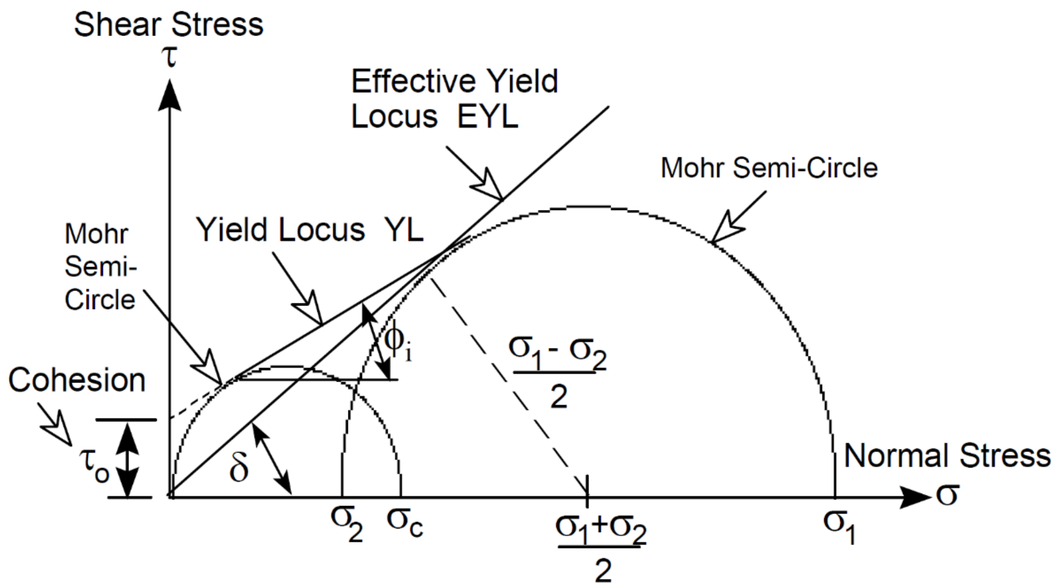

Figure 3.2 – Yield Loci for consolidated bulk material (Roberts, 1998).

One of the most fascinating phenomena to occur within bulk materials is that shear stresses are able to occur whilst the bulk material is not under load. Unlike a Newtonian fluid which will yield a zero radius Mohr circle when at rest (since there are stress states for all loading conditions, including at rest for a bulk material) the state of stress cannot be completely described by a single numerical value [5]. For the determination of the shear strength characteristics of a bulk material for different loading conditions, it is possible for the minor principal stress, σ_2, to have different values for the same major principal stress, σ_1. From this, it can be determined that the Mohr stress circle will only be clearly defined if at least two numerical values are determined [5].

Once a major principal stress is defined, the Instantaneous Yield Locus (IYL) which represents the instantaneous consolidation condition, can be plotted. The IYL lies tangential to the major Mohr semi-circle which pass through σ_1 and σ_2. To fully define the IYL, a smaller Mohr semi-circle, which lies through the origin and the Unconfined Yield Strength, σ_c, will also lie tangential to the IYL [1]. Furthermore, if the IYL is linearly extrapolated to the shear stress axis the amount of cohesion, τ_o, is determined.

The work of Jenike [4] which has been further developed by Nedderman [60], Roberts [1] and Schulze [5], shown above, has demonstrated the importance that stresses acting in bulk materials will have on the design of bulk material handling systems. This theory has been further developed to consider the relationship of the stresses acting on a bulk material and how this changes when the voidage and bulk density are considered. This work is summarised in the following section.

3.2.2 HVORSLEV-ROSCOE YIELD SURFACE

The work that has been presented in Section 3.2.1 identified that the flow of a bulk material is initiated once the material is allowed to deform and shear on itself. This can be thought of as the failure of the bulk material where cohesive elements that are present tend to collapse. The initial work of Coulomb [62] in 1776 hypothesized that soils fail along a ruptured plane. It was further reported by Roberts [63] in 1882 that the weight of granular materials measured at the base of a bin reduced with an increase in material head height. This was attributed to wall effects supporting the granular material. To further develop this theory, Janssen [64] used a continuum approach and demonstrated analytically and also with experimental evidence the results of wall effects supporting the granular material. In 1885, the work of Reynolds [65] determined that all compacted bulk materials expand as they are sheared and will continue to expand until failure occurs, which is typically referred to as dilation.

The combination of the results produced by Coulomb and Reynolds can be used to form a three-dimensional stress-strain-porosity diagram, which can be referred to as the Hvorslev diagram [66]. This was further developed by Roscoe et al. [67], where a failure surface is produced by plotting the Instantaneous Yield Loci (IYL) and the porosity of the granular material forming a failure surface. Figure 3.3 illustrates this failure surface in the p, q and w domain which will correlate to σ (normal stress), τ (shear stress) and ε (voidage) respectively. The initial work of Hvorslev [66] is represented as the Hvorslev surface (right of the critical state line) and the work of Roscoe et al. [67] represented as the Roscoe, Schofield and Wroth surface (left of the critical state line).

Hvorslev [66] conducted tests under a compressive regime where the tensile stress conditions were not considered. This led to the surface of Figure 3.3 to have an edge at the $\sigma = 0$ plane which can be interpreted as a tension cut-off. To expand further on this, Roscoe et al. [67] considered the consolidation of soil samples, where the changes in the voidage between the particles was observed. Samples were subjected to changing stresses within a tri-axial tester where the relationship of the critical state line to voidage between particles was observed.

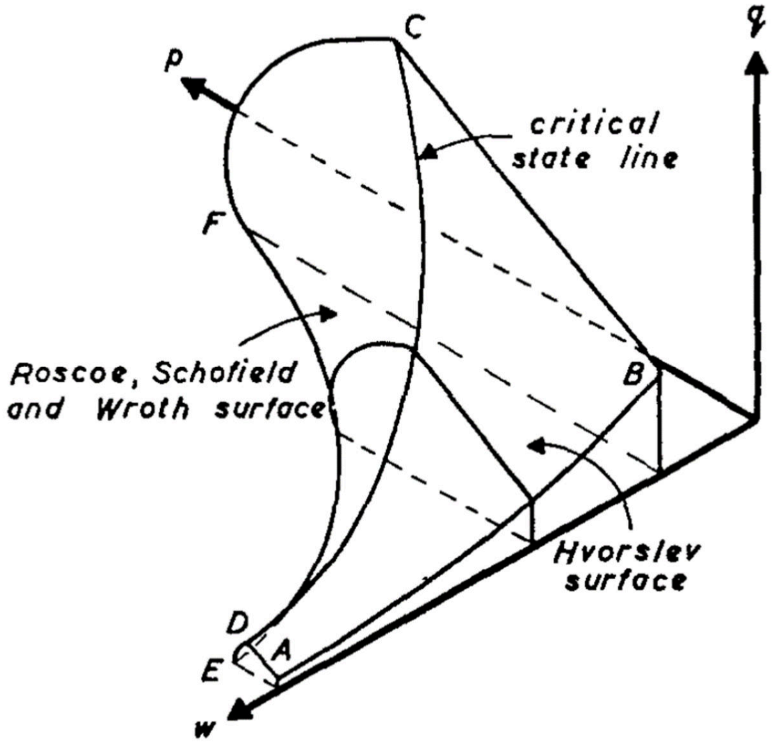

Figure 3.3 – Hvorslev yield surface (modified from Roscoe et al., 1958).

Dividing the Hvorslev surface, seen in Figure 3.3, into the two defined segments either side of the critical state line, leads to two different phenomena occurring within the bulk material. When the right segment is considered, the material fails under shear while at the left segment, consolidation of the material occurs provided that sufficient normal stresses are present. The critical state line is formed by joining the points where the Effective Yield Locus (EYL) intersects the major Mohr semi-circle tangentially at different voidage, ε, conditions. The corresponding yield surface is a result of projecting a series of yield loci which correspond to different consolidation loads (voidage between the particles). This is described in detail by Roberts [1].

To further expand on the work of Hvorslev [66] and Roscoe et al. [67] a yield surface was considered with the bulk density, ρ_{bulk}, and voidage, ε, between the particles of the bulk material. For an increase in the bulk density of a bulk material an associated decrease in the voidage between the particles is experienced [68]. Additionally, with an increase in the bulk density an associated increase in the strength of the bulk material can be seen and is shown in Figure 3.4. By considering the bulk density for the yield surface an assumption into the way the tensile strength curve would correlate to the above theories was gained.

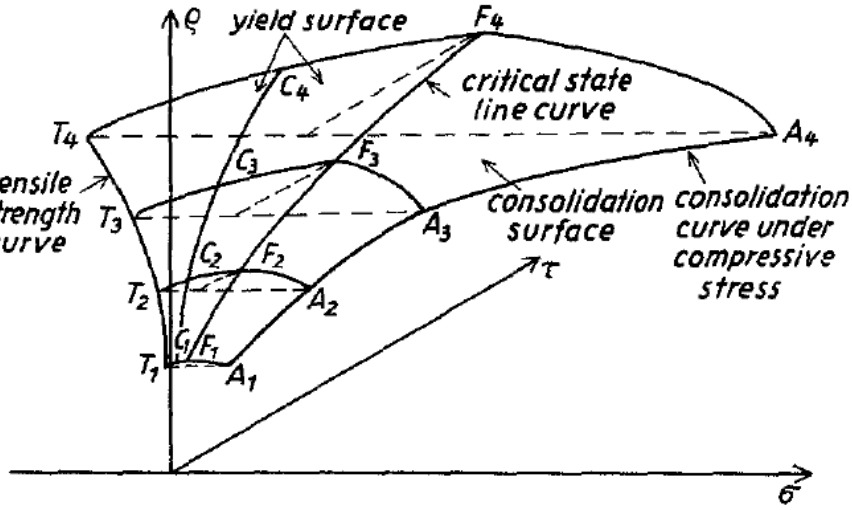

Figure 3.4 – Consolidation yield surface (Ashton et al., 1965).

It could be identified that for low bulk densities, the particles are generally loosely packed with a low tensile strength. However, for high bulk densities, the particles are packed together more closely, where small changes in the bulk density leads to large changes in the tensile strength [68]. Similar to the Mohr coulomb strength theory outlined in Section 3.2.1, assumptions are made into the tensile strength component of the yield surface, shown in Figure 3.4, which are implied from the compressive shear testing (as outlined in Section 2.4.8).

The determination of a new measurement methodology for the tensile strength of the bulk material is considered and presented in Section 3.3. This theory is an expansion to the above methodologies, where a yielding surface is proposed. The yielding surface gives an indication into the strength of a bulk material, for both compressive and tensile loading conditions.

3.3 BULK MATERIAL ADHESIVE TENSILE STRENGTH MODELLING

The determination of the cohesive and adhesive stresses of bulk materials are usually estimated by linear extrapolation of the Instantaneous Yield Locus (IYL) of the Mohr circle theory, presented above. By using a linear extrapolation, the estimation of the adhesion is typically overestimated. Additionally, a linear extrapolation cannot give a true value for adhesion as the intersection point must lie perpendicular to the normal stress axis, where no shear stresses are present.

In order to gain a more accurate estimation of the adhesion present in bulk materials, a revised methodology is presented by the author [71, 72] as shown in Figure 3.5. This methodology utilises a series of internal friction angles (φ_t) which increase as the stresses acting on the bulk material sample reduce and enter the negative (tension) region, i.e. $\varphi_{t3} > \varphi_{t2} > \varphi_{t1}$. It has been shown that the curvature of the IYL for low normal loads can be quite pronounced. In some cases, it can be possible for the angle of internal friction, φ_t, to increase all the way to 90^0 at the point of intersection with the shear stress axis [4, 58, 59]. Furthermore, work conducted by Orband and Geldart [69] have shown that the cohesion of powders can be overestimated if a linear extrapolation of the IYL is assumed. It should be noted that the consolidation conditions may produce slight variances between methods however care is taken to ensure the consolidation between different testing procedures is on an equivalent basis.

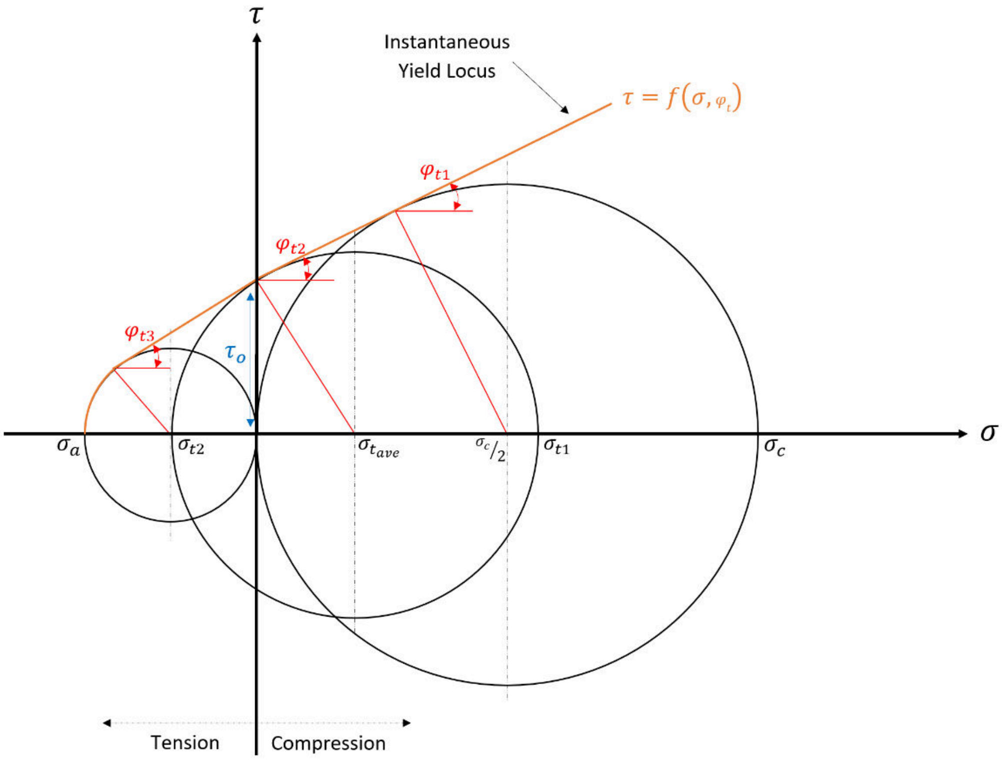

Figure 3.5 – Schematic of modified yield locus with increasing internal friction angles.

The direct measurement of cohesion can be quite difficult to achieve any form of accurate determination. Methods do exist for the measurement of the cohesion of powders, however, limitations exist, and assumptions have been made to obtain experimental data. Two methods that are commonly used for the determination of cohesion in powders are the Warren Spring–Bradford Cohesion Tester (WSBCT) [69] and the Powder Flow Analyser (PFA) [70].

The testing procedure of the WSBCT and PFA typically consist of a bulk material sample (sieved at 1 mm to prevent undesirable increases in shear strength at the plane of failure [69]) that is placed into a Perspex container, where a consolidation load is applied. A vaned paddle attached to a shaft is then lowered into the sample where a normal load is applied. Hereafter, the paddle is slightly retracted, so no normal load will be acting when the measurement of the torque occurs. Finally, the determination of the cohesion is undertaken from the moment balance around the paddle [69]. The assumptions that are made while using these testers include [69]:

1. The friction produced between the paddle and bulk material is negligible;
2. The shear stress distribution at this interface will be uniform.

When considering the iron ore samples used in this research, the above cohesion testers are unsuitable due to the size fraction they are limited to. The effects of the friction produced between the paddle and bulk material also becomes much more significant with the increase in moisture content of the samples. Additionally, tests conducted by Orband and Geldart [69] showed that the cohesion measured by the WSBCT for a copper powder were inaccurate as the normal load acting on the shear plane was always present. This is a result of the weight of the dense copper powder in between the veins of the tester which would also occur for other dense bulk materials such as iron ore. It can therefore be deduced, that experimental measurements of the adhesion of the bulk material is more suitable using an inter-particle adhesion tester (shown in Section 2.4.9.2).

The active stress states present within a bulk material sample from the point of tangency of the small Mohr semi-circle through to the vertex intersecting in the tensile component (negative value) on the normal stress axis (as shown in Figure 3.5), will typically go through three transition stages. The first stage occurs from the point of tangency of the small Mohr semi-circle through to the shear stress axis where the amount of cohesion, τ_o, is found. During this transition stage the bulk material is under pure shear and the angle of internal friction will progressively increase as the yield locus approaches the shear stress axis, i.e. as: $\sigma_n \to 0$. This can be attributed to the reduction in the normal load acting on the bulk material sample.

The second stage is arguably of most interest and acts between the point of cohesion up until the point of intersection in the tensile component. During this stage the bulk material is under a combination of shear and an additional tensile force. As the yield locus approaches the intersection point where adhesion is found, the angle of internal friction significantly increases. This increase in internal friction angle can be attributed to the transition of the active stress state, where the reduction of the shear stress and the increase in the tensile stress occurs. The final stage is found at the point intersecting in the tensile component where the adhesion can be determined. The stress state of the bulk material at this point exhibits pure tension where no shear stresses are present.

A simplified version of the model proposed by the author [71, 72] is shown in Figure 3.5 which uses a parabolic profile for the extrapolation of the IYL. This parabolic profile is considered tangential to the intersection point of the IYL at the shear stress axis (where the amount of cohesion, τ_o is found) and has its vertex intersecting in the tensile component (negative value) on the normal stress axis [71, 72]. A parabolic profile has been assumed as the intersection point on the normal stress axis where adhesion is present must lie normal to the axis. This can be attributed to no shear forces being present when the adhesion of a bulk material is determined.

A schematic of the adjusted Yield Locus is shown in Figure 3.6. This simplified model has been developed using the work of Ashton et al. [68] as a basis, where an empirical model was used to fit the points of the IYL. The points of this model are determined using an inter-particle adhesion tester and the Jenike direct shear tester, where a value of the cohesion, τ_o was estimated. It is appropriate to identify that the developed methodology uses points of the IYL which consider a linear fit for the determination of the minor principal stress, σ_2, and the unconfined yield strength, σ_c. Additionally, the linear extrapolation of this line is used for the determination of the cohesion, τ_o. By using this methodology, it is possible to obtain a value of the adhesion of a bulk material sample by conducting the Jenike direct shear test alone. This will be a significant reduction into the time required from traditional testing methods to determine the adhesion of a bulk material sample.

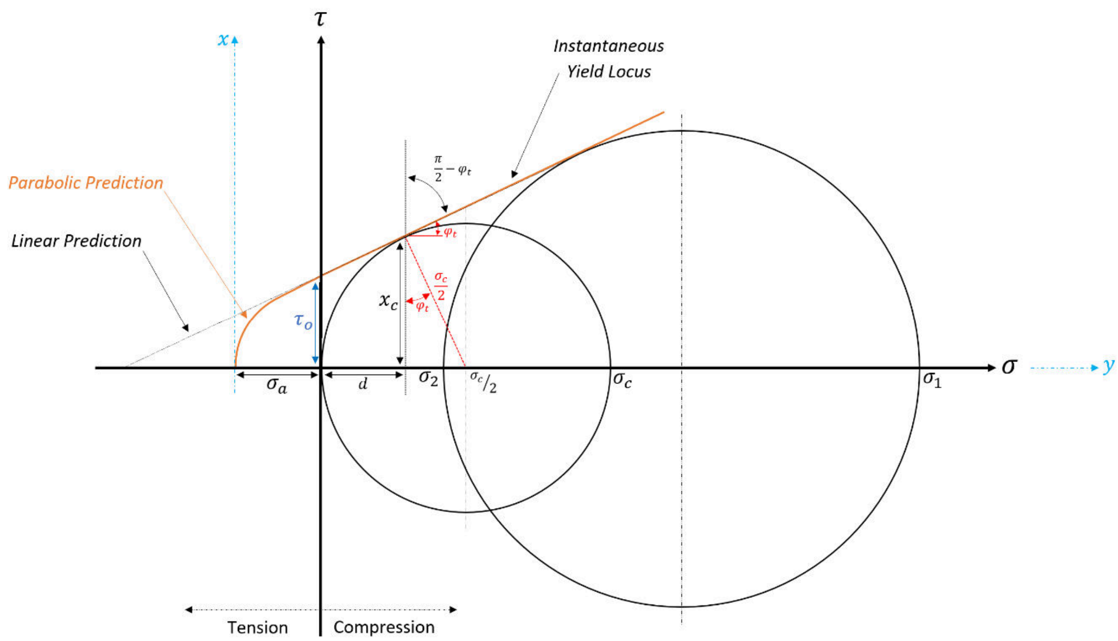

Figure 3.6 – Schematic of modified Instantaneous Yield Locus using parabolic profile for determination of adhesion.

Solving for the cohesion and adhesion values from the schematic in Figure 3.6, an estimation of these values can be found. Firstly, the cohesion, τ_o, of the bulk material occurs when:

$$x_c = \frac{\sigma_c}{2}(\cos\varphi_t) = \tau_o + d\tan\varphi_t \qquad y = \frac{\sigma_c}{2}(1-\sin\varphi_t) \tag{3.2}$$

Solving yields:

$$\tau_o = \frac{\sigma_c}{2}\left[\frac{1-\sin\varphi_t}{\cos\varphi_t}\right] \tag{3.3}$$

At the point of tangency to the intersection point of the shear stress axis, i.e. at: $x = \tau_o$. The slope can be determined as:

$$y' = 2cx = 2c\tau_o \tag{3.4}$$

But also at the point of tangency to the intersection point of the shear stress axis, i.e. at: $x = \tau_o$. The slope can be determined as:

$$y' = \tan\left(\frac{\pi}{2} - \varphi_t\right) = \frac{\cos\varphi_t}{\sin\varphi_t} \tag{3.5}$$

Solving for the derivative constant yields:

$$c = \frac{\cos\varphi_t}{2\tau_o\sin\varphi_t} \tag{3.6}$$

Hence the parabola is determined using:

$$y = \frac{x^2\cos\varphi_t}{2\,\tau_o\sin\varphi_t} \tag{3.7}$$

The adhesion, $\sigma_{a(par)}$, of the bulk material will occur when $y = \sigma_a \; and \; x = \tau_o$. Solving yields:

$$\sigma_{a(par)} = \frac{\tau_o\cos\varphi_t}{2\sin\varphi_t} \tag{3.8}$$

It will also be appropriate to determine the adhesion for a linear extrapolation of the IYL for the comparison between both methods which is undertaken in Section 3.5. The adhesion, $\sigma_{a(lin)}$, of the bulk material for a linear extrapolation is determined using:

$$\sigma_{a(lin)} = \frac{\sigma_c}{2}\left[\frac{1}{sin\,\varphi_t - 1}\right] \tag{3.9}$$

The prediction of the adhesion using the above method can be measured experimentally using an inter-particle adhesion tester modified by the author and explained in detail by Ashton et al. [19] and Plinke et al. [8], where the comparison between the estimated adhesion to experimentally determined results are shown in Section 3.5. By applying the methodology above to consider the voidage between the particles, a surface failure model can also be developed. This three-dimensional model is explained in the Section 3.3.2.

3.3.1 INSTANTANEOUS YIELD LOCUS CONSOLIDATION STRESS CONDITIONS

The stress conditions present within a bulk material sample whilst Jenike direct shear measurements are undertaken are of critical importance. An understanding of the relationship between the pre-consolidation condition through to the failure shear stress is essential in order to fully determine the compaction state of the sample. If the consolidation state of the inter-particle adhesion measurements is considered, the most appropriate comparison to the Jenike direct shear measurements is using the pre-consolidation of the sample. This can be attributed to both testing methods not being subjected to any form of shear stress during the initial pre-consolidation phases, and to be regarded as an equivalent stress state. These equivalent stress states are critical when comparing the predicted adhesion values, outlined in Section 3.3, to the experimentally measured adhesion using an inter-particle adhesion tester (explained in detail by Ashton et al. [19] and Plinke et al. [8]).

The determination of the IYL and corresponding Mohr circles in relation to the pre-consolidation stress is shown in Figure 3.7. The pre-consolidation normal stress, σ_p, can be regarded to as the compaction state of the sample. This will have an equivalent compaction state and therefore stress state when the Jenike direct shear measurements and inter-particle adhesion measurements are considered. Once the pre-consolidation normal stress, σ_p, has been applied to the Jenike direct shear tester, the pre-shear of the sample is undertaken until a steady state value is obtained. The pre-consolidation shear stress, τ_p, gives a point (shown in Figure 3.7) which must lie on the major Mohr circle and below the IYL. This can be attributed to the sample not yielding during the pre-shear phases of the Jenike testing regime.

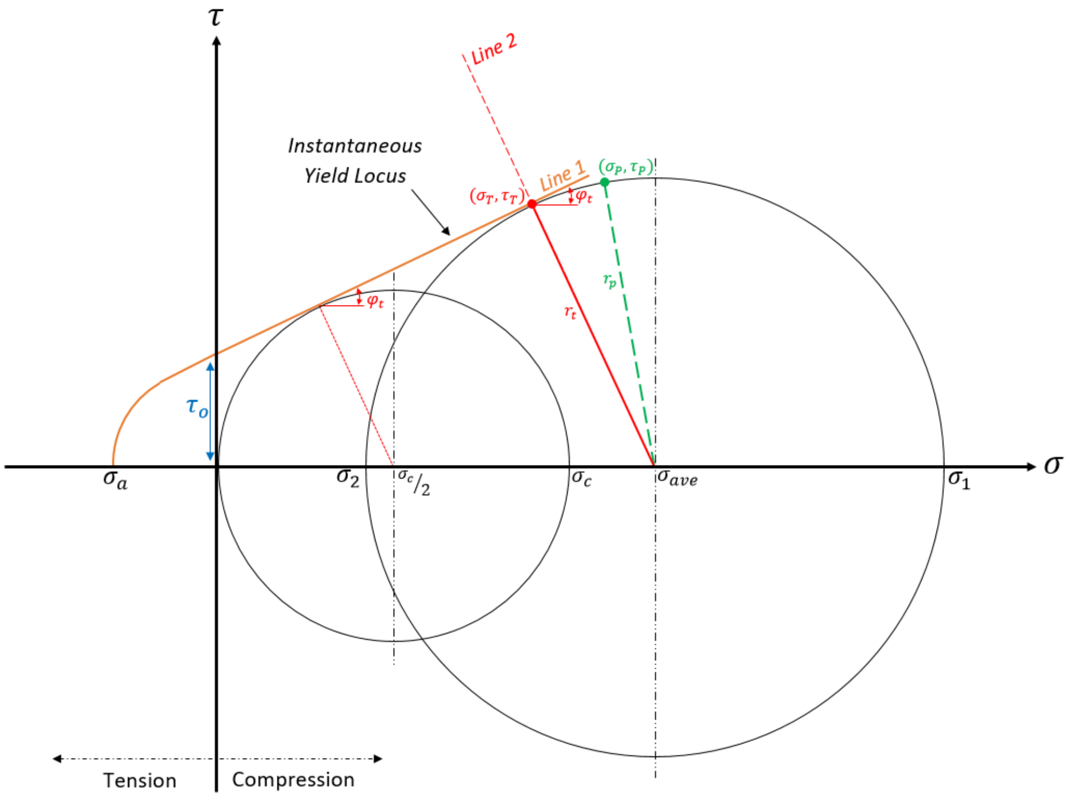

Figure 3.7 – Schematic of Instantaneous Yield Locus showing pre-consolidation stress condition.

Once the pre-shear of the sample has been undertaken, the shear to failure stage commences. This is undertaken for a range of normal stresses, where typically a minimum of five stresses below the pre-consolidation stress are considered. These failure stresses form the IYL where a linear fit will be assumed. Additionally, the extrapolation of the IYL to the intersection point of the shear stress axis gives the cohesion. Once the IYL and pre-consolidation point are defined, the relationship between both can be solved. It will be appropriate to acknowledge that the following calculations have been undertaken in conjunction with Donohue [73]. Solving for the pre-consolidation point and the IYL, the radius of both lines must be equal, i.e. $r_t = r_p$ as shown in Figure 3.7. Firstly, the equations of Line 1 and Line 2 are given using:

$$y_{Line\ 1} = \tau_o + \sigma_T \tan\varphi_t \qquad y_{Line\ 2} = b - \frac{\sigma_T}{\tan\varphi_t} \tag{3.10}$$

Solving for the intersection point of Line 1 and Line 2, the tangent point of the IYL and major Mohr circle, yields:

$$\sigma_T = \frac{b\tan\varphi_t - \tau_o\tan\varphi_t}{1+\tan^2\varphi_t} \qquad \tau_T = \frac{b\tan^2\varphi_t - \tau_o\tan^2\varphi_t}{1+\tan^2\varphi_t} + \tau_o \tag{3.11}$$

where: b is the intersection point on the shear stress axis [Pa].

Using Line 2, the centre of the major Mohr circle, σ_{ave}, occurs when no shear stress will be acting, i.e. at: $\tau = 0$. The centre can therefore be determined as:

$$\sigma_{ave} = b \tan \varphi_t \tag{3.12}$$

To solve for the only unknown, b, the equation for equidistance points can be used, i.e.:

$$\sqrt{(\sigma_T - \sigma_{ave})^2 + {\tau_T}^2} = \sqrt{(\sigma_P - \sigma_{ave})^2 + {\tau_P}^2} \tag{3.13}$$

For simplification purposes, the following constants are used:

$$\begin{aligned} K &= \frac{\tan \varphi_t}{1 + \tan^2 \varphi_t} & L &= \frac{\tau_o \tan \varphi_t}{1 + \tan^2 \varphi_t} \\ M &= \frac{\tan^2 \varphi_t}{1 + \tan^2 \varphi_t} & N &= \frac{\tau_o \tan^2 \varphi_t}{1 + \tan^2 \varphi_t} \end{aligned} \tag{3.14}$$

Solving Equation 3.13 substituting using the values above results in a quadratic equation which can be solved for, b, using the quadratic equation:

$$b = \frac{-C_2 \pm \sqrt{{C_2}^2 - 4C_1C_3}}{2C_1} \tag{3.15}$$

where:

$$C_1 = K^2 - 2K \tan \varphi_t + M^2 \tag{3.16}$$

$$C_2 = 2L \tan \varphi_t - 2KL - 2MN + 2\tau_o M + 2\sigma_P \tan \varphi_t \tag{3.17}$$

$$C_3 = L^2 - 2\tau_o N + N^2 + {\tau_o}^2 - {\sigma_P}^2 - {\tau_P}^2 \tag{3.18}$$

The major principle stress, σ_1, and the minor principle stress, σ_2, are determined using:

$$\sigma_1 = b \tan \varphi_t + r_t \qquad \sigma_2 = b \tan \varphi_t - r_t \tag{3.19}$$

The radius of the major Mohr circle, r_t, is determined using:

$$r_t = \sqrt{\sigma_{ave}{}^2 - 2\sigma_{ave}\sigma_P + \sigma_P{}^2 + \tau_P{}^2} \quad (3.20)$$

By relating the pre-consolidation stress to the IYL and the major principle stress, σ_1, an understanding into stress state acting in the bulk material sample can be gained. Furthermore, by considering the pre-consolidation state of the sample in the Jenike direct shear test, equivalent stress states occur when the inter-particle adhesion tester (explained in detail by Ashton et al. [19] and Plinke et al. [8]) is considered. These equivalent stress states are essential when comparing the predicted adhesion values to experimentally measured values, as outlined in Section 3.5.

3.3.2 ADHESIVE STRENGTH VOIDAGE SURFACE MODEL

Following the previous discussion, the presented methodology can also be applied to the theory of Hvorslev [66] and Roscoe et al. [67] by considering the voidage between the particles of the bulk material. It was outlined in Section 3.2.2, if a yield surface was considered with the bulk density, ρ_{bulk}, and voidage, ε, between the particles of the bulk material, an increase in the bulk density of a bulk material would occur when an associated decrease in the voidage between the particles is experienced [68]. The original work of Hvorslev [66] and Roscoe et al. [67] assumed a tension cut-off where the linear interpolation of the IYL to the shear stress axis was used. To consider the adhesion present in powders, the work of Ashton et al. [68] determined the yield loci of lithopone via measurements using the Jenike direct shear tester [4] and a tensile testing apparatus developed at Warren Spring Laboratory [19], which the inter-particle adhesion tester presented in Section 2.4.9.2 was further developed from. The results of the yield locus measurements were found to conform to the following:

$$\left(\frac{\tau}{C_{JDST}}\right)^n = \frac{\sigma}{T} + 1 \quad (3.21)$$

where: τ is the shear stress [Pa].

n is the shear index, known to vary between 1 and 2.

C_{JDST} is the cohesion from the Jenike direct shear tester [Pa].

σ is the normal stress [Pa].

T is the tensile strength from the tensile tester [Pa].

The equation above can be explained in terms of a simple model where it can be assumed that if the stresses present in the bulk material sample remain below a critical level it deforms elastically, according to Hooke's law for both compressive and tensile stresses [69]. It was also determined that in general, the shear index, n, is independent of the bulk density of any given bulk material at any given particle size and distribution [68]. It was further observed that a correlation of the shear index and Jenike's classification of the *"flowability of solids"* [4] could be shown. The shear index, n, can be classified as 1 for a free-flowing material up to 2 for very cohesive bulk materials. It will be appropriate to identify that when $n = 1$ Coulombs equation, ($\tau = \mu\sigma + C_{JDST}$), results which is used extensively in soil mechanics. For a hypothetical case of a perfectly free-flowing bulk material where C_{JDST} and T are zero, the shear stresses at failure will be proportional to the normal stresses [68].

The extrapolation of the measured yield loci of the lithopone into the $\rho - axis$ as presented in the work of Ashton et al. [68] results in a yielding surface similar to Figure 3.4. The tensile strength curve is shown to be asymptotic to the $\rho - axis$ at low bulk densities and a constant value is found at higher bulk densities. It could be identified that for low bulk densities, the particles are typically *"loosely packed"* with a low tensile strength. However, for high bulk densities, the particles are packed together more closely, where small changes in the bulk density leads to large changes in the tensile strength [68]. Although the methodology proposed by Ashton et al. [68] was able to establish a yielding surface which included the adhesive nature of the tested powders, assumptions into the shear index were still required. By using the application of a parabolic profile tangential to the intersection point of the IYL at the shear stress axis (where the amount of cohesion, τ_o is found) and having its vertex intersecting in the tensile component (negative value) on the normal stress axis a yielding surface (shown in Figure 3.8) can be produced. This surface is directly formulated from results obtained using a Jenike direct shear tester.

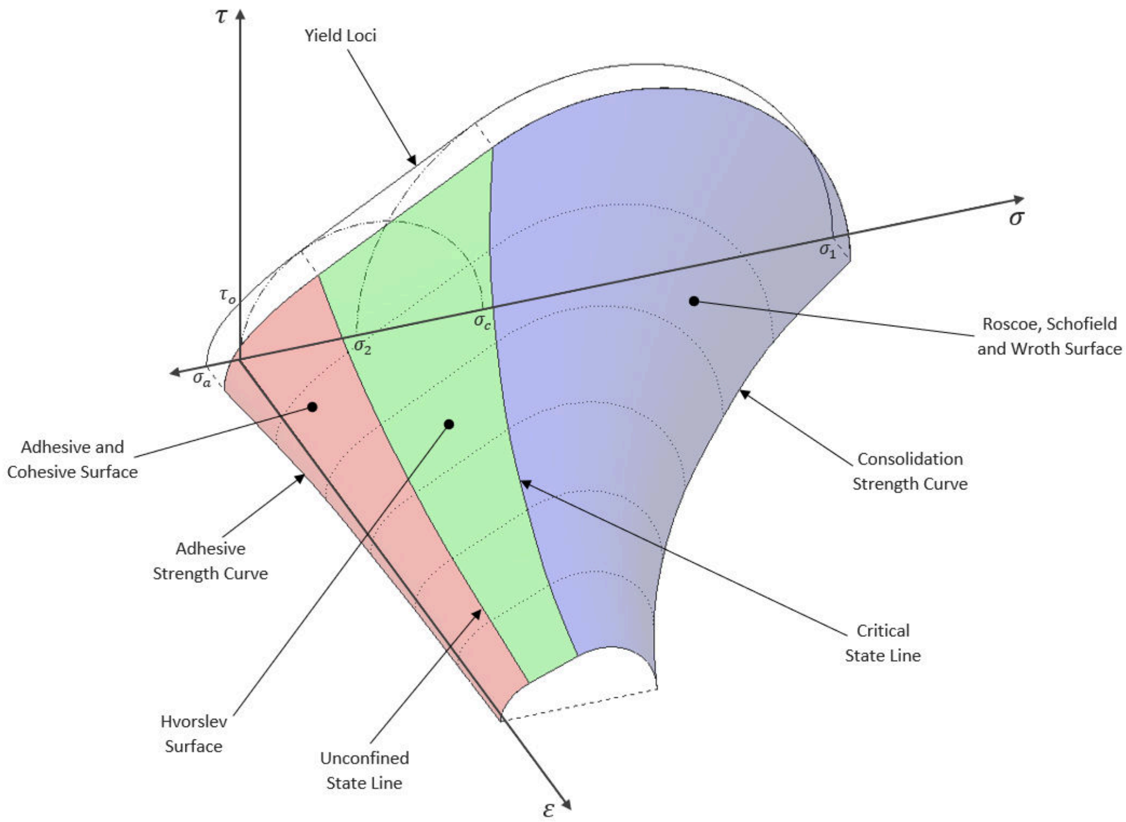

Figure 3.8 – Hvorslev yield surface incorporating assumed profile for adhesion and cohesion.

If the surface in Figure 3.8 is compared to the existing theory of Hvorslev [66] and Roscoe et al. [67] the consolidation strength curve, critical state line and yield loci remain the same, and the Roscoe, Schofield and Wroth surface (shown in blue) remain unmodified. If the Hvorslev surface (shown in green) is considered, it has been proposed by the author that there is a reduction in the area of this surface compared with the original theory of Hvorslev [66]. This reduction will be a result of the yield locus only being considered to the point of tangency of the small Mohr semi-circle. This point can now be defined as the Unconfined State Line when extrapolated into the voidage, ε, direction (shown in Figure 3.8). Looking to the left of the unconfined state line, the Adhesive and Cohesive Surface (shown in red) is produced which is based off the assumption presented above of a parabolic profile.

The use of a tensile testing apparatus, such as the one developed at Warren Spring Laboratory [19], for the determination of the inter-particle adhesion of a sample during the calculation of the yield locus results in the potential for experimental error. This error depends on the experience level of the user and the reproducibility of measurements, where it can be difficult to reach the critical consolidation of the sample. By using a parabolic assumption presented above, the need for an experienced operator is negated as the measurements of the yield loci points in the Jenike direct shear tester [4] can be quite reproducible in relation to the consolidation of the sample as explained in ASTM D 3080 [6]. The comparison between the estimated adhesion and measured results from an inter-particle adhesion tester (presented in Section 2.4.9.2) will be undertaken in Section 3.5.

3.4 YIELDING THEORY OF BULK MATERIALS

In the design of bulk material handling systems, the need for quantitative measurements of the bulk material characteristics is essential. These measurements are used during the design phases or when new ore bodies are used to negotiate existing bulk material handling systems. For the latter, handling problems can exist which can be broken down into two main categories [1]:

- *Type 1 – Arching and Ratholing;*
- *Type 2 – Blockages in Chutes and Transfers.*

Furthermore, each type of handling problem can be further broken down into the following sub categories which include [1]:

- *H1.1 – Arching over openings during gravity flow;*
- *H1.2 – Hang-ups and ratholing;*
- *H2.1 – Adhesion and friction at low contact pressures;*
- *H2.2 – Sliding in chutes and hoppers at low contact pressures.*

The main types of handling problems which are the focal point of this research, are H2.1 and H2.2 which are mainly confined to chutes and transfer systems. The correct design and choice of wall lining material for these types of problems are critical for the reliable flow of the bulk material and for the reduction of downtime of the system [1]. It will be appropriate to identify that these handling problems may also be found in storage bins, although this is not in the scope of this research. Additionally, the H1.1 and H1.2 handling problems are not considered in any analysis but are merely identified for completeness of the thesis.

The contact pressures experienced within chutes and transfer systems are typically low, which will lead to high wall friction angles. Handling problems can therefore arise as a result of this higher friction in conjunction with the cohesion and adhesion which is present [74, 75]. When the IYL and WYL are both considered, different follow regimes can arise. These regimes are dependent on the consolidation the bulk material is subjected to and whether the adhesion and cohesion of the WYL or IYL are the dominating cause of potential handling problems [76]. When the voidage between the particles of the Hvorslev yield surface, presented in Section 3.3.2, is considered, three distinct failure envelopes can occur. The first regime occurs when the IYL is greater than the WYL for the full range of consolidation, as shown in Figure 3.9. For this failure envelope, applied shear stresses which fall below the WYL result in the bulk material not yielding. Conversely, applied shear stresses which fall above the IYL result in the bulk material yielding for the full range of consolidation. When the boundary formed between both yield loci is considered, failure occurs at the boundary, where the bulk material will slide as a clump if a transfer chute or bin is considered. This failure envelope usually occurs for low voidage between the particles leading to high bulk densities.

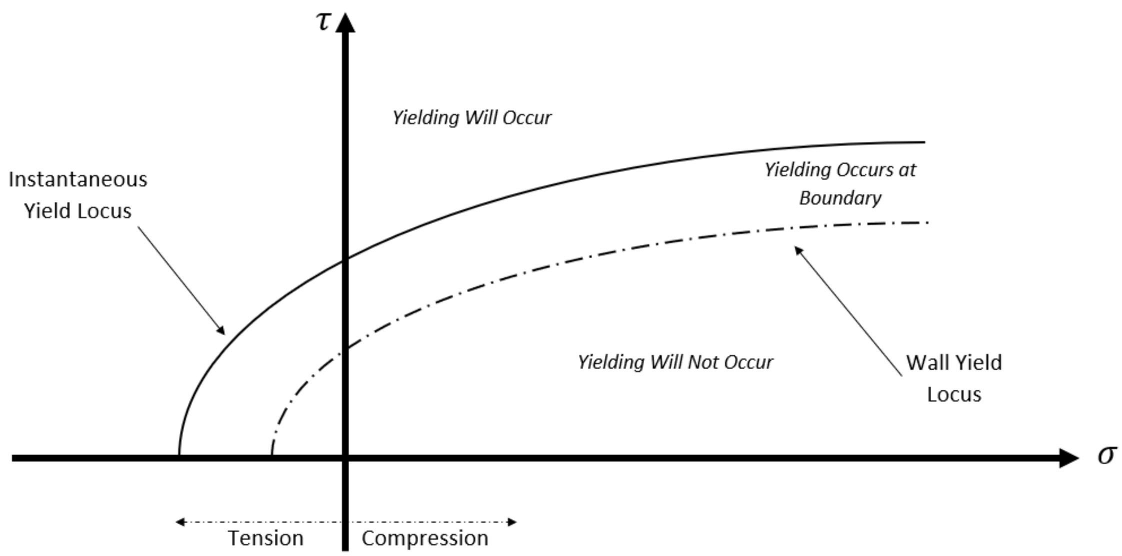

Figure 3.9 – Yielding failure envelope for regime with IYL greater than WYL.

The second regime occurs when the WYL is greater than the IYL for the full range of consolidation, as shown in Figure 3.10. For this failure envelope, applied shear stresses which fall below the IYL results in the bulk material not yielding. Conversely, applied shear stresses which fall above the WYL results in the bulk material yielding for the full range of consolidation. When the boundary formed between both yield loci is considered, failure occurs within the bulk material, where the bulk material does not fail at the boundary surface but rather forms its own bulk material failure surface. This would occur when a bulk material begins to build-up at the boundary surface but then shears on itself, failing to produce a blockage in the instance of a transfer chute. This failure envelope typically occurs for high voidage between the particles, leading to lower bulk densities.

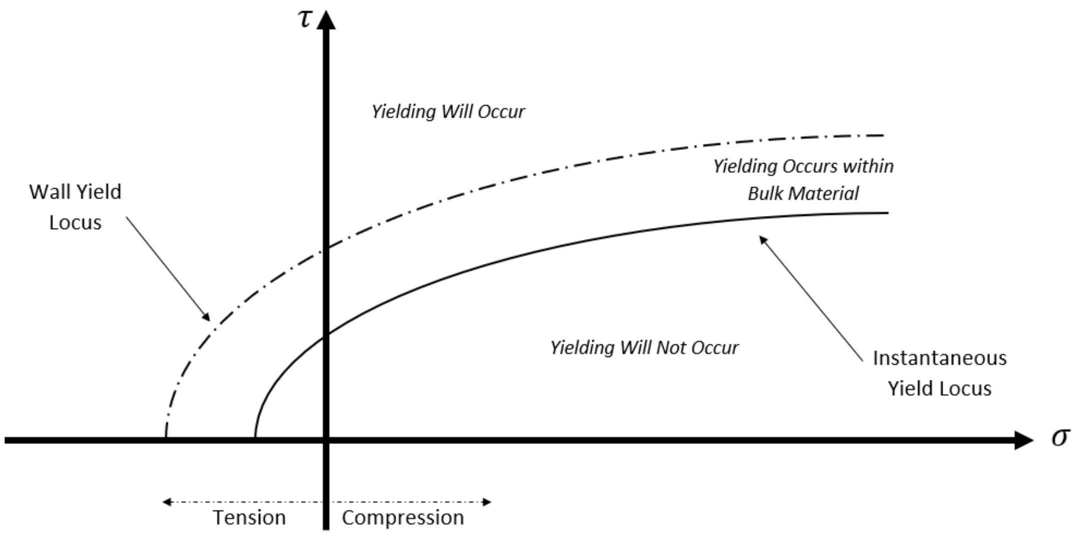

Figure 3.10 – Yielding failure envelope for regime with WYL greater than IYL.

The final regime can be regarded as a special case. This will occurs when the WYL and IYL overlap each other and either may be greater depending on the consolidation of the bulk material, as shown in Figure 3.11. For this failure envelope, applied shear stresses which fall below the WYL results in the bulk material not yielding when higher consolidations are considered. Conversely, applied shear stresses which fall above the IYL for higher consolidations results in yielding which would be typically found in bins and stockpiles. Similar to the first failure regime, if the boundary formed between both yield loci is considered, failure occurs at the boundary, when higher consolidations are considered. As stated previously, these range of higher consolidations are not considered in any analysis but are merely identified for completeness.

When lower consolidations, cohesion and adhesion are considered, it can be feasible for the adhesion determined from the WYL to be greater than the adhesion of the IYL even when the yielding envelope for higher consolidations are the opposite, as shown in Figure 3.11. Furthermore, it can also be possible for the respective cohesion values to swap i.e. the cohesion from the IYL can be greater than the cohesion of the WYL, as shown in Figure 3.11. It will therefore be appropriate and essential to consider the cohesion and adhesion of both yield loci to determine the failure envelope which applies to a particular bulk material. For instance, if the build-up of transfer systems is considered, it is critical to determine if the adhesion of the WYL is greater than the adhesion of the IYL. If this was found to be the case it would be advisable to either change the wall lining material or potentially change the geometry of the transfer system to reduce the adhesion of the WYL. If the adhesion of the WYL was now found to be lower than that of the IYL adhesion, the prevention of build-up could result. A design protocol for the reduction of dynamic adhesion based on the above yielding regimes is presented in Section 6.4.4.

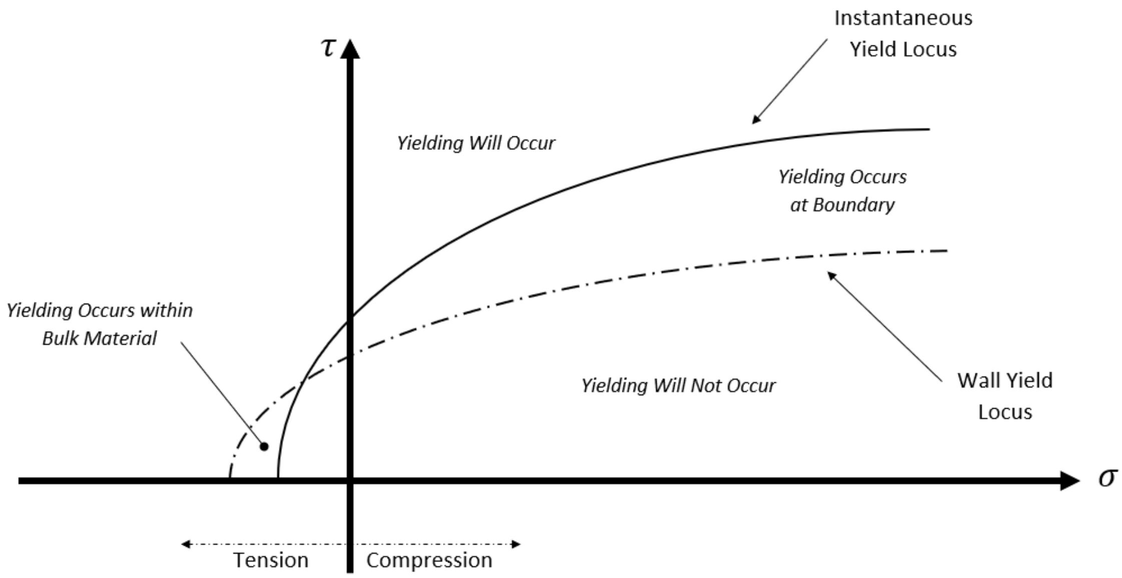

Figure 3.11 – Yielding failure envelope for special case regime.

For the comparison of the cohesion and adhesion of the IYL and WYL to determine which flow regime is present, it will be appropriate to determine these values for the WYL. The method which was proposed by Ashton et al. [68] for the determination of the IYL can be utilised when the wall adhesion tester (outlined in Section 2.4.9.1) is considered with the WYL. The WYL for most bulk materials and wall lining materials tend to be slightly convex upward in shape where the amount of cohesion and adhesion could be estimated [1]. A schematic of the shape of the WYL is shown in Figure 3.12. If the generalised shape of the WYL and IYL are compared (i.e. comparing Figure 3.12 and Figure 3.5) one can immediately identify the similarities of both yield loci. Furthermore, with the work conducted by Ashton et al. [68] it could be assumed that the cohesion of the WYL can be estimated using a similar method. This would be a result of a measured value for the wall adhesion and measurements obtained from an adapted Jenike direct shear tester (outlined in Section 2.5.2.1) to be used to determine the WYL.

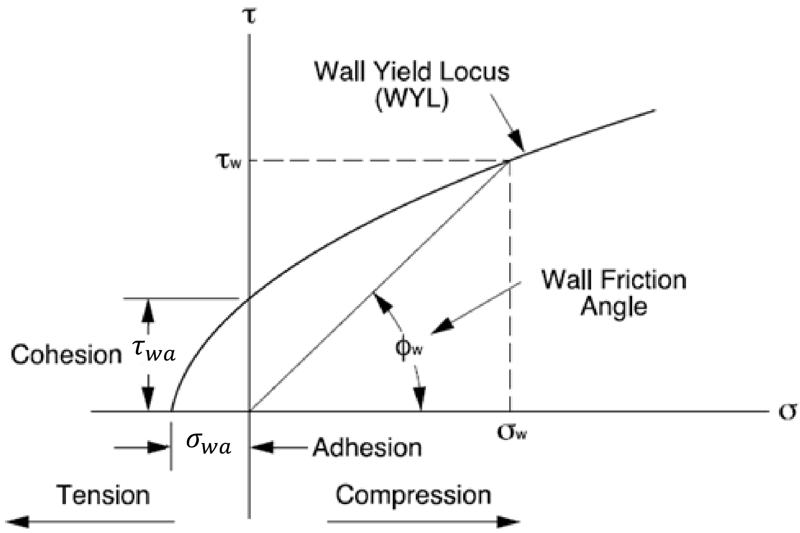

Figure 3.12 – Adhesive stresses determined from WYL (modified from Roberts, 1998).

Using an adapted method initially performed by Ashton et al. [68] for the IYL, as outlined above, the determination of the WYL will be found using the following:

$$\left(\frac{\tau_w}{\tau_{wa}}\right)^m = \frac{\sigma_w}{\sigma_{wa}} + 1 \tag{3.22}$$

where: τ_w is the shear stress at the boundary [Pa].
m is the shear index, proposed to vary between 1 and 2.
τ_{wa} is the cohesion at the boundary [Pa].
σ_w is the normal stress at the boundary [Pa].
σ_{wa} is the tensile strength from the wall adhesion tester [Pa].

The shear index, m, is proposed to be classified as 1 for a free-flowing material up to 2 for very cohesive bulk materials. Ashton et al. [68] determined that in general, the shear index for the IYL is independent of the bulk density of any given bulk material at any given particle size and distribution [68]. It would be expected that the WYL would also be independent of the bulk density, where, the suitability of the proposed model above is investigated in Section 3.6.

Once the flow regime has been determined for a bulk material using the developed methodology above, it will be appropriate to classify the handleability of the bulk material using a method similar to Jenike's classification of the *"flowability of solids"* [4]. This step is critical in determining the severity of how problematic the supplied iron samples are. It was outlined in Section 1.2 that the handleability of a bulk material can be defined as a measure of the cohesive strength of the bulk material. The higher the cohesive strength, the more difficult the handling becomes. It was also established that when considering WSMs, there is an increased focus on the cohesive strength, hence, handleability must be considered rather than the flowability.

The typical ranking assessment of a flow function produced from direct shear testing techniques was outlined in Section 1.2 and a summary of the cohesion handleability ranking assessment used is also shown in Table 1.1. A similar ranking procedure can also be applied to the inter-particle adhesion tester presented in Section 2.4.9.2. Additionally, the ranking methodology may also be applied to the estimated adhesion using the developed methodology presented in Section 3.3 above. Inter-particle adhesion tests are typically repeated for a range of consolidation pressures and moisture contents to gain an understanding of the threshold consolidation and moisture content of a problematic material in relation to the adhesion characteristics for particle-to-particle contact. Once experimental measurements have been obtained it is appropriate to apply a ranking assessment similar to the method applied to the Jenike direct shear tester outlined in Section 1.2. By way of example, a typical ranking assessment, labelled A, produced from the inter-particle adhesion testing is shown in Figure 3.13.

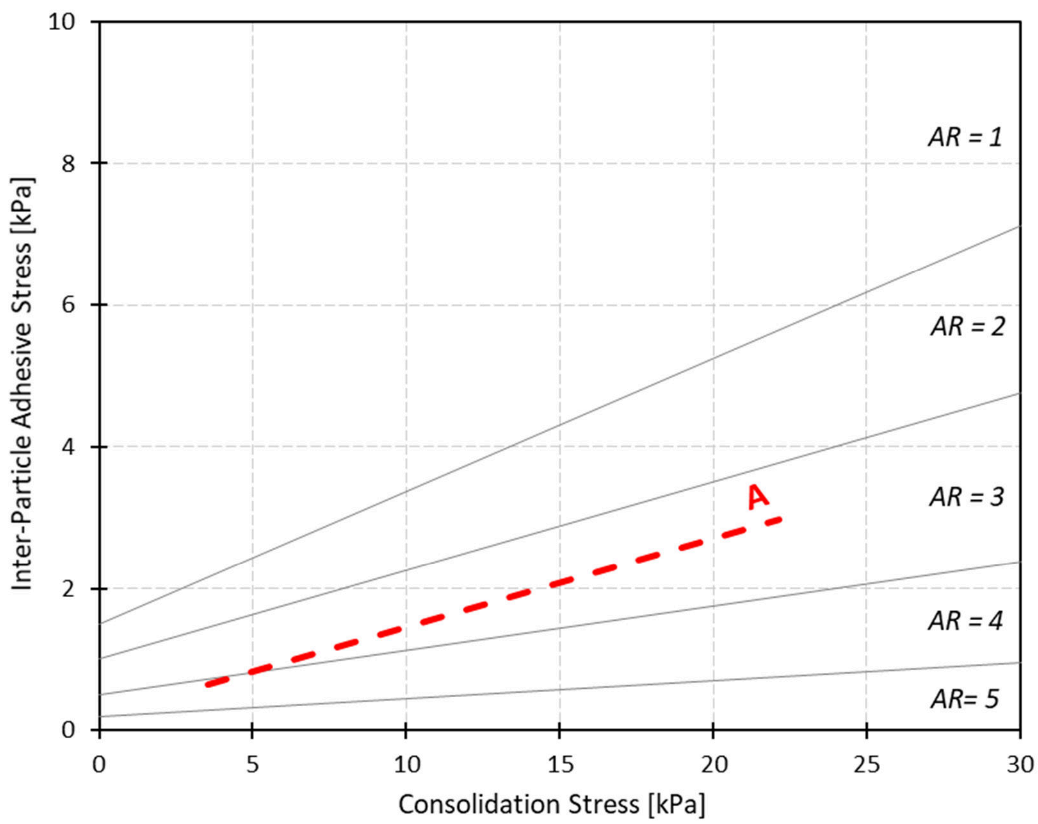

Figure 3.13 – Typical adhesive handleability ranking (AR) assessment from the inter-particle adhesion testing.

The ranking assessment for the inter-particle adhesion testing is determined using the following equation:

$$\sigma_t = K_a(\sigma_{ao} + d\sigma_{1c}) \tag{3.23}$$

where:
- σ_{1c} is the nominated consolidation pressure [Pa].
- σ_t is the tensile adhesive strength [Pa].
- σ_{ao} is the adhesive strength of the bulk material [Pa].
- K_a is the adhesive handleability ranking (see Table 3.2).
- d is a scaling factor [-].

The adhesive strength of the bulk material is given as $\sigma_{ao} = 2kPa$ and a scaling factor of $d = 0.25$ is proposed. Each of the regions, indicated from the four solid lines, are given a ranking depending on the adhesive handling characteristics which are experienced. This ranking is determined from the adhesive handleability ranking K_a, used in Equation 3.23. The adhesive handleability ranking assessment is summarised in Table 3.2.

Table 3.2 – Adhesion Handleability Ranking Assessment

Adhesive Handleability Ranking Assessment	*Adhesive Handleability Ranking (AR)*	*Adhesive Handleability Characteristic*
$\boldsymbol{K_a \geq 0.75}$	*1*	Extremely Adhesive
$\boldsymbol{0.5 \leq K_a \leq 0.75}$	*2*	Very Adhesive
$\boldsymbol{0.25 \leq K_a \leq 0.5}$	*3*	Adhesive
$\boldsymbol{0.1 \leq K_a \leq 0.25}$	*4*	Free Flowing – High Adhesive Strength
$\boldsymbol{0 \leq K_a \leq 0.1}$	*5*	Free Flowing – Moderate Adhesive Strength

Once a bulk material sample has been ranked regarding the adhesion and cohesion handleability using the methodology presented above, the yielding strength of the material can be plotted against the consolidation stress as shown in Figure 3.14. If the yielding strength of the bulk material is considered, three regions are evident for the full range of consolidation. In the positive yielding strength region, the bulk material sample will be in compression, where two phenomena occur. If a stress is induced onto the bulk material that is above the flow function for a particular consolidation stress, the bulk material yields and flow of the bulk material can occur. Stress values below this line results in the material failing to yield, which can also be referred to as no flow, as seen in Figure 3.14.

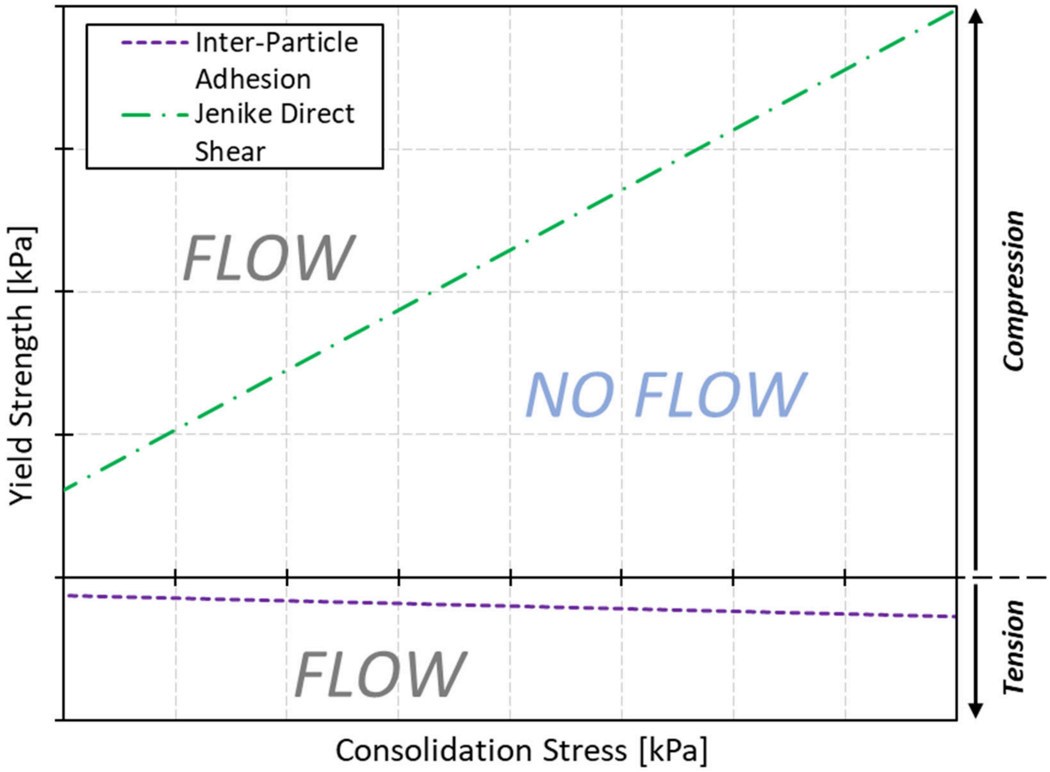

Figure 3.14 – Yielding theory showing boundary conditions for flow and no flow regime.

Similarly, for the negative yielding strength region, the bulk material sample is in tension, where two phenomena also occur. If a stress is induced onto the bulk material that is above the inter-particle adhesion line for a particular consolidation stress, the sample does not yield resulting in no flow as seen in Figure 3.14. Stress values below this line result in the material yielding which can be referred to as the flow of the bulk material as seen in Figure 3.14. The above yielding theory is an expansion on the existing theories of Jenike [4] and Roberts [1] whereby ranking the adhesion in conjunction with the cohesion of the bulk material, the adequate design of bulk material handling systems can be undertaken. This will be evaluated further in Section 3.6.

3.5 EXPERIMENTAL MEASUREMENTS

The comparison of the overestimation of adhesion by linear extrapolation of the yield locus can be compared to the predicted adhesion which is estimated using the methodology presented in Section 3.3. This methodology considers a simplified parabolic estimation which is tangential to the intersection point of the IYL at the shear stress axis (where the amount of cohesion, τ_o is found) and have its vertex intersecting in the tensile component (negative value) on the normal stress axis. Both of these estimations are compared to the experimental measurements using an inter-particle adhesion tester modified by the author [71, 72] and explained in detail by Ashton et al. [19] and Plinke et al. [8].

Repeats of the experimental measurements and visual checks of the failure zone are undertaken for each measurement. Typically, five successful repeat measurements are undertaken for each consolidation pressure where visual checks of the split zone are recorded with each measurement. In the case where a significant difference in the measured force was observed, the visual break (at the failure zone) would be significantly different to that outlined in Figure 2.3. This would generally lead to a much larger surface area which would be difficult to determine with any accuracy. In the case where this form of *"outlier"* measurement occurred, these data were neglected, and a further measurement was undertaken. It is noted that the cells outlined in the work of Ashton et al. [19] employed helical springs for the determination of the inter-particle adhesive force. With the aim of obtaining improved, and reliable adhesion measurements, for the current test program, the split cell apparatus incorporated an electronic load cell. Additionally, the size of the cell was increased to allow for the measurements of a larger range of bulk materials, focusing more specifically on mineral ores, to be undertaken.

Figure 3.15 and Figure 3.16 show the comparison of the measured adhesion data from an inter-particle adhesion tester and the estimation from the extrapolation of the IYL for IOA at 7.8% MC and IOA at 13.1% MC respectively. The inclusion of the linear estimation shows the over prediction of the adhesion which is estimated to be approximately 50% more than the parabolic estimation. When Figure 3.15 and Figure 3.16 are considered it can be shown that the assumption of a simplified parabolic estimation is significantly closer to the measured data than the existing linear extrapolation, which is shown to overestimate the adhesion. This becomes much more significant, with increasing consolidation stress for both cases.

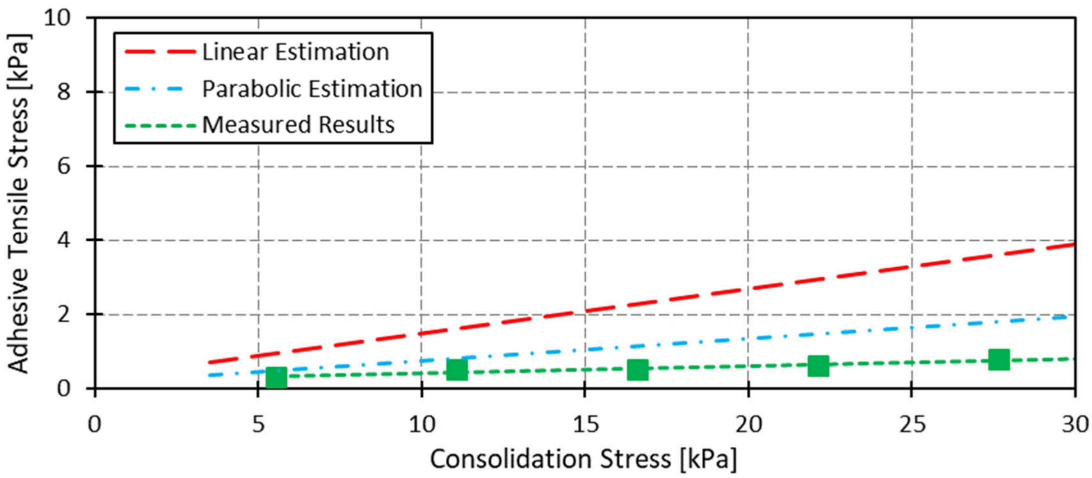

Figure 3.15 – Adhesion estimation for linear and parabolic profiles in comparison to inter-particle adhesion testing for IOA at 7.8% MC.

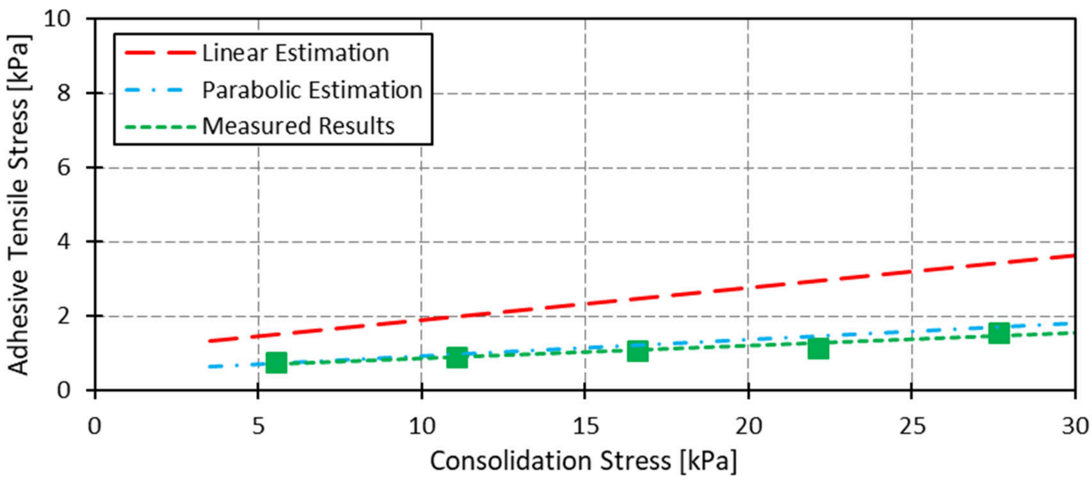

Figure 3.16 – Adhesion estimation for linear and parabolic profiles in comparison to inter-particle adhesion testing for IOA at 13.1% MC.

Figure 3.17 and Figure 3.18 show the comparison of the measured adhesion data from an inter-particle adhesion tester and the estimation from the extrapolation of the IYL for IOB at 14.2% MC and IOB at 17.8% MC respectively. It is shown that the assumption of a simplified parabolic estimation is significantly closer to the measured data than the existing linear extrapolation, which is shown to overestimate the adhesion. This is certainly the case when Figure 3.18 is considered where an excellent correlation is shown. The lower measured adhesion shown in Figure 3.17 when compared to the estimated results could be attributed to the breakdown of the clay elements in this sample as the need for drying to obtain the desired moisture content was required.

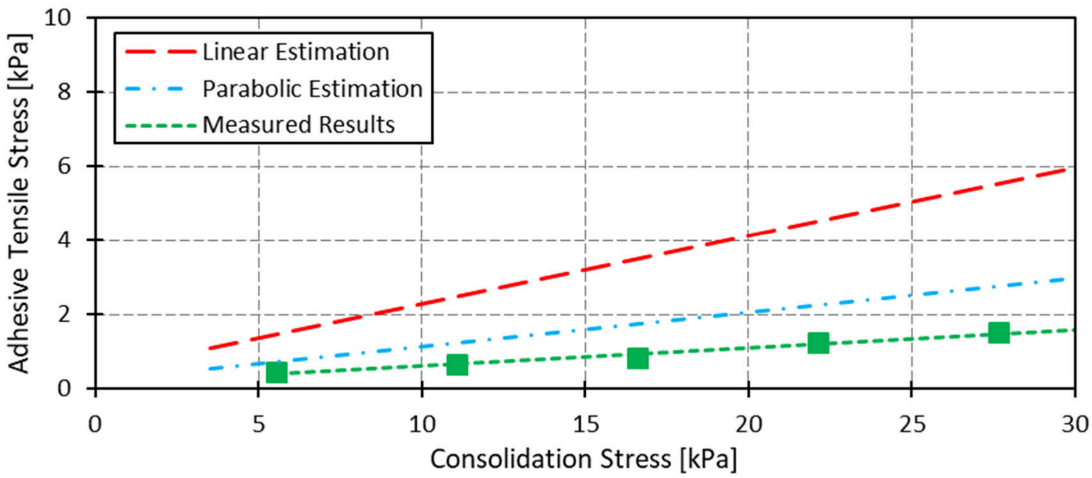

Figure 3.17 – Adhesion estimation for linear and parabolic profiles in comparison to inter-particle adhesion testing for IOB at 14.2% MC.

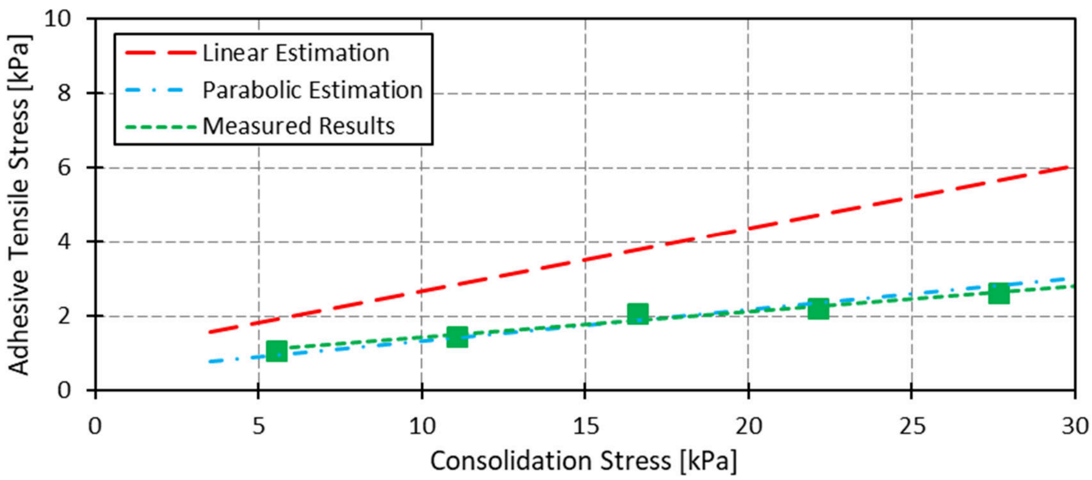

Figure 3.18 – Adhesion estimation for linear and parabolic profiles in comparison to inter-particle adhesion testing for IOB at 17.8% MC.

Figure 3.19 and Figure 3.20 show the comparison of the measured adhesion data from an inter-particle adhesion tester, and the estimation from the extrapolation of the IYL for IOC at 14.6% MC and IOC at 18.2% MC respectively. As before, the assumption of a simplified parabolic estimation is significantly closer to the measured data than the existing linear extrapolation. Although the parabolic estimation is a closer representation in comparison to a linear prediction, the over prediction is still shown for both of the cases for IOC. This can be attributed to limitations in the testing capabilities for the Jenike direct shear tester when bulk materials with high clay contents are considered. An approximate over estimation of 50% is seen for both cases considered, however, this can still be regarded as a much more accurate estimation compared to a linear prediction which would be approximately three times the measured values. It is important to note that comparisons for IOB at 21.3% MC and IOC at 21.9% MC have not been included due to the significant variances between the estimated and measured adhesion values. This can be attributed to limitations of the Jenike direct shear tester where samples which exhibit excessive adhesive and/or cohesive properties may produce results which underestimate the internal strength of the bulk material especially when low consolidation conditions are considered.

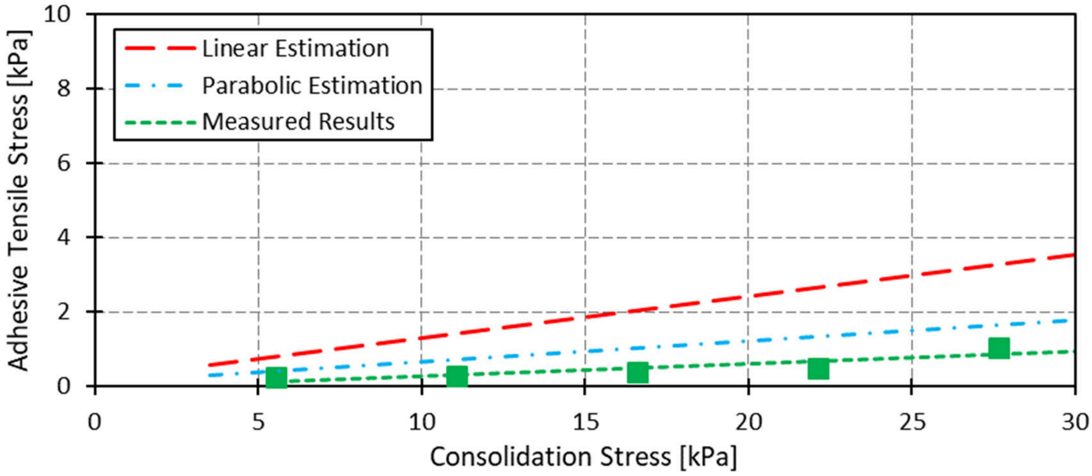

Figure 3.19 – Adhesion estimation for linear and parabolic profiles in comparison to inter-particle adhesion testing for IOC at 14.6% MC.

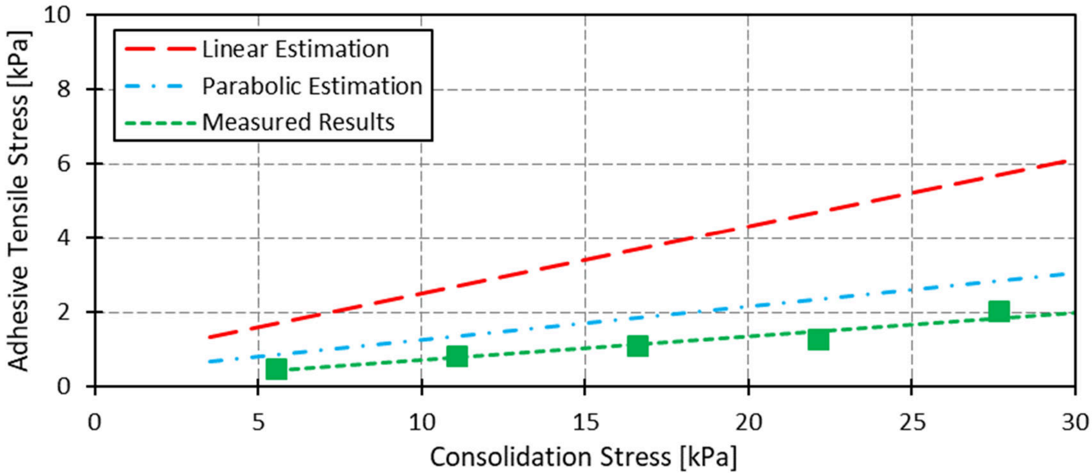

Figure 3.20 – Adhesion estimation for linear and parabolic profiles in comparison to inter-particle adhesion testing for IOC at 18.2% MC.

To further gain an understanding if the above methodology would be applicable to different bulk commodities, five additional bulk material samples have been analysed. The samples tested include; nickel concentrate, black coal, stone dust, zircon sand and limestone.

The PSD of each respective sample is shown in Figure 3.21. By testing a vast range of bulk materials with significantly different PSDs, the suitability of the revised methodology can be achieved for different bulk commodities. It is appropriate to identify that the samples have been sieved to -4 mm size fractions to undertake Jenike direct shear testing in accordance with AS 3880 [20]. The direct shear testing is required for the determination of the IYL of each of the samples. Additionally, the nominated consolidation stresses are attributed to the industrial application of the tested sample. For instance, a manufactured powder or a low cohesive relatively free flowing powder, such as a stone dust, would be subjected to very low consolidations. On the other hand, in the case of *"heavy"* industry such as the iron ore or coal mining sectors, the pressures vary widely from relatively low values under mass-flow to significantly higher values under funnel-flow as is the case of gravity reclaim mineral stockpiles. To obtain a more accurate comparison between the experimental measurements of the inter-particle adhesion tester and the predictions using the developed method, consolidations similar to the Jenike direct shear tester measurements are therefore used which are based on typical applications in industry. It is also important to note that the current testing program has also only considered the as supplied moisture content for each of the respective samples.

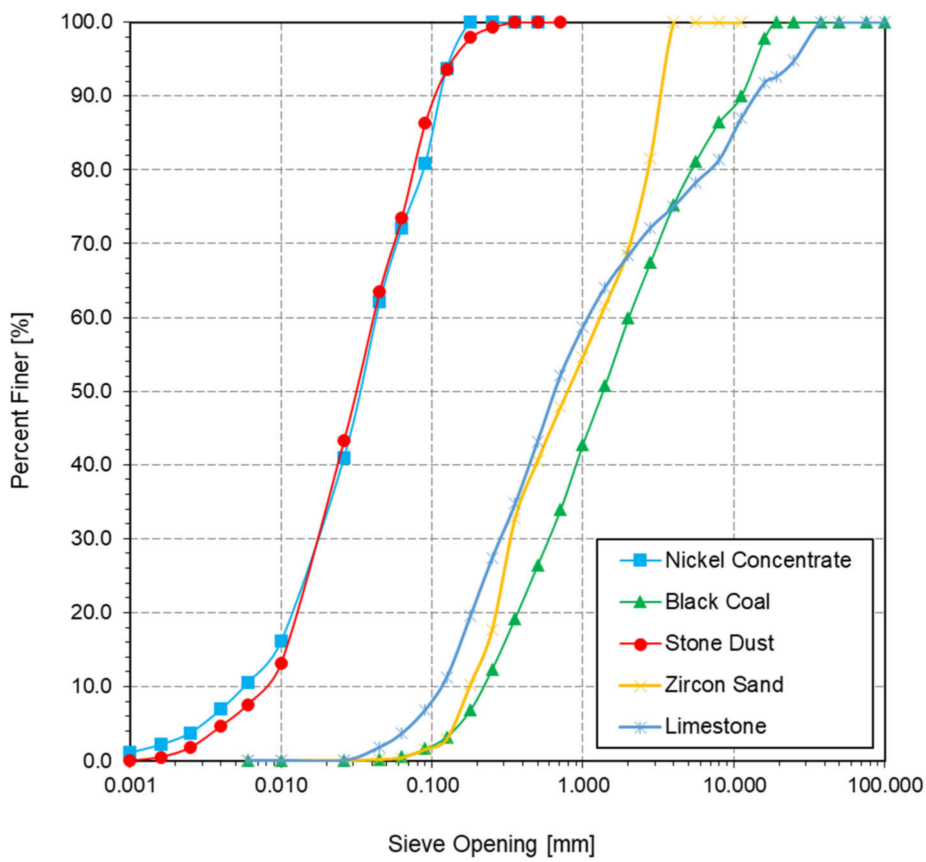

Figure 3.21 – Particle Size Distribution (PSD) of additional bulk material samples.

Figure 3.22 shows the comparison of the measured adhesion data from an inter-particle adhesion tester and the estimation of adhesion from the extrapolation of the IYL for a nickel concentrate sample at 9.4% MC. When Figure 3.22 is considered, it can be shown that the assumption of a simplified parabolic estimation is significantly closer to the measured data than the existing linear estimation. This becomes much more significant with increasing consolidation stress as shown in Figure 3.22. For the full range of consolidation stresses, a very good correlation of predicted adhesion values and measured data from an inter-particle adhesion tester is shown.

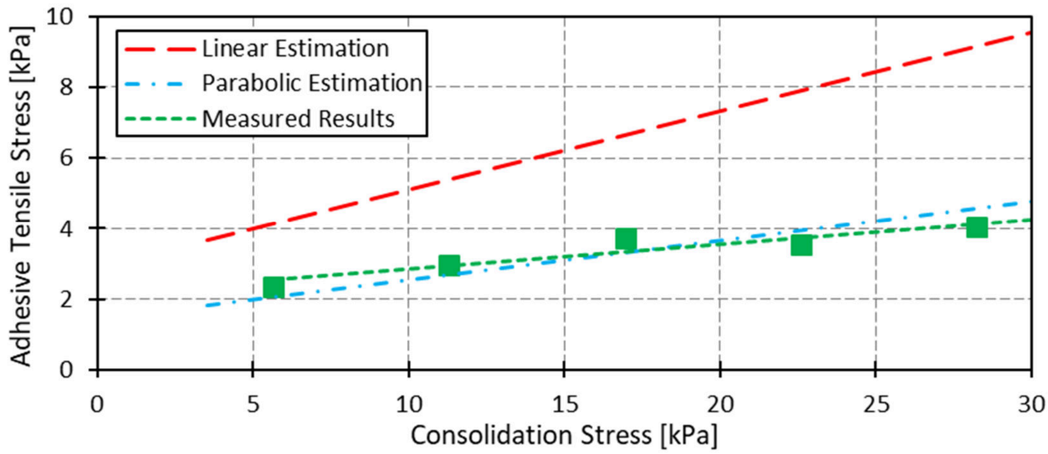

Figure 3.22 – Adhesion estimation for linear and parabolic profiles in comparison to inter-particle adhesion testing for Nickel Concentrate at 9.4% MC.

Figure 3.23 shows the comparison of the measured adhesion data from an inter-particle adhesion tester and the estimation of adhesion from the extrapolation of the IYL for a black coal sample at 12.7% MC. When Figure 3.23 is considered, it can be shown that the assumption of a simplified parabolic estimation is significantly closer to the measured data from an inter-particle adhesion tester than the existing linear estimation. This becomes much more significant with increasing consolidation stress as shown in Figure 3.23.

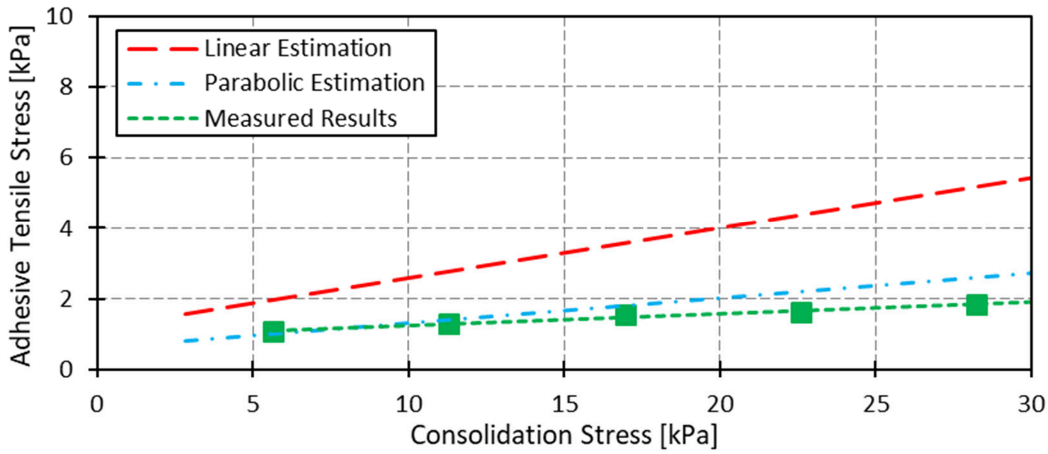

Figure 3.23 – Adhesion estimation for linear and parabolic profiles in comparison to inter-particle adhesion testing for Black Coal at 12.7% MC.

Figure 3.24 shows the comparison of the measured adhesion data from an inter-particle adhesion tester and the estimation of the adhesion from the extrapolation of the IYL for a stone dust sample at 2.0% MC. When Figure 3.24 is considered, it can be shown that the assumption of a simplified parabolic estimation is substantially closer to the measured inter-particle adhesion data than the existing linear estimation. A discrepancy does become evident with increasing consolidation stress as shown in Figure 3.24 which overestimates the adhesion using the revised methodology. If the previous adhesion estimation of a linear approximation of the IYL is considered, the overestimation of the adhesion at higher consolidation stresses will be significantly greater in comparison to the revised methodology.

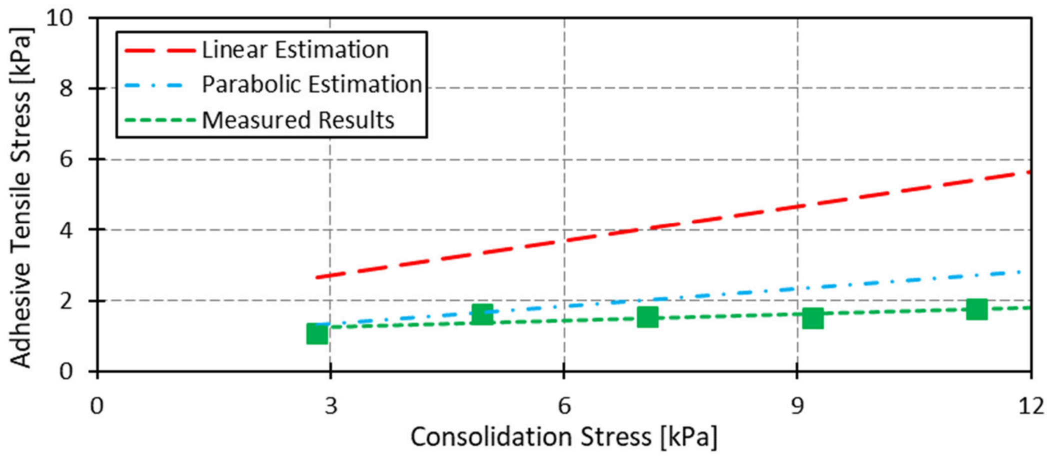

Figure 3.24 – Adhesion estimation for linear and parabolic profiles in comparison to inter-particle adhesion testing for Stone Dust at 2.0% MC.

Figure 3.25 shows the comparison of the measured adhesion data from an inter-particle adhesion tester and the estimation of the adhesion from the extrapolation of the IYL for a zircon sand sample at 6.8% MC. When Figure 3.25 is considered, it can be shown that the assumption of a simplified parabolic estimation is significantly closer to the measured inter-particle adhesion data than the existing linear estimation. This becomes much more significant with increasing consolidation stress as shown in Figure 3.25. For the full range of consolidation stresses, an extremely good correlation of predicted adhesion values and measured data from an inter-particle adhesion tester is shown.

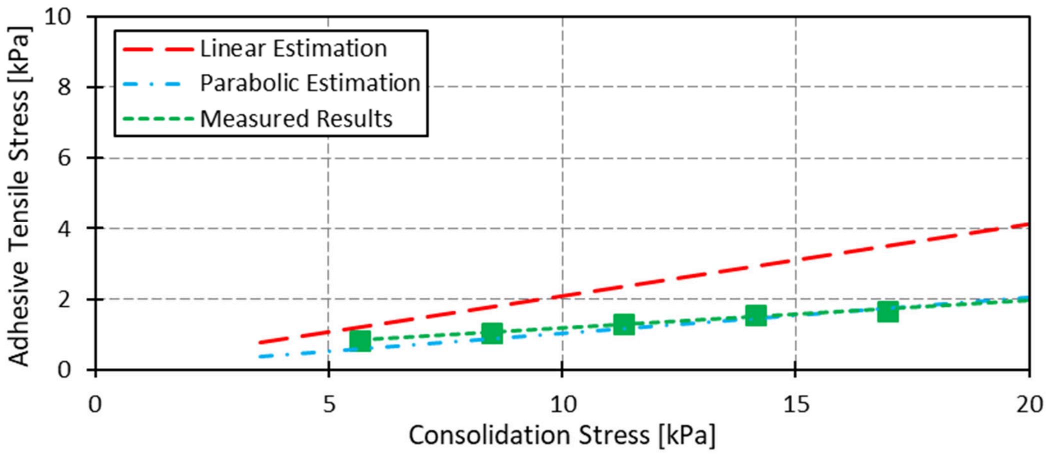

Figure 3.25 – Adhesion estimation for linear and parabolic profiles in comparison to inter-particle adhesion testing for Zircon Sand at 6.8% MC.

Figure 3.26 shows the comparison of the measured adhesion data from an inter-particle adhesion tester and the estimation of the adhesion from the extrapolation of the IYL for a limestone sample at 8.7% MC. When Figure 3.26 is considered, it can be shown that the assumption of a simplified parabolic estimation is significantly closer to the measured inter-particle adhesion data than the existing linear estimation.

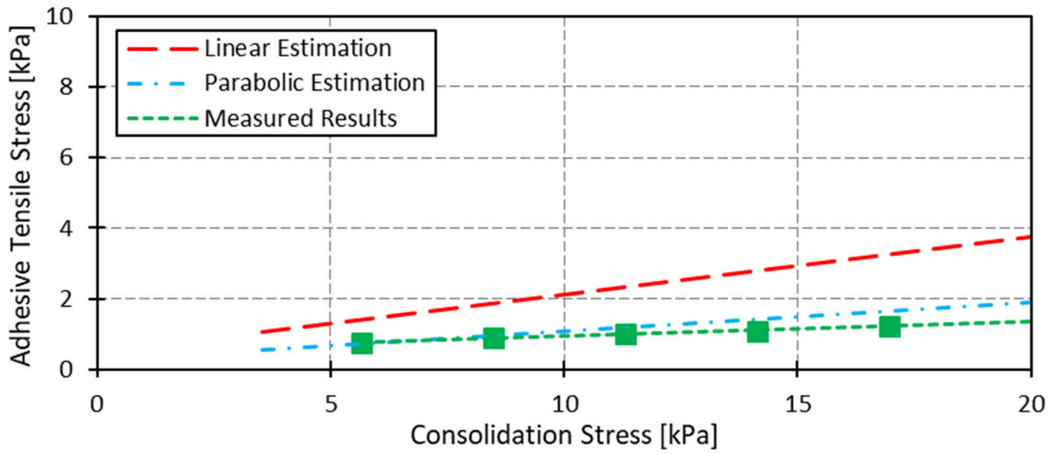

Figure 3.26 – Adhesion estimation for linear and parabolic profiles in comparison to inter-particle adhesion testing for Limestone at 8.7% MC.

Similar to the black coal (shown in Figure 3.23) and the stone dust (shown in Figure 3.24), slight variances resulting in the over prediction of the adhesion are shown when higher consolidation stresses are considered. This may be attributed to the stress states within the bulk material samples not achieving critical compaction which can result in the reduction of the adhesion. It would be recommended to undertake further testing using a linear transducer for both Jenike direct shear and inter-particle adhesion tests to ensure the sample reaches an equivalent compaction state during the consolidation phases of testing. Although this form of testing has not been investigated, a robust model has been developed as shown in the samples analysed.

3.6 RESULTS AND DISCUSSION

It has been demonstrated for all tested samples in Section 3.5, the revised adhesion prediction methodology produces results which are significantly closer than the linear extrapolation of the IYL which is typically used. This is especially found to be the case when IOA at 13.1% MC (shown in Figure 3.16), IOB at 17.8% MC (shown in Figure 3.18), nickel concentrate (shown in Figure 3.22), and zircon sand (shown in Figure 3.25) are considered. The discrepancies for the comparison of the predicted and measured adhesion values for the remaining samples can be attributed to the loss or reduction in moisture content of the sample. When the moisture content of a bulk material sample is reduced, the loss of surface water surrounding the particles occurs where the inherent moisture within the particle remaining much the same. This loss of particle surface water leads to the breakdown of any present clays ultimately changing the behaviour of the bulk material. Although a greater difference in the predicted and measured adhesion values is present for the remaining samples, when higher consolidation stresses are considered, the revised methodology is still significantly closer than the existing methods which are commonly used.

The yielding theory proposed in Section 3.4 considered three regimes of flow, which may be experienced depending on the consolidation pressure, voidage between the particles and moisture content (adhesion and cohesion) of the bulk material sample. Since this research is primarily focused on rapid induced blockages within transfer systems, it will be appropriate to consider low consolidation pressures which typically lead to high wall friction angles. Handling problems can therefore arise as a result of higher friction in conjunction with the cohesion and adhesion which will be present [74, 75]. The flow regimes proposed in Section 3.4 can be utilised when the IYL and WYL are both considered. The first regime occurs when the IYL is greater than the WYL for the full range of consolidation, as shown in Figure 3.9. This failure envelope typically occurs for low voidage between the particles leading to high bulk densities. These types of bulk materials, such as IOB and IOC, exhibit high compressibility due to the high percentage of friable clays which are present. When IOC (21.9% MC) is considered, the extremely high strength which is exhibited internally in comparison to the wall friction suggests this material will follow the first regime when a transfer chute is considered. This can be shown when the inter-particle adhesion results, shown in Figure 2.25, and wall adhesion testing results, shown in Figure 2.21, are considered.

The second regime occurs when the WYL is greater than the IYL for the full range of consolidation, as shown in Figure 3.10. This would occur when a bulk material begins to build-up at the boundary surface but then shears on itself failing to produce a blockage in the instance of a transfer chute. This failure envelope usually occurs for high voidage between the particles which leads to lower bulk densities. These types of bulk materials, such as IOA, typically exhibit low compressibility due to the lower percentage of friable clays and harder particles which are present.

The final regime was regarded to as a special case and occurs when the WYL and IYL overlap each other and either may be greater, depending on the consolidation of the bulk material, as shown in Figure 3.11. When lower consolidations, cohesion and adhesion are considered, it can be feasible for the adhesion determined from the WYL to be greater than the adhesion of the IYL even when the yielding envelope for higher consolidations are the opposite. Furthermore, it can also be possible for the respective cohesion values to interchange where the cohesion from the IYL can be greater than the cohesion of the WYL, as shown in Figure 3.11. It is therefore appropriate and essential to consider the cohesion and adhesion of both yield loci to determine the failure envelope applies to a particular bulk material. This is also essential in determining the geometric constraints required when designing a materials handling system.

If the build-up of a transfer chute system is considered, it is critical to determine if the adhesion of the WYL is greater than the adhesion of the IYL (regime two). If this was found to be the case, it would be advisable to either change the wall lining material or potentially change the geometry of the transfer system to reduce the adhesion of the WYL. If the adhesion of the WYL was now found to be lower than that of the IYL adhesion (regime one), the prevention of build-up could result. It is therefore essential to rank the cohesion and adhesion of bulk material as outlined in Section 3.4. By using a ranking procedure, outlined in Figure 3.14, the consideration of both cohesion (typical flow function assessment) and adhesion will enable for the reduction in the build-up of problematic bulk materials.

3.7 CONCLUSION

This chapter has presented a revised methodology for the estimation of the cohesion and adhesion of bulk materials determined from the extrapolation of the Instantaneous Yield Locus (IYL). Typical methods used a linear interpolation of the IYL for the estimation of cohesion and adhesion that would in most cases overestimate these values. The revised methodology assumes a parabolic profile which lies tangential to the intersection point of the IYL at the shear stress axis (where the amount of cohesion, τ_o is found) and has its vertex intersecting in the tensile component (negative value) on the normal stress axis. The predicted adhesion values from this methodology were compared to experimental testing measurements from an inter-particle adhesion tester (shown in Section 2.4.9.2) where good correlation was found. Additionally, a yielding theory has been presented to expand on the existing theories of Jenike [4] and Roberts [1] where the adhesion of the bulk material is also ranked which can assist in the adequate design of bulk material handling systems.

This page is left intentionally blank

CHAPTER FOUR – DYNAMIC ADHESION MODELLING & ANALYSIS OF BULK MATERIALS

The following chapter builds on the existing continuum mechanics-based methodologies available for the design and flow analysis of bulk materials through transfer chutes. When impact plate transfers are considered, the existing methodologies fail to incorporate the build-up of the bulk material into the continuum analysis. A theoretical model which considers the build-up onto inclined impact plates is proposed and verified with experimentally measured values determined using the inclined plate recirculating system (outlined in Section 6.2).

4.1 INTRODUCTION

During the transportation of bulk materials, conveyor belts are typically used to transfer the bulk material from mine site to processing plants or export terminals (ports). Due to the vast terrain and dissimilar layouts that belt conveyors usually negotiate, multiple conveyors are commonly used where transfer chutes are required to guide the bulk material from one conveyor to another. There are a vast range of transfer chute systems utilised in industry which include the common hood and spoon arrangement, the use of impact wear plates and *"rock-box"* systems. The use of *"rock-box"* systems allow the bulk material to build-up on itself reducing wear. The positioning of transfer chutes to guide and assist the material flow is of critical importance, where a poorly designed system can cause blockages leading to the downtime of the operation. For a well-designed transfer chute, and to the degree possible, the direction and magnitude of the exit velocity of the bulk material should be the same as the outgoing (receiving) conveyor [77]. Additionally, the normal velocity component should be minimised to reduce the propensity for material spillage and reduce the wear and damage of the outgoing conveyor (i.e. damage to support idlers, ripping of belt etc.) [78].

When designing a transfer chute there are three key factors which require consideration. These include the wear of the conveyor belt, the wear of the transfer chute itself, and sufficient slope angles of the chute wall to reduce the propensity to build-up. It is common to optimise for two of these factors, however, difficulties arise when the optimisation of all three parameters is considered. Depending on the length of the conveyor, it is common practice to sacrifice for chute wear where the reduction in transfer chute build-up and belt wear are optimised. This can be attributed to the cost and time required to replace a conveyor belt in comparison to the wall lining material within a transfer chute.

To model the flow of bulk materials through transfer systems, continuum mechanics-based methodologies are commonly utilised. These methodologies consider the bulk material as a continuous stream, which is assumed to be similar to that of a fluid. When granular free flowing materials are considered, the use of a continuum mechanics-based approach is quite feasible. When WSMs are considered, however, the existing methodologies fail to incorporate the cohesion and/or adhesion of bulk materials into the continuum models that leads to material build-up. Furthermore, when the discontinuous (clumping) nature of the flow (as outlined in Section 6.2.2) is considered, the use of continuum mechanics-based approaches fail to solve most problems which relate to systems that exhibit discontinuous behaviour. To accurately depict the discontinuous behaviour of WSMs, numerical modelling simulations are typically utilised (outlined in Section 7.5). It is appropriate to identify that it is common practice to use both methods together to ensure confidence in the continuum calculations and the numerical modelling simulations.

The following chapter gives a brief overview of the existing continuum mechanics-based methodologies and explains the current limitations in relation to modelling WSM behaviours from a modelling perspective. When impact plate transfers are considered, the existing methodologies fail to incorporate the build-up of the bulk material into the continuum analysis. A theoretical model which considers the build-up onto inclined impact plates is proposed and verified with experimentally measured values determined using the inclined plate recirculating system (outlined in Section 6.2).

4.2 CONTINUUM MECHANICS OF BULK MATERIALS

The correct implementation of transfer chutes in the mining sector is key when the operational efficiency is considered. Transfer chutes are typically regarded as the *"bottle-neck"* within the materials handling stream where they require the most maintenance [79]. Some of the issues which arise from insufficient chute design include; conveyor belt wear and damage, spillage of the bulk material, bulk material degradation, off centre belt loading, wear of the transfer chute, transfer chute blockages and dust generation. For the case of this research, emphasis has been placed onto the blockages of transfer chutes which are typically caused by WSMs. It is appropriate to identify that the remaining problems which arise from *"bad"* transfer chute design are also of critical importance, however, they are not considered in the scope of this thesis.

When industrial transfer chutes in the iron ore industry are considered, it is common practice for manufacturing to be undertaken from rectangular wear resistant flat plates. This reduces wear and enables for ease of fabrication and installation [80]. Materials handling issues do arise for such systems however, especially when bulk materials with high moisture contents or high percentages of clays are present. To overcome these limitations, curved chutes are typically utilised to aid in centralising the outgoing bulk material stream and to aid in the prevention of chute build-up [81]. Even with the use of curved transfer chutes, WSMs can still lead to blockage behaviours. The properties of WSMs allow the bulk material to *"stick"* to inclined and vertical surfaces where the time dependent build-up can result in blockages within the transfer chute [82]. Furthermore, failures of the transfer chute supporting structure can also result from blockages caused by WSMs [83].

The main causes of blockages in transfer chutes is attributed to the velocity and trajectory impact angle of the bulk material. If the velocity drops below a threshold value or the impact trajectory changes significantly, the adhesive and cohesive properties of the bulk material cause the transfer chute to block. This is attributed to the material stream is not being fast enough to clear the chute [82]. If a blockage does occur, significant problems arise, where the outgoing conveyor can either be flooded and/or overloaded resulting in spillage even when skirts are installed on the system [84]. Overloaded belts occur when a prior blockage has dislodged and fallen onto the outgoing conveyor. These types of events commonly cause damage to the conveyor belt, idler rolls and supporting structure. The cost that WSMs can add to the price of bulk materials due to transfer chute blockages is attributed to system downtime where some cases have reported downtimes of approximately 7-30 hours per week [3].

To prevent blockages in transfer chutes, design procedures must be followed which are typically undertaken in five separate sections. The major areas which require consideration include; discharge models, material trajectory models, impact models, sliding flow models and free fall models [85]. A simplified schematic of a conveyor-to-conveyor *"hood"* and *"spoon"* transfer system is shown in Figure 4.1. For the case of this research, emphasis has been placed onto the blockages of transfer chutes caused by WSMs which are commonly experienced in the impact zones. The following section outlines the available continuum mechanics-based trajectory and discharge methodologies available which are utilised as inputs for the developed impact model (outlined in Section 4.3.1.2).

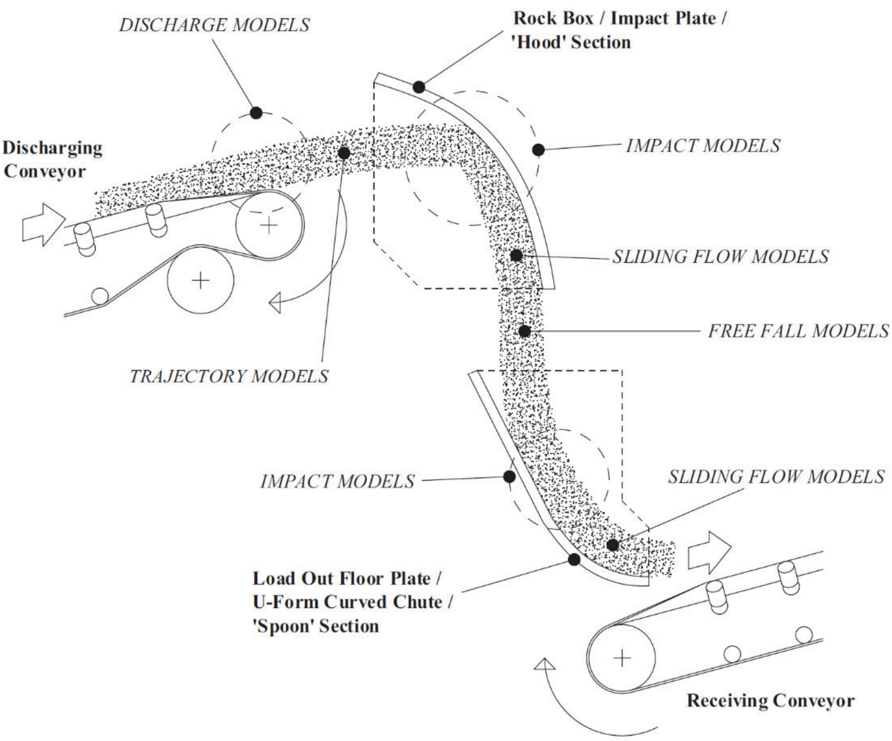

Figure 4.1 – Simplified schematic of conveyor-to-conveyor "hood " and "spoon" transfer system (Huque, 2004).

4.2.1 DISCHARGE AND TRAJECTORY METHODOLOGIES

As bulk materials travel over the head pulley of a conveyor belt, discharge and trajectory models are used to describe the flow of the bulk material. When continuum mechanics-based approaches are considered, numerous methods exist which are used to model the discharge and trajectory of the bulk material. Some of the notable methods include; the CEMA method [86], the MHEA method [87], the method of Korzen [88, 89], the method of Booth [90], the method of Golka [91, 92], the Dunlop method [93], the Goodyear method [94] and the method developed by Roberts [78, 95 – 97]. Each of these methods can be used for the placement of the *"hood"* section of a transfer chute where optimisation for the parameters outlined in the previous section must be considered. The trajectory calculations consider both low-speed and high-speed discharge. When low-speed discharge is considered, the bulk material wraps around the head pulley before entering the trajectory stage. High-speed trajectories result in the bulk material to discharge tangentially from the head pulley where the bulk material does not wrap around the head pulley [80].

When the adhesion of WSMs is considered, the majority of the methods presented above are unsuitable as they neglect to incorporate the adhesive properties into the discharge and corresponding trajectory calculations. The method of Roberts [78, 95 – 97] and Korzen [88] incorporates adhesion into the trajectory calculations where air drag is neglected. To consider the effects of air drag, Korzen [89] considered an alternative approach which is the most complex of all the methods outlined. Research undertaken by Hastie [80] showed that the method of Korzen [89] which incorporates air drag typically underestimates the trajectory of the bulk material stream. This results in the stream to fall closer to the head pulley in comparison to the alternative methods. Additionally, the method of Korzen [89] was found to further underestimate the trajectory of the bulk material stream with increasing belt velocity.

Since WSMs have excessive adhesive properties, the method of Korzen [88] and the method of Roberts [78, 95 – 97] are deemed to be the most suitable for the determination of the trajectories which are used as inputs into the developed impact model (outlined in Section 4.3.1.2). As outlined in the work of Hastie [80], this is especially found to be the case when a low-speed discharge is considered, where the effects of adhesion become much more important. One of the critical inputs required for the trajectory calculations is the determination of the discharge angle, α_d, and the discharge velocity. The angle of discharge of the bulk material using the method of Roberts [78, 95 – 97] is determined when the normal force, N, is zero. At this point, discharge of the bulk material will occur. A schematic of the conveyor discharge model showing the bulk material element travelling around head pulley is shown in Figure 4.2.

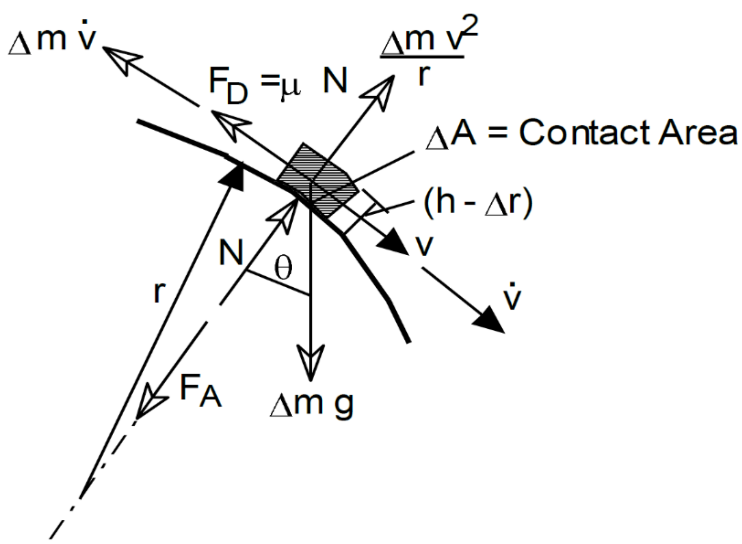

Figure 4.2 – Conveyor discharge model showing bulk material element travelling around head pulley (Roberts, 2001).

The angle of discharge is determined using:

$$\frac{v^2}{R_h} = g \cos \alpha_d + \frac{F_A}{\Delta m} \tag{4.1}$$

where: v is the velocity of the mass element [m/s].

R_h is the radius of the head pulley [m].

g is the gravitational acceleration [m/s^2].

α_d is the angle of discharge [°].

F_A is the adhesive force [N].

Δm is the element mass [kg].

The element mass (Δm) is determined using:

$$\Delta m = \rho_{bulk} \Delta A (h_b - \Delta r) \tag{4.2}$$

where: ρ_{bulk} is the bulk density of the bulk material [kg/m^3].

ΔA is the element contact area [m^2].

h_b is the material stream height [m].

Δr is the change in radius [m].

When the bulk material discharges at the point of contact when the conveyor belt and head pulley first come into contact, the velocity is considered to be high-speed [78]. The minimum belt velocity required for high-speed discharge to occur is determined using:

$$V_b = \sqrt{g R_h \left(\cos \alpha_b + \frac{\sigma_a}{\rho_{bulk} g h_b} \right)} \tag{4.3}$$

where: V_b is the belt velocity [m/s].

α_b is the inclination angle of the conveyor [°].

σ_a is the adhesive stress [Pa].

The method of Korzen [88] is similar in approach to that of Roberts [78, 95 – 97] where the produced discharge condition equations are the same. The belt velocity is considered to be high-speed if the following condition is met:

$$\frac{{V_b}^2}{gR_b} - \frac{\sigma_a}{\rho_{bulk} g h_b} \geq \cos \alpha_b \tag{4.4}$$

The belt velocity is considered to be low-speed if the following condition is met:

$$\frac{{V_b}^2}{gR_b} - \frac{\sigma_a}{\rho_{bulk} g h_b} < \cos \alpha_d \tag{4.5}$$

where:

$$R_b = R_h + 0.5 h_b \tag{4.6}$$

Once the discharge conditions are determined, the trajectory calculations are undertaken which are then used as input parameters for the impact and sliding flow models. It is appropriate to identify that the use of experimental measurements (outlined in Section 6.2) will be undertaken for the trajectory calculations and determination of the stream thickness due to the significant wrap of the tested iron ore samples on the head pulley. Additionally, limitations of the maximum belt velocity which could be obtained for the inclined plate recirculating system (outlined in Section 6.2.1) resulted in significant differences between the predicted and measured trajectories. This would not be the case when industrial systems are considered where higher belt velocities would be used. In this case, the trajectory methods outlined in the method of Roberts [78, 95 – 97] and Korzen [88] should be utilised. The following section outlines the existing transfer chute impact models where the method of Korzen [88], which considers the impact of cohesive bulk materials onto flat impact plates, is described in detail.

4.2.2 TRANSFER CHUTE IMPACT AND FLOW METHODOLOGIES

The impact of bulk materials within transfer chutes typically occurs at either the upper *"hood"* portion or lower *"spoon"* portion of the system. When the upper impact section of a transfer chute is considered, the main design criteria is to redirect the bulk material to the lower portions of the transfer chute and outgoing conveyor. The initial angle of incidence should be designed to be less than 15°, which minimises numerous factors such as, loss of velocity, material attrition, dust generation and wear [98]. In the case where a transfer chute is deemed to be *"well-designed"*, it is important to note that manufacturing quality is key. If the design is not followed or poor manufacturing techniques are used, blockages in the system can result [99]. When bulk material impacts in transfer chutes are considered, methods exist to describe the interaction of the flow stream and the impact. Some of the notable technical works include; Colijn and Conners

[77], Lonie [83], Roberts [78, 95 – 97] and Page [100] among others. One limitation of these impact models which used to describe the interaction between the flow stream and impact zone is they fail to incorporate the adhesion and plastic deformation of WSMs.

To describe the mechanics of impact plate transfer chutes which consider cohesive bulk materials a method is proposed by Korzen [88]. This method incorporates the adhesion and plastic deformation effects for bulk materials which impinge on vertical or inclined impact plates. When the iron ore industry is considered, impact plates are commonly utilised to direct the bulk material in place of curved transfer chutes. This is attributed to impact plates being a sacrificial component with the associated manufacturing costs being significantly lower to the curved transfer chute equivalent. Additionally, wear resistant materials are commonly utilised which reduce the required maintenance of the system. The location of the impact plate and angle of impact of the incoming bulk material stream are critical for the optimum performance of the system [101].

The method of Korzen [88], considers the variation of the resultant velocity prior to and after impact to determine the stream thickness and forces exerted by the bulk material onto the impact surface. The Korzen [88] model considers the conveyor inclination angle, α_b, the inclination angle of the impact plate, β_p, and the conditions of discharge. The conditions of discharge include the discharge velocity, V_d, the discharge angle, $\mathrm{\alpha_d}$, and the thickness of the bulk material stream, h_b. A schematic of the Korzen [88] model is shown in Figure 4.3. As the incoming bulk material stream impacts onto a flat plate, the formation of a pseudo chute surface, typically referred to as a *"rhino-horn"*, above the mainstream is possible. The formation of a *"rhino-horn"* will depend on the impingement angle and the friction acting between the bulk material and impact plate surface [101].

The build-up zone, shown as NZ in Figure 4.3, introduces the plastic deformation of the bulk material which acts between the build-up zone and the flowing bulk material stream. The use of continuum methods which utilise a fluids mechanics approach fail to incorporate these plastic characteristics where the method of Korzen [88] evaluates the flow of the bulk material using a two-dimensional analysis.

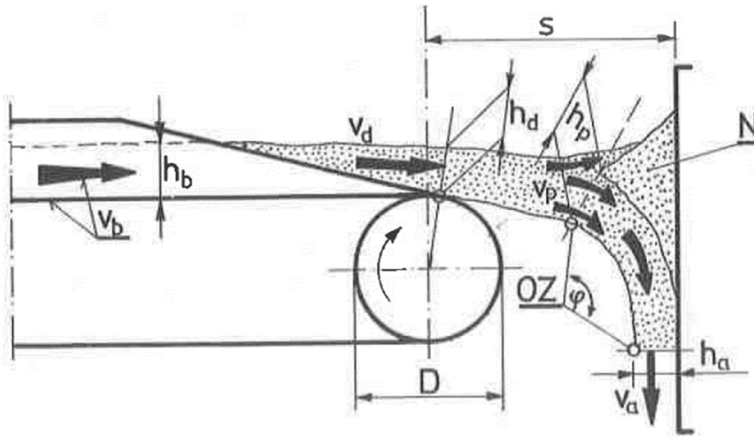

Figure 4.3 – Plastic deformation of a bulk material onto a flat impact plate (Korzen, 1988).

The differential equation used in the model developed by Korzen [88] is given by:

$$\frac{dv^2}{d\varphi_f} + 4\mu v^2 = 2gR_{OZ}\left[\sin\varphi_f + \mu\cos\varphi_f - \frac{c_b b_w}{\gamma_b A(\varphi_f)}\right] \tag{4.7}$$

This yields the following when solving for the velocity:

$$v^2(\varphi_f) = Ce^{-4\mu\alpha_p} + \frac{2gR_{OZ}}{1+16\mu^2}\left[5\mu\sin\varphi_f + (4\mu^2-1)\cos\varphi_f\right] - \frac{c_b b_w g R_{OZ}}{2\mu\gamma_b A(\varphi_f)} \tag{4.8}$$

where:

$$\varphi_f = \begin{cases} \dfrac{\pi}{2} - \beta_p & \text{for an inclined impact plate.} \\ \dfrac{\pi}{2} & \text{for a vertical impact plate.} \\ \dfrac{\pi}{2} + \beta_p & \text{for a declined impact plate.} \end{cases} \tag{4.9}$$

The integration constant, C, can be determined when the following initial conditions (just prior to impact) are substituted into Equation 4.8:

$$\varphi_f = \theta_a \tag{4.10}$$

$$v(\varphi_f) = v_p \tag{4.11}$$

$$A(\varphi_f) = A_p = \frac{\dot{m}}{\rho_{bulk} v_p} \tag{4.12}$$

$$R_{OZ} = h_p = \frac{\dot{m}}{\rho_{bulk} v_p b_w} \tag{4.13}$$

After the determination of the integration constant, a multi-step approximation procedure is followed to determine the value of v_a, which is the velocity of the bulk material stream after impingement with the impact plate. The first approximation step is given by:

$$R_{OZ} = R_{OZ1} = h_p \tag{4.14}$$

$$A(\varphi_f) = A_{a1} = A_p = \frac{\dot{m}}{\rho_{bulk} v_p} \Rightarrow v_a = v_{a1} \tag{4.15}$$

$$h_{a1} = \frac{\dot{m}}{\rho_{bulk} v_{a1} b_w} \tag{4.16}$$

The second approximation step is given by:

$$R_{OZ} = R_{OZ2} = \frac{h_p + h_{a1}}{2} \tag{4.17}$$

$$A(\varphi_f) = A_{a2} = \frac{\dot{m}}{\rho_{bulk} v_a} \Rightarrow v_a = v_{a2} \tag{4.18}$$

$$h_{a2} = \frac{\dot{m}}{\rho_{bulk} v_{a1} b_W} \tag{4.19}$$

The multi-step approximation procedure is followed until convergence results using:

$$\left| \frac{v_{a(k)} - v_{a(k-1)}}{v_{a(k)}} \right| \times 100 \leq \varepsilon_c \tag{4.20}$$

where: ε_c is the admissible relative deviation value [%].

There are limitations of the Korzen [88] model where the ability to accurately determine the velocity and thickness of the stream after impact results in discrepancies between the predicted values and observations produced from experimental measurements. This can be attributed to the lateral spreading of the bulk material where secondary streams are generated after impingement occurs [101]. Additionally, limitations exist where the Korzen [88] model states that the bulk material stream exits tangentially from the impact plate (chute) surface. In practice, some degree of rebound of the bulk material from the chute surface can be observed which results in part of the stream impact in the lower section of a transfer chute to occur at a different location to what is calculated [80].

When WSMs are considered, the plastic deformation of the bulk material must be considered where the Korzen [88] model incorporates these effects to some degree. The propensity for build-up to occur can be analysed using the Korzen [88] model where the thickness of the bulk material stream is considered. Such a method fails to determine the geometrical constraints of the build-up section itself where emphasis is typically on the flowing section of the bulk material stream. Korzen [88] observed that changes to the impact plate inclination angle and distance from the discharge drum were critical in the optimisation of impact plate placement. Although the Korzen [88] model can be used for the optimisation of impact plate placement, when WSMs negotiate such systems blockages still occur. To consider the geometrical constraints of a build-up, the following section outlines the developed theoretical model where the predicted build-up height is verified with measured values.

4.3 DYNAMIC ADHESION ANALYSIS OF BULK MATERIALS

To incorporate the build-up of problematic bulk materials onto inclined impact plates into the existing continuum mechanics-based methodologies, a theoretical model is proposed. The following section outlines the developed model where the predicted build-up height is verified with experimentally measured values determined using the inclined plate recirculating system (outlined in Section 6.2). Additionally, the projected ore surface angle and build-up mass are also predicted using IOB at 18.5% MC.

4.3.1 MECHANICS OF PROBLEMATIC BULK MATERIAL TRANSFER SYSTEM BUILD-UP

For the prediction of the adhesive and cohesive behaviours that WSMs exhibit, it is necessary to identify the forces acting on the bulk material as it negotiates a transfer system. Figure 4.4 shows a schematic of a typical low-speed transfer system that is using an impact plate arrangement rather than a conventional hood and spoon. It is appropriate to identify that the analysis of spoon type transfers is also possible with the slight modification of the geometrical inputs into the developed impact model.

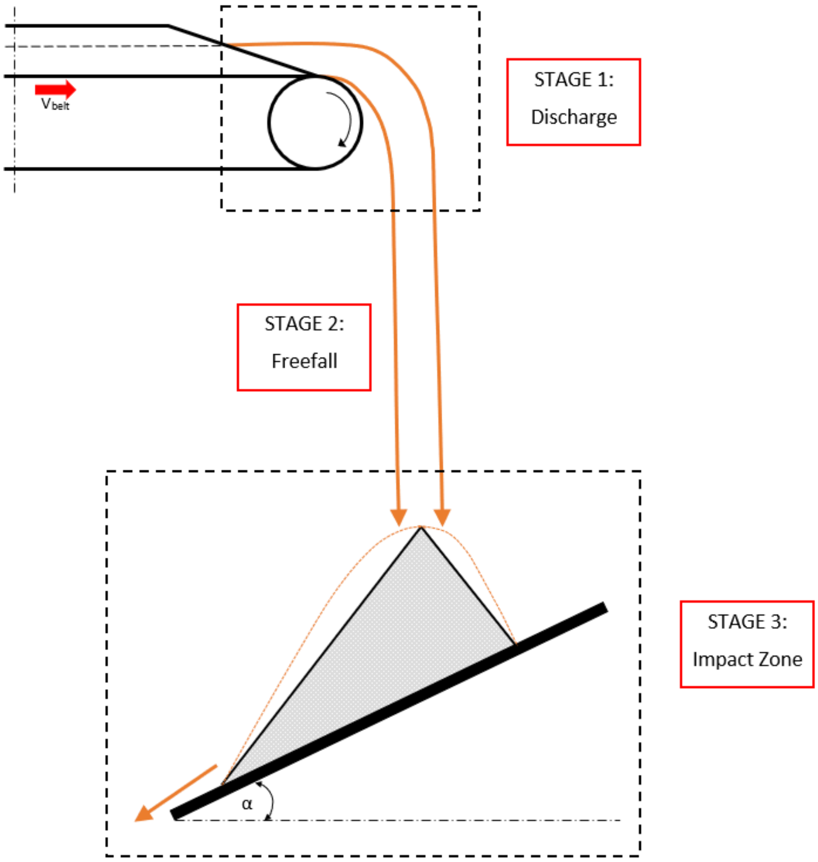

Figure 4.4 – Transfer system schematic indicating stages of flow regime.

When Figure 4.4 is considered, the transfer system has been broken down into three distinct stages; namely discharge, freefall and the impact zone. It is appropriate to identify that the freefall stage considers the stream thickness as an input into the modelling undertaken in the impact zone. This is measured from the experimental measurements (outlined in Section 6.2.2) but can also be estimated in the case where measurement data is not available. The following section outlines and derives the discharge mechanisms for WSMs (Stage 1) and the impact build-up model (Stage 3), as shown in Figure 4.4.

4.3.1.1 DISCHARGE MECHANISMS

An approach similar to that of Roberts [78, 95 – 97] and Korzen [88, 89] can be used to determine the discharge of a WSM from a head pulley of a conveyor belt. The model proposed by Roberts [78, 95 – 97] uses an arbitrary value for the adhesion found between the conveyor belt wrapping around the head pulley and the bulk material itself (as outlined in Section 4.2.1). To expand further on this assumption, it has been proposed to separate the adhesion into two different components. This is undertaken for the adhesion between the belt and the bulk material (wall adhesion), which is the same method used by Roberts [78, 95 – 97] and the inter-particle adhesion of the bulk material. Figure 4.6 to Figure 4.8 illustrate schematics of the forces acting between the conveyor belt and the bulk material with the addition of the inter-particle adhesion for different discharge cases. In the work of Korzen [89] the surface friction and adhesion of bulk materials on conveyor belts is considered, where two cases for both static and kinematic resistance as shown in Figure 4.5 result.

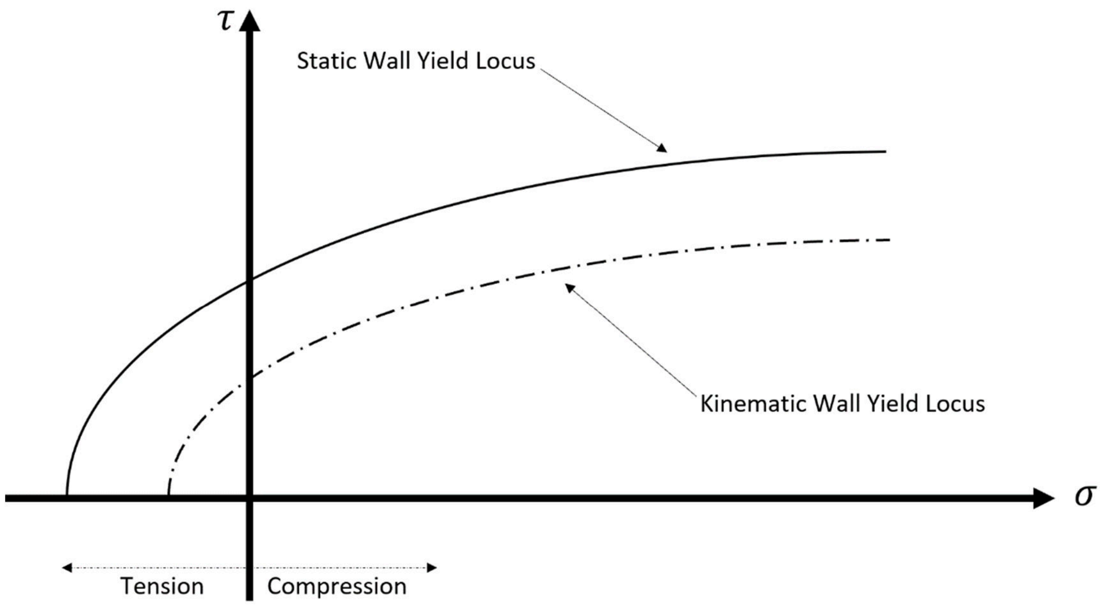

Figure 4.5 – Wall yield locus showing both static and kinematic cases.

The wall yield locus for the static shear stress, τ_s, and the kinematic shear stress, τ_k, are determined using:

$$\tau_s = (\sigma_n + \sigma_{WA})\mu_{st} \tag{4.21}$$

$$\tau_k = \sigma_n \, \mu_k \tag{4.22}$$

where:

σ_n	is the normal stress [Pa].
σ_{WA}	is the wall adhesive stress [Pa].
μ_{st}	is the static surface friction [-].
μ_k	is the kinematic surface friction [-].

If *"slip"* between the belt and bulk material is not present, static friction should be considered. If the adhesion between the belt and the bulk material is large enough failure may occur between the particles themselves. This case occurs when $\sigma_{WA} > \sigma_{IPA}$, where σ_{IPA} is the inter-particle adhesive stress (as discussed in Section 2.4.9.2). If slip is considered, the kinematic friction must be used and this occurs when $\sigma_{IPA} \geq \sigma_{WA}$. With the assumptions stated above, there are three cases that need consideration when looking at the element mass on the head pulley and are found in Figure 4.6 to Figure 4.8. It should be noted that when $\sigma_{WA} > \sigma_{IPA}$, belt carry back may occur, but this will only be the case when the wall adhesive stress is greater than the self-weight of the carry back as this will be time dependent.

For Case A, a schematic of the forces present are found in Figure 4.6 below. This case will be predominantly found during the start-up procedure where static friction needs to be overcome for the continuation of flow to occur from the head pulley. Slip is not considered in this case between the conveyor belt and the bulk material. In this case the internal strength of the material will be equal to or greater than the wall adhesion produced between the conveyor belt and the bulk material (i.e. $\sigma_{IPA} \geq \sigma_{WA}$).

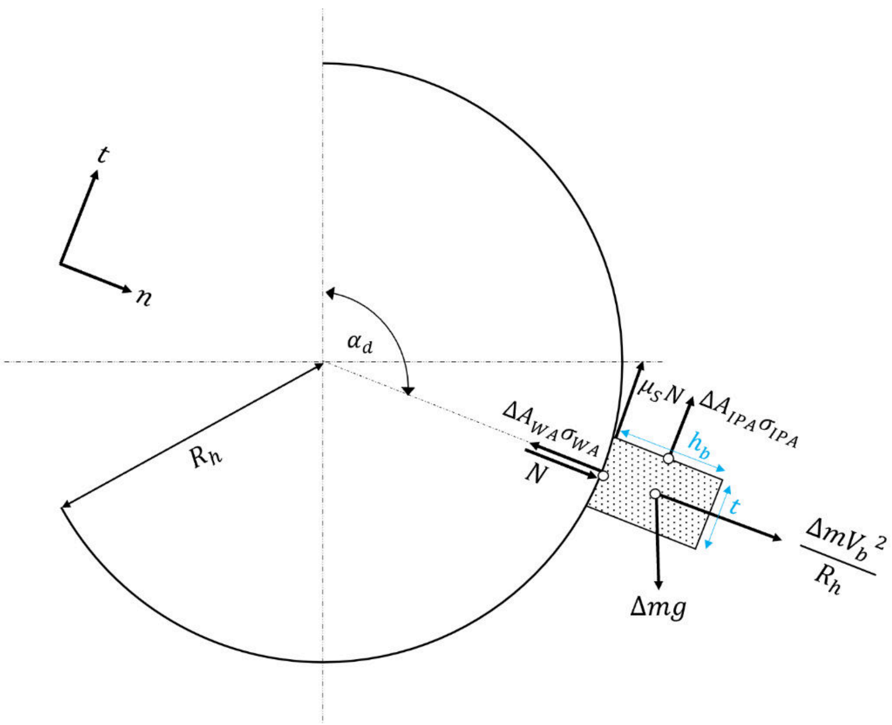

Figure 4.6 – Schematic of the forces acting between the conveyor belt and the bulk material (Case A).

Looking at each component from the schematic in Figure 4.6, the conditions of bulk material stream separation from the belt conveyor discharge drum occurs using the following:

The element mass (Δm) is determined using:

$$\Delta m = \rho_{bulk} h_b \Delta A_{WA} \tag{4.23}$$

where: ρ_{bulk} is the bulk density of the bulk material [kg/m^3].
h_b is the height of the bulk solid stream [m].
$\Delta A_{WA}$is the area connecting the element being analysed and belt [m^2].

Expanding further from Equation 4.23 we have:

$$h_b = \frac{\dot{m}}{\rho_{bulk} V_b b_w} \tag{4.24}$$

where: $\dot{m}$ is the mass flow rate of the bulk material [kg/s].
V_b is the conveyor belt velocity [m/s].
b_w is the width of the bulk material stream [m].

$$\Delta A_{WA} = b_w t \tag{4.25}$$

where: t is the thickness of the element being analysed [m].

Finally, if we rearrange and substitute Equations 4.24 and 4.25 into Equation 4.23 we have:

$$\Delta m = \frac{\dot{m}}{V_b} t \tag{4.26}$$

The process of separation of the element mass, Δm, from the conveyor belt surface takes place due to the centrifugal force, ΔF_c, which is given as:

$$\Delta F_c = \frac{\Delta m {V_b}^2}{R_t} \tag{4.27}$$

where:

$$R_t = R_h + \frac{h_b}{2} \tag{4.28}$$

R_t is the centroid radius of the element being analysed [m].

R_h is the radius of the head pulley and belt thickness [m].

The gravitational force, ΔG, acting on the centroid of the element being analysed is given as:

$$\Delta G = \Delta mg \tag{4.29}$$

where: g is the acceleration due to gravity [m/s^2].

The frictional force, F_D, acting between the bulk material and conveyor belt interface during the point of discharge is given as:

$$F_D = \mu N \tag{4.30}$$

where: μ is determined for the case being analysed [-].

N is the normal load acting on the element [N].

Finally, the adhesive force, F_A, acting on the element being analysed is given as:

$$F_A = \Delta A_{WA/IPA} \sigma_{WA/IPA} \tag{4.31}$$

where: ΔA_{WA} is the area between the element being analysed and the belt [m^2].

ΔA_{IPA} is the area between the inter-particle bonds of the element [m^2].

σ_{WA} is the stress between element and belt surface [Pa].

σ_{IPA} is the stress between inter-particle bonds of the element [Pa].

For a <n, t> coordinate system the following system of equations can be determined for Case A:

$$\sum\nolimits_n = -\Delta A_{WA}\sigma_{WA} + N + \frac{\Delta m V_b{}^2}{R_t} + \Delta mg \sin\alpha_d = 0 \tag{4.32}$$

$$\sum\nolimits_t = \Delta A_{IPA}\sigma_{IPA} + \mu_s N - \Delta mg \cos\alpha_d = 0 \tag{4.33}$$

Solving Equation 4.32 and Equation 4.33 simultaneously and rearranging for the element mass, Δm, gives:

$$\Delta m = \frac{b_w h_b \sigma_{IPA} + \mu_s b_w t \sigma_{WA}}{\frac{\mu_s {V_b}^2}{R_h + \frac{h_b}{2}} + \mu_s g \sin \alpha_d + \frac{V_b v}{t} + g \cos \alpha_d} \tag{4.34}$$

Similar to Case A, a schematic of the forces present for Case B is found in Figure 4.7 below. This case will be predominantly found during the running procedure of the conveyor system where kinematic friction is evident at the head pulley for the conveyor belt to bulk material interface. Slip is considered in this case between the conveyor belt and the bulk material. In this case the internal strength of the material is equal to or greater than the wall adhesion produced between the conveyor belt and the bulk material (i.e. $\sigma_{IPA} \geq \sigma_{WA}$).

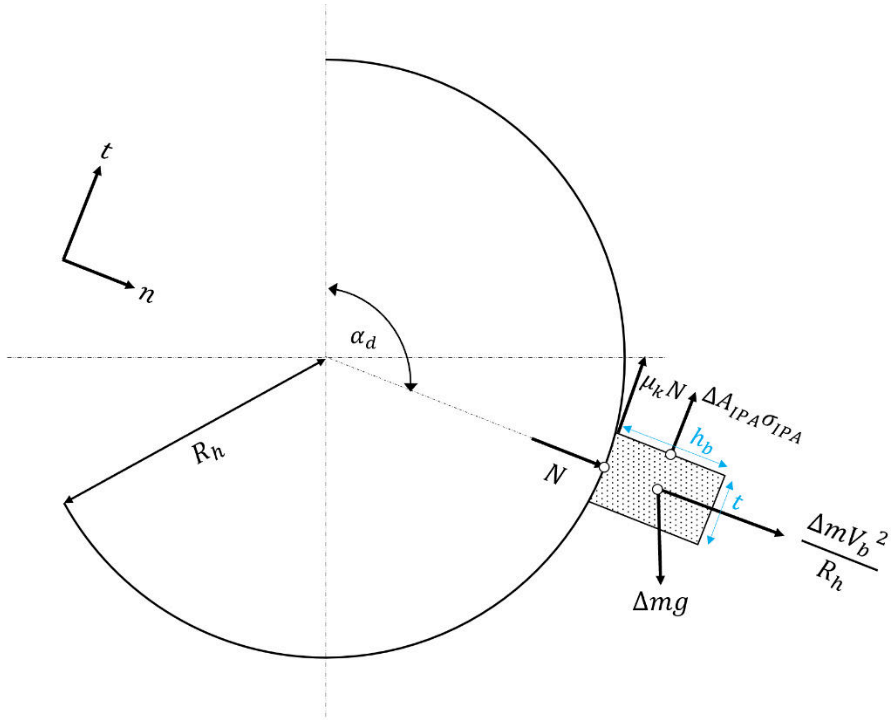

Figure 4.7 – Schematic of the forces acting between the conveyor belt and the bulk material (Case B).

For a <n, t> coordinate system the following system of equations can be determined for Case B:

$$\sum\nolimits_n = N + \frac{\Delta m {V_b}^2}{R_t} + \Delta m g \sin \alpha_d = 0 \tag{4.35}$$

$$\sum_t = \Delta A_{IPA}\sigma_{IPA} + \mu_k N - \Delta mg\cos\alpha_d = 0 \tag{4.36}$$

Solving Equation 4.35 and Equation 4.36 simultaneously and rearranging for the element mass, Δm, gives:

$$\Delta m = \frac{b_w h_b \sigma_{IPA}}{\dfrac{\mu_k {V_b}^2}{R_h + \dfrac{h_b}{2}} + \mu_k g\sin\alpha_d + \dfrac{V_b v}{t} + g\cos\alpha_d} \tag{4.37}$$

Finally for Case C, a schematic of the forces present is found in Figure 4.8 below. This case will be predominantly found during the running procedure of the conveyor system where excessive wall adhesion is evident at the head pulley for the conveyor belt to bulk material interface. Slip is not considered in this case between the conveyor belt and the bulk material. In this case the wall adhesion produced between the conveyor belt and the bulk material is greater than the internal strength of the material (i.e. $\sigma_{WA} > \sigma_{IPA}$). It should be noted that when $\sigma_{WA} > \sigma_{IPA}$ belt carry back may occur, but this will only be the case when the wall adhesive stress is greater than the self-weight of the carry back as this will be time dependent.

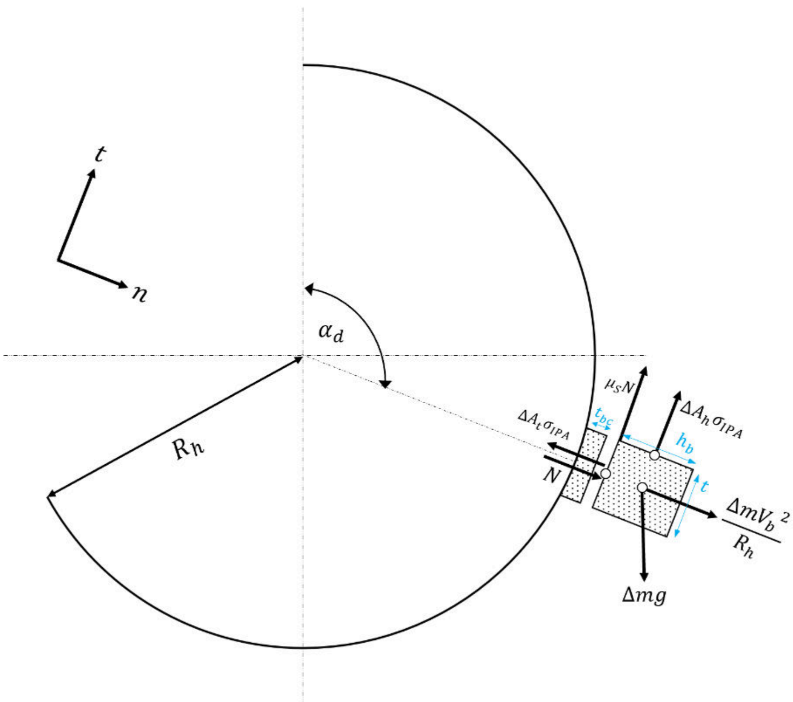

Figure 4.8 – Schematic of the forces acting between the conveyor belt and the bulk material (Case C).

For a <n, t> coordinate system the following system of equations can be determined for Case C:

$$\sum\nolimits_n = -\Delta A_t \sigma_{IPA} + N + \frac{\Delta m {V_b}^2}{R_t} + \Delta mg \sin \alpha_d = 0 \tag{4.38}$$

$$\sum\nolimits_t = \Delta A_h \sigma_{IPA} + \mu_s N - \Delta mg \cos \alpha_d = 0 \tag{4.39}$$

Solving Equation 4.38 and Equation 4.39 simultaneously and rearranging for the element mass, Δm, gives:

$$\Delta m = \frac{b_w(h_b - t_{bc})\sigma_{IPA} + \mu_s b_w t \sigma_{IPA}}{\dfrac{\mu_s {V_b}^2}{R_h + t_{bc} + \dfrac{h_b}{2}} + \mu_s g \sin \alpha_d + \dfrac{V_b v}{t} + g \cos \alpha_d} \tag{4.40}$$

The discharge methods presented above govern the flow of the bulk material as it enters freefall (Stage 2). Once the bulk material enters freefall (Stage 2) the stream thickness is typically assumed to increase with a rise in vertical drop height. This is attributed to the differential velocity when the top and bottom components of the stream are considered. It is appropriate to identify that the freefall stage considers the stream thickness as an input into the modelling undertaken in the following section for the impact zone. This is measured from the experimental measurements (outlined in Section 6.2.2) but can also be calculated as described above, in the case where measurement data is not available.

4.3.1.2 IMPACT BUILD-UP MODELLING

The build-up of a WSM on inclined impact plates, when observed from the side, has been noted to form a triangular shape. The rear consolidated profile is generally steeper than the front and can be assumed to form normal to the impact plate itself. The general shape of the build-up observed during the experimental measurements is shown in Figure 4.9. The removal of the loose iron ore which is supported by the build-up is shown in Figure 4.9b for clarity into the final build-up shape. It is appropriate to note that slight changes in the angle relative to the normal force act as the bulk material builds. Additionally, the shape of the build-up when viewed perpendicularly to the face of the wall liner results in a parabolic profile as shown in Figure 4.9b. This is attributed to the profile of the bulk material as it discharges from the head pulley (outlined in Figure 6.9).

a) Supporting loose iron ore *b) Loose iron ore removed*

Figure 4.9 – Shape measurement volume for iron ore build-up.

Using the assumption of a triangular build-up shape when viewed from the side, the geometrical boundaries can be determined. Figure 4.10 shows the assumed build-up cross-sectional shape and the characterising parameters.

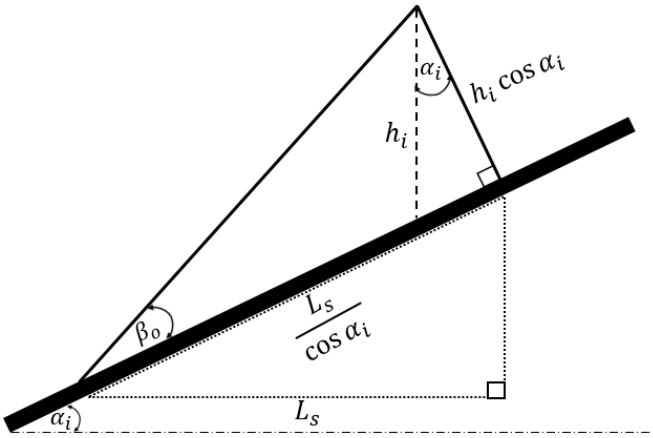

Figure 4.10 – Assumed build-up shape and characterising parameters.

The total inclination angle (θ) is the sum of the plate inclination and material build-up inclination angles and is given by:

$$\theta = \alpha_i + \tan^{-1}\left(\frac{h_i \cos^2 \alpha_i}{L_s}\right) \tag{4.41}$$

where: h_i is the build-up height as defined in Figure 4.10 [m].

L_s is the stream thickness [m].

The stream thickness was determined to be approximately 0.25 m from the experimental measurements (outlined in Section 6.2). As previously mentioned, however, the stream thickness can also be calculated using the various trajectory predictions, which are outlined in Section 4.2.1. Figure 4.11 shows the force balance on an arbitrary element at a total inclination angle of θ.

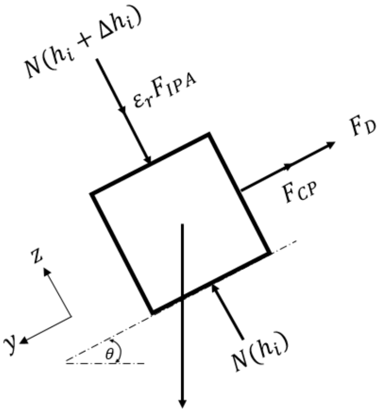

Figure 4.11 – Force balance on an element at a total inclination angle of θ.

By summing forces under equilibrium conditions in the z-direction the following relationship for the change in normal force as a function of the build-up height can be shown:

$$N(h_i) - N(h_i + \Delta h_i) = \varepsilon_r \left(\dot{m}\sqrt{2g(h_0 - h_i)}\cos\theta + F_{IPA}\right) \tag{4.42}$$

where: N is the normal force [N].
ε_r is the coefficient of restitution [-].
$\dot{m}$ is the mass flow rate of the material [kg/s].
g is the acceleration due to gravity [m/s^2].
h_0 is the stream drop height [m].
θ is the total inclination angle [°].
F_{IPA} is the inter-particle adhesion force [N/kg].

Solving Equation 4.42 and assuming that the angle between $N(h_i)$ and $N(h_i + \Delta h_i)$ is negligible allows $N(h)$ to be obtained as a sum of the solved terms of Equation 4.42. Summing forces in the y-direction, it can be shown that the flow velocity as a function of build-up height is given by:

$$v_{out}(h_i) = \frac{\varepsilon_r \dot{m}\sqrt{2g(h_0 - h_i)}\sin\theta}{\dot{m}_{out}} - \frac{F_{CP}}{\dot{m}_{out}} - \frac{\mu_p\, N(h_i)}{\dot{m}_{out}} \tag{4.43}$$

where: v_{out} is the stream velocity off the build-up [m/s].

$\dot{m}_{out}$ is the solids mass flow rate coming off the build-up [kg/s].

F_{CP} is the particle cohesion force [N/kg].

μ_p is the particle-to-particle friction [-].

Substituting Equation 4.41 and 4.42 into Equation 4.43 allows the flow velocity of the build-up area to be predicted as a function of build-up height only. The point at which the velocity equals zero is the critical height above which all the bulk material will flow without further build-up occurring. The condition that therefore needs to be solved for in Equation 4.43 is:

$$v_{out}\big(h_{crit}(\alpha_i)\big) = 0 \tag{4.44}$$

To identify the thresholds where problematic behaviours no longer occur, the developed model must consider the flow velocity of the build-up to be zero. This is the point where all the bulk material will flow without further build-up occurring. A comparison between the predicted threshold value and experimental measurement where build-up no longer occurs is analysed in the following section. This is undertaken for IOB at 18.5% MC.

4.4 VERIFICATION OF DYNAMIC ADHESION ANALYSIS

Once the theoretical models above have been developed, it is essential to verify their accuracy. To verify the theoretical models, the build-up of a bulk material is considered. This is undertaken using the inclined plate recirculating system (outlined in Section 6.2). The experimental measurements and theoretical prediction results are outlined in the following section. The iron ore sample which has been considered for this analysis is IOB at 18.5% MC where a size fraction of -11.2 mm was used.

4.4.1 IMPACT BUILD-UP MODELLING VERIFICATION

The model developed in Section 4.3.1.2 allows for the prediction of the build-up height (as defined in Figure 4.10) as a function of bulk material and system properties. Testing utilising the inclined plate recirculating system (outlined in Section 6.2) was used as validation of the model.

For the inclined plate recirculating system, the stream thickness reduces with build-up and is assumed to be linear as follows:

$$L_s = L_0 \left(1 - \frac{h}{h_0}\right) \tag{4.45}$$

where: h is the adjusted bulk material stream drop height (i.e. $h_0 - h_i$) [m].
L_0 is the initial stream thickness [m].
h_0 the initial stream drop height [m].

Similarly, the mass flow rate flowing off the build-up for the inclined plate recirculating system is assumed to decrease linearly with build-up height and has the following form:

$$\dot{m}_{out} = \dot{m} \left(1 - \frac{h}{h_0}\right) \tag{4.46}$$

Figure 4.12 shows the measured and predicted build-up heights as a function of the plate inclination angle for the three wall lining materials (outlined in Section 2.5.1) which were considered for use in the inclined plate recirculating system. Since the model predicts that build-up is a function of the bulk material properties only, a single prediction curve is obtained. This provides good agreement to the experimental measurements for all three wall lining materials.

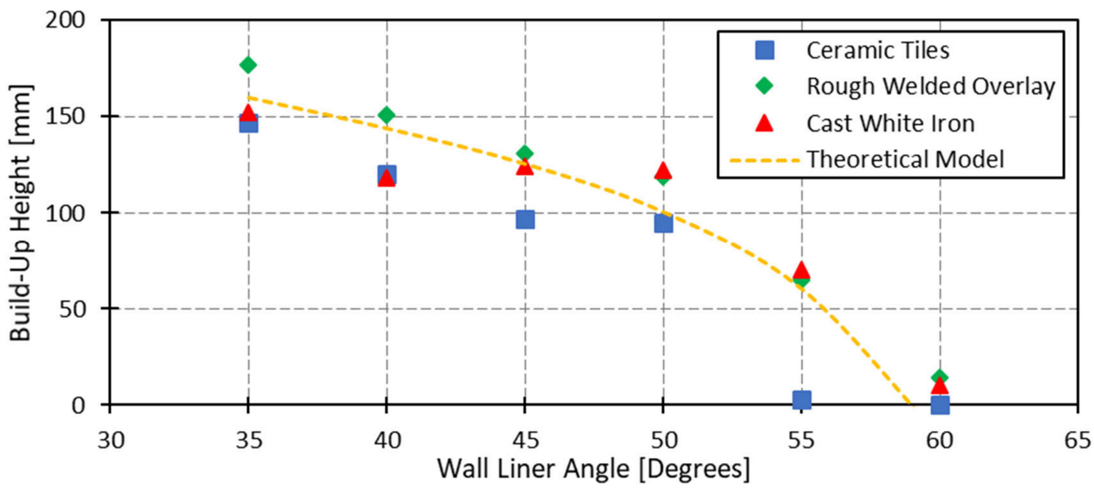

Figure 4.12 – Measured and predicted build-up height as a function of plate inclination angle.

To relate the predicted build-up height to the build-up mass, the experimental build-up heights and masses were examined for a relationship. Figure 4.13 shows the measured build-up mass as a function of build-up height for all three wall lining materials. A parabolic curve fit through the origin is also shown and was found to provide good agreement for the entire data-set, further supporting that the build-up process is bulk material dependent and not significantly influenced by the material of the wall liner (boundary). Furthermore, the results of Figure 4.13 suggest that the relationship between the build-up height and mass is independent of the impact plate inclination angle.

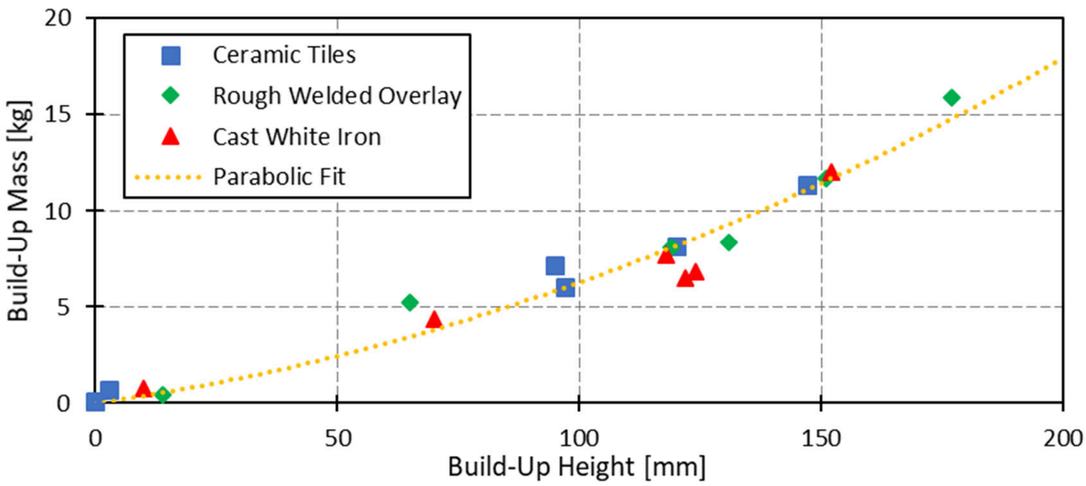

Figure 4.13 – Measured build-up mass versus measured build-up height and parabolic fit.

The independence of the build-up height and mass to the impact plate material and inclination angle is further demonstrated when examining the total inclination (θ) of the build-up. Figure 4.14 shows the total inclination angle against the impact plate inclination angle. The trend for the measurement and prediction is almost constant at a value that on average is between 55 and 60 degrees, regardless of inclination angle or wall lining material. These values are slightly greater than the effective internal friction angle of the bulk material, suggesting that the build-up occurs until the material can shear on itself, with an angle slightly greater required to overcome the impacts of cohesion/adhesion as well.

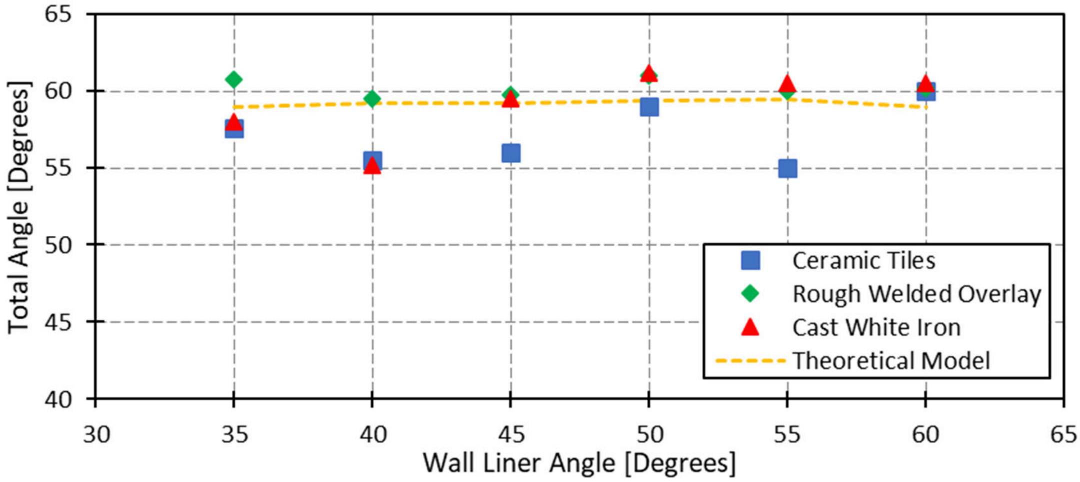

Figure 4.14 – Total build-up inclination angle versus impact plate inclination angle.

Utilising the parabolic relationship from Figure 4.13 the build-up mass can be predicted, with the results shown in Figure 4.15. The prediction provides good agreement to the measured data. It is appropriate to identify that the ceramic wall liner showed some tendency to be less problematic in comparison to the white cast iron and rough welded overlay wall liners. The further development of a model to capture the influences of the boundary conditions in relation to bulk material build-up is discussed in Section 8.3.3.

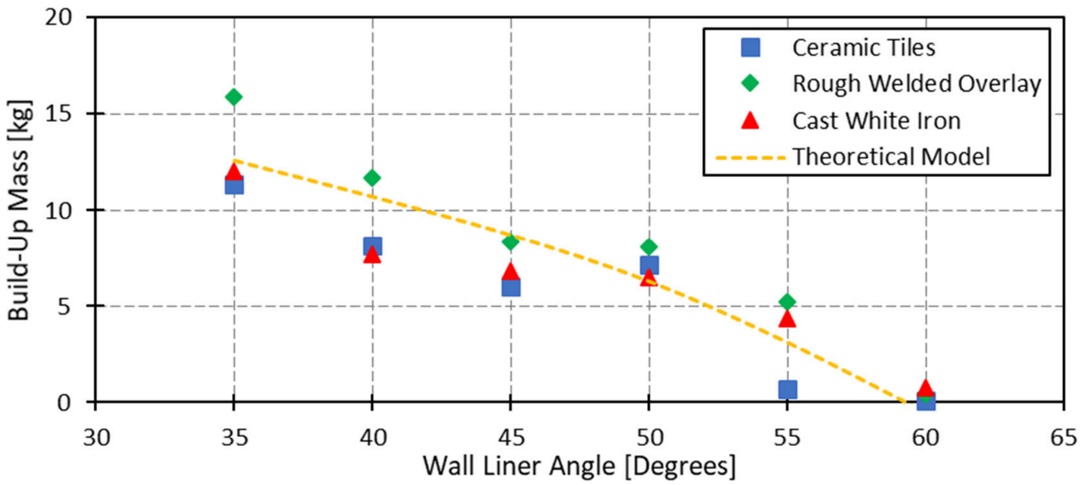

Figure 4.15 – Measured and predicted build-up mass as a function of plate inclination angle.

4.5 RESULTS AND DISCUSSION

The developed impact model (outlined in Section 4.3.1.2) determines the height of the bulk material build-up where sound correlation between experimental measurements and predicted values, as shown in Figure 4.12, can be observed. This analysis has been undertaken using IOB at 18.5% MC where a summary of the testing parameters required as inputs into the developed model are shown in Table 4.1. It is important to note that the coefficient of restitution and particle-to-particle friction values have been estimated due to the complexity of obtaining accurate measurement results.

Table 4.1 – Inclined Plate Impact Model Parameters for IOB at 18.5% MC

Input Parameter	*Units*	*Value*
Inclination Angle (θ)	[Degrees]	35, 40, 45, 50, 55, 60
Coefficient of Restitution (ε_r)	[-]	0.4
Stream Thickness (L_s)	[m]	0.25
Mass Flow Rate ($\dot{m}$)	[kg/s]	6.34
Acceleration due to Gravity (g)	[m/s^2]	9.81
Stream Drop Height (h_0)	[m]	1.5
Inter-Particle Adhesion Force (F_{IPA})	[N/kg]	3.5
Particle Cohesion Force (F_{CP})	[N/kg]	4.5
Particle-to-Particle Friction (μ_p)	[-]	1.5

Currently the impact model predicts the mass of the build-up using a curve fit for the obtained experimental data, as shown in Figure 4.13. The expansion of the model to predict the bulk material build-up mass analytically without the need for experimental inputs would be rather difficult. This is attributed to the volumetric shape of the build-up being difficult to estimate when WSMs, such as IOB at 18.5% MC, are considered. The build-up forms a crude pyramid shape which has no real resemblance of the trajectory shape which is observed for the lower moisture content samples. This trajectory shape is parabolic in nature and can be observed when the build-up in Figure 4.9b is considered.

If the build-up height and build-up mass are considered, a relationship to the impact plate material and inclination angle is further demonstrated when examining the total inclination (θ) of the build-up. Figure 4.14 shows the total inclination angle against the impact plate inclination angle. The trend for the measurement and prediction results with a constant value that on average is between 55 and 60 degrees. This occurs regardless of inclination angle or wall lining material. These values are slightly greater than the internal friction angle of the bulk material, suggesting that the build-up occurs until the material reaches a threshold and begins to shear on itself.

The developed model determined the build-up process is bulk material dependent and not significantly influenced by the material of the wall liner (boundary). The critical release angle where an effective build-up height equates to zero was then predicted for an inclined impact plate transfer system. The estimated critical release angle was determined to be approximately

60 degrees for IOB at 18.5% MC (as determined from Figure 4.15). This was found to be similar to the experimental measurement values for all three wall liners, as outlined in Table 6.15. It is appropriate to identify that the influence of the wall lining material should be incorporated into the model where the critical release angles for different wall lining materials can be determined. The presented methodology only considers impact plate transfers. It is therefore essential that other types of transfer systems be considered to check the validity of the developed model. This is discussed further in Section 8.3.3.

4.6 CONCLUSION

This chapter has given a brief overview of the existing continuum mechanics-based methodologies and explained the current limitations in relation to modelling WSM behaviours from a modelling perspective. When impact plate transfers were considered, the existing methodologies failed to incorporate the build-up of the bulk material into the continuum analysis. A theoretical model which considers the build-up onto inclined impact plates is proposed and verified with experimentally measured values determined using the inclined plate recirculating system (outlined in Section 6.2). The developed model determined the build-up process is bulk material dependent and not significantly influenced by the material of the wall liner (boundary). Additionally, the developed model predicted the critical release angle which was determined to be approximately 60 degrees for IOB at 18.5% MC (as determined from Figure 4.15).

This page is left intentionally blank

CHAPTER FIVE – METHODOLOGY FOR THE REDUCTION OF ADHESIVE BONDS

The following chapter explores the natural agglomeration of iron ore and the potential benefits to the iron ore mining industry. An investigation is undertaken on the effects of agglomeration on the materials handling sector where the benefits of reduced build-up and reduction of dust generation is also explored. A comparison of an agglomerated iron ore sample, investigated using IOB, is compared to the ROM equivalent for a range of materials handling properties.

5.1 INTRODUCTION

During the initial experimental phases of the research using the inclined plate recirculating system (outlined in Section 6.2), it was observed by the author that the natural agglomeration of the iron ore samples assisted in the flow through transfer systems. Additionally, it was observed that the formed agglomerates also reduced the amount of dust generated during transportation. It was therefore deemed necessary to explore the phenomenon of agglomeration and the potential effects agglomeration will have on the materials handling stream.

The following chapter outlines the fundamentals of agglomeration, typically referred to as granulation, where the applications to the mining sector are identified. From this, the effects for the reduction of problematic behaviours that WSMs show within the materials handling stream are also explored. Additionally, the industrial systems suitable for implementation to the materials handling sector are proposed. To quantify the reduction in problematic behaviours and dust generation, a comparison of an agglomerated iron ore sample, investigated using IOB, is compared to the as supplied ROM sample. Two agglomeration samples are considered which are outlined in Section 5.3.1. This is undertaken for an equivalent moisture content for all samples which are analysed in Section 5.3.

5.2 METHODS FOR THE REDUCTION OF ADHESION IN BULK MATERIALS

Materials handling problems which are associated with WSMs cause significant downtimes which can be attributed to the adhesive properties of the bulk material. By reducing the adhesive properties of a WSM before it negotiates the materials handling stream, methods can be set in place to increase the overall efficiency and reduce the potential downtime. Depending on the moisture content of the bulk material, different methods can be considered to reduce the adhesive properties.

For bulk materials which are over saturated, mechanical dewatering systems can be utilised to reduce the adhesive properties, by reducing the moisture content. Some of the notable mechanical dewatering systems include belt filters, vibratory screens and dewatering chutes. It is appropriate to identify that the use of mechanical dewatering systems are not applicable for use in the case of the iron ore samples considered in this research as they are not oversaturated when negotiating the materials handling stream.

When bulk materials which are not oversaturated, yet still problematic within the materials handling stream are considered, alternative methods can be utilised. As outlined in Section 6.4.4, methods such as changing the geometry to improve flow, blending with a non-problematic ore or simply diverting of the system can reduce the propensity for problematic bulk material behaviours. One method which can be used to reduce the adhesive properties of a bulk material is by *"drying"*. Thermal drying systems can be beneficial to improve handleability, however, these systems can significantly increase the propensity for dust generation within the bulk materials themselves.

Another method to reduce the apparent adhesive properties of bulk materials is using vibration. Roberts et al. [102 - 106] showed the benefits of vibration in the materials handling stream where the internal strength of the bulk material reduced significantly. Additionally, when the interaction of the bulk material interacting with a wall lining surface were considered, reductions in the wall yield locus were shown with an increase in vibration amplitude. Although great benefits into the reduction in strength and adhesive properties of bulk materials was shown, employing vibration into the rigid structures which support transfer systems would be quite difficult in practice.

When the limitations outlined above are considered, the implementation into a mining operation make these methods unfeasible in most instances. The use of agglomeration within the materials handling stream can result in a novel method to reduce problematic material behaviours (outlined in Section 5.3.2) whilst maintaining the requirements of dust suppression (outlined in Section 5.3.1.3). The agglomeration of iron ore is a well-known and researched field which is used extensively in the steel making industry. When the materials handling sector is considered however, the benefits of agglomeration are not readily available in published literature. The following sections outline the fundamentals of agglomeration and some of the industrial systems used in the steel making industry are also outlined.

5.2.1 FUNDAMENTALS OF AGGLOMERATION

Agglomeration is a size enlargement process which is used extensively in the steel making and chemical processing industries. It is used to improve the utility of fine particles in further processing operations or to produce a final product of agglomerated material [107]. When the chemical processing industry is considered, the use of agglomeration results in several benefits, most notably the benefits include the improvement of flow properties, improved dispersion properties, ensured composition uniformity and reduced dustiness [108]. When the steel making industry is considered, the use of agglomeration results in the benefit of a larger range of iron ore products (fines) for use directly into the blast furnace. Additionally, greater sinter quality results when using agglomerated iron ore fines in conjunction with coking coal [109].

The agglomeration of particles is typically undertaken using either *"dry"* or *"wet"* mechanisms. The principle of *"dry"* agglomeration, which results in the compaction of particles, is undertaken using mechanical processes [110]. Mechanical agglomeration processes include tabletting, roll compaction, pelletisation and briquetting among others [110]. It is appropriate to identify that the use of *"dry"* agglomeration processes are not applicable for use in the case of the iron ore samples considered in this research as they agglomerate using *"wet"* agglomeration mechanisms.

The principle of *"wet"* agglomeration, also referred to as tumble-growth agglomeration, consists of a powder, for the chemical processing industry, liquid (usually water) and in some instances, a binder [111]. The use of binders assists the *"wet"* agglomeration process to form agglomerate particles which are mechanically stable [112]. In the case of the iron ore samples considered for agglomeration, the need for a binder material is not required. This is attributed to the kaolinitic clays which are present in IOB and IOC which act as the binding agent. It is appropriate to identify, in the case where high grade iron ores required the agglomeration process to be undertaken, binding materials would be required. This is attributed to greater haematite and lower goethite percentages in high grade iron ores, such as IOA. Agglomeration could be undertaken by blending lower grade ores which contain kaolinitic clays, such as IOB or IOC, to act as the binding material.

The typical particle size enlargement process by *"wet"* agglomeration is undertaken in three stages [111]. The first stage requires the bulk material (powder), liquid and binder to be combined and mixed. The next stage occurs when moist particles are joined together to form so-called *"green"* agglomerates [111]. The final stage is when curing takes place which will generally be in the form of drying. During the *"wet"* agglomeration process, a nuclei is initially formed which then grows into larger agglomerates by either layering or coalescence [111]. During the initial nucleation stages of agglomeration formation, the seed agglomerates are weakly bonded where they tend to disintegrate into their original particle form [111]. This initial stage can be extremely time consuming, however, once larger agglomerates begin to form the growth of the agglomerate particles is accelerated where layering or coalescence begins to take place.

When layering is considered, extra particles are bound to the surface of an existing agglomerate [113]. During the layering process, the mass and size of the primary agglomerate particles in the system increases until a threshold is reached where the agglomerate size remains constant. When coalescence is considered, two agglomerate particles (commonly referred to as granules) collide to form one larger agglomerate [113]. The collision is only successful if the net forces are sufficient to hold the newly formed agglomerate together. It is appropriate to identify that the optimal moisture content for *"wet"* agglomeration to take place is in the order of 40% - 90% of the SDMC [111].

When a liquid, typically water, is added to a dry bulk material, liquid bridges begin to form at contact points between particles [111]. Newitt and Conway-Jones [114] and Barlow [115] classified the amount of water between the particles using three characteristic states, namely: pendular, funicular and capillary as shown in Figure 5.1. For the pendular stage of saturation, the free moisture is attracted to the interfaces between the solid particles. This is generally attributed to the capillary effects, where surface tension draws the particles together [116]. During increasing levels of saturation, the funicular stage is reached where all internal solid surfaces become surrounded by liquid. Once this stage is reached, the mixture becomes saturated, where tensional forces begin to disappear, leading to weaker agglomerates [111]. When the bulk material, iron ore for the case of this research, becomes fully saturated, it reaches its capillary state. This leads the agglomerate material to behave more as a slurry which is attributed to higher moisture levels. For the case where oversaturation occurs, there is a so-called *"dropping"* state, as shown in Figure 5.1d. This occurs when there is an excess of binding liquid where such systems exist solely due to the surface tension of a liquid drop [114].

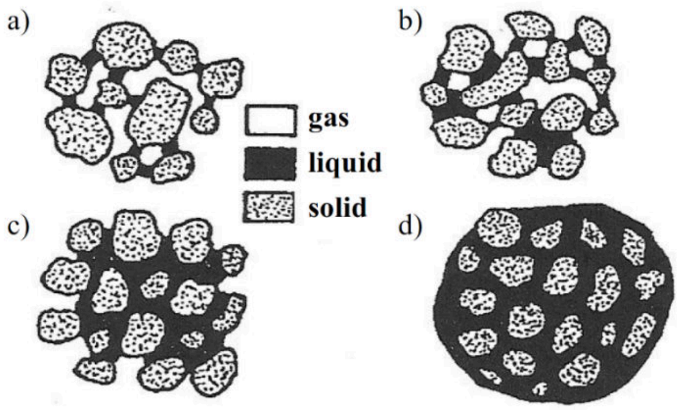

Figure 5.1 – Agglomerate particle structures in relation to the amount of binding liquid, a) pendular state; b) funicular state; c) capillary state; d) dropping state (Newitt and Conway-Jones, 1958).

When under-saturated bulk materials are considered, the conversion to a saturated state by compaction during *"dry"* agglomeration processes is possible. This occurs without the need for the addition of moisture. Similarly, pendular and funicular states of the same bulk material can be obtained at different SDMCs. The minimum moisture content is crucial when the strength of agglomerates is considered. Low moisture contents lead to agglomerates which are brittle. Additionally, higher moisture contents lead to highly plastic agglomerates which deform easily during transportation [117]. From this, the optimal amount of liquid which must be added during the agglomeration formation process to resist breakage often depends on the device and properties of the bulk material undergoing agglomeration [111]. Typical devices used for the formation of agglomerates are outlined in the following section.

5.2.2 INDUSTRIAL AGGLOMERATION METHODS AND APPLICATIONS

The mechanisms required for agglomeration to occur is undertaken using a range of methods. The method used depends on the required properties of the agglomerate particles and whether a continuous or batch system can be used. Such methods have been developed for industrial cases and can be broken down into systems which will undertake the agglomeration process for *"dry"* or *"wet"* mechanisms, as outlined above. The agglomeration of particles is used for a range of industrial processes where some of the notable processes range from fertilizer production through to fine chemical manufacture, pharmaceuticals and the steel making industry. The magnitude of production also governs the type of agglomeration system used where systems range from kilograms per day to tonnes per hour [113]. A summary of the methods used for agglomeration for a range of bulk materials are outlined in Table 5.1.

Table 5.1 – Typical Agglomeration Methods Showing Applicable Bulk Materials (Sochon and Salman, 2010)

Agglomeration Method	Applicable Bulk Materials
• Tumbling granulators • Drums • Discs	Fertilizers, iron ore, non-ferrous ore, agricultural chemicals
• Mixer and Planetary granulators • Continuous high shear • Batch high shear	Chemical, detergents, clays, carbon black pharmaceuticals, ceramics
• Fluidized granulators • Fluidized beds • Spouted beds	*Continuous*: fertilizers, inorganic salts, detergents *Batch*: pharmaceuticals, agricultural chemicals, nuclear wastes
• Centrifugal granulators	Pharmaceuticals, agricultural chemicals
• Spray Methods • Spray drying • Prilling	Instant foods, dyes, detergents, ceramics, urea, ammonium nitrate
• Compression agglomeration • Extrusion • Roll press • Tablet press • Pellet mill	Pharmaceuticals, catalysts, inorganic chemicals, organic chemicals, plastic preforms, metal parts, ceramics, clays, minerals, animal feeds

The typical method used for *"dry"* agglomeration is using compression agglomeration, as outlined in Table 5.1. Compression agglomeration is used for pellet formation commonly of definite sizes and shapes which are prepared by compacting mixtures or blends of active ingredients and excipients under pressure. The process variables controlling the quality of pellets prepared are similar to those used in tablet manufacturing [118]. It is appropriate to identify that the methods used for *"dry"* agglomeration processes are not applicable for use in the case of the iron ore samples considered in this research as they agglomerate using *"wet"* agglomeration mechanisms.

When *"wet"* agglomeration is considered, the typical methods used consist of systems which mix the bulk material, liquid and binder to form agglomerated particles. Some of the methods used in the pharmaceutical and chemical processing industries include fluidized bed granulators [119 - 121], high shear granulators [122 - 124] and centrifugal granulators [125 - 127], as outlined in Table 5.1. When the agglomeration of iron ore for the steel making industry is considered, three methods are commonly used which include belt conveyor, drum and disc (pan) agglomeration systems [128]. The following section outlines the agglomeration methods suitable for the materials handling sector in detail and the potential benefits for the use of agglomeration are also outlined.

5.2.3 INDUSTRIAL SYSTEMS SUITABLE FOR THE MATERIALS HANDLING SECTOR

The field of agglomeration is an area where extensive research has been undertaken, where key benefits of agglomeration are outlined above. When the materials handling sector is considered, the benefits of agglomeration are not readily available in published literature. Some of the potential benefits include the reduction of problematic behaviours of WSMs and the reduction for the propensity of dust generation. To consider the use of agglomeration in the materials handling sector, industrial systems must be considered. Some of the suitable industrial systems include belt conveyor, drum and disc (pan) agglomeration systems [128].

Belt conveyor agglomeration systems, as shown in Figure 5.2, are generally suited for ores which contain less than 15% of sub 104 µm fine particles. Agglomeration occurs when particles touch each other when negotiating transfer stations between belts or when the particles bounce on the belt upon landing [129]. Belt velocities of 1.25-1.50 m/s are generally used [128]. Dispersion bars hanging at the belt discharge improves mixing of the bulk material during free fall where the number of transfer points increases with increasing fine content [129].

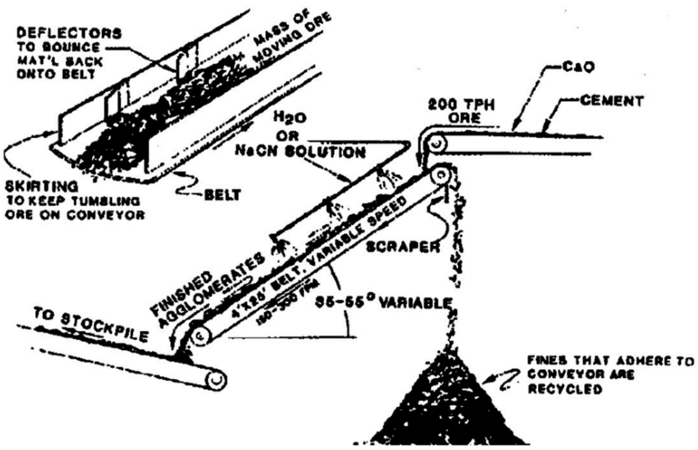

Figure 5.2 – Steep angle belt conveyor agglomeration (Chamberlin, 1986).

Rolling drum agglomeration systems, as shown in Figure 5.3, are the simplest form of continuous industrial system. They are typically are used in the fertilizer and iron ore industries [113]. The central axis is slightly inclined from the horizontal to aid in the movement of material through the mixer. Liquid is sprayed onto the bed of the bulk material by spray nozzles which are commonly located near the entrance, where the tumbling action of the drum aids size enlargement by aggregation [113]. Drum agglomeration is well suited for ores containing high percentages of clays or a large fines content. In the case where binders must be added, Chamberlin [128] prefers drum agglomeration systems to belt conveyor agglomeration systems. This is attributed to the efficiency of mixing found in drum agglomeration systems.

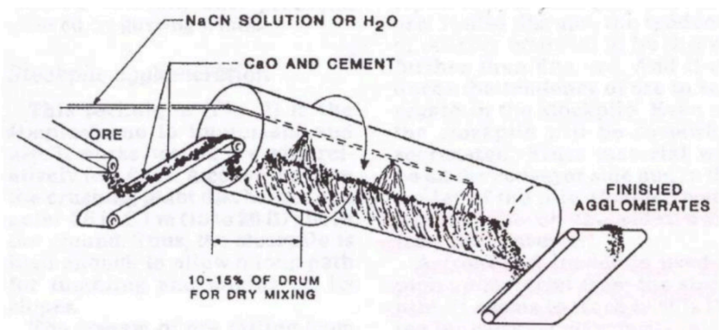

Figure 5.3 – Industrial drum agglomeration system (Chamberlin, 1986).

Disc or pan agglomeration systems consist of a rotating tilted disc with a rim where a schematic is shown in Figure 5.4. Similar to drum agglomeration methods, disc agglomeration systems are used in the fertilizer and iron ore industries. The influence of agglomeration performance and pellet structure are significantly influenced by solid feed and spray nozzle locations [129]. A key feature of this type of system is the inherent size classification [113]. Disc agglomeration produces uniform pellets with a narrow product size range where little to no solid recycling is found [129].

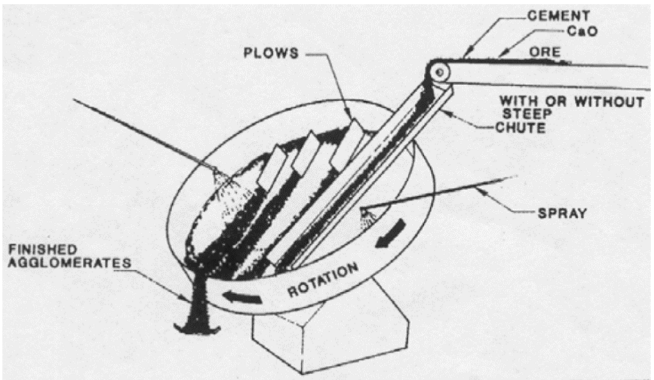

Figure 5.4 – Industrial disc (pan) agglomeration system (Chamberlin, 1986).

The breakage, attrition and shatter of agglomerated particles generally occurs when wet or dried agglomerates fracture due to impacts occurring in industrial agglomeration systems or during subsequent product handling [113, 130]. Breakage can also be attributed to the effects of binder and moisture where the quantity of each component is critical for the formation of stable agglomerates. To consider the stability of agglomerated particles, two different agglomeration methods are considered. This is undertaken using an agglomeration drum and the inclined plate recirculating system (outlined in Section 6.2). The properties and breakage of agglomerated particles are analysed using IOB within the context of the materials handling sector where the findings are summarised in the following section.

5.3 EXPERIMENTAL MEASUREMENTS AND VERIFICATION

During the initial experimental measurements on the inclined plate recirculating conveyor system (outlined in Section 6.2), it was observed that the supplied iron ore samples with clays present (namely IOB and IOC) were agglomerating. During these experiments it was further observed that the agglomerated particles were less problematic compared to the ROM iron ore sample at a similar moisture content. Some of the notable findings from the initial research included:

1. Agglomerated particles were less problematic when compared to ROM iron ore sample at an equivalent moisture content (analysed further in Section 5.3.2).
2. Less dust generation was experienced for agglomerated particles in comparison to ROM iron ore sample (analysed further in Section 5.3.1.3).

To quantify the reduction in problematic behaviours and dust generation, a comparison of an agglomerated iron ore sample (investigated using IOB) is compared to the as supplied ROM sample. Two different agglomerated samples are considered where the first sample is produced on the inclined plate recirculating system. Additionally, a sample is produced using a granulation drum, as seen in Figure 5.5, to consider the agglomeration process which is used extensively in the steel making industry. The granulation drum used is 490 mm in diameter, 305 mm wide, contains six lifter bars which are 7 mm high and are orientated at 25° from the drum surface to the centreline height. The following section outlines the experimental measurements where each type of agglomerate is compared to the ROM equivalent to identify the limitations where problematic behaviours become less prevalent. The moisture content for the agglomeration analysis and ROM comparisons is approximately 16.0% MC using IOB.

Figure 5.5 – Granulation drum located at Centre for Ironmaking Materials Research.

5.3.1 AGGLOMERATE PROPERTIES

To gain an understanding if differences arise between the two agglomeration methods, it is appropriate to analyse the properties of the agglomerates. The key properties which are considered include the particle size distribution, the bulk density, the dust extinction moisture content, the dynamic adhesion, the compressive strength of the agglomerates and time required for agglomeration to occur. Additionally, the shape and handling characteristics (outlined in Section 5.3.3) also require consideration.

The formation of agglomerates using the inclined plate recirculating system were analysed every sixteen transfers, equating to approximately 200 seconds of conveying time, to identify the approximate time for agglomeration to occur. The qualitative measurements of the agglomeration formation using the inclined plate recirculating system are shown in Figure 5.6. It is appropriate to identify that the addition of moisture during the agglomeration formation process may assist in reducing the time required.

a) As supplied

b) 16 transfers

c) 32 transfers

d) 48 transfers

Figure 5.6 – Agglomeration formation using inclined plate recirculating system.

The formation of agglomerates using a granulation drum were analysed every 120 seconds to identify the approximate time for agglomeration to occur. The qualitative measurements of the agglomeration formation using a granulation drum are shown in Figure 5.7. Similar to the agglomerates formed using the inclined plate recirculating system, the addition of moisture during the agglomeration formation process may assist in reducing the required time. When each of the agglomeration sample types are compared it can be observed that the time required for agglomeration to occur is substantially quicker using a granulation drum. It is appropriate to identify that the agglomerates from the inclined plate recirculating system were *"harder"* than those produced using a granulation drum (analysed further in Section 5.3.3.1). This can be attributed to the larger impacts experienced on the inclined plate recirculating system where compaction of the agglomerates occurs.

a) As supplied

b) 120 seconds

c) 240 seconds

d) 360 seconds

Figure 5.7 – Agglomeration formation using a granulation drum.

The testing conditions during the agglomeration formation for the inclined plate recirculating system are outlined in Section 6.2.2. For the agglomeration formation using a granulation drum, the following testing conditions and test rig parameters were used:

1. Sample Mass = 6.5 kg per batch.
2. Rotation Speed = 20 rev/min (v = 1.03 m/s at drum surface).
3. Ore Steady State Surface Rolling Angle = Approximately 37°.

5.3.1.1 PARTICLE SIZE DISTRIBUTION

The determination of the Particle Size Distribution (PSD) of a bulk material can give an indication into the potential moisture retention of a sample due to a higher fines component. Highly friable *"soft"* ores will tend to breakdown at a much greater rate when compared to *"harder"* ores [22]. PSD comparisons have been undertaken in accordance with ISO 4701:2008(E) [23] on a dry sieving basis where the PSD distribution curves are shown in Figure 5.8. It can be observed that the significant reduction in fines occurs for the agglomerated samples in comparison to the ROM sample. It is important to note that during the PSD measurements, the agglomerate samples could potentially break down. This can be attributed to the drying required to undertake measurements in accordance with ISO 4701:2008(E) [23] and also due to the sieve shaker apparatus itself which undergoes vibration (as outlined in Section 2.4.4).

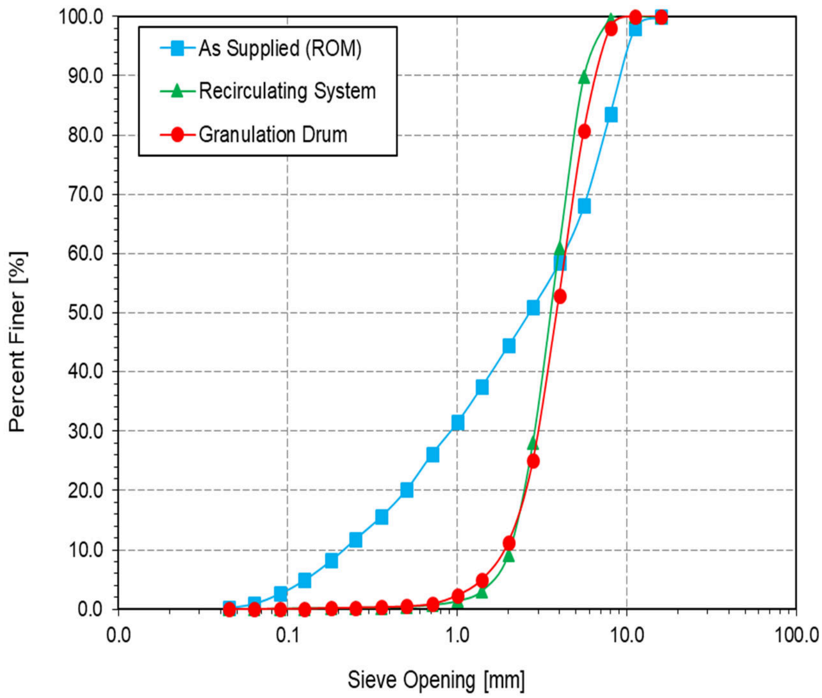

Figure 5.8 – Particle size distribution comparison between ROM and agglomerate samples.

5.3.1.2 BULK DENSITY MEASUREMENTS

The determination of the compressibility of the bulk material samples has been conducted using the large bulk density (compressibility) tester (outlined in Section 2.4.6). This test is a modified version of the test outlined in AS 3880: 2017 [20] and is used to measure the bulk density of the sample as a function of the major consolidation pressure. Variable normal loads are applied to the sample by means of a consolidation lid and hydraulic cylinder, and the compression of the sample is measured with a displacement transducer. It is important to note that the consolidation lid did not rotate during the measurements. This was critical as any form of twisting may lead to an undesirable influence of the bulk density for the formed agglomerates. Additionally, the moisture content which has been tested was determined once the agglomerated samples were formed. The conducted bulk density measurements for the ROM and agglomerate samples are shown in Figure 5.8. It can be observed that there is no apparent difference when the agglomerated and ROM samples are compared.

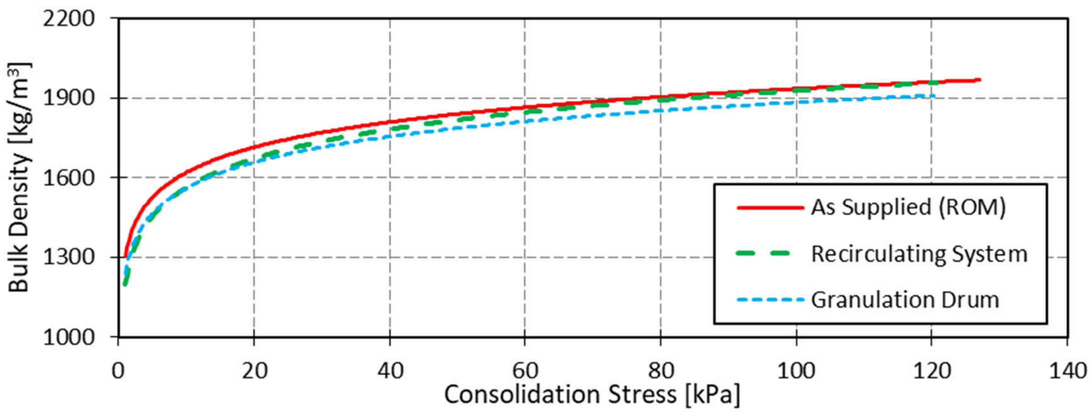

Figure 5.9 – Bulk density (compressibility) comparison between ROM and agglomerate samples.

5.3.1.3 DUST EXTINCTION MOISTURE CONTENT MEASUREMENTS

To compare the ROM and agglomerated samples for the propensity of dust, Dust Extinction Moisture Content (DEMC) tests have been undertaken in accordance with the DEMC Coal Standard AS 4156.6 [21] where a sample volume is maintained for iron ore. This equates to an increased sample mass from 1 kg to 2.5 kg. The size fraction which has been tested was -11.2 mm for both the ROM and agglomerated samples. The laboratory testing conditions must lie within the limits of $20°C \pm 2°C$ for temperature and $63\% \pm 2\%$ for the relative humidity. The Dust Number is determined using Equation 2.4. The DEMC of a bulk material is found when a dust number of ten is achieved. The DEMC for the ROM and agglomerate samples are presented in Table 5.2. Tests were undertaken at the As Supplied (AS) moisture content and air dried in an oven at 40°C for approximately 16 hours.

Table 5.2 – DEMC Comparison Between ROM and Agglomerate Samples

Bulk Material Sample	*Moisture Content [% MC]*	*Dust Number*
Run-of-Mine (ROM) Sample		
As Supplied	15.9	1.5
Air Dried (16 hours)	7.5	360.8
Inclined Plate Recirculating System Sample		
As Supplied	16.1	1.4
Air Dried (16 hours)	7.4	40.0
Granulation Drum Sample		
As Supplied	16.2	1.2
Air Dried (16 hours)	6.8	128.4

** Agglomerated sample was air dried and the DEM test was subsequently conducted.*

5.3.1.4 COMPRESSIVE STRENGTH MEASUREMENTS

To analyse the strength of the agglomerated particles, it is appropriate to undertake compressive testing which determines the load required for fracture and/or breakage to occur. The compression testing was undertaken using a Shimadzu AGS-X autograph precision universal tester, as shown in Figure 5.10. A testing rate of 1 mm/min was used where this was deemed appropriate to not induce any premature breakage of the agglomerate particles. The current testing program allows for the measurement of the forces required for breakage to occur which can be used to estimate the performance of the agglomerates to negotiate the materials handling stream. These measurements have been undertaken for the agglomerates formed on the inclined plate recirculating system and agglomerates formed using a granulation drum.

Figure 5.10 – Shimadzu AGS-X autograph precision universal tester.

Each sample had twenty-five particles selected at random for the testing program to be undertaken. The approximate particle diameter for each of the respective samples was 5 mm where the tested particles are outlined in Figure 5.11. It is appropriate to identify that the tested samples were air dried in an oven at 40^{o}C for approximately 48 hours to ensure the agglomerates formed on the inclined plate recirculating system (shown in Figure 5.11a) and agglomerates formed using a granulation drum (shown in Figure 5.11b) were analysed at an equivalent state. Furthermore, the propensity for breakage will be much greater when the agglomerated particles have been dried. This would be expected in the conditions typically exhibited in the Pilbara region.

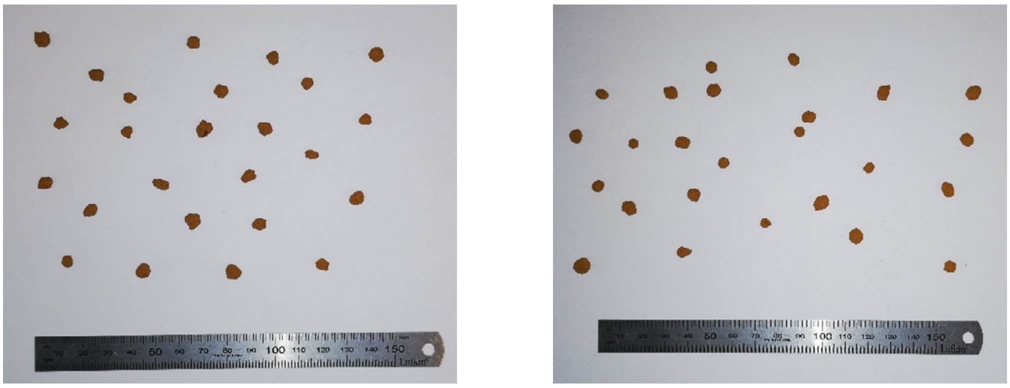

a) Inclined plate recirculating system agglomerates *b) Granulation drum agglomerates*

Figure 5.11 – Compression testing particle samples with mean particle diameter of 5 mm.

During the compression measurements, two distinct types of agglomerated particles were observed. The first were particles which did not consist of a central nucleus and were comprised of ultra-fine particles only. Figure 5.12a shows an agglomerated particle prior to the compression measurements in the Shimadzu AGS-X autograph precision universal tester and Figure 5.12b shows an agglomerated particle after the compression measurement.

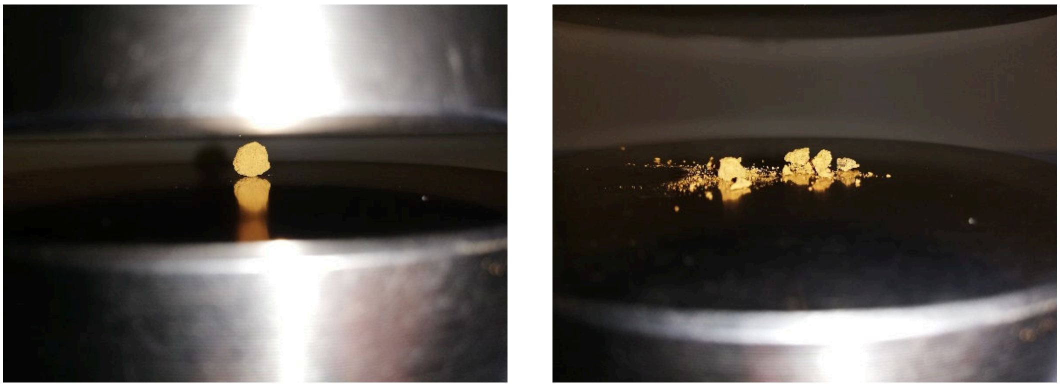

a) Sample prior to compression measurement *b) Sample after compression measurement*

Figure 5.12 – Compression testing for agglomerated particle without central nucleus (comprised of ultra-fine particles only).

The particles which did not consist of a central nucleus and were comprised of ultra-fine particles only had relatively low strength and crumbled upon initial impact. The strength of the agglomerates formed on the inclined plate recirculating system was approximately 13.9±10 N and the strength of the agglomerates formed using a granulation drum was approximately 15.7±10 N. The second type of agglomerated particles observed consisted of a central nucleus and contained a Goethite core particle. Figure 5.13a shows an agglomerated particle upon completion of the compression measurements in the Shimadzu AGS-X autograph precision universal tester where a hairline crack is evident. Figure 5.13b shows the same particle which has been broken open to show the central nucleus where the darker (deep red) Goethite is evident.

a) Sample showing hairline crack *b) Sample showing central Goethite nucleus*

Figure 5.13 – Compression testing for agglomerated particle with central nucleus (containing Goethite core particle).

The particles containing a central nucleus had relatively high strength in comparison to the agglomerates which were comprised of ultra-fine particles only and did not crumble upon initial impact. The strength of the agglomerates formed on the inclined plate recirculating system was approximately 125±60 N and the strength of the agglomerates formed using a granulation drum was approximately 133±60 N. It is important to note that the agglomerates formed using a granulation drum exhibited a very marginal increase in strength in comparison to the agglomerates formed on the inclined plate recirculating system. Additionally, it can be observed that both types of agglomerated particles showed approximately nine times the strength when a central nucleus was present.

5.3.2 DYNAMIC ADHESION EXPERIMENTAL MEASUREMENTS

To compare the ROM and agglomerated samples for the propensity to build-up, dynamic adhesion tests have been undertaken. These tests are conducted using the inclined plate recirculating system, where the procedure used is outlined in Section 6.2. The qualitative measurements of the build-up experienced using the inclined plate recirculating system are shown in Figure 5.14. These measurements are for the comparison between the ROM sample and the agglomerates which are produced using the inclined plate recirculating system. It is appropriate to identify that from a build-up perspective, there was no apparent difference when the agglomerated samples are compared to each other. However, the opposite is found when the agglomerates are compared to the ROM sample where a significant reduction in build-up results.

a) ROM build-up (15.9% MC)

b) Agglomerate build-up (16.1% MC)

Figure 5.14 – Comparison of build-up between ROM sample and inclined plate recirculating system agglomerates at similar moisture content.

5.3.3 AGGLOMERATE HANDLING PROPERTIES

To obtain an idea whether the use of agglomerated particles within the materials handling stream is feasible, it is appropriate to analyse the handling characteristics. This is undertaken by looking at the potential breakage of the agglomerates. Additionally, the shape is considered to give an indication into the potential flow characteristics which are analysed using the shear box and draw down tests. The following section presents a summary of breakage and handling measurements which compare the agglomerates formed on both the inclined plate recirculating system and using a granulation drum.

5.3.3.1 BREAKAGE MEASUREMENTS

Breakage measurements of the agglomerates are required to obtain an idea for the propensity of the agglomerates to break during transportation. Two experimental measurements have been conducted which consider high impact and compaction (consolidation) conditions. The first conducted experiment, shown in Figure 5.15, uses an impact drop test which replicates conditions of a transfer chute which can found onsite. The second test uses the large bulk density tester (outlined in Section 5.3.1.2) to analyse the propensity to breakage under high consolidation pressures.

Figure 5.15 – Impact test rig used for agglomeration breakage measurements.

The impact drop test consists of a 6.8 m drop height where a circular impact chute is fixed with an impingement angle of 20° relative to the falling stream of the agglomerate sample. Measurements are conducted on both agglomerate samples, produced on the inclined plate recirculating system and using a granulation drum, where two impacts are considered. To analyse the propensity to breakage, PSD tests have been undertaken in accordance with ISO 4701:2008(E) [23] on a dry sieving basis. The PSD distribution curves for each impact test for the agglomerates formed using the impact plate recirculating system are shown in Figure 5.16. When the conducted impact drop tests are compared to the as supplied agglomerates a small amount of breakage is prevalent. It is appropriate to identify that when a second drop test is conducted no further breakage of the sample is evident, as shown in Figure 5.16.

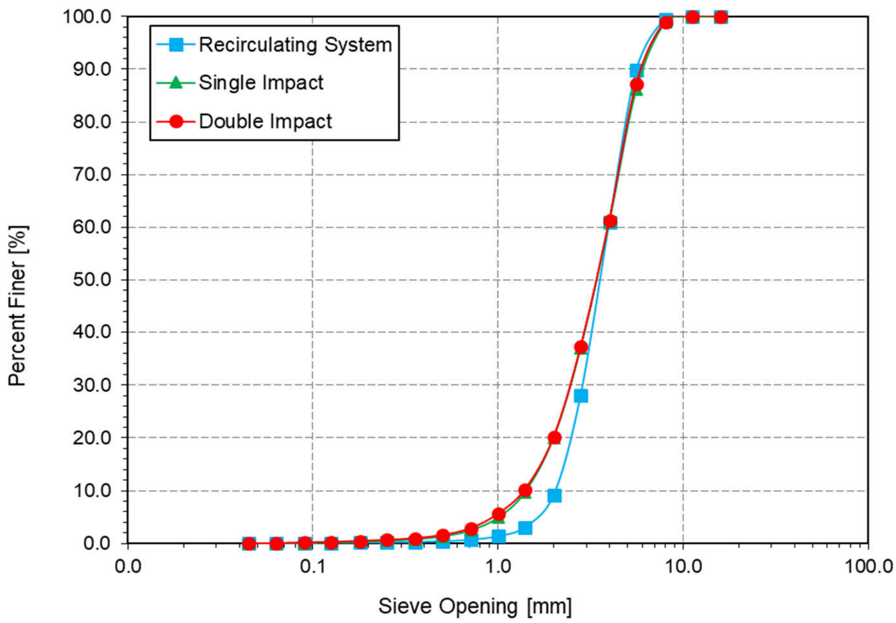

Figure 5.16 – Particle size distribution comparison between inclined plate recirculating system agglomerates showing propensity to breakage from impact testing.

The PSD distribution curves for each impact test for the agglomerates formed using a granulation drum are shown in Figure 5.17. When the conducted impact drop tests are compared to the as supplied agglomerates, a small amount of breakage is prevalent. Unlike the breakage measurements for the agglomerates formed using the impact plate recirculating system, when a second drop test is conducted further breakage of the sample is evident, as shown in Figure 5.17.

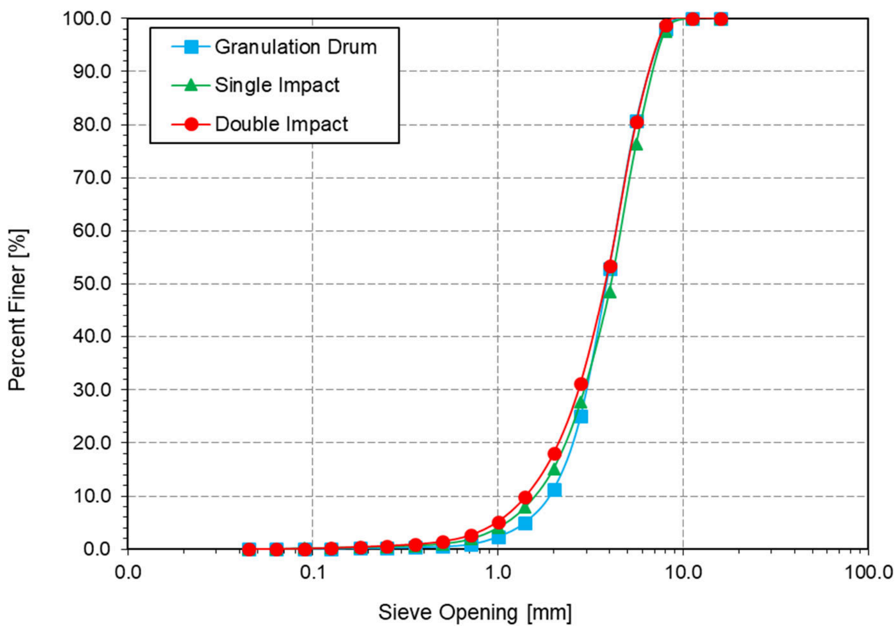

Figure 5.17 – Particle size distribution comparison between granulation drum agglomerates showing propensity to breakage from impact testing.

To analyse the potential breakage under high consolidation pressures, large bulk density tests (outlined in Section 5.3.1.2) are conducted. The PSD distribution curves for each large bulk density test for the agglomerates formed using the inclined plate recirculating system are shown in Figure 5.18. When the conducted bulk density tests are compared to the as supplied agglomerates, a small amount of breakage is prevalent.

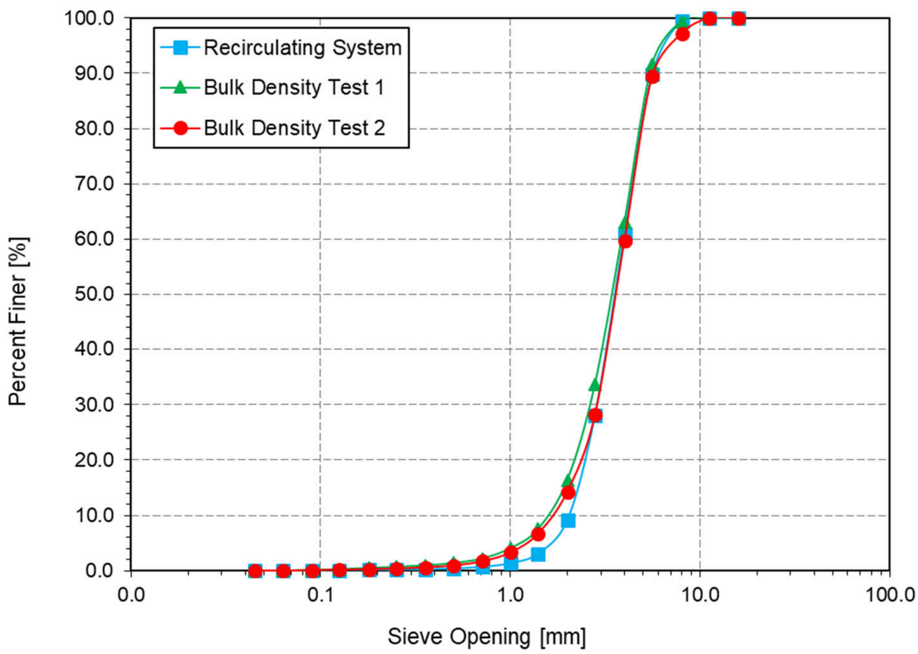

Figure 5.18 – Particle size distribution comparison between inclined plate recirculating system agglomerates showing propensity to breakage from large bulk density testing.

The PSD distribution curves for each large bulk density test for the agglomerates formed using a granulation drum are shown in Figure 5.19. When the conducted large bulk density tests are compared to the as supplied agglomerates a small amount of breakage is prevalent. Similar to the breakage measurements for the agglomerates formed using the impact plate recirculating system, only a small percentage of breakage is evident. This can be observed when Figure 5.18 and Figure 5.19 are considered.

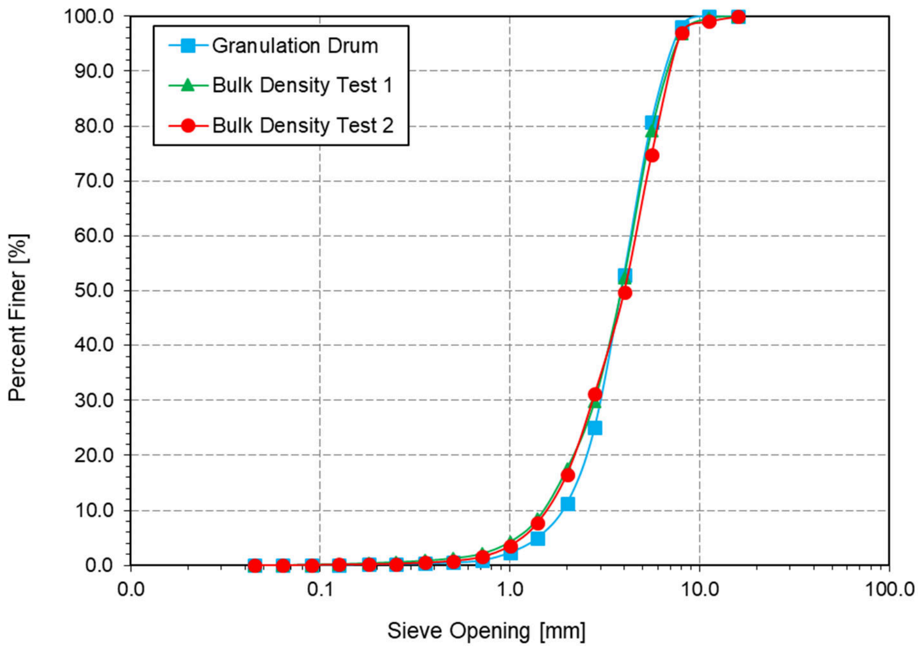

Figure 5.19 – Particle size distribution comparison between granulation drum agglomerates showing propensity to breakage from large bulk density testing.

5.3.3.2 MICROSCOPY ANALYSIS

Once the formation of agglomerates was conducted on both the inclined plate recirculating system and using a granulation drum, it was deemed essential to analyse the shape and constituents of the agglomerate particles using optical microscopy. The optical microscopy analysis of the samples has been undertaken by the author in conjunction with the staff at the Centre for Ironmaking Materials Research from the University of Newcastle. To undertake the optical microscopy of the samples, a small sub sample was air dried in an oven at 60^{o}C for approximately 48 hours. Once the agglomerate particles were dry, they were placed into a coloured epoxy resin and allowed to set. These were then cut in half and polished using a range of different grades of wet and dry sandpaper. The microscopy samples were polished using a final grade of 3000 grit sandpaper.

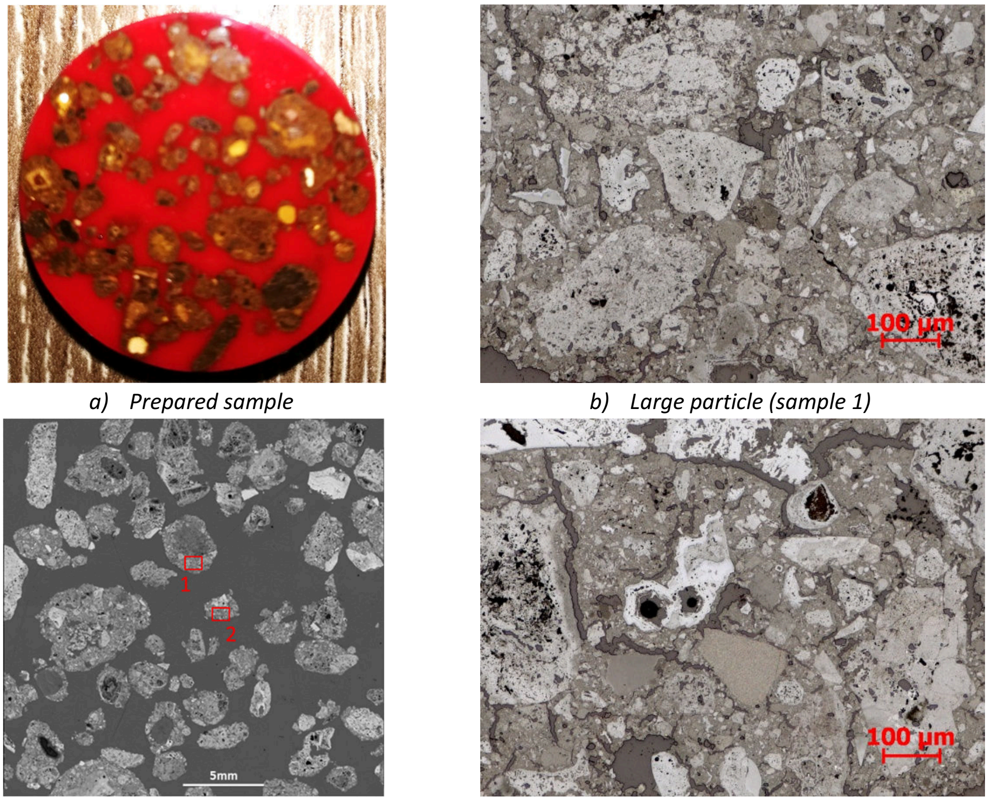

a) Prepared sample *b) Large particle (sample 1)*

c) Microscopy image *d) Small particle (sample 2)*

Figure 5.20 – Microscopy analysis for agglomerates formed using the inclined plate recirculating system.

The epoxy resin and microscopy analysis for the agglomerates formed using the inclined plate recirculating system are shown in Figure 5.20. Two different sized particles had a detailed analysis undertaken as shown in Figure 5.20b and Figure 5.20d. The observations for these two particles and majority of the remaining agglomerate particles consisted of chips of goethite of varying textures which are bonded together with ultra-fines. The ultra-fines consisted of fine ochreous goethite and kaolinitic clay material. Some larger nuclei are present however majority of the agglomerate particles could be identified as smaller nuclei.

The epoxy resin and microscopy analysis for the agglomerates formed using a granulation drum are shown in Figure 5.21. Two different sized particles had a detailed analysis undertaken as shown in Figure 5.21b and Figure 5.21d. Similar to the agglomerates formed using the inclined plate recirculating system, the granulation drum agglomerates consisted of chips of goethite of varying textures which are bonded together with ultra-fines. The ultra-fines consisted of fine ochreous goethite and kaolinitic clay material. It is appropriate to identify that *"dehydration"* cracks within the ultra-fine bonding material is evident for the agglomerates formed using a granulation drum. This can be attributed to the less dense agglomerates where the compaction is significantly reduced in comparison to the agglomerates formed using the inclined plate recirculating system.

a) Prepared sample

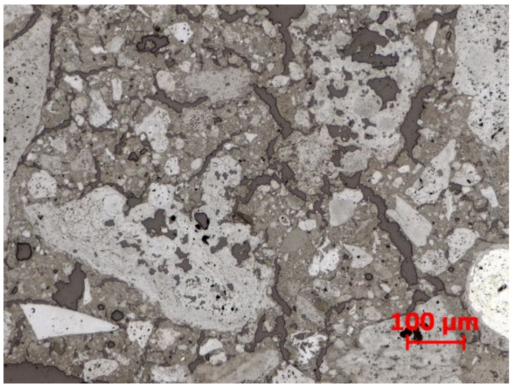

b) Large particle (sample 1)

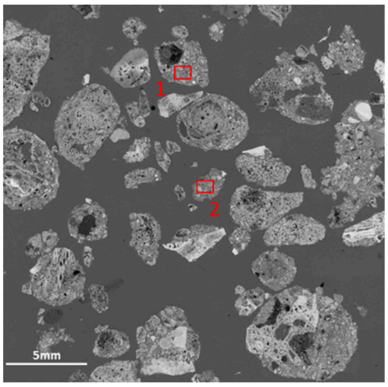

c) Microscopy image

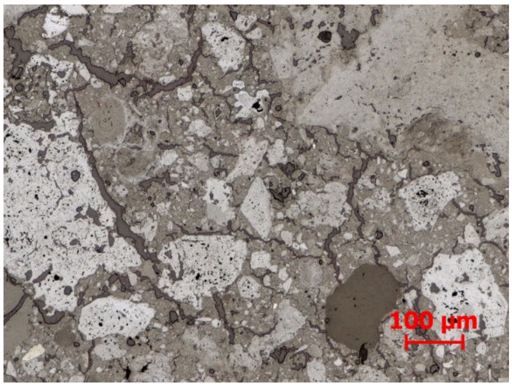

d) Small particle (sample 2)

Figure 5.21 – Microscopy analysis for agglomerates formed using a granulation drum.

5.3.3.3 SHEAR BOX TESTING

Shear box experiments, typically referred to as slump tests, are used to identify the internal strength of a bulk material when no consolidation loads are applied (similar to loose poured bulk density tests outlined in Section 2.4.6.1). A schematic of the shear box testing apparatus is shown in Figure 5.22. The shear box used is constructed from Perspex and has a length, width and height of 300 mm. One of the vertical walls is removable to allow the bulk material to flow (slump) out of the shear box.

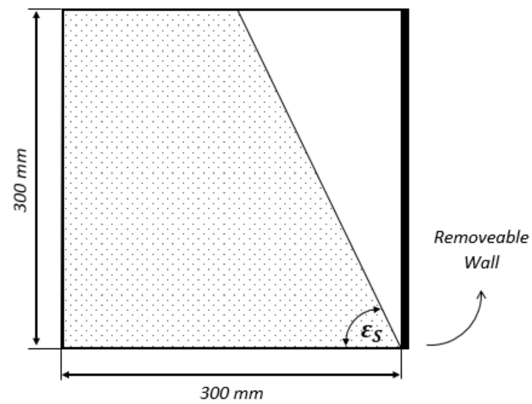

a) Schematic

b) Experimental measurement

Figure 5.22 – Shear box testing apparatus.

For the conducted shear box experiments, approximately 40 kg of sample was required. Each sample was carefully filled to the top of the shear box without adding additional consolidation. The sample was then screed, to result in a known volume of bulk material. After this stage, the flap was rapidly opened, and the sample allowed to flow out of the shear box. The residual bulk material in the shear box forms a slope which is typically referred to as the shear angle. Upon completion of each experiment, the residual mass and the shear angle, ε_S, are determined and recorded to be used as reference values for the comparison of the handling characteristics between the agglomerate and ROM samples. A summary of the shear box experimental results for the tested ROM and agglomerate samples are summarised in Table 5.3.

Table 5.3 – Shear Box Testing Results for IOB at 18.5% MC

Bulk Material Sample	*Initial Mass [kg]*	*Residual Mass [kg]*	*Shear Angle [°]*
Run-of-Mine (ROM)	37.8	30.2±0.5	68.6±1.2
Recirculating System	34.9	24.4±0.2	59.8±0.8
Granulation Drum	34.7	23.6±0.3	57.9±0.9

5.3.3.4 DRAW DOWN TESTING

To replicate the discharge of a hopper or bin, the draw down test has been developed. The draw down test, as shown in Figure 5.23, consists of an upper and lower box where each box is 500mm high, 500mm wide and 100mm deep. The upper box has a discharge gate (flaps) and an adjustable rectangular opening at the bottom. The discharge gate is rapidly opened (0.3 seconds) and the bulk material sample is allowed to discharge into the lower box. The outflowing bulk material forms a stock pile in the lower box (AOR measurement), while the remaining bulk material forms two slopes in the upper box (shear angle measurement). For the conducted draw down experiments, approximately 30 kg of sample was required. The sample was carefully filled into the upper box without adding additional consolidation to the analysed sample. The sample was then screed, to be level and the height of the material was measured (360 mm). After this stage, the discharge gates were rapidly opened, and the sample allowed to flow out of the upper box.

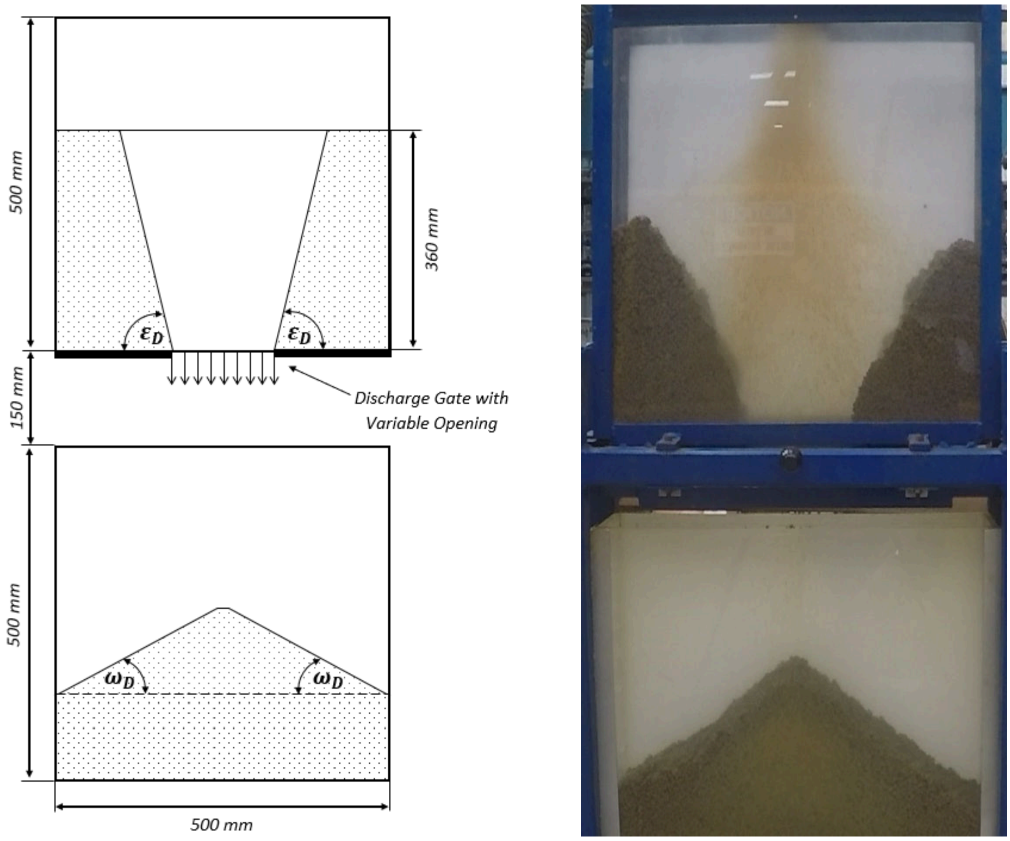

a) Schematic *b) Experimental measurement*

Figure 5.23 – Draw down testing apparatus.

The residual bulk material in the lower box forms a stockpile which is typically referred to as the Angle of Repose (AOR) where the remaining slope angles in the upper box gives the shear angle of the bulk material. Upon completion of each experiment, the residual mass in the lower box, AOR, ω_D, and shear angle, ε_D, are determined and recorded to be used as reference values for the comparison of the handling characteristics between the agglomerate and ROM samples. A summary of the draw down experimental results for the tested ROM and agglomerate samples are summarised in Table 5.4.

Table 5.4 – Draw Down Testing Results for IOB at 18.5% MC

Parameter	*Units*	*Run-of-Mine (ROM)*		*Recirculating System*		*Granulation Drum*	
Initial Mass	[kg]	27.7	27.7	23.5	23.5	23.3	23.3
Opening Dimension	[mm]	150	75	150	75	150	75
Upper Box Sample Height	[mm]	360	360	360	360	360	360
Residual Mass (Lower Box)	[kg]	13.6±0.6	1.8±0.3	15.1±0.4	13.9±0.5	14.8±0.4	1.6±0.2
Angle of Repose	[°]	28.2±1.2	N/A	33.5±0.7	35.4±0.9	33.4±0.8	N/A
Shear Angle	[°]	79.2±2.2	N/A	63.9±1.9	76.6±1.8	70.9±1.6	N/A
Regime	N/A	Flowed	Arched	Flowed	Flowed	Flowed	Arched

5.4 RESULTS AND DISCUSSION

The agglomeration of iron ore is a well-known and researched field which is used extensively in the steel making industry. When the materials handling sector is considered however, the benefits of agglomeration are not well-known or available in published literature. The following section summarises the conducted experimental measurements where comparisons are made between the agglomerate samples and the ROM equivalent.

It was observed during the experimental measurements that the agglomerated samples showed a significantly reduced propensity for problematic behaviours when compared to the ROM sample (outlined in Section 5.3.2). The significant reduction in problematic behaviours, as shown in Figure 5.14, demonstrates the benefits of agglomeration to the materials handling sector. This reduction of problematic behaviours can be attributed to the ultra-fines which adhere to larger particles forming larger nuclei. This effectively reduces the amount of ultra-fine clays, kaolinite for IOB, which typically lead to problematic behaviours. By reducing the amount of exposed clays, the effective adhesive properties reduce even when the overall chemical properties and moisture content remain the same.

One method which can be used to reduce the adhesive properties of a bulk material is by *"drying"*. This, however, leads a bulk material to significantly increase the propensity for dust generation. To analyse the propensity for dust generation of the agglomerate samples, DEMC tests were undertaken (outlined in Section 5.3.1.3) where the agglomerated samples showed a significantly reduced propensity for dust generation in comparison to the ROM sample. When the DEMC results are considered in Table 5.2 a significant reduction in the dust number of the agglomerate samples can be observed. This becomes evident when the ROM sample at 7.5% MC yields a dust number approximately nine times larger than the agglomerates formed using the inclined plate recirculating system at an equivalent moisture content.

To obtain an idea whether the use of agglomerated particles within the materials handling stream is feasible, the handling characteristics were analysed. This was undertaken by looking at the potential breakage of the agglomerates. Drop tests were undertaken where the agglomerates from the inclined plate recirculating system were *"harder"* than those produced using a granulation drum. This is shown when the PSD distribution curves, shown in Figure 5.16, are considered. Some breakage of the agglomerates was evident however when additional impacts are considered further breakage did not occur. This was not observed when the agglomerates using a granulation drum are considered where further breakage can be observed with additional impacts, as shown in Figure 5.17. The *"harder"* agglomerates are attributed to the larger impacts experienced on the inclined plate recirculating system where compaction results.

The study of agglomeration contained within this research only touches the surface into this extremely interesting and well documented field. Although the use of agglomeration is well known within the steel making industry, the benefits to the materials handling stream are not so well known. It is therefore essential that a much more detailed analysis be conducted as outlined in Section 8.3.4.

5.5 CONCLUSION

This chapter has outlined the fundamentals of agglomeration, typically referred to as granulation, where the applications to the materials handling stream were identified. The methods of agglomeration which are used extensively within the steel making industry are outlined and the possible implementation of these systems to the materials handling stream are also proposed. From this, the effects for the reduction of problematic behaviours that WSMs show within the materials handling stream are explored. To quantify the reduction in problematic behaviours and dust generation which can be experienced onsite, a comparison of an agglomerated iron ore sample, investigated using IOB, is compared to the as supplied ROM sample.

Two agglomeration samples are considered, one which is formed using the inclined plate recirculating system (outlined in Section 6.2) and one using a granulation drum (shown in Figure 5.5). This is undertaken for an equivalent moisture content for all samples. The agglomerated samples showed a significantly reduced propensity for problematic behaviours when compared to the ROM sample (outlined in Section 5.3.2). Additionally, DEMC tests were undertaken (outlined in Section 5.3.1.3) where the agglomerated samples showed a significantly reduced propensity for dust generation in comparison to the ROM sample.

This page is left intentionally blank

CHAPTER SIX – MEASUREMENT OF DYNAMIC ADHESION & TRANSFER SYSTEM OPTIMISATION

The following chapter outlines the developed recirculating conveyor testing apparatus and the procedure used for the experimental measurements. A summary of the key testing results is included, where a comparison of the obtained experimental measurements are used to verify the theoretical model developed in Section 4.3. Additionally, the areas where dynamic adhesion can be prevalent in the materials handling stream are identified and a design protocol for the reduction of dynamic adhesion is also proposed.

6.1 INTRODUCTION

The measurement of experimental data from an in-plant transfer chute can be extremely difficult to implement the measurement equipment correctly for accurate data acquisition. Additionally, the logistics around access to data acquisition equipment can also be problematic. Another potential problem may arise from induced noise to the data acquisition equipment caused by electromagnetic pulses from conveyor drives. Due to this, it was deemed more appropriate and necessary to develop a pilot scale system to measure the required parameters to verify the developed theoretical model in Section 4.3.

The pilot scale testing facility, referred to as the inclined plate recirculating system, was developed by the author and consisted of four recirculating belt conveyors. The inclined plate recirculating system includes four impact zones (three with inclined impact plates and one with a *"rock-box"*). The following chapter will explain the details of the inclined plate recirculating system and the procedure used to obtain the experimental measurements. The procedure outlined was developed to ensure the experimental measurements would be undertaken in a reproducible manner where confidence in the experimental data would result. The key experimental measurements are explained in detail where the thresholds for dynamic adhesion in relation to the moisture content of the iron ore samples are also identified. Additionally, the estimated shape of the iron ore build-up is also analysed. This will give an insight into the severity of the build-up that occurred during the experimental measurements. Finally, the zones where dynamic adhesion can be prevalent in the materials handling stream are identified and a design protocol for the reduction of dynamic adhesion is also proposed.

6.2 INCLINED PLATE EXPERIMENTAL MEASUREMENTS

The main intention of the inclined plate experimental measurements is to obtain data that will give an indication of the severity of a bulk material build-up. This is in relation to the impingement angle (φ_{imp}) of the bulk material relative to the wall liner. A simplified schematic of an impact zone of the inclined plate recirculating system is shown in Figure 6.1. A relationship of the bulk material build-up can also be found in relation to the moisture content of the bulk material and the material of the wall liner itself. The measurement criteria that is required for validation of the developed theoretical model found in Section 4.3, will be the shape (maximum build-up height) and mass of the bulk material build-up. To achieve the desired measurement criteria, load cells are utilised to gain a quantitative measurement of the transient force of the bulk material impact. This is undertaken at each of the four transfer zones where the remaining mass will also be calculated. To identify the cross-sectional shape of the build-up, video cameras are used.

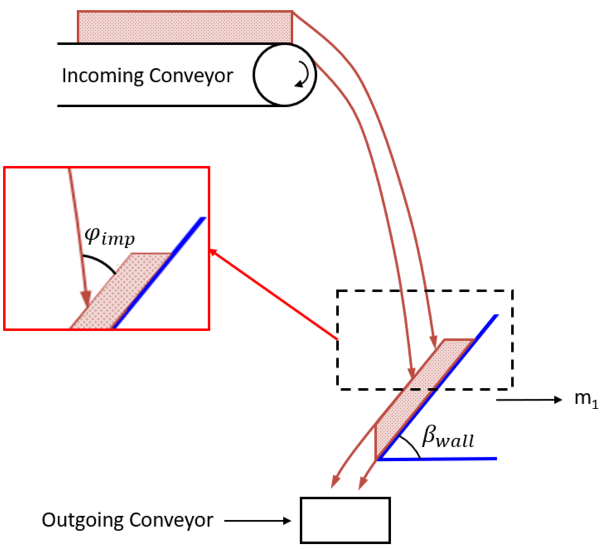

Figure 6.1 – Schematic of impact zone of inclined plate recirculating system.

In order to accurately develop thresholds for problematic behaviour of the supplied iron ore samples, a range of testing variables are required to be investigated. The variables in question are: testing of the iron ore samples at different moisture contents, a range of impingement angles of the bulk material in relation to the wall liner and different wall lining materials which show different characteristics (as explained in Section 2.5). The moisture contents tested for each of the respective iron ore samples are summarised in Table 6.1.

Table 6.1 – Recirculating System Moisture Content of ROM (-11.2 mm) Samples

Bulk Material Sample	*As Supplied Moisture Content*	*Moisture Content 2*	*Moisture Content 3*
IOA	6.3% MC (~40% SDMC)	9.3% MC (~60% SDMC)	11.5% MC (~75% SDMC)
IOB	13.4% MC (~50% SDMC)	15.9% MC (~60% SDMC)	18.5% MC (~70% SDMC)
IOC	11.5% MC (~50% SDMC)	14.8% MC (~65% SDMC)	18.2% MC (~80% SDMC)

It is appropriate to identify the impingement angle (φ_{imp}) is the resultant angle formed between the freefall stream of the bulk material and the wall liner (as shown in Figure 6.1). The range of impingement angles which are investigated include 60° to 25° in five-degree increments. The following section discusses the measurement apparatus used for the experimental measurements in detail. Additionally, the testing parameters are discussed in detail in Section 6.2.2.

6.2.1 MEASUREMENT APPARATUS

The inclined plate recirculating system consists of four belt conveyors where each belt conveyor is six metres in length and are comprised of a 450 mm wide belt. The troughing angle of the idlers of each belt conveyor is 20° and each belt conveyor is fixed to an inclination angle of 24.5° to give an approximate impact height of 1500 mm. A photograph of the testing apparatus is shown in Figure 6.2. The system contains four impact zones where three wall liners and a *"rock-box"* are included for a detailed analysis into the influence of the geometrical constraints onto the build-up of the bulk material relative to the moisture content. At three of the four impact zones, shown in Figure 6.2, the wall liner materials selected for investigation are impact and wear resistant materials typically used in industry. The wall liners used include: ceramic tiles, rough welded overlay and cast white iron alloy where the dimensions of the wall liners were approximately 350 mm wide and 450 mm long. It is important to note that at the three selected impact zones one liner type, as outlined above, was utilised. This allowed all liners to be examined simultaneously for each of the tested iron ore samples. The selected wall lining materials are generally hard faced and range considerably in mechanical properties as outlined in Section 2.5.

The remaining impact zone consists of a *"rock-box"* (use of ledges) transfer system. This type of system has been included to investigate the tendency for a bulk material to build-up on itself. It can be typical for use of rock-box transfer systems in industry for hard wearing ores, where the mode of flow is dependent on the internal friction of the bulk material rather than the friction that is produced between the bulk material and wall lining material surface. From a wear perspective, by allowing the bulk material to shear on itself minimal wear to the transfer system will be found. However, as these systems typically handle WSMs, especially further down the handling chain closer to the port, blockages can occur and significant downtimes result.

Figure 6.2 – Final configuration of the inclined plate recirculating system located at TUNRA Bulk Solids.

For the impact zones consisting of the wall lining materials, a mechanism was required which would allow for the adjustment of the wall lining angle to be undertaken with high accuracy. The mechanism would also allow for the adjustment of the wall lining angle to be the same at all three transfer stations (required for reproducible experiments). The designed mechanism is shown in Figure 6.3. The angle adjusting mechanism, shown in Figure 6.3b, consisted of a series of holes machined into a piece of flat plate which were geometrically matched to the holders which were attached directly to the load cells. The set of matching holes enabled for the angle to be adjusted in five-degree increments. The load cells were then fixed to a piece of flat bar (painted dark blue in Figure 6.3b) which was then fixed onto slotted sections of RHS. This was required to ensure the impact of the bulk material onto the centre of the wall liner would be perpendicular for an impingement angle of 90°. The wall liner clamping mechanism, shown in Figure 6.3c, was required to ensure the wall liner will remain fixed whilst the experimental measurements were conducted.

a) Impact zone with impact plate *b) Angle adjusting mechanism* *c) Wall liner clamping mechanism*

Figure 6.3 – Impact zone showing wall liner assembly.

The impact zone consisting of the *"rock-box"* was constructed primarily of steel, however, the sides were constructed from Perspex. This allowed for the visualisation of the ore angle to be observed whilst the experimental measurements were conducted. The final configuration of the rock-box is shown in Figure 6.4a. A piece of flat bar welded to the supporting frame of the rock-box was centrally fixed to a load cell, as shown in Figure 6.4b. The internal dimensions of the rock-box were 300 mm wide, 150 mm deep and 300 mm high. The width was calculated to be sufficient, in relation to the estimated width of the incoming stream of the bulk material. Additionally, the depth and height were determined using the internal friction angles which were calculated in the testing undertaken in Section 2.4.8.

The components for the inclined plate recirculating system have been designed using the relevant standards to ensure that a safe and reliable testing apparatus was constructed. The primary components which required detailed design included the stands used for the belt conveyors and the guarding which was used to surround and isolate the system. These components were deemed to be essential and critical during the design brief of the testing equipment, to ensure the safety of the personnel which will be utilising the testing facility. The manufacturing drawings have been undertaken in accordance with AS1100 [131]. Once the testing facility had been constructed, it was necessary to complete a Standard Operating Procedure and Risk Assessment. These were required to be cited and understood by each individual user to ensure their safety.

a) Impact zone with rock-box *b) Rock-box mounting configuration*

Figure 6.4 – Impact zone showing the rock-box assembly.

Each load cell required calibration of the output voltage, prior to and upon completion of the experimental measurements. Figure 6.5 shows the method used to calibrate each of the seven load cells. This procedure would give an indication if any drift in the output of the load cell occurred during the experimental measurements. In the case where drift was found the load cell was recalibrated and the experimental measurement was repeated. The load cells used were single point load beams rated to 100 kg, where it was deemed to be most accurate if a load frame was used for the calibration which would result in a single point load (as shown in Figure 6.5). The maximum calibration mass used was approximately 50 kg, where a calibration was conducted in 10 kg increments from zero through to the maximum. An average output voltage value was then used for the final calibration value. The output calibrated value (gain) was required to convert the voltage into a mass which was then used for the determination of a bulk material build-up.

Figure 6.5 – Load cell calibration method undertaken prior to and upon completion of experimental testing.

To analyse the bulk material build-up shape and size, video cameras were placed perpendicular to the wall liner and rock-box transfer stations, as shown in Figure 6.6a and Figure 6.6b respectively. Additionally, 50 mm by 50 mm reference grids were placed at the rear of each transfer station so the input and output velocities could also be calculated. The recorded video footage was critical in determining the threshold moisture contents and impingement angles where a resultant zero bond depth was experienced. This was determined in conjunction with the residual mass of the bulk material acquired from the load cell data. Furthermore, the recorded video footage was also critical for the determination of the dynamic shear angle in the rock-box which will be experienced whilst the experimental measurements were conducted. It is appropriate to identify that the dynamic shear angle will typically be greater than the static equivalent. The static shear angle of the rock-box transfer would occur when the transient flow of the bulk material is not present.

a) Wall liner video camera location

b) Rock-box video camera location

Figure 6.6 – Location of video cameras for both types of transfer station.

In addition to the data acquisition equipment identified above, it was also deemed necessary to accurately determine the dimensions of the bulk material stream coming off the head pulley. This would be used to determine the input parameters of the theoretical model developed in Section 4.3. Additionally, the free fall of the bulk material stream required careful consideration to determine if the velocity profile across the width of the stream was uniform. This process would also be utilised to determine if the flow of the bulk material was continuous or discontinuous in nature. To record the parameters for the bulk material stream, a Sony RX10 M3 DSLR camera was used. This camera is capable of recording up to 1000 frames per second at High Definition quality. This was deemed to be sufficient when the estimated impact velocities were considered. The calculated bulk material stream parameters for the three iron ore samples are determined in the following section.

6.2.2 EXPERIMENTAL TESTING PARAMETERS

The experimental measurements are required to be undertaken in a reproducible manner. This will allow for comparisons to be made between the behaviours which each of the three iron ore samples exhibit. To achieve accurate and comparable experimental measurements, some parameters were required to be held constant. The parameters which were fixed for all the conducted experimental measurements included; the conveyor velocity which was 0.6 m/s, the experiment testing time which was 90 seconds and the impact height which was 1500 mm at the point of impact.

During the experimental measurements of the inclined plate recirculating system, the belt conveyors were loaded manually once the bulk material sample was prepared. The preparation procedure of the sample is discussed in Section 6.2.3. For reproducible experimental measurements, a consistent burden profile was created on each of the four belt conveyors (as shown in Figure 6.7). This was undertaken by ensuring that a belt edge clearance of approximately 100 mm and an approximate surcharge angle of 15 degrees was maintained on all four conveyors. It is important to also note that moisture content measurements prior to and upon completion of the experimental measurements were undertaken to monitor changes in the moisture content of each sample.

Figure 6.7 – Recirculating system burden profile loading.

The dimensions of the burden profile, which are required as input parameters of the theoretical model developed in Section 4.3, were recorded prior to and upon completion of the experimental measurements. A summary of the approximate mass of the iron ore sample on the full system, estimated mass flow rate, burden properties and the moisture content were recorded for each of the iron ore samples upon completion of the experimental measurements. This was undertaken at each of the respective moisture contents tested, where a summary of these values are found in Table 6.2.

Table 6.2 – Recirculating System Burden Parameters

Bulk Material Sample	Moisture Content	Approximate Mass [kg]	Estimated Mass Flow Rate [kg/s]	Burden Width [mm]	Burden Depth [mm]
IOA	6.3% MC (~40% SDMC)	266.5	6.7	223.1	33.1
	9.3% MC (~60% SDMC)	275.0	6.9	211.2	38.4
	11.5% MC (~75% SDMC)	283.5	7.1	206.3	40.4
IOB	13.4% MC (~50% SDMC)	233.5	5.8	236.3	36.5
	15.9% MC (~60% SDMC)	243.5	6.1	220.9	38.0
	18.5% MC (~70% SDMC)	253.5	6.3	205.6	42.4
IOC	11.5% MC (~50% SDMC)	266.6	6.7	207.1	37.9
	14.8% MC (~65% SDMC)	276.6	6.9	198.6	38.5
	18.2% MC (~80% SDMC)	286.6	7.2	196.6	38.7

The general trend for the burden dimensions of each tested sample resulted in the decrease of the burden width and increase in burden height when the moisture content of the iron ore sample increased (shown in Table 6.2). This general trend could be attributed to the clumping nature of the sample when additional moisture is added (shown in Figure 6.8).

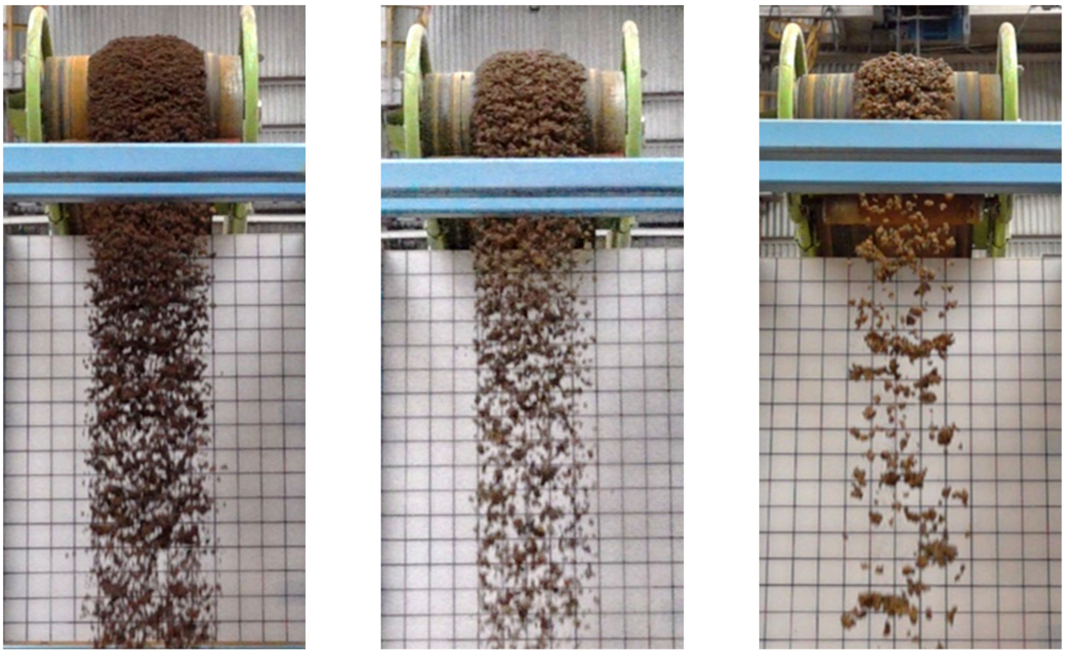

a) 13.4% MC *b) 15.9% MC* *c) 18.5% MC*

Figure 6.8 – IOB freefall trajectories (front view).

The burden profile dimensions, which are required as input parameters of the theoretical model developed in Section 4.3, were measured at the point of discharge where the iron ore samples leave the head pulley of the belt conveyor (shown in Figure 6.8). The conversion from a pixel count to the measurement values found in Table 6.2, was undertaken using the width of the conveyor belt as a reference guide. Additionally, the flow of the burden profile in freefall was analysed to determine if a continuous or discontinuous flow was experienced during the experimental measurements. This analysis has been completed for a front and side view for each of the tested iron ore samples. The results for IOB are shown in Figure 6.8 and Figure 6.9 for each of the respective views.

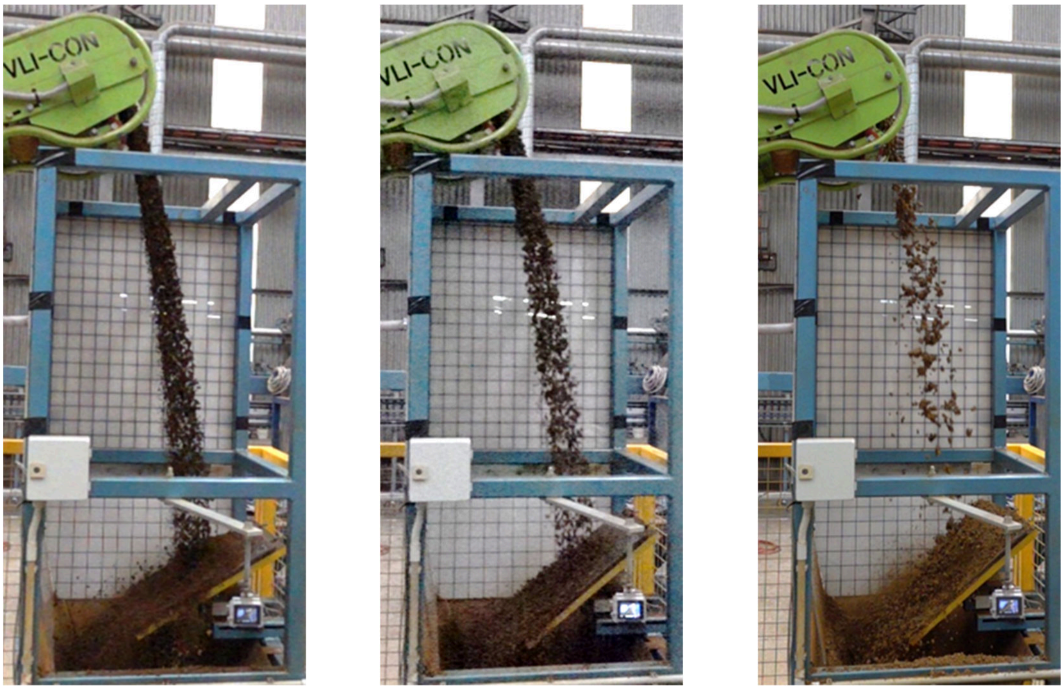

a) 13.4% MC *b) 15.9% MC* *c) 18.5% MC*

Figure 6.9 – IOB freefall trajectories (side view).

The clumping characteristics which were observed for IOB (shown in Figure 6.8 and Figure 6.9) were also observed for IOA and IOC when additional moisture was added to each of the respective samples. It is appropriate to identify that the observed clumping of the samples may not be experienced if the same bulk material was found at an equivalent moisture content without the need for additional moisture. The observed clumping nature of the iron ore samples is discussed further in the numerical modelling aspect of the research in Section 7.1.

6.2.3 EXPERIMENTAL TESTING PROCEDURE

The following section outlines the testing procedure used during the inclined plate recirculating system experiments. For each of the three supplied iron ore samples, testing was conducted at the as supplied moisture content and two additional moisture contents, which were determined from the characterisation testing in Section 2.4. The as supplied moisture content would be used as a baseline to assess for problematic behaviour where the addition of moisture would allow for the determination of the critical threshold moisture content for problematic (blockage) behaviours. The moisture contents used for the recirculating system experiments of each sample are found in Table 6.1.

The procedure used for the addition of the moisture required for Moisture Content 2 and Moisture Content 3 was undertaken by weighting one of the sub sampled bags (outlined in Figure 2.4) and placing into a mixing drum where the required amount of water was added until the desired moisture content was achieved. The material was then thoroughly mixed until a consistent sample resulted. The sample was then stored in a sealed bucket for approximately 24 hours to allow the sample to equilibrate and then used for the inclined plate recirculating system experimental measurements. The sample was remixed prior to loading onto the inclined plate recirculating system and a sample was taken from the conveyor belt for the analysis of the moisture prior to testing (shown in Figure 6.10).

Figure 6.10 – Method used for moisture content sampling.

Once the samples were prepared and ready for the experimental measurements to be conducted, the following procedure was followed:

1. Check belt conveyor velocities, ensuring that the velocity is set to 0.6 m/s;
2. Load iron ore sample onto conveyor belts (shown in Figure 6.7);
3. Conduct moisture content determination prior to testing (shown in Figure 6.10);
4. Set all impact plate angles to desired angle;
5. Start data logging for all load cells and recording video footage at each transfer station;
6. Start system and run for 90 seconds, allowing the system to reach steady state (or until build-up occurs);
7. Once the system has reached the end of a testing run, stop all belt conveyors and isolate the system;
8. Stop all video cameras and data logging for all load cells from recording (save the data);
9. Clean the impact plates and redistribute the material that has built-up;
10. Repeat steps 4 – 9 for all desired angles (maximum of four repeated runs per sample tested);
11. Conduct moisture content determination after testing (shown in Figure 6.10);
12. Once all testing is finalised, remove the sample from the belt conveyors and store in sealed drums;
13. Repeat steps 1 – 12 for each sample (moisture content) to be tested;

Upon completion of the experimental measurements using the procedure above, it is appropriate to analyse the relevant properties to be used to determine the threshold moisture contents where problematic behaviours are shown. Additionally, the experimental measurements are required for validation of the theoretical model developed in Section 4.3. The following section will give a summary of key and notable results from the inclined plate recirculating system experimental measurements for all three iron ore samples. Due to the significant amount of exposed surface area and high number of transfer points per test, it was deemed necessary to monitor the moisture content of each sample. A summary of the sample moisture contents prior to and upon completion of the experimental measurements are summarised in Table 6.3.

Table 6.3 – Recirculating System Moisture Content Measurements

Bulk Material Sample	*Initial Moisture Content*	*Final Moisture Content*
IOA	*6.5% MC*	*6.3% MC*
	9.5% MC	*9.3% MC*
	11.8% MC	*11.5% MC*
IOB	*13.8% MC*	*13.4% MC*
	16.3% MC	*15.9% MC*
	19.1% MC	*18.5% MC*
IOC	*11.9% MC*	*11.5% MC*
	15.2% MC	*14.8% MC*
	19.5% MC	*18.2% MC*

A reduction of approximately 0.2-0.3% MC for IOA, 0.4-0.6% MC for IOB and 0.4-1.3% MC for IOC was experienced during the experimental measurements on the recirculating system (shown in Table 6.3). It is important to note that the final moisture content measurements have been used for the analysis undertaken throughout the analysis of this research to neglect any potential issues which may arise from the loss of moisture during testing.

6.3 INCLINED PLATE EXPERIMENTAL MEASUREMENT ANALYSIS

Once the experimental measurements were completed, the analysis of the obtained data was undertaken. This data was utilised to determine the threshold moisture contents where problematic behaviours began to arise. Furthermore, the experimental measurement analysis is critical for validation of the theoretical model developed in Section 4.3. The following section will give a summary of results from the inclined plate recirculating system.

6.3.1 ESTIMATED BULK MATERIAL BUILD-UP PROFILE

To gain an understanding of the severity of the build-up found for each of the respective iron ore samples, the approximate build-up height, length and cross-sectional area were analysed. This was undertaken by taking a screenshot from the recorded video footage and using the image processing toolbox available in MATLAB version R2016a [132]. An example of the determination of these parameters can be found in Figure 6.11, where the original image and processed image are shown for IOB at 18.5% MC with a corresponding impingement angle of 55°.

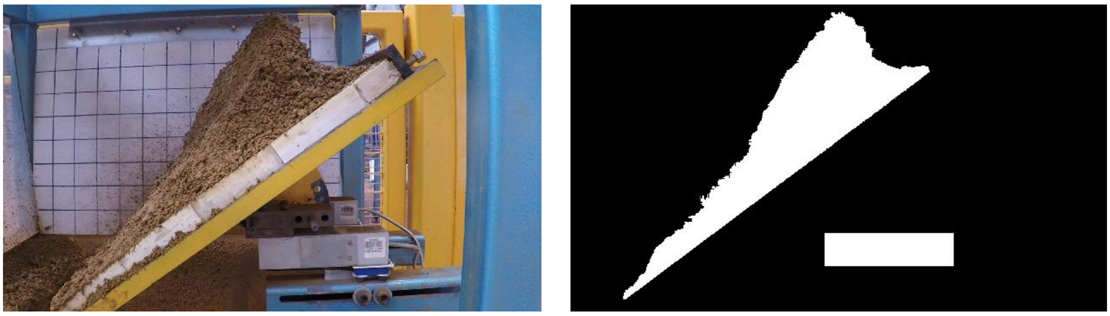

a) Original image *b) Processed image*

Figure 6.11 – Determination of build-up height and estimated cross-sectional area.

The approximate cross-sectional area was generally found to increase with increasing impingement angle and moisture content of the iron ore sample. A summary of the approximate cross-sectional area can be found in Table 6.4 for IOB at 18.5% MC, which will correspond to the worst-case iron ore sample tested.

Table 6.4 – IOB (18.5% MC) Approximate Cross-Sectional Area

Bulk Material Sample and Moisture Content	*Impingement Angle [Degrees]*	*Cross-sectional Area of Build-Up [mm^2]*		
		Ceramic Tiles	*Rough Welded Overlay*	*Cast White Iron*
IOB – 18.5% MC	*55*	24324.9	44044.6	40341.3
	50	19384.4	37848.6	31275.5
	45	15114.0	29026.6	32273.6
	40	16259.0	29950.2	27432.8
	35	N/A	19963.5	N/A*

** An accurate determination of the cross-sectional area was unable to be obtained as there was a lack of residual mass on the wall liner.*

Similar to the cross-sectional area, the build-up height was generally found to increase with increasing impingement angle and moisture content of the iron ore sample. A summary of the build-up height can be found in Table 6.5 for IOB at 18.5% MC. Figure 6.12 shows the measurement procedure used. To account for any parallax error which may be evident by using an optical camera to obtain measurements, it was deemed appropriate to also conduct physical measurements. In the case where errors were found to arise, the optical measurements were adjusted to correspond with the physical measurements.

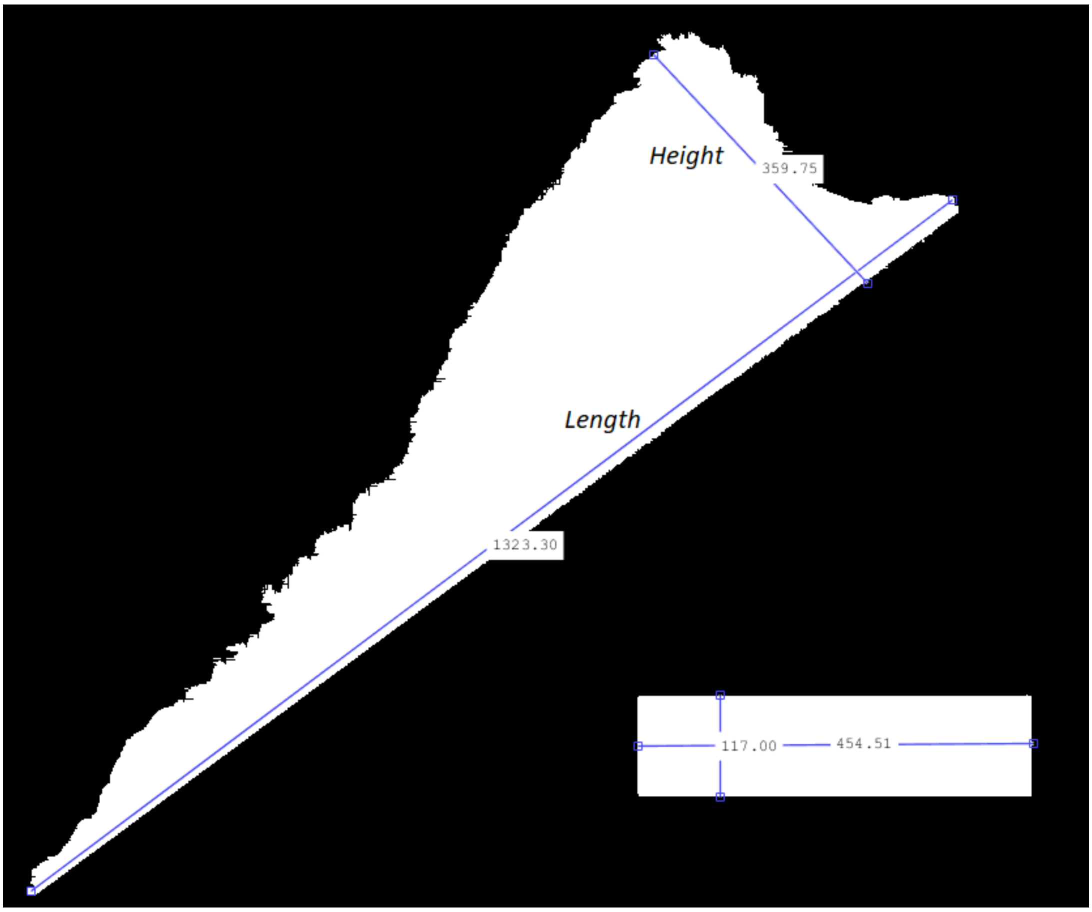

Figure 6.12 – Determination of build-up height and length.

Table 6.5 – IOB (18.5% MC) Maximum Build-Up Height

Bulk Material Sample and Moisture Content	*Impingement Angle [Degrees]*	*Build-Up Height [mm]*		
		Ceramic Tiles	*Rough Welded Overlay*	*Cast White Iron*
IOB – 18.5% MC	*55*	114.1	161.2	143.7
	50	86.4	131.2	114.3
	45	67.8	105.4	98.8
	40	66.5	99.1	96.7
	35	N/A	56.3	N/A*

** An accurate determination of the build-up dimensions was unable to be obtained.*

Similar to the cross-sectional area and the build-up height, the build-up length was generally found to increase with increasing impingement angle and moisture content of the iron ore sample. A summary of the build-up length can be found in Table 6.6 for IOB at 18.5% MC. Figure 6.12 shows the measurement procedure used.

Table 6.6 – IOB (18.5% MC) Maximum Build-Up Length

Bulk Material Sample and Moisture Content	*Impingement Angle [Degrees]*	*Build-Up Length [mm]*		
		Ceramic Tiles	*Rough Welded Overlay*	*Cast White Iron*
IOB – 18.5% MC	*55*	451.7	465.8	462.6
	50	432.4	463.0	387.5
	45	387.8	454.8	468.9
	40	388.7	439.0	431.2
	35	N/A	446.0	N/A*

** An accurate determination of the build-up dimensions was unable to be obtained.*

The calculation of the values for the cross-sectional area, build-up height and build-up length (shown in Table 6.4, Table 6.5 and Table 6.6 respectively) have been achieved by converting the pixel count to the measurement values, using a known reference. The reference used for the analysis was the side face of the load cell found in each of the analysed images. A summary of the worst-case bulk material (IOB at 18.5% MC) was included due to the significant build-up that was shown for higher impingement angles. This analysis has only been conducted for IOB at 18.5% MC due to the significant build-up which was experienced during these experimental measurements (outlined in Section 6.3.3).

6.3.2 TRANSIENT FORCE ANALYSIS

The correlation for the required time for build-up to occur and the overall mass of the build-up was achieved using a transient force analysis. The force was recorded via bending beam load cells attached to the wall liner holder as shown in Figure 6.3. The load cells were calibrated prior to commencing experimental measurements and upon completion of experimental measurements. This was undertaken to determine whether the reading of the load cells had drifted during the experimental measurements on the inclined plate recirculating system. A sample of the recorded transient force is shown in Figure 6.13. This particular series of force measurements is for IOB at 18.5% MC on ceramic tiles. As the wall liner angle increases (impingement angle decreases) it can be shown in Figure 6.13 that a reduction of the build-up of the iron ore sample results. The full range of transient force results have not been included in this thesis as it was deemed unnecessary due to the vast range of data which had been obtained. A summary of the residual masses has been included where these can be viewed in Section 6.3.3.

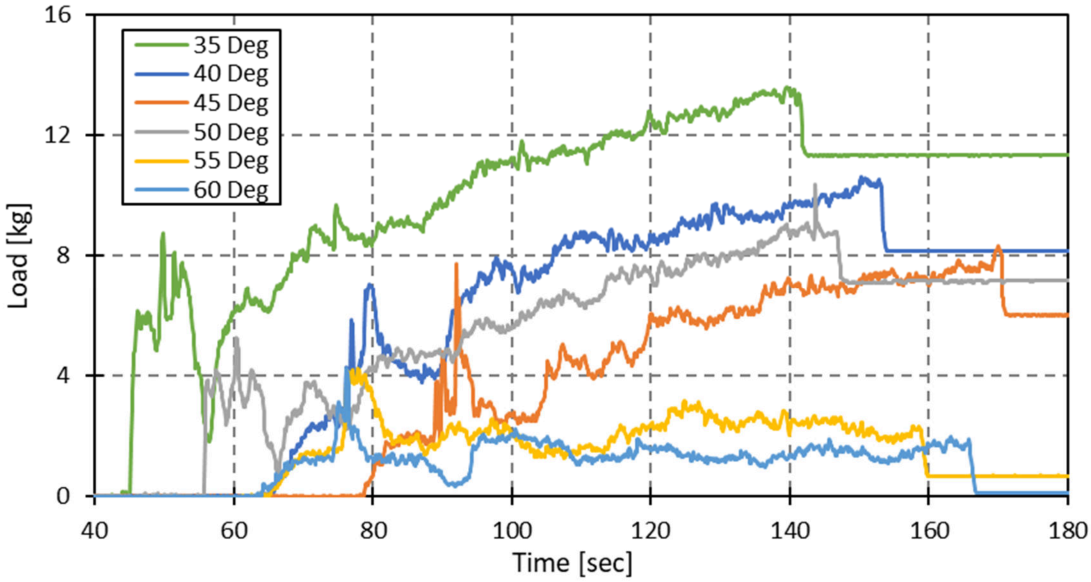

Figure 6.13 – Raw transient force measurements for IOB (18.5% MC) on ceramic tile for various wall liner angles.

The transient force analysis was utilised to give an insight into the time required for build-up to occur as well as the amount of residual mass that remained upon completion of the experimental measurement testing run. The residual mass can be shown in Figure 6.13 where the constant load value is shown to begin at 160 seconds for a wall liner angle of 55°. These residual mass values are used in the following section and for the dynamic adhesion ranking assessment in Section 6.4.2.

6.3.3 RESIDUAL MASS ON WALL LINING MATERIALS

The residual mass of each moisture content of the respective iron ore samples was recorded to give an insight into the amount of build-up present. This gave a relationship into the build-up experienced in relation to the moisture content for each of the wall lining materials which have been tested. A summary of the residual mass for each respective testing run for IOA is found in Table 6.7. Similar to the shape analysis of Section 6.3.1, it was generally found that the residual mass increased with increasing impingement angle and moisture content of the iron ore sample.

Table 6.7 – IOA Residual Mass on Wall Liners

Moisture Content	*Impingement Angle [Degrees]*	*Residual Mass on Wall Liners [kg]*		
		Ceramic Tiles	*Rough Welded Overlay*	*Cast White Iron*
6.3% MC	*60*	1.49	1.18	1.56
	55	0.17	0.34	0.67
	50	0.01	0.01	0.12
	45	N/A	N/A	0.01
9.3% MC	*55*	1.10	2.15	2.34
	50	0.43	0.61	0.68
	45	0.23	0.21	0.28
	40	0.14	0.08	0.09
11.5% MC	*55*	3.01	10.14	10.73
	50	3.13	14.92	11.87
	45	2.94	6.85	8.19
	40	1.81	6.59	8.56
	35	3.26	5.10	4.89
	30	1.17	1.31	6.94

A similar summary of the residual mass values for each respective testing run for IOB is found in Table 6.8. Similar to IOA and the shape analysis of Section 6.3.1, it was found that the residual mass increased with increasing impingement angle and moisture content of the iron ore sample. It will be appropriate to identify that the residual mass for IOB was observed to be greater in comparison to IOA for all tested moisture contents.

Table 6.8 – IOB Residual Mass on Wall Liners

Moisture Content	*Impingement Angle [Degrees]*	*Residual Mass on Wall Liners [kg]*		
		Ceramic Tiles	*Rough Welded Overlay*	*Cast White Iron*
13.4% MC	*60*	1.81	1.87	1.93
	55	0.67	1.11	1.04
	50	0.87	0.86	0.80
	45	0.77	0.64	0.61
	40	0.48	0.47	0.43
	35	0.30	0.26	0.25
15.9% MC	*55*	1.69	3.54	2.55
	50	0.42	0.79	0.67
	45	0.23	0.20	0.25
	40	0.12	0.01	0.06
18.5% MC	*55*	11.33	15.89	12.05
	50	8.15	11.68	7.68
	45	6.01	8.39	6.82
	40	7.17	8.11	6.47
	35	0.67	5.23	4.39
	30	0.12	0.45	0.79

A summary of the residual mass values for each respective testing run for IOC is found in Table 6.9. Similar to both IOA and IOB, the residual mass increased with increasing impingement angle. It is appropriate to identify that the residual mass for IOC at 18.2% MC was observed to have the consistency closer to a slurry rather than a WSM, which can explain the lower residual mass values when compared to IOA at 11.5% MC and IOB at 18.5% MC.

Table 6.9 – IOC Residual Mass on Wall Liners

Moisture Content	*Impingement Angle [Degrees]*	*Residual Mass on Wall Liners [kg]*		
		Ceramic Tiles	*Rough Welded Overlay*	*Cast White Iron*
11.5% MC	*60*	1.12	1.17	1.23
	55	0.24	0.47	0.48
	50	0.42	0.40	0.31
	45	0.17	0.27	0.18
	40	0.12	0.15	0.18
14.8% MC	*55*	2.46	3.34	2.89
	50	1.42	2.21	1.81
	45	0.19	0.77	0.74
	40	0.06	0.08	0.04
18.2% MC	*55*	3.64	3.99	4.21
	50	2.26	4.52	3.40
	45	3.30	3.87	4.33
	40	0.98	0.84	0.98
	35	1.24	0.78	1.11

The residual mass for each of the respective test runs of the three supplied iron ore samples increased when the impingement angle formed between the vertical freefall stream of the bulk material and the wall liner (as shown in Figure 6.1) increased. This was also observed when the moisture content of the iron ore samples was increased as shown in Table 6.7, Table 6.8 and Table 6.9 for each of the respective iron ore samples. By increasing the impingement angle and moisture content of the bulk material the thresholds for problematic behaviour have been identified. These residual mass values form the basis for the developed dynamic adhesion ranking assessment outlined in Section 6.4.2.

6.3.4 ROCK-BOX ANALYSIS

Rock-box transfer systems are used in industry for hard wearing ores, where the mode of flow is dependent on the internal friction of the bulk material. These systems typically handle WSMs, where blockages can occur and significant downtimes result. For completeness of this thesis, it is therefore essential to investigate how the supplied iron ore samples will perform when a rock-box transfer is considered. Additionally, by considering a rock-box transfer system, it is possible to examine the internal shear patterns under consolidation and rapid flow. Since the shear box (outlined in Section 7.5.1.1) only examines shear patterns under loose-poured conditions, a rock-box transfer offers an alternative way to investigate how well shear box results will either scale up or accurately predict the flow which can be experienced in an industrial rock-box transfer system.

As explained in Section 6.2.1, a rock-box was constructed and fixed to a bending beam load cell to give an indication of the build-up experienced for each of the iron ore samples. This would also act as a quality control measure, where the amount of build-up should remain constant within a specified tolerance. It would be expected that this will be the case when the same moisture content of a bulk material sample is tested. A tolerance threshold of ±5% was used where differences outside these specified values would result in the experimental measurement to be repeated. In addition to the analysis above, the shearing angles for both static and dynamic conditions and the density profile of the iron ore build-up are also analysed. This analysis will be undertaken in the subsequent sections.

6.3.4.1 SHEAR ANGLE DETERMINATION

The shear angle for a rock-box transfer system is defined as the angle at which the build-up of the bulk material reaches a critical volume. At this critical volume, the static shear angle (γ_s) occurs when a surficial ore surface is formed with no additional bulk material falling onto this surface. This was observed to occur at the conclusion of the experimental measurements, when the bulk material being conveyed around the experimental testing apparatus had ceased. In the case where a blockage is present, the formation of a surficial ore surface will not occur. The dynamic shear angle (γ_d) occurs when the bulk material impacts the surficial ore surface of the rock-box and does not adhere. This will result in the excess bulk material that has not adhered to the ore surface flowing out of the rock-box transfer. The dynamic shear angle (γ_d) will typically be lower than the static shear angle, γ_s. A simplified schematic of the determination of both static and dynamic shear angles experienced for a rock-box transfer system is shown in Figure 6.14.

For the designed rock-box used in the experimental measurements, the width of the static zone, w_s, has been fixed to be 150 mm. This results in the corresponding height (h_s) to be dependent on the flow properties of the bulk material. Furthermore, the width of the dynamic zone (w_d) is governed by the dynamic shear angle, γ_d. This will be found to be the case when the height (h_s) is assumed to be constant for both a static and dynamic case. It will be appropriate to identify that a fixed height will occur once an experimental measurement has reached steady state. This steady state value can be best explained if the density of the bulk material is considered. If a density profile is taken from the static zone, an increase from the base of the rock-box up until the surficial ore surface will be observed. This analysis is detailed in the following section.

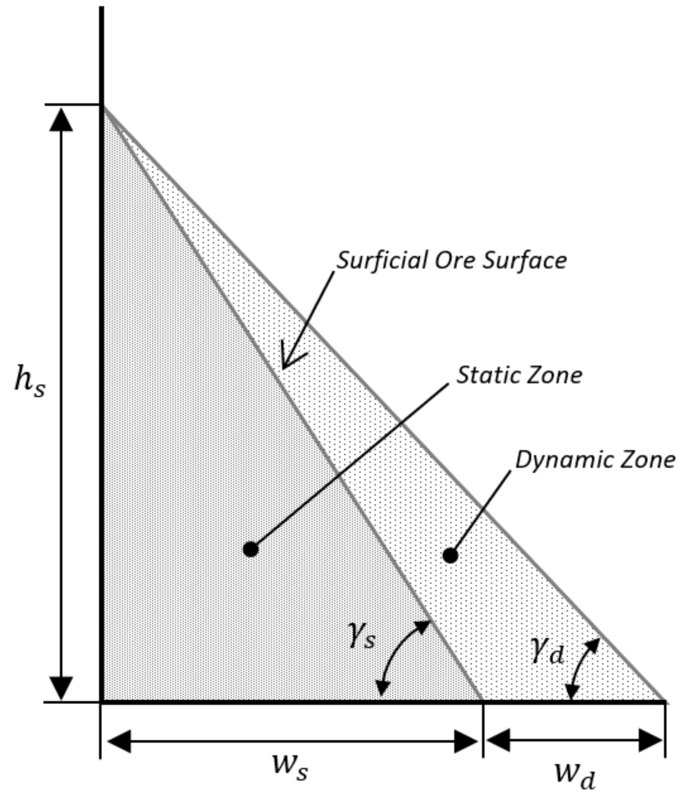

Figure 6.14 – Simplified schematic of rock-box transfer system for static and dynamic conditions.

The determination of the shear angles is undertaken using screenshots from the recorded video footage during the experimental measurements within the rock-box transfer system. This was undertaken for both a dynamic (bulk material flowing over surficial surface) and for a static case (no flow of the bulk material evident). The rock-box shear angles have been measured for each individual experimental measurement run, where an average value has been used for each moisture content. An example of a processed image for a static shear angle and dynamic shear angle are shown for IOB at 15.9% MC in Figure 6.15 . It will be appropriate to identify that in the case where a defined surficial surface is not present, this bulk material will be deemed to have created a blockage in the system.

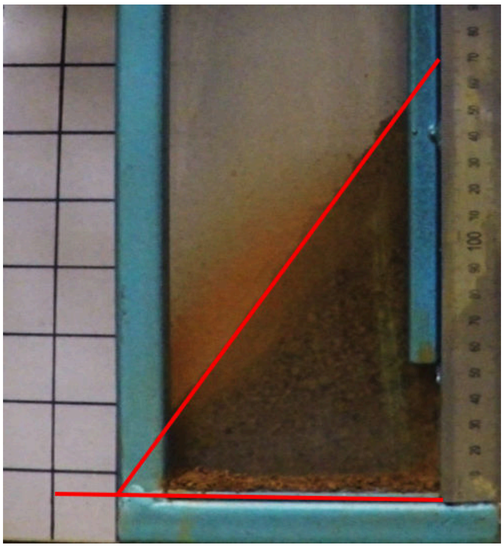

a) Static case

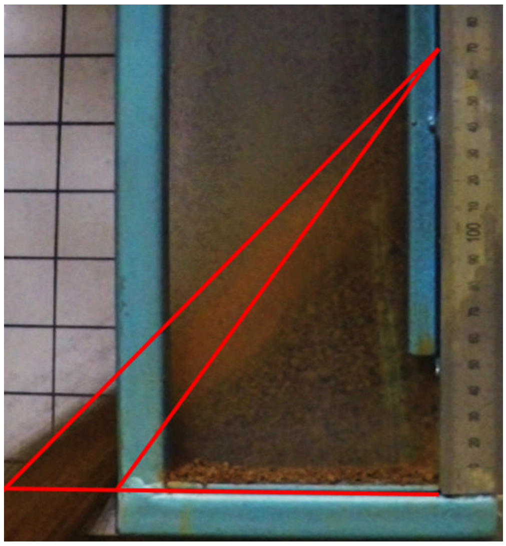

b) Dynamic case

Figure 6.15 – Determination of shear angles for rock-box transfer system.

The summaries of the residual mass measurements and measured shear angles for both static and dynamic conditions, are outlined in Table 6.10 and Table 6.11 respectively. This has been undertaken for each of the tested iron ore samples. Similar to the shape analysis (outlined in Section 6.3.1) and residual mass analysis (outlined in Section 6.3.3) for the wall liner experimental measurements, it was observed that the residual mass of the rock-box increased, with increasing moisture content of the iron ore sample.

Table 6.10 – Rock-Box Residual Mass for Iron Ore Samples

Bulk Material Sample	*Moisture Content*	*Residual Mass [kg]*
IOA	*6.3% MC*	*3.5*
	9.3% MC	*4.0*
	11.5% MC	*10.2*
IOB	*13.4% MC*	*3.6*
	15.9% MC	*4.1*
	18.5% MC	*10.5*
IOC	*11.5% MC*	*3.3*
	14.8% MC	*5.3*
	18.2% MC	*9.0*

Additionally, a similar relationship was observed for the static shear angle (γ_s) where the approximate dynamic shear angle (γ_d) was observed to reduce by approximately 9° from the static equivalent (as shown in Table 6.11). It will be appropriate to identify that a defined shear plane was unable to be measured for IOA at 11.5% MC, as shown in Figure 6.16. This can be attributed to the lack of compressibility shown for IOA (as outlined in the bulk density measurements in Figure 2.8). Additionally, the adhesion of the sample to the Perspex side walls was also a contributing factor in a defined shear plane not being observed. It is also important to note when Figure 6.16 is considered, it can be observed that a distinct shear angle is present in the central section of the remaining material in the rock-box. However, as this was not defined across the entire face of the remaining material in the rock-box, a non-defined shear angle has been considered for the analysis in this research.

Table 6.11 – Rock-Box Shear Angles for Iron Ore Samples

Bulk Material Sample	*Moisture Content*	*Shear Angle [Degrees]*	
		Static	*Dynamic*
IOA	*6.3% MC*	50.9	41.1
	9.3% MC	52.6	43.5
	11.5% MC	N/A	N/A
IOB	*13.4% MC*	48.9	39.4
	15.9% MC	54.2	44.8
	18.5% MC	63.5	63.1
IOC	*11.5% MC*	48.1	37.9
	14.8% MC	49.6	39.3
	18.2% MC	57.4	46.6

To consider the compressibility of the iron ore samples within the rock-box transfer station, a density analysis has been undertaken. This analysis will give some insight into the potential causes for a bulk material blockage to occur within a rock-box transfer. Highly compressible bulk materials exhibit the tendency for blockages to occur due to the increased inherit strength, which results from the high levels of compaction. An analysis of the density profile within the rock-box transfer for each of the supplied iron ore samples, is undertaken in the subsequent section.

Figure 6.16 – Rock-box build-up for IOA (11.5% MC) showing a non-defined shear plane.

6.3.4.2 DENSITY PROFILE TESTING

During the inclined plate recirculating system experimental measurements, it was observed that the bulk density of the iron ore samples within the static zone of the rock-box altered with depth from the surficial surface. Additionally, it was observed that a dense compacted top surface formed above a less dense loose poured central section. Another dense compacted bottom layer of material was also observed which formed beneath the less dense middle section. Due to these observations, it was determined that additional experimental measurements were required to include an assessment of this unforeseen phenomena.

A piece of equipment was therefore developed that allowed for the removal of a cylindrical section of the bulk material build-up within the rock-box transfer. The method used for the sample analysis would use a similar concept to what is used by metallurgists during the exploration phases of a mine. The developed piece of equipment, referred to as the drill core density sampler, would be used to break a cylindrical cross section of the rock-box build-up into segments with a consistent volume. The sampler has an inner diameter of 47 mm and is 300 mm long. By taking the mass of these segments the density can be calculated. This allows for the development of a density profile throughout the build-up of the bulk material sample within the rock-box.

To remove a cylindrical section of the rock-box build-up, the drill core density sampler, as shown in Figure 6.17, was developed. The sampler is designed using a section of stainless pipe which could be pushed into the sample within the rock-box. To aid in removing the captured sample from the cylindrical sampler, the section of stainless pipe was halved, with each half welded to one side of a piano hinge. The hinge runs along majority of the length of the pipe and allows for the cylindrical section to be opened and shut. To allow the sampler to be inserted into the tested iron ore sample, the leading edge at one end of the stainless pipe was sharpened to aid in breaking through the bulk material build-up without disturbing the sample. It is appropriate to identify that slight disturbances on the outer edges of the sample are unavoidable, however, care is taken to minimise these disturbances.

a) Opened *b) Closed*

Figure 6.17 – Drill core density sampler for use in rock-box transfer system.

Once the inclined plate recirculating measurements had been conducted, the assessment of the density profile of each iron ore sample was undertaken using the following procedure:

1. Press the sharpened end of the drill core density sampler into the centre of the bulk material build-up within the rock-box;
2. Carefully remove the sampler by removing the bulk material surrounding the sampler and then dragging the sampler off the rock-box onto a flat plate (shown in Figure 6.18);
3. Lay the sampler flat and open. Measure 10 mm sections of the bulk material build-up starting from the bottom surface and carefully slide the measured material section into a tray and record the mass;
4. Repeat step 3 until the 10 mm material sections exhaust the total sample depth;

Figure 6.18 – Rock-box build-up for IOB (18.5% MC) showing removed drill core sample.

The drill core density samples were conducted for each moisture content of the supplied iron ore samples. Figure 6.19 shows the density distribution within the rock-box transfer for IOA at each of the respective moisture contents tested. The observed general trend of the density profile shows a denser bottom and top section which can be attributed to the impact of the material onto the bottom ledge of the rock-box and the impact of the bulk material on itself for the top layer. This impact leads to the compressibility of the material where a greater bulk density results in comparison to the central section of the sample.

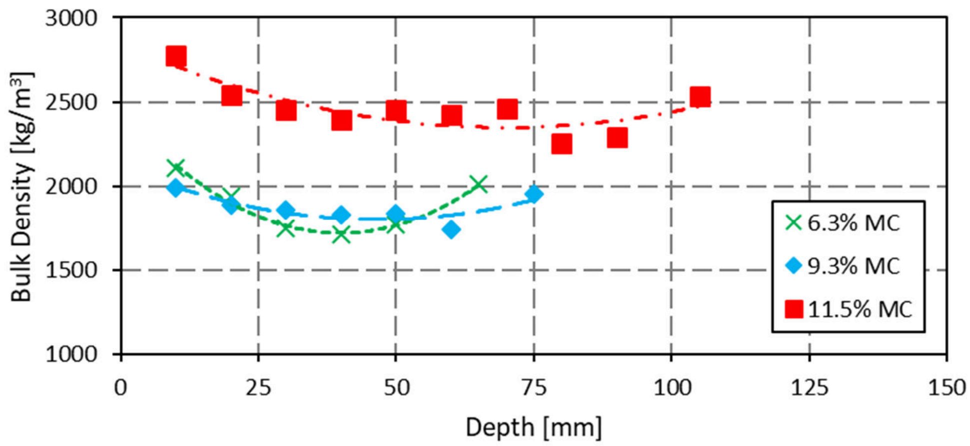

Figure 6.19 – Drill core density profile for IOA at different moisture contents.

Figure 6.20 shows the density distribution within the rock-box transfer for IOB at each of the respective moisture contents tested. It is appropriate to identify that a sample for IOB at 13.4% MC was unable to be obtained as the sample crumbled during the analysis. This could be attributed to the lower moisture content where insufficient adhesion and cohesion properties were unable to hold the sample together. Similar to the observed general trend for IOA, the density profile shows a denser bottom and top section which can be attributed to the impact of the bulk material. The curvature for IOB at 15.9% MC (as shown in Figure 6.20) can be attributed to the friable clays present which typically lead to higher compressibility. The flatter curve IOB at 18.5% MC (as shown in Figure 6.20) however, can be attributed to the relative saturation of the sample where the peak strength of the bulk material has been reached. This would result in a similar bulk density for the range of normal pressures which are found for the impacts tested in the rock-box transfer.

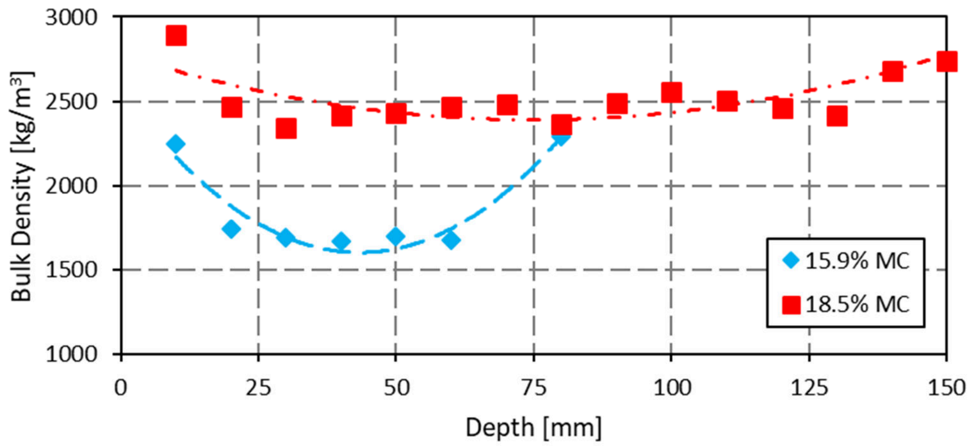

Figure 6.20 – Drill core density profile for IOB at different moisture contents.

Figure 6.21 shows the density distribution within the rock-box transfer for IOC at each of the respective moisture contents tested. Similar to the observed general trends for IOA and IOB, the density profile shows a denser bottom and top section which can be attributed to the impact of the bulk material. The curvature for all tested moisture contents of IOC (as shown in Figure 6.21) can be attributed to the friable clays present which typically lead to higher compressibility.

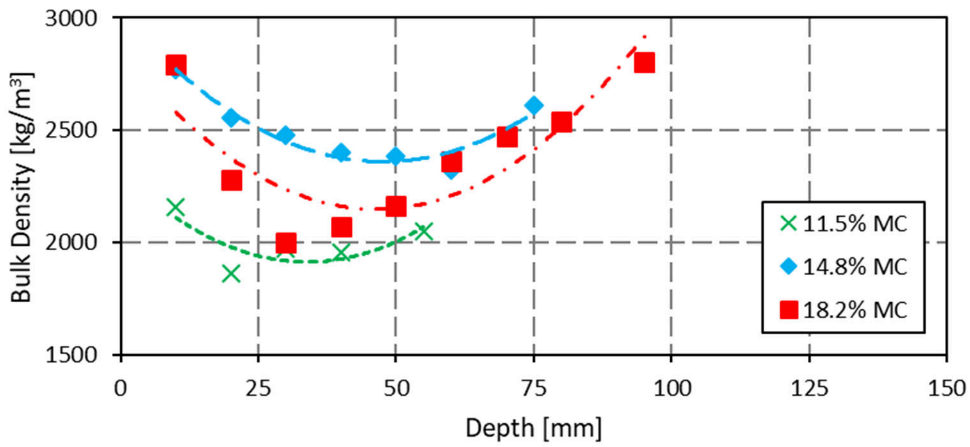

Figure 6.21 – Drill core density profile for IOC at different moisture contents.

The much larger variability of the curve for IOC at 18.2% MC (as shown in Figure 6.21) can be attributed to the relative saturation of the sample where the peak strength of the bulk material has been exceeded and the moisture migration of the sample has commenced. It is appropriate to identify that IOC at 18.2% MC had a consistency closer to a slurry rather than a WSM leading to some slight moisture migration to be observed. It is important to note when higher moisture content results are considered, the bulk density measurements in Figure 6.19

to Figure 6.21 tend to be higher than the measurements of the large bulk density tester, shown in Figure 2.8 to Figure 2.10 for each respective iron ore sample. This can be attributed to the volume of the sample in the drill core density sampler and possible errors which could arise whilst using the sampler and cutting the slices during the measurement procedure.

6.4 DYNAMIC TRANSFER SYSTEM OPTIMISATION

When WSMs negotiate the materials handling stream, significant downtimes can be caused which are attributed to events such as blockages of bins, hoppers and transfer chutes, remains left in train wagons and dump trucks as well as conveyor belt carry back [1, 2]. The properties of WSMs are due to the excessive inherent moisture found within the bulk material as they are typically mined from beneath the water-table [9]. Another source of excessive moisture can be caused by heavy rainfall and tropical storms which can lead to a reasonably free flowing ore to turn problematic relatively quickly leading to handling problems. In addition, downtimes can also be caused from belt runoff events where mistracking of the conveyor belt can cause costly damage to the materials handling operation whether it's from damage to the structure and idler rolls or the conveyor belt itself. These types of events are commonly caused from overloaded belts where a prior blockage has dislodged and fallen onto the conveyor. The cost that WSMs can add to the price of bulk materials due to sub-optimal running conditions outlined above is attributed to system downtime where some cases have reported downtimes of approximately 7-30 hours per week [3]. It is therefore essential to set protocols in place which optimise mining operations to reduce the downtimes caused by WSMs.

The following section explains the area's most susceptible to dynamic adhesion blockages in the materials handling sector. To identify the threshold moisture contents where blockage problems may become evident for the supplied iron ore samples, a dynamic adhesion classification is proposed. Additionally, the critical release angle where an effective build-up height equates to zero is identified for transfer chute systems. Finally, a design protocol for the reduction of dynamic adhesion is also proposed.

6.4.1 MATERIALS HANDLING SYSTEMS SUSCEPTIBLE TO DYNAMIC ADHESION

The adhesion and cohesion of problematic bulk materials is commonly caused by either the excessive moisture or increasing clay content which is found from mining ore bodies below the water-table. These types of bulk materials are problematic due to the nature of their physical properties (as explained in Chapter Two) and the mechanisms that are present when they negotiate the materials handling stream. WSMs are problematic within all facets of the materials handling stream from exploration through to exportation (ship loading). Figure 6.22 shows a flow chart for a typical mining operation which includes all stages from exploration to exporting (ship loading). From a materials handling perspective, the areas where handling issues become most prevalent start at the load and haul stages of the operation through to ship loading (as shown in Figure 6.22). It is appropriate to identify that emphasis for this research is on transfer systems that typically exhibit rapid induced bulk material blockages which are commonly experienced in the process stream (as shown in Figure 6.22).

Although an emphasis has been placed onto the processing sector due to majority of downtimes originating at this point, rapid induced bulk material blockages are seen within all sectors of the materials handling stream. For completeness, it should be noted that materials handling problems closer to the port lead to a much larger *"bottle-neck"* as they handle a considerably larger range of bulk materials with significantly different physical properties. This is also attributed to iron ore products containing more fines and throughputs are generally greater. Common problems experienced is the blockage of transfer chutes which result in hours of lost tonnage (and as a result, revenue) through the port system. As the supplied iron ore samples are directly from the pit of the mine, it is more appropriate to consider the process stream rather than the port where more handling issues typically occur for the supplied iron ore samples.

Figure 6.22 – Mining industry flow chart showing typical process stream from exploration through to export (Rio Tinto, 2013).

When the processing sector (as shown in Figure 6.22) is considered, several areas where materials handling issues arise can be identified. Figure 6.23 shows a flow chart for a typical bulk materials handling processing stream.

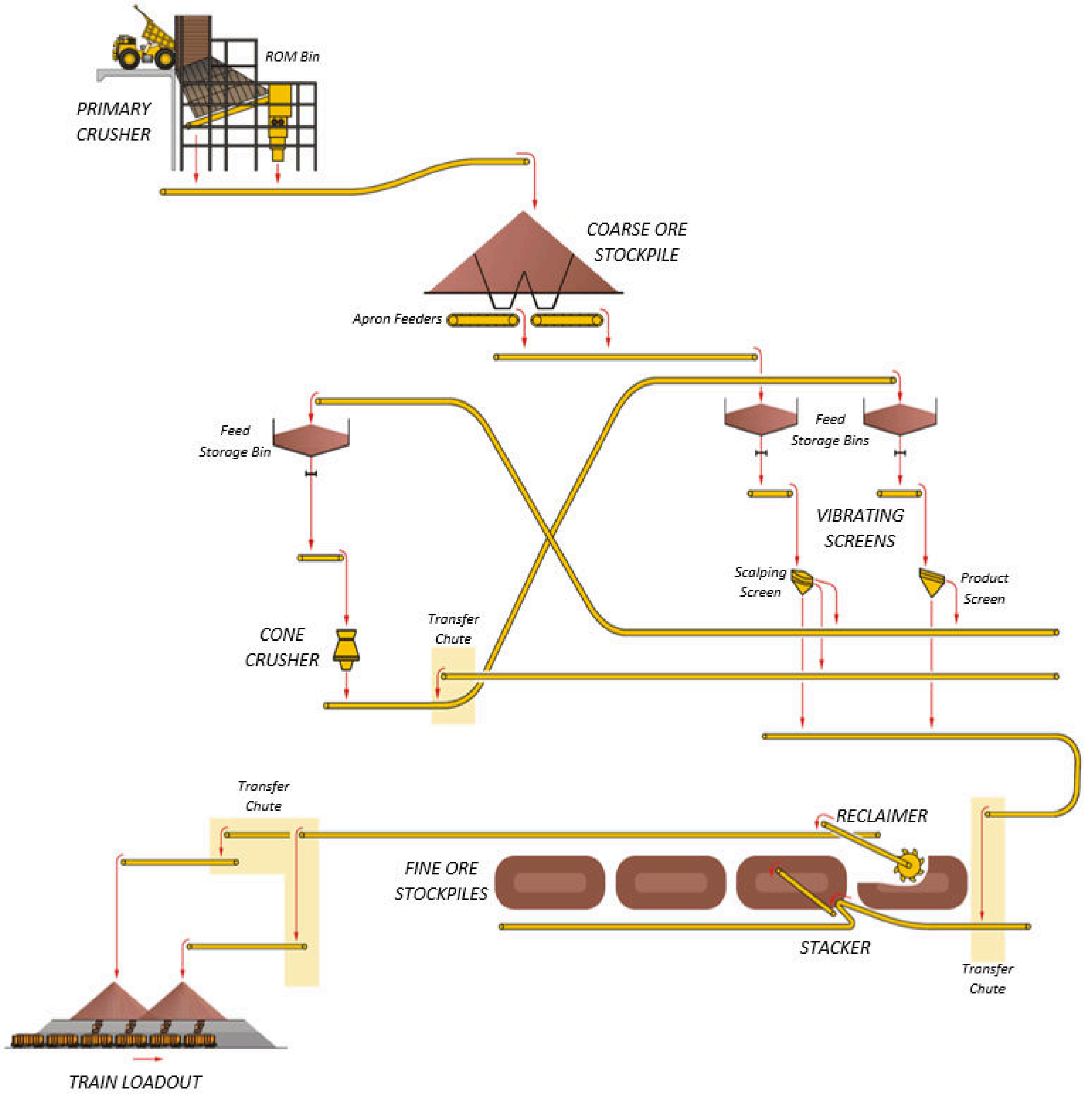

Figure 6.23 – Process flow chart for typical bulk materials handling stream (modified from BHP, 2018).

The usual areas most prevalent to blockages and other related materials handling issues include transfer chutes, vibrating screens, storage bins and hoppers, stackers and reclaimers and train load out systems. Each of the identified components of the materials handling processing stream commonly experience downtimes due to blockages attributed to the adhesive and cohesive properties of problematic bulk materials. As the bulk material is *"processed"* finer products result which have a higher propensity to cause materials handling problems. This is attributed to the higher percentage of friable clay ridden fines which typically exhibit much more problematic properties (higher moisture retention) in comparison to *"hard"* lump products. To reduce the propensity for materials handling issues in the processing stream it is appropriate to identify the threshold moisture content where these behaviours begin. The following section proposes a dynamic adhesion classification to rank each iron ore sample in relation to the moisture content and the potential handling issues onsite.

6.4.2 CLASSIFICATION AND RANKING OF DYNAMIC ADHESION

The severity of build-up from the recirculating system experiments (outlined in Section 6.3) have been given a dynamic adhesion ranking. This has been conducted on the three iron ore samples where four classifications are used. The classifications include:

1. No Build-up: no bulk material build-up was shown;
2. Partial Build-up: partial bulk material build-up resulted;
3. Moderate Build-up: moderate bulk material build-up resulted;
4. Severe Build-up: severe bulk material build-up experienced;

The visual representation of each classification is shown in Figure 6.24. These classifications are based upon the visual inspection of the screenshots from the recorded video footage used in Section 6.3.1 in conjunction with the residual mass analysis outlined in Section 6.3.3.

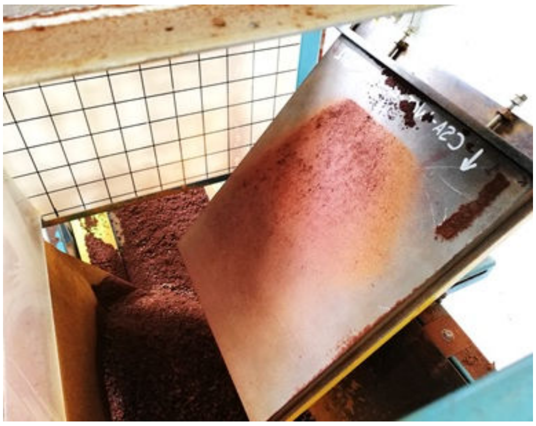

a) No build-up

b) Partial build-up

c) Moderate build-up

d) Severe build-up

Figure 6.24 – Dynamic adhesion ranking assessment classifications.

The dynamic adhesion ranking assessment is determined from the residual mass when the maximum build-up experienced (15.89 kg for IOB at 18.5% MC with a corresponding impingement angle of 55^{o}) is considered to be the limiting threshold. This method gives a percentage of build-up in relation to the defined limiting threshold. Using the classifications shown in Figure 6.24, the percentage threshold values for each classification are given as:

1. No Build-up: 0% – 1%
2. Partial Build-up: 1% – 6%
3. Moderate Build-up: 6% – 60%
4. Severe Build-up: 60% – 100%

A summary of the dynamic adhesion ranking assessment can be found in Table 6.12 for IOA at each of the respective tested moisture contents. Similar to the shape analysis of Section 6.3.1, it was found that the dynamic adhesion ranking reduced with decreasing impingement angle. Additionally, the dynamic adhesion ranking increased with increasing moisture content of the iron ore sample. It is appropriate to identify that for IOA at 11.5% MC for an impingement angle of 30° the dynamic adhesion ranking assessment overestimates the visual build-up which has been observed. This can be attributed to a thin layer of material which covered the top and sides of the wall liner where no noticeable clumps were observed.

Table 6.12 – IOA Dynamic Adhesion Ranking Assessment

Moisture Content	*Impingement Angle [Degrees]*	*Dynamic Adhesion Ranking [%]*		
		Ceramic Tiles	*Rough Welded Overlay*	*Cast White Iron*
6.3% MC	*60*	9.4	7.4	9.8
	55	1.1	2.1	4.2
	50	0.1	0.1	0.8
	45	*N/A*	*N/A*	0.1
9.3% MC	*55*	6.9	13.5	14.7
	50	2.7	3.8	4.3
	45	1.4	1.3	1.7
	40	0.9	0.5	0.6
11.5% MC	*55*	18.9	63.8	67.5
	50	19.7	93.9	74.7
	45	18.5	43.1	51.5
	40	11.4	41.5	53.9
	35	20.5	32.1	30.7
	30	7.3*	8.2*	43.7

** No noticeable clumps were observed, however, a thin layer that covered the top and sides of the wall liner was present.*

A summary of the dynamic adhesion ranking assessment can be found in Table 6.13 for IOB at each of the respective tested moisture contents. Similar to the shape analysis of Section 6.3.1 and the dynamic adhesion ranking assessment for IOB, it was found that the dynamic adhesion ranking reduced with decreasing impingement angle. Additionally, the dynamic adhesion ranking increased with increasing moisture content of the iron ore sample. It will be appropriate to identify that the dynamic adhesion ranking assessment has been undertaken using a combination of the residual mass analysis (as shown in Section 6.3.3) and using images for a visual assessment.

Table 6.13 – IOB Dynamic Adhesion Ranking Assessment

Moisture Content	*Impingement Angle [Degrees]*	*Dynamic Adhesion Ranking [%]*		
		Ceramic Tiles	*Rough Welded Overlay*	*Cast White Iron*
13.4% MC	*60*	11.4	11.8	12.1
	55	4.2	7.0	6.5
	50	5.5	5.4	5.0
	45	4.8	4.0	3.8
	40	3.0	3.0	2.7
	35	1.9*	1.6*	1.6*
15.9% MC	*55*	10.6	22.3	16.0
	50	2.6	5.0	4.2
	45	1.4	1.3	1.6
	40	0.8	0.1	0.4
18.5% MC	*55*	71.3	100.0	75.8
	50	51.3	73.5	48.3
	45	37.8	52.8	42.9
	40	45.1	51.0	40.7
	35	4.2	32.9	27.6
	30	0.8	2.8	5.0

** No noticeable clumps were observed, however, a very dense hard thin layer remained on the wall liner.*

A summary of the dynamic adhesion ranking assessment can be found in Table 6.14 for IOC at each of the respective tested moisture contents. Similar to the shape analysis of Section 6.3.1 and the dynamic adhesion ranking assessment for IOA and IOB, it was found that the dynamic adhesion ranking reduced with decreasing impingement angle. Additionally, the dynamic adhesion ranking increased with increasing moisture content of the iron ore sample. It is appropriate to identify that for IOC at 18.2% MC for an impingement angle of 40° and 35° the dynamic adhesion ranking assessment overestimates the visual build-up which has been observed. This can be attributed to a thin layer of material which covered the top and sides of the wall liner where no noticeable clumps were observed (outlined in Figure 6.25). Furthermore, IOC at 18.2% MC had a consistency closer to a slurry rather than a WSM.

Figure 6.25 – IOC at 18.2% MC showing no noticeable clumps.

Table 6.14 – IOC Dynamic Adhesion Ranking Assessment

Moisture Content	*Impingement Angle [Degrees]*	*Dynamic Adhesion Ranking [%]*		
		Ceramic Tiles	*Rough Welded Overlay*	*Cast White Iron*
11.5% MC	*60*	7.0	7.4	7.7
	55	1.5	3.0	3.0
	50	2.6	2.5	2.0
	45	1.1	1.7	1.1
	40	0.8	0.9	1.1
14.8% MC	*55*	15.5	21.0	26.5
	50	8.9	13.9	11.4
	45	1.2	4.8	4.7
	40	0.4	0.5	0.3
18.2% MC	*55*	22.9	25.1	26.5
	50	14.2	28.4	21.4
	45	20.8	24.4	27.2
	40	6.2*	5.3*	6.2*
	35	7.8*	4.9*	7.0*

** No noticeable clumps were observed, however, a thin layer that covered the top and sides of the wall liner was present. Additionally, IOC at 18.2% MC had a consistency closer to a slurry rather than a WSM.*

Once each of the tested samples has been given a ranking using the dynamic adhesion ranking assessment, it is appropriate to identify the critical release angle where zero bond depth of the bulk material results. This allows for the identification of the geometrical constraints where the propensity for materials handling issues in the processing stream can be reduced. The following section identifies the critical release angle for each of the tested samples in relation to the three wall liners which have been considered. Additionally, these threshold values can be utilised with the proposed design protocol (shown in Section 6.4.4) to reduce the dynamic adhesion and potential handling issues which are experienced onsite.

6.4.3 CRITICAL RELEASE ANGLE DETERMINATION

The critical release angle is essential to determine the thresholds where an effective zero bond depth of the bulk material is experienced. This will determine the parameters required for the effective design of an industrial system to reduce the downtime of the operation. This analysis is conducted for each of the tested samples in relation to the three wall liners which have been considered. A summary of the critical release angle can be found in Table 6.15 for each of the respective tested moisture contents for each of the supplied iron ore samples. Additionally, a comparison between each of the three wall lining materials is also outlined in Table 6.15.

Table 6.15 – Critical Release Angle for Iron Ore Samples

Bulk Material Sample	*Moisture Content*	*Critical Release Angle [Degrees]*		
		Ceramic Tiles	*Rough Welded Overlay*	*Cast White Iron*
IOA	*6.3% MC*	40	40	40
	9.3% MC	50	50	50
	11.5% MC	60	65	65-70
IOB	*13.4% MC*	50	50	50
	15.9% MC	50	50	50
	18.5% MC	60	65	65
IOC	*11.5% MC*	45	45	45
	14.8% MC	50	50	50
	18.2% MC	55*	55*	55*

** No noticeable clumps were observed, however, a thin layer that covered the top and sides of the wall liner was present. Additionally, IOC at 18.2% MC had a consistency closer to a slurry rather than a WSM.*

Similar to the shape analysis of Section 6.3.1, it was found that the critical release angle increased with increasing moisture content of the tested samples. It is appropriate to identify that the critical release angle has the same orientation as the wall liner angle (as outlined in Figure 6.1). When each of the tested wall liners are analysed, the ceramic tiles in some instances were less susceptible to build-up. The general trend, however, resulted in no real discernible difference observed between each of the wall lining materials where the bulk material is significantly more dominating to the critical release angle. The prediction of the critical release angle (an effective zero bond depth) for the tested samples is undertaken in Section 4.3.1.

6.4.4 DESIGN PROTOCOL FOR REDUCTION OF DYNAMIC ADHESION

To reduce the potential downtime of industrial materials handling systems, protocols must be set in place. A design protocol, as outlined in Figure 6.26, has been proposed which outlines a strategy aiming to reduce the downtime caused by WSMs. The protocol is centralised around the dynamic adhesion ranking assessment (outlined in Section 6.4.2) where three key categories can be identified. The categories, or modes of flow, include non-problematic (free flowing), moderately problematic and severely problematic. The recommended actions for non-problematic bulk materials is to continue ore processing. Moderately problematic materials can either turn severely problematic with the addition of moisture or could turn non-problematic by blending with a free flowing ore. For these bulk materials, it is recommended that caution be used where blockages may result. For severely problematic bulk materials, these are typically the main cause of rapid induced blockages within transfer systems where strategies must be set in place to prevent the downtime of the system.

Three strategic streams are proposed to prevent blockages caused by problematic bulk materials and include changing the geometry to improve flow (modular transfer chutes), blend with a non-problematic ore (improve handleability) or to divert off the system (reduce moisture). Once any of the strategic streams are used, the dynamic adhesion ranking assessment needs to be undertaken again to identify if the bulk material now falls into the non-problematic category. This process can be time consuming, where in its current state the dynamic adhesion ranking assessment relies on lab scale experiments (outlined in Section 6.2).

To reduce the need for lab scale experiments the use of Discrete Element Method (DEM) simulations (as explained in Chapter Seven) can be used as a predictive tool when any of the strategic methods above are used. It is appropriated to identify that the need for DEM calibration experiments are also required, however, these are much simpler and quicker to complete. In most instances the DEM calibration experiments could be completed onsite where an assessment is undertaken, and simulations conducted to predict whether changes in either ore properties or geometry are sufficient in reduce the propensity of problematic behaviours.

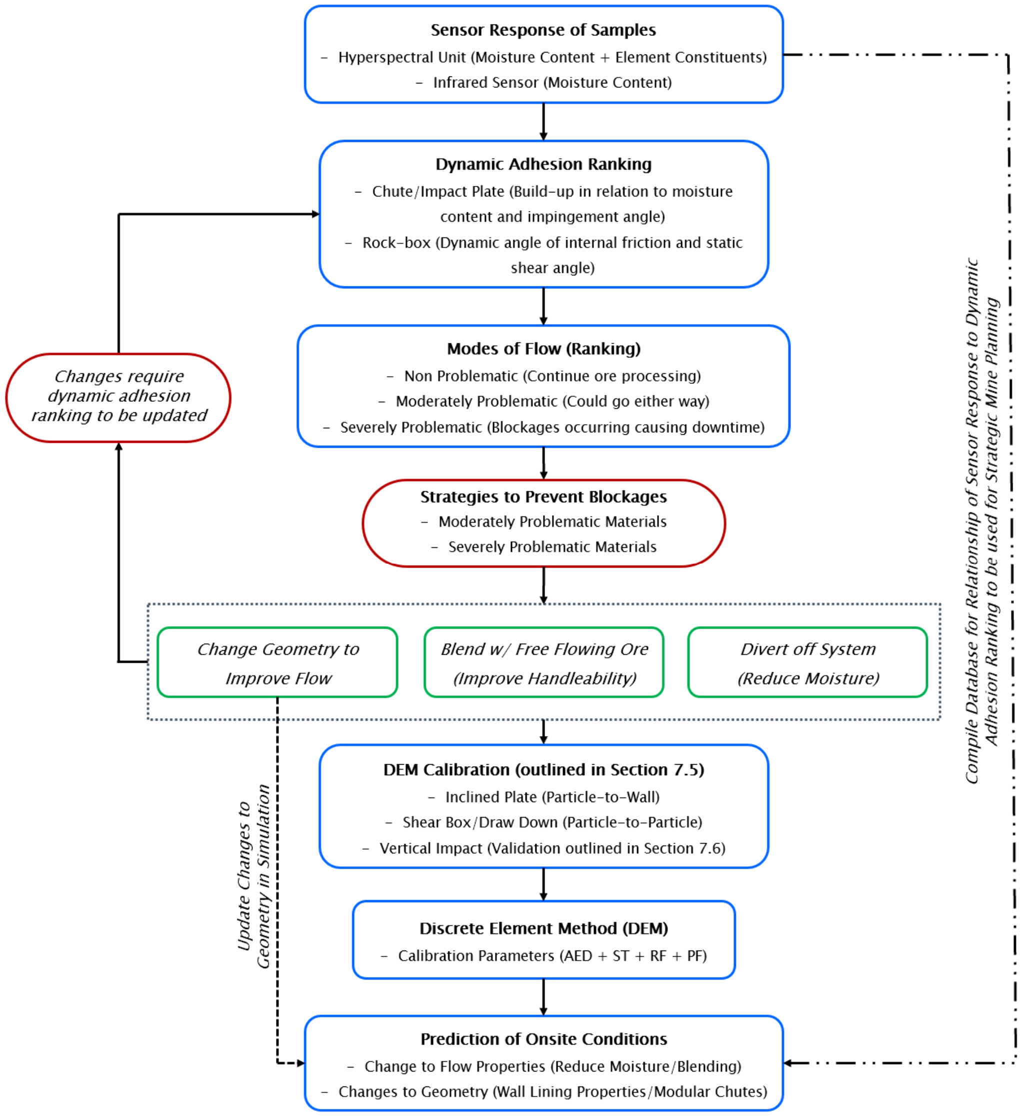

Figure 6.26 – Design protocol procedure for reduction of dynamic adhesion.

Another predictive method which can be used to assess the handling characteristics of bulk materials is by reflectance spectroscopy sensors. As way of background, spectroscopy is the study of light as a function of wavelength that has been emitted, reflected or scattered from a solid, liquid or gas [135]. Research undertaken by Plinke [136], showed that spectroscopy sensors can be used for applications such as process monitoring and integration of materials characterisation during processing in real-time where great benefits were shown. Furthermore, studies have also been undertaken to assess the grades and elemental constituents of bulk materials using spectroscopy sensors [137, 138]. By using spectroscopy sensors, it is possible to compile a database for the relationship of the sensor response to dynamic adhesion ranking assessment (outlined in Section 6.4.2). This can be used for strategic mine planning where the need for lab scale experiments would no longer be required.

6.5 CONCLUSION

This chapter explained the details of the inclined plate recirculating system and the procedure used to obtain the experimental measurements. The procedure outlined was developed to ensure the experimental measurements would be undertaken in a reproducible manner where confidence in the experimental data would result. The key experimental measurements are explained in detail where the thresholds for dynamic adhesion in relation to the moisture content of the iron ore samples have also been identified. Additionally, the estimated shape of the iron ore build-up was analysed to give an insight into the severity of the build-up that occurred during the experimental measurements.

The area's most susceptible to dynamic adhesion blockages in the materials handling stream are identified. To identify the threshold moisture contents where blockage problems may become evident for the supplied iron ore samples, a dynamic adhesion classification has been proposed where IOB at 18.5% MC for an impingement angle of 55° was identified as the most problematic for the samples tested. Additionally, the critical release angle where an effective build-up height equates to zero has been identified for transfer chute systems. From this, a design protocol for the reduction of dynamic adhesion was also proposed.

This page is left intentionally blank

CHAPTER SEVEN – NUMERICAL MODELLING OF WET & STICKY BULK MATERIALS

The following chapter presents a methodology for the numerical modelling of wet and sticky bulk materials. The presented methodology considers three models capable of replicating cohesive material behaviours, where a calibration procedure is proposed. A series of calibration simulations with systematic parameter variation are undertaken to define a set of calibration matrices. These calibration matrices are used for the formation of a parameter database, which can be used for the simulation of on-site applications to optimise plant geometry and other operational parameters.

7.1 INTRODUCTION

Numerical modelling of bulk material handling systems is essential to accurately depict the discontinuous behaviour they portray. The conventional continuum mechanic-based approaches (as outlined in Section 4.2) fail to solve most problems which relate to systems that exhibit discontinuous behaviour. By assuming that the flow of the bulk material acts more like a fluid, which is quite common for granular free flowing materials, the use of a continuum mechanics-based approach will be quite feasible. This, however, is a reasonably difficult assumption to use when WSMs are considered due to the discontinuous (clumping) nature of the flow (as outlined in Section 6.2.2).

One of the most common and well-known methods used to model the discontinuous nature of bulk materials negotiating the materials handling stream is the Discrete Element Method (DEM). The use of DEM simulations allows the user to undertake a more detailed analysis, where it is generally the preferred method of analysis in the materials handling sector. There are numerous methods that are capable of modelling discontinuous systems in the simulation domain. Some of the notable methods include: Modal Methods, Discontinuous Deformation Analysis, Momentum-Exchange Methods, Multibody Dynamics Methods, Structural Mechanics Methods, Mean Field Method and the Energy Minimisation Method [139]. It is beyond the scope of this research and not feasible to discuss all the methods available for modelling discontinuous systems and the fundamental principles of how they work in detail. It will be appropriate, however, to acknowledge these models for completeness of the thesis.

The following chapter gives a brief overview of DEM and explains, in detail, the three cohesion models which are used to replicate the behaviours of WSMs in the simulation domain. Additionally, a calibration procedure is proposed, where a series of calibration simulations with systematic parameter variation is also undertaken. The developed calibration matrices enabled the formation of a parameter database, which can be used for the simulation of on-site applications to optimise plant geometry and other operational parameters. Finally, numerical modelling validation was undertaken using a lab scale vertical impact testing facility (as outlined in Section 7.6).

7.2 DISCRETE ELEMENT METHOD (DEM) OVERVIEW

The Discrete Element Method (DEM) was first developed by Cundall [140] in 1971 for the simulation of large-scale movements in blocky rock systems. Cundall and Strack [141] then further developed DEM in 1979 to include granular assemblies, where the interaction of particle assemblies could be analysed. Continual research has been conducted into DEM which has resulted in a number of varying implementations to the original methodology. Some of the notable variations include works which can be cited in the following literature [142 - 145]. The fundamental modelling principal of DEM utilises Newtonian rigid-body mechanics to simulate the translational and rotational motion of particles in the simulation domain.

DEM particles are typically modelled as bodies with elastic interaction, without change in shape, where the deformation is neglected due to the very small values they possess when compared to the displacement of the individual particles. The particle contact, however, does allow overlap where contact forces are determined from the stiffness and damping characteristics of the particles. These contact forces are calculated using classical mechanics where the elasticity, damping and friction are considered. The friction is typically considered to be in separate components for both sliding friction (commonly referred to as particle friction) and rolling friction (commonly referred to as rolling resistance). As with any numerical modelling process, the forces and moments acting on a particle are calculated for each specified timestep. Additionally, for every timestep, the system of equations update, where the forces acting upon a particle are calculated for any immediate neighbours. This is undertaken for any surrounding particles and boundaries that are in contact with the particle being analysed.

The sliding and rolling resistance of spherical particles enable a user to replicate the behaviours a bulk material show in reality. These parameters ultimately influence the macroscopic behaviour of non-cohesive bulk materials [146]. As with most numerical modelling procedures, assumptions are required, and this will naturally be the case for DEM. By using spherical particles, a calibration procedure is essential to replicate the behaviour of the bulk material. During the calibration procedure, the stiffness in conjunction with the shape of the particles will typically dictate the required solve time [147, 148]. It is quite common to reduce the stiffness of the particles to improve the efficiency of the simulation solve time. Additionally, shape factors are commonly used to improve efficiency which make the sliding and rolling resistance calibration to be of critical importance. This leads to the calibration being able to account for limited geometric resistance.

Calibration procedures for dry non-cohesive bulk materials exist, which typically alter the simulation parameters using a systematic variation of parameter approach [146, 149]. Additionally, the use of optimisation algorithms have been used to conduct DEM calibrations with a higher degree of accuracy [150 - 153]. To determine the friction parameters for dry non-cohesive bulk materials there are many calibration experiments which exist. Some of the notable calibration experiments include: the Angle of Repose (AOR) experiment [146, 154 - 164], the shear box experiment [165, 166] and more recently the draw down experiment [167 - 169]. General calibration procedures commonly use a single experiment to determine the sliding and rolling friction parameters for dry non-cohesive bulk materials. This results in a multitude of parameter combinations which can replicate the experiment which is being simulated. By only using a single calibration experiment, the selection of a unique parameter combination is extremely difficult to obtain [146]. In the work of Roessler et al. [167] a procedure for the calibration of non-cohesive bulk materials using a range of calibration experiments is considered. This allowed for the use of several calibration experiments to be conducted which would then result in several reference values for the calibration. This in turn results in a unique parameter combination. A similar method for the calibration of WSMs is proposed for this research and is presented in Section 7.5.2.

DEM simulations are being used more extensively for the design and audit of bulk material handling systems. The application of DEM for industrial applications is well documented in the readily available literature. There are numerous investigations conducted into the validation of DEM simulations for a vast range of bulk material handling processes. The most notable bulk material handling system modelled numerically are transfer chutes. Numerical simulations of transfer chutes are well documented (see references [170 - 177]) due to the difficulties in visualising the flow for an industrial system. Additionally, extensive research has been conducted into the numerical simulation of transfer chutes due to the tendency for blockages to effect materials handling systems to operate effectively. Some of the other notable materials handling applications of DEM include: shear cell testers [178 - 180], pneumatic conveying [181 - 183], flow in hoppers and mixers [184 - 186], vibrating screens [187, 188], grinding mills [189, 190] and more recently bucket and chain conveyors [191] which are coupled using Multibody Dynamics.

In more recent times, the progression of DEM also considers various particle shapes which aim to replicate real world problems with a higher degree of accuracy. Some of the notable work which has been conducted on the topic of particle shape implementation include: modelling the dynamic behaviour of circular disks [141, 142, 192], clusters of spheres (multi-sphere) [193 - 198], 3-D ellipsoids [199, 200], super-quadrics [200 - 202] and other non-spherical shapes [203 - 208]. As with any numerical modelling simulation, the number of contacts and particle size dictates the time required for the simulation to solve. Furthermore, the complex contact models required to simulate cohesive bulk materials (as explained in Section 7.3.1) can also significantly increase the simulation solve time. It will be appropriate to identify that for these reasons: spherical particles are used for the simulations conducted in this research. The identification of the particle shapes available for implementation into DEM have been included for completeness of this thesis.

As with any numerical modelling simulation, the timestep required to conduct an accurate solution is directly proportional to the required solve time of the simulation. The timestep for an accurate DEM simulation is of critical importance and much research has been conducted on this topic (see references [209 - 211]). The most detailed of these was undertaken by O'Sullivan and Bray [209], who proposed that a timestep less than $0.17\sqrt{m/k}$ (where m is the total mass of the particle and k is the particle stiffness) should be utilised.

The efficiency of DEM simulations is attributed to the stiffness in conjunction with the shape of the particles [147, 148]. DEM simulation solve times can also significantly increase when the method of contact detection for neighbouring particles is considered. The contact detection will be directly related to the quantity of particles in the simulation domain and to a more important extent the particle shape which can have a greater influence on the solve time.

Both of these factors dictate the required solve time for a simulation to be completed [212]. If a single particle is considered, a boundary distance, typically referred to as the neighbour list, is required. This will effectively set a searching distance for the surrounding neighbours of each individual particle. By using this method, the need to analyse every neighbour particle in the simulation domain at each timestep will not be required. Due to the significant number of particles which can be required to simulate an industrial system, it is essential that the cut-off distance is set to an appropriate value. Typically, the cut-off distance should be approximately two to three times the largest particle radii [212].

It has been previously outlined that the computational power and time required for a DEM simulation to solve are typically associated with the quantity of particle contacts found within the simulation domain. The amount of contacts can be linked with the diameter of the particles and the quantity of particles simulated, where solve times are exponentially greater as the particle diameter is reduced. For this reason, it is not always feasible to simulate particles which use the same PSD of the bulk material to be replicated into DEM. If the actual PSD of a bulk material, such as the supplied iron ore samples, was simulated, the time required to simulate a simple materials handling system would be both impractical and almost impossible to complete with the current computational power at hand.

The DEM simulations undertaken within this research use particles which utilise a scalped PSD. By scalping the particles, the replication of the supplied iron ore samples into DEM simulations can be undertaken. Additionally, by using a scalped PSD, the systematic variation of contact model parameters is required to replicate the lab scale experiments (as explained in Section 7.5). The discussion of the parameters for the DEM contact models and calibration procedure are discussed in the subsequent sections.

7.3 DISCRETE ELEMENT METHOD (DEM) CONTACT MODELS

To analyse the interaction of particles in DEM, contact models are required. These contact models will govern how a particle responds to an external force acting on the particle being analysed. These contact forces are calculated using classical mechanics where the elasticity, plasticity, damping and friction are considered. The particle interaction is typically modelled using a soft contact approach where rigid particles are allowed to overlap. Although the particles themselves don’t deform, the overlap in effect acts as a deformation. This overlap ultimately result in the motion of the particle where the position and velocity of each particle are analysed at each specified timestep.

There are numerous contact models which describe the rolling friction, μ_r, and sliding friction, μ_s, which acts on a spherical particle in the normal and tangential directions for particle-to-particle contact. As discussed in the previous section and further in Section 7.5.2, the use of spherical particles requires the calibration of contact parameters as an essential process for an accurate simulation. This is necessary to replicate the calibration experiments which are outlined in Section 7.5.1. It will therefore be necessary to outline the contact models available and detail the rolling friction and sliding friction models, which have been used for the simulations undertaken for this research.

When the rotation of the particles is considered, rolling friction models have been implemented into DEM which effectively incorporate the resistance to rotation. This rotational resistance, typically referred to as rolling friction, is required for the spherical particles to take the shape of the real particles and asperities on the particles into account [146, 155, 213]. Ai et al. [214], have conducted detailed studies into the different rolling friction models available for use in DEM. Each of the available rolling resistance models were classified into four categories [214]:

1. Directional constant torque models (Model A).
2. Viscous models (Model B).
3. Elastic plastic spring-dashpot models (Model C).
4. Contact-independent models (Model D).

The rolling friction model which is used for the simulations conducted in this research, is defined as type Model C. More specifically, the rolling friction model used has been developed by Wensrich and Katterfeld [146]. This model considers the rolling stiffness to be derived from the shear stiffness where the rolling damping has been neglected. This allows for the systematic parameter variation to be undertaken for the friction alone where the damping is not considered in this model. It is beyond the scope of this research and not feasible to discuss each of these categories in detail. It will be appropriate, however, to acknowledge these categories for completeness of the thesis where further information can be found in the research of Ai et al. [214].

Sliding friction models have been implemented into DEM which govern the motion of the particles. The sliding friction models account for the forces acting in the normal and tangential directions for particle-to-particle and particle-to-wall contacts. The two most common sliding friction models used in DEM include the linear spring model [141] and the Hertz-

Mindlin (no slip) model [215]. The linear spring model is an elastic contact model based on the work undertaken by Hooke [216] in 1678, typically referred to as Hooke's law, and is by far the simpler of the two sliding contact models. This model includes a dash-pot and slider which account for energy dissipation in the contact region.

The sliding friction model which is used for the simulations conducted in this research, is the Hertz-Mindlin (no slip) model [215]. This model is based upon the work conducted by Hertz [217] in 1882, where a solution was developed to determine the resulting contact of two elastic spheres which were brought into contact. When the normal force-displacement relationship was analysed, a resulting non-linear relation acting between the spheres in contact was discovered. This work was then further developed into the tangential direction by Mindlin and Deresiewicz [218] in 1953. The model developed by Mindlin and Deresiewicz [218] determined the force-displacement of two spheres in contact in the tangential direction. When both of these models are combined, the Hertz-Mindlin contact model is formed and has been implemented into the majority of the commercial and open source DEM packages. A simplified schematic of the Hertz-Mindlin contact model is shown in Figure 7.1. It is important to note that the tangential model used for this research is the tangential history model which considers the *"tangential overlap"* between the particles for the duration of the time they are in contact.

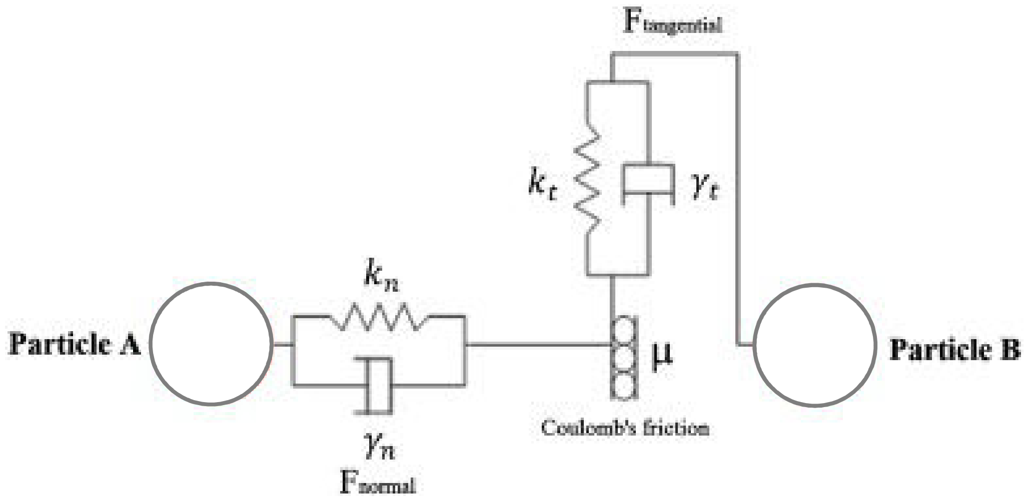

Figure 7.1 – Simplified schematic of Hertz-Mindlin contact model (Derakhshani et al., 2015).

The contact models outlined are only a small representation of the models available. Some of the other contact models which have been implemented into DEM include hysteretic spring models, which allow the conservation of energy resulting in an elastic contact, and bonded models, which allow the contact between two particles to have a finite strength. It is beyond the scope of this research and not feasible to discuss every contact model available in detail. It will be appropriate, however, to acknowledge that these models are implemented into DEM and are used extensively.

7.3.1 COHESION CONTACT MODELS

With the expansion of computation power, it is currently more feasible to use DEM for the contact models, required to describe the adhesion and cohesion mechanisms that encapsulate the behavioural traits WSMs show. Cohesion contact models incorporate an additional force which essentially *"hold"* the particles together, acting as the cohesion and/or adhesion which is present. This additional force is incorporated into the contact models described in the previous section. This is undertaken in both the normal and tangential components for particle-to-particle and particle-to-wall contacts. There are numerous cohesion contact models available in several commercial and open source DEM packages. Each of the available cohesion contact models can be classified into three categories:

1. Elastic adhesive normal contact models.
2. Adhesive normal contact models including plasticity.
3. Capillary force (liquid bridging) contact models.

It is beyond the scope of this research and not feasible to discuss every contact model available in detail. It will be appropriate, however, to outline the differences between each of the categories and acknowledge the contact models which are available in DEM. Furthermore, for the simulations conducted in this research, the open source DEM software LIGGGHTS® [220] version 3.8.0 is used. For completeness it is also appropriate to identify that a CPU solver was utilised. LIGGGHTS® [220] version 3.8.0 has implemented cohesion contact models from each of the categories outlined above. In the following sections, the cohesion contact model used from each category are outlined in detail.

The elastic adhesive normal contact models available are typically used to simulate fine cohesive powders which are generally affected by surface forces (shown as without material bridges in Table 3.1). There are numerous causes for the forces of fine cohesive powders where several cohesion contact models have been developed to replicate these behaviours. Some of the notable models include: the Bradley model [221], the Johnson-Kendall-Roberts (JKR) model [222], the Derjaguin-Muller-Toporov (DMT) model [223, 224] and the linear cohesion model [225]. Each of these models adds an additional pull-off force which is governed by the contact area and a cohesion energy density which *"stick"* the particles together. For the simulations conducted in this research, the model analysed is based on the Johnson-Kendall-Roberts (JKR) model [222] where a detailed outline is undertaken in Section 7.3.1.1.

Adhesive normal contact models including plasticity consider the hysteretic effects which include the plastic deformation and history dependent adhesion. These models are commonly used to simulate bulk materials which show plastic characteristics (such as a WSM). The models follow a defined loading path until yielding occurs where the material reaches a plastic state. At this stage of plastic deformation, energy dissipation occurs leading to an unloading path which describes the plastic characteristics (adhesion) of the bulk material. Both linear and non-linear models exist where some of the notable linear models include: the Luding model [226 - 230] and the Walton and Johnson model [231]. The more complex non-linear models which have been developed include: the Thornton and Ning model [232], the Tomas model [233 - 237] and the Edinburgh Elasto-Plastic Adhesion (EEPA) model [212, 238]. Each of these models typically contains five parameters: the loading stiffness, the plastic deformation parameter, the adhesive stiffness, the plastic overlap range of the model and the viscous dissipation parameter. For the simulations conducted in this research, the model analysed is the Edinburgh Elasto-Plastic Adhesion (EEPA) model [212, 238] where a detailed outline is undertaken in Section 7.3.1.2.

The capillary force (liquid bridging) contact models available are typically used to simulate bulk materials which have liquid bridges present between the particles (shown as with material bridges in Table 3.1). These models are generally used to simulate bulk materials which exhibit higher moisture contents (such as a WSM). Some of the notable models include: the Lian et al. model [239], the Mikami et al. model [240], the Soulie et al. model [241], the Nase et al. model [242] and the Rabinovitch et al. model [243]. The capillary force models typically add an additional liquid bridge force which are governed by the volume and surface tension of the liquid bridge. For the simulations conducted in this research, the model analysed is based on the work of Easo and Wassgren [244] which is typically referred to as the Easo model. The Easo model is a composition of the Lian et al. model [239], the Soulie et al. model [241] and the Nase et al. model [242]. A detailed outline is undertaken in Section 7.3.1.3.

7.3.1.1 SIMPLIFIED JOHNSON-KENDALL-ROBERTS (SJKR) CONTACT MODEL

The Johnson-Kendall-Roberts (JKR) model [222], is an expansion to the well-defined contact model that was investigated in 1882 by Hertz [217]. The classical Hertz Contact Theory provides an explanation for the elastic deformation of bodies in contact. Hertz Theory, although verified experimentally, neglected to incorporate the effects of both cohesion and adhesion. This could be attributed to the Hertz model only incorporating the compressive forces and neglecting the tensile forces that can be experienced in the contact zone between two bodies when they are separated.

The experimental work of Roberts in 1968 [245], Kendall in 1969 [246] and Johnson et al. in 1971 [222], showed that for lower loads at the area of contact acting between the particles, the estimated contact areas between these bodies were significantly higher than those predicted by Hertz Theory. As the loads were reduced towards zero, the additional contact forces became increasingly important, which formed the basis of the JKR model. It was also observed, that behaviour closely matched the Hertz Theory when higher loads were considered. The use of the JKR model for the numerical modelling of particle systems has steadily increased with the popularity of DEM. The majority of the conducted research occurred in the late 1980's with the development of atomic force microscopy [212], where the analysis of the tensile forces acting between particles could be undertaken.

When two spherical particles are considered, the acting adhesion force, F_{ad}, will not be dependent on the elastic modulus of the spherical particles. This can be shown when the contact radius, a, is considered. Although the elastic modulus effects the contact radius, when both the surface energy and elastic work are considered to vary with the contact area, i.e. a^2, the adhesion force, F_{ad}, can be shown to be independent of the contact radius, a, and hence elastic modulus [222]. Mechanical work is therefore necessary to separate the adhesive forces which are present when two particles are in contact. This mechanical work can also be thought of as the energy which is required to separate the particles. This energy creates new surfaces which can be defined as the free surface energy of the solid. The overlap caused by the additional surface force can be described by:

$$\delta_{JKR} = \frac{a^2}{R^*} - \sqrt{\frac{2\pi\Delta\gamma a}{E^*}} \tag{7.1}$$

where: a is the contact radius [m].

R^* is the equivalent radius [m].

E^* is the equivalent Young's modulus [Pa].

$\Delta\gamma$ is the contact surface energy [N/m] (see Equation 7.2).

The contact surface energy, $\Delta\gamma$, is determined as the surface energies of the two contact partners and the interfacial energy:

$$\Delta\gamma = \gamma_1 + \gamma_2 - \gamma_{1,2} \tag{7.2}$$

where: γ is the surface energy of the particle [N/m].

The hertz equation modified to include surface energy is determined as:

$$F_{JKR} = \frac{4E^* a^3}{3R^*} - 4\sqrt{2\pi\Delta\gamma E^* a^3} \tag{7.3}$$

While the contact radius will be given as:

$$a_{JKR}{}^3 = \frac{d_p}{2E^*}\left[F_n + \frac{3}{2}\Delta\gamma\pi d_p + \sqrt{3\pi\Delta\gamma d_p F_n + \left(\frac{3\pi\Delta\gamma d_p}{2}\right)^2}\right] \tag{7.4}$$

where: F_n is the external normal force acting on the particle [N].
d_p is the diameter of the particle [m].

The force required to separate the two contacting particles, also referred to as the critical pull-off force, can be found using the following:

$$F_{PO} = -\frac{3}{2}\pi\Delta\gamma R^* \tag{7.5}$$

It will be appropriate to identify that when the contact surface energy is zero ($\Delta\gamma$ =0), Equation 7.4 reverts to the simple Hertz equation, $\mathrm{a_{JKR}}^3 = d\mathrm{F_n}/2E^*$. For the JKR model to be implemented into the DEM technique, a simplified version was considered. The Simplified Johnson-Kendall-Roberts (SJKR) model [247] has two main parameters which need to be considered. These parameters include the radius of the particle and the Cohesion Energy Density (CED) for particle-to-particle contact. Additionally the Adhesion Energy Density (AED) is used for particle-to-wall contact. All of these will be found within the contact region. The Cohesion Energy Density (CED), Ω_{CED}, and the Adhesion Energy Density (AED), Ω_{AED}, are constant numerical parameters for the energy needed to separate the contact and has units (*J/m³*). A schematic for particle-to-particle and particle-to-wall contacts is shown in Figure 7.2.

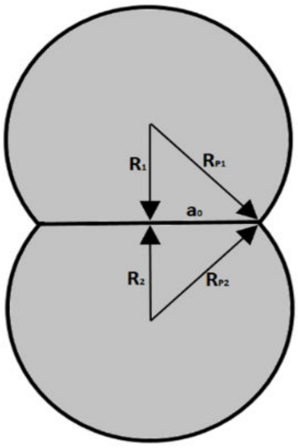

a) Particle-to-Particle contact

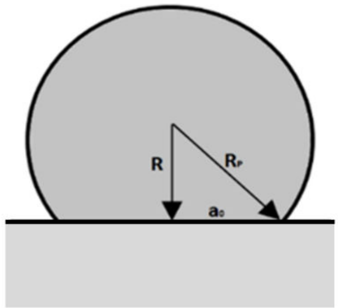

b) Particle-to-Wall contact

Figure 7.2 – Simplified schematic of Simplified Johnson-Kendall-Roberts (SJKR) contact model (Carr et al., 2016).

The additional force required to separate two contacting particles which use the CED and AED is given as:

$$F_{SJKR} = F_n + \Omega_{CED/AED} A_{cont} \tag{7.6}$$

where: $\Omega_{CED/AED}$ is the cohesion/adhesion energy density [J/m^3].

$A_{cont} = \pi({R_p}^2 - R^2)$ is the contact area [m^2].

R_p is the radius of the particle [m].

R is the radius of the particle centre to the contact point [m].

The SJKR model [247] has been implemented into the open source DEM software LIGGGHTS® [220] version 3.8.0. The SJKR model [247] is typically used to simulate cohesive powders which are generally affected by surface forces (shown without material bridges in Table 3.1). This results in a stiffer more rigid flow of the particles in comparison to the hysteresis and liquid bridging models which show plastic characteristics. It is important to note the complete JKR model (outlined in Equation 7.3) is capable of modelling contacts with negative overlap (long distance forces). When the SJKR model is considered, the simplification results in the detachment and pull off forces to be substantially different to that implemented in the JKR theory. Additionally, the SJKR model has a near linear relationship to the overlap and applied JKR force. This results in low normal overlap where the JKR force is low but increases with overlap. When the original JKR model is considered however, higher JKR forces are provided at low overlap. This aids the model to be more cohesive at low consolidation. Although the SJKR model [247] is typically not suited to modelling WSMs for particle-to-particle contact, there are significant benefits when particle-to-wall contacts are considered. This has been shown by the author in the research of Carr et al. [166, 247] and in Section 7.3.1.4, where the coupling of two contact models has produced the most realistic representation of a WSM. From this, the Adhesion Energy Density (AED) for particle-to-wall contact is coupled with the Easo liquid bridging model for particle-to-particle contact to gain a better representation of a WSM into DEM. The coupling of these models is outlined further in Section 7.3.1.4.

7.3.1.2 EDINBURGH ELASTO-PLASTIC ADHESION (EEPA) CONTACT MODEL

When problematic bulk materials such as WSMs are considered, plastic behaviours can result. The flow and consolidation of these bulk materials are highly dependent on the stress history, which the bulk material is subjected to. These behaviours are typically attributed to higher moisture contents and clays which can be present in the bulk material. Ignoring the stress history in the numerical modelling process can lead to models which fail to replicate plastic behaviours. To obtain a more accurate numerical modelling solution, adhesive normal contact models which include plasticity, typically referred to as hysteresis models, replicate the behaviour of cohesive bulk materials. These models consider the hysteretic effects, which include the plastic deformation and history dependent adhesion. Hysteresis contact models are commonly used to simulate bulk materials which show plastic characteristics (such as a WSM).

The available elastic adhesive normal contact models, such as the JKR, DMT and linear cohesion model, add an additional pull-off force which are governed by the contact area and a cohesion energy density which *"stick"* the particles together. Although these models can replicate scenarios which consider low consolidation or small amounts of cohesion, they may still fail to capture the correct stress history behaviour. Furthermore, when the plasticity of WSMs is considered, the elastic adhesive models will not be able to capture the stress history behaviour. There are numerous hysteresis contact models, as outlined in Section 7.3.1, which have been implemented into DEM. Although each of the proposed hysteresis models consider the stress history behaviour, they still have limitations. The model developed by Thornton and Ning [232] proposed a non-linear adhesion model which considered the plastic deformation between particles, however, the model still utilised the elastic JKR theory for the adhesive force. The model proposed by Walton and Johnson [231] considered a hysteretic linear spring model which did not include the tensile strength for the determination of the adhesion. To account for this, extra parameters were required which made the model significantly difficult to calibrate experimentally.

To overcome these limitations, a model has been proposed by Morrissey [212], which is referred to as the Edinburgh Elasto-Plastic Adhesion (EEPA) model. The EEPA contact model is the most accurate hysteresis model to date, where the determination of the force-overlap relationship is shown in Figure 7.3. The EEPA model can replicate the behaviour of two particles or agglomerates in contact, where the particles will experience elastic and plastic deformations when pressed together. This causes an increase in the adhesive force as the plastic contact area increases with deformation. The EEPA model is either linear or non-linear (depending on the value of n_p), which accurately captures both the plastic and elastic effects of the particles in contact with one another. It does this by having clearly defined loading and unloading paths which are identifiable as k_1 and k_2, as shown in Figure 7.3, for each of the respective loading conditions. These values act as a stiffness parameter for the particle contact to normal force-overlap curves of Figure 7.3. When the particles are in contact, the loading path is followed where the contact switches to the unloading path when the load is removed. After this stage, the corresponding maximum adhesion force is applied to the contact area which typically occurs below the plastic overlap, δ_p. From here the particle returns to the loading path, where a maximum load is obtained. Once a contact has been separated, however, all of the previously obtained stress history is lost. This model does not consider the hysteretic behaviour during the unloading sequence if a contact is found to be below δ_{min}.

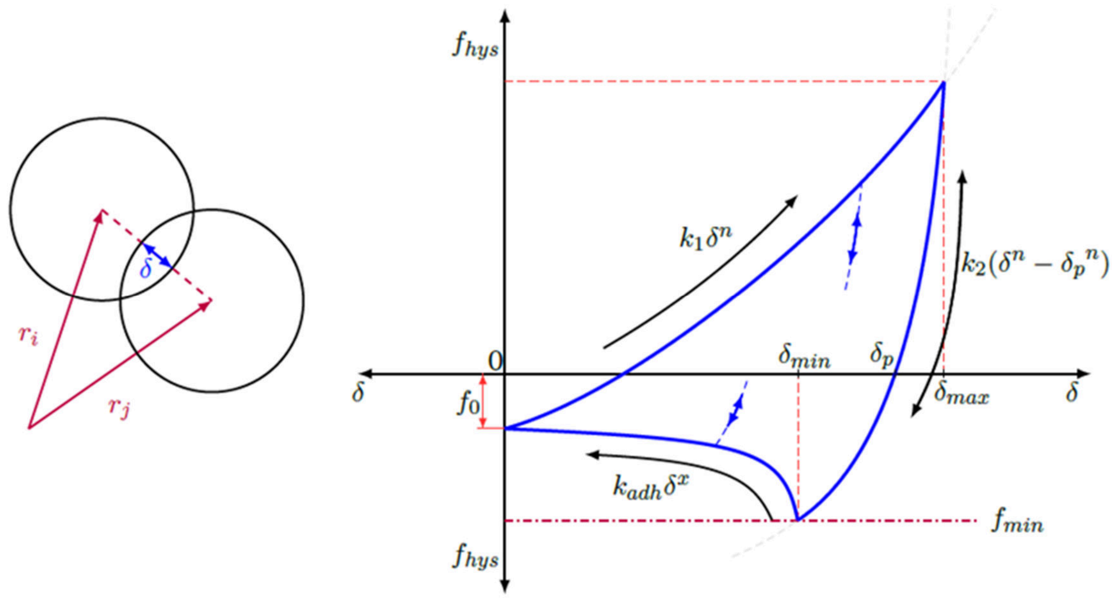

Figure 7.3 – Schematic of Edinburgh Elasto-Plastic Adhesion (EEPA) contact model (Morrissey, 2013).

The hysteresis contact model proposed by Morrissey [212], mathematically determines the normal force, f_n, using the following equation:

$$f_n = (f_{nd} + f_{hys})\vec{u} \tag{7.7}$$

where: f_{nd} is the normal damping force [N] (see Equation 7.8).
f_{hys} is the sum of the hysteretic spring force [N] (see Equation 7.11).
$\vec{u}$ is the unit normal vector from contact point to particle centre [-].

The normal damping force is calculated using:

$$f_{nd} = -2\sqrt{\frac{5}{6}}\beta\sqrt{K_n m^*}v_n{}^{\overrightarrow{rel}} \tag{7.8}$$

where: β is the damping coefficient [-] (see Equation 7.9).
K_n is the Hertzian normal stiffness [N/m] (see Equation 7.10).
m^* is the equivalent particle mass [kg].
$v_n{}^{\overrightarrow{rel}}$ is the normal component of the relative velocity [m/s].

The damping coefficient, β, is determined using:

$$\beta = \frac{\ln e}{\sqrt{\ln^2 e + \pi^2}} \tag{7.9}$$

where: e is the coefficient of restitution [-].

The Hertzian normal stiffness, K_n, is determined using:

$$K_n = 2E^*\sqrt{R^*\delta_n} \tag{7.10}$$

where: E^* is the equivalent Young's modulus [Pa].
R^* is the equivalent particle radii [m].
δ_n is the overlap of the particles in the normal direction [m].

The EEPA model has been simplified in the calculation process where the yield point has been neglected. It has been proposed during the model development, that a force-displacement relationship that is non-linear is experienced throughout all branches for the entire model for both loading and unloading conditions [212]. The EEPA model is primarily controlled in relation to the non-linearity, with use of the power n_p for both the initial loading condition and unloading/reloading condition where a linear model results when $n_p = 1$. It will be appropriate to identify that the adhesion determination utilises a separate parameter, considered as x, which controls the adhesive unloading stiffness. By using a different parameter, it is possible for the EEPA model to replicate the excessive adhesive nature of WSMs especially when lower consolidation loads are considered. The normal force relationship of the EEPA model, as shown in Figure 7.3, is determined using:

$$f_{hys} = \begin{cases} f_0 + k_1 {\delta_{po}}^{n_p} & \text{if } k_2\left({\delta_{po}}^{n_p} - {\delta_p}^{n_p}\right) \geq k_1 {\delta_{po}}^{n_p} \\ f_0 + k_2\left({\delta_{po}}^{n_p} - {\delta_p}^{n_p}\right) & \text{if } k_1 {\delta_{po}}^{n_p} > k_2\left({\delta_{po}}^{n_p} - {\delta_p}^{n_p}\right) > -{k_{adh}}^{x} \\ f_0 - {k_{adh}}^{x} & \text{if } -{k_{adh}}^{x} > k_2\left({\delta_{po}}^{n_p} - {\delta_p}^{n_p}\right) \end{cases} \quad (7.11)$$

where: f_0 is the pull-off force [N].

k_1 is the initial loading stiffness [N/m] (see Equation 7.12).

k_2 is the unloading/loading stiffness [N/m].

k_{adh} is the adhesive stiffness [N/m].

δ_{po} is the plastic overlap [m].

δ_p is the plastic particle overlap [m] (see Equation 7.13).

n_p is the power value for the force overlap relationship [-].

x is the power value for the adhesion branch [-].

At each specified timestep, the contact forces for both loading and unloading/reloading conditions are calculated and checked against the selection criteria of Equation 7.11. This determines which loading condition of the particle overlap applies and therefore which branch of the EEPA model should be used for this timestep. The non-linear form of the initial loading stiffness, k_1, is based on the Hertz contact theory and is determined using:

$$k_1 = \frac{4}{3}\sqrt{R^* E^*} \quad (7.12)$$

Once a zero force has been obtained during the unloading/reloading stiffness sequence, a resulting overlap occurs. The unloading/reloading stiffness sequence is given using k_2. The resulting overlap is defined as the plastic overlap, δ_p, where the maximum historical normal overlap is recorded as the history parameter for the EEPA contact model in a custom contact property being updated as necessary [212]. The plastic overlap, δ_p, is determined using:

$$\delta_p = \left(1 - \frac{k_1}{k_2}\right)^{\frac{1}{n_p}} \delta_{po} \tag{7.13}$$

The EEPA contact model is typically used to simulate bulk materials which exhibit plastic behaviours. Bulk materials which show these characteristics typically have higher clay and moisture contents. Additionally, these bulk materials fail to fully yield where they continue to plastically deform when consolidation loads are applied. By considering the hysteresis of the loading conditions, the EEPA contact model is capable of replicating bulk materials which exhibit plastic characteristics. Although the EEPA model is typically suited to modelling WSMs, the vast array of parameters which require calibration make the calibration procedure, as outlined in Section 7.5.2, significantly time consuming. This becomes much more evident when a comparison to the elastic adhesive normal and liquid bridging contact models is made. A comparison of required input parameters with solve times for the EEPA contact model and hybrid model, detailed in Section 7.3.1.4, is undertaken in Section 7.4. This gives an indication into the most appropriate model for use on an industrial basis. The criteria for the most appropriate model is in relation to the ability to replicate the calibration experiments and the required time for the simulation to solve.

7.3.1.3 EASO LIQUID BRIDGING CONTACT MODEL

The formation of a liquid bridge between either particle-to-particle or particle-to-wall contact can be attributed to the capillary forces that are formed due to the surface tension of the medium in the liquid bridge [54]. The capillary force contact models are typically used to simulate bulk materials which have liquid bridges present between the particles (shown as with material bridges in Table 3.1). These models are typically used to simulate bulk materials which exhibit higher moisture contents (such as a WSM). Israelachvili [249] developed a formulation to determine the capillary force present within a liquid bridge in relation to the total energy of the bridge. This model described the capillary force well, however, the formulation failed to capture the effect of the liquid bridge being pulled apart for a fixed volume. To consider the effects of the liquid bridge breaking, an approach was developed by Rabinovich et al. [243] which utilised the pressure difference that is found across the liquid bridge. This resulted in a more accurate formulation of the capillary force. A simplified schematic of the capillary force present in a liquid bridge for both particle-to-particle and particle-to-wall contacts is shown in Figure 7.4.

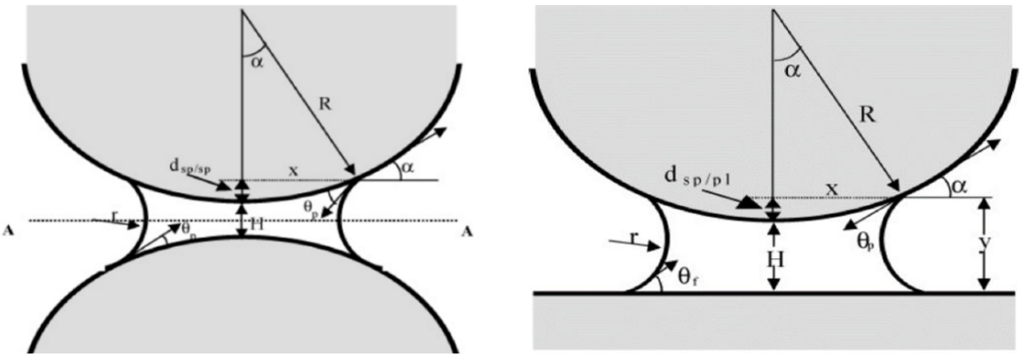

a) Particle-to-Particle contact *b) Particle-to-Wall contact*

Figure 7.4 – Schematic of capillary forces within a liquid bridge (Rabinovich, Y. I. 2005).

The expression determined by Rabinovich et al. [243] to calculate the capillary force, $\mathrm{F_{sp/pl}}$, of a particle-to-wall liquid bridge contact as illustrated in Figure 7.4a is given as:

$$\mathrm{F_{sp/pl}} = \frac{4\pi\gamma \mathrm{R_p} \cos\theta_c}{1 + \mathrm{H}_{lb}\sqrt{\pi \mathrm{R_p}/\mathrm{V}_{lb}}} - 2\pi\gamma \mathrm{R_p} \sin\alpha_c \sin(\theta_c + \alpha_c) \tag{7.14}$$

where: γ is the surface tension [N/m].

θ_c is the contact angle [°].

α_c is the embracing angle [°].

$\mathrm{R_p}$ is the radius of the particle [m].

H_{lb} is the minimum distance of the liquid bridge [m].

V_{lb} is the volume of the liquid bridge [m^3].

It is appropriate to identify that in Equation 7.14, the left term is the expression as determined by Israelachvili [249]. The right term gives the force of the vertical component of the surface tension, which was neglected in the initial development of this expression. Furthermore, the total energy of the liquid bridge was determined as:

$$\mathrm{W_{Tot}} = -2\pi\gamma {\mathrm{R_p}}^2 {\alpha_c}^2 \cos\theta_c \tag{7.15}$$

It was assumed for the derivation of the total energy formulation, that only the energy of the solid surface under the liquid bridge was considered and the surface energy produced by the meniscus was neglected. Similarly, the expression determined by Rabinovich et al. [243] to calculate the capillary force of a particle-to-particle liquid bridge contact, as illustrated in Figure 7.4b is given as:

$$\mathrm{F_{sp/sp}} = -\frac{2\pi \mathrm{R_p} \gamma \cos\theta_c}{1 + [\mathrm{H}_{lb}/2\mathrm{d_{sp/sp}}]} - 2\pi\gamma \mathrm{R_p} \sin\alpha_c \sin(\theta_c + \alpha_c) \tag{7.16}$$

Furthermore, the expression of $\mathrm{d_{sp/sp}}$, which is the interaction of two spheres is given as:

$$\mathrm{d_{sp/sp}} = \frac{\mathrm{H}_{lb}}{2}\left(-1 + \sqrt{1 + \frac{2\mathrm{V}_{lb}}{\pi \mathrm{R_p} {\mathrm{H}_{lb}}^2}}\right) \tag{7.17}$$

The above model assumes smooth spherical particles and that both particles for a particle-to-particle contact have the same size. An extension of this model, as shown in Figure 7.5, has been undertaken by Soulie et al. [241], where unequal sized particles are considered. This model also assumes that particles are spherical and smooth where the surface roughness has been neglected. The liquid bridge formed is in the pendular state, which is assumed to be relatively small where the effects due to gravity are neglected. Additionally, the capillary force is analysed in a quasi-state configuration, where the viscosity of the liquid is not considered [241].

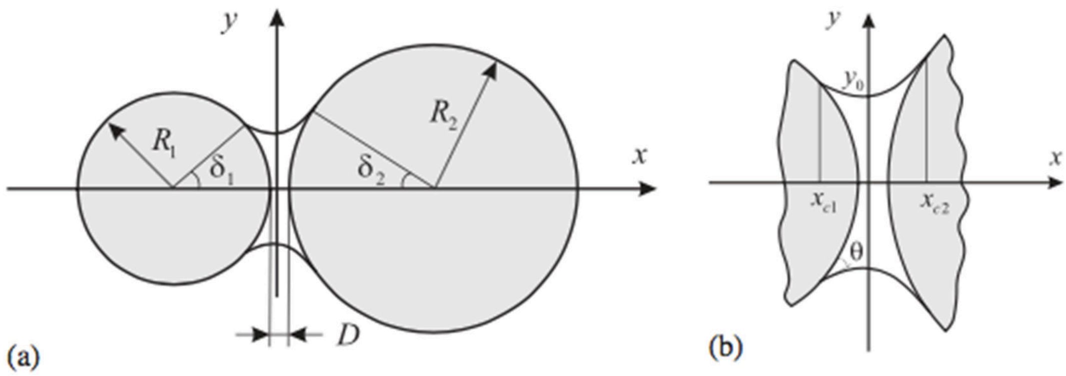

Figure 7.5 – (a) Geometry of a liquid bridge between two particles of uneven sizes. (b) Detailed view of liquid bridge (Soulié, 2006).

To determine the capillary force, first the volume of the liquid bridge must be determined, which is given as:

$$V_{lb} = \int_{x_{c1}}^{x_{c2}} y^2(x)dx - \frac{1}{3}\pi R_1^3(1 - \cos\delta_1)^2 (2 + \cos\delta_1) - \frac{1}{3}\pi R_2^3(1 - \cos\delta_2)^2 (2 + \cos\delta_2) \tag{7.18}$$

where: R_1 and R_2 are the particle radii [m].

δ_1 and δ_2 are the half filling angles [°].

x_{c1} and x_{c2} are the distances from y-axis to edge of liquid bridge [m].

In addition, the inter-particle distance, D, is given as:

$$D = R_2(1 - \cos\delta_2) + x_{c2} + R_1(1 - \cos\delta_1) - x_{c1} \tag{7.19}$$

From the geometry presented above in Figure 7.5, the capillary force acting within a liquid bridge between two particles of different size can be calculated when the surface tension, σ_{ST}, is known. This is given as:

$$F_c = \pi\sigma_{ST}\sqrt{R_1R_2}\left[c + \exp\left(a\frac{D}{R_2} + b\right)\right] \tag{7.20}$$

where:

$$a = -1.1\left(\frac{V_{lb}}{R_2^3}\right)^{-0.53} \tag{7.21}$$

$$b = \left(-0.148\ln\left(\frac{V_{lb}}{R_2^3}\right) - 0.96\right){\theta_c}^2 - 0.0082\ln\left(\frac{V_{lb}}{R_2^3}\right) + 0.48 \tag{7.22}$$

$$c = 0.0018\ln\left(\frac{V_{lb}}{R_2^3}\right) + 0.078 \tag{7.23}$$

θ_c is the contact angle of liquid bridge [°].

The capillary force model presented by Soulie et al. [241] has been implemented into the open source DEM software LIGGGHTS® [220] version 3.8.0. This capillary force model in conjunction with the model of Lian et al. [239] and the model of Nase et al. [242] form the Easo liquid bridging contact model [244]. This contact model essentially adds a liquid bridge force that is caused by a surface liquid film on the particles. The model can also solve for the transfer of surface liquid from one particle to another, however, dynamic conditions for the breakup of the liquid film are not considered. It is appropriate to identify that when a breakup of the liquid bridge occurs, it is assumed that the surface liquid distributes evenly between the two particles. The current state of this model also indicates that the surface liquid is assumed to be small and has no effect on the particle mass, diameter or density [250].

To consider the formation of the liquid bridge to include the break-up and surface liquid transfer, a simplified model has been developed by Easo and Wassgren [244]. The volume of the liquid bridge is given as:

$$V_{bond} = 0.05(V_{sLi} + V_{sLj}) \tag{7.24}$$

where: V_{sLi} is the surface liquid volume attached to particle *i* [m^3].
V_{sLj} is the surface liquid volume attached to particle *j* [m^3].

The Easo model assumes that the bridge formation occurs upon particle contact and the rupture distance is given using the model developed by Lian et al. [239]:

$$d_0 = \left(1 + \frac{\theta_{eff}}{2}\right)(V_{bond})^{\frac{1}{3}} \tag{7.25}$$

where: θ_{eff} is the effective contact angle between particles *i* and *j* [°].

Finally, the Easo model assumes that the normal and tangential components of the viscous force are calculated using the formulation developed by Nase et al. [242]. Each of the respective components are given using:

$$F_{viscN} = 6\pi\mu_f R^* v_n \frac{R^*}{S} \tag{7.26}$$

$$F_{viscT} = \left(\frac{8}{15}\ln\left(\frac{R^*}{S}\right) + 0.9588\right) 6\pi\mu_f R^* v_t \tag{7.27}$$

where: R^* is the effective particle radius [m].
μ_f is the viscosity of the fluid [m^2/s].
v_n is the particle normal relative velocity [m/s].
v_t is the particle tangential relative velocity [m/s].

S is the separation distance between the particles [m].

The Easo liquid bridging model is commonly used to simulate bulk materials which exhibit higher moisture contents (such as a WSM), where liquid bridges are present between the particles. This results in the replication of bulk materials which exhibit plastic characteristics. Although the Easo model is typically suited to modelling WSMs, when particle-to-wall contacts are considered, the replication of problematic bulk material build-up behaviour is difficult to achieve. This can be shown when the build-up of the bulk material onto a vertically mounted wall liner, as shown in Section 7.6, is considered. To replicate the behaviour of WSMs, the coupling of two contact models is proposed. The coupled model is a combination of the SJKR model for particle-to-wall contact and the Easo liquid bridging model for particle-to-particle contact. The coupling of these models is outlined further in the following section.

7.3.1.4 COUPLED HYBRID CONTACT MODEL

To replicate the characteristics that WSMs show in practice, the coupling of two contact models is proposed. The coupled contact model, referred to as the hybrid model, has produced the most realistic representation of a WSM. This is shown in research by the author (Carr et al. [166, 247]). The hybrid model is a combination of the SJKR model (outlined in Section 7.3.1.1), for particle-to-wall contacts and the Easo liquid bridging model (outlined in Section 7.3.1.3), for particle-to-particle contacts. The coupled model has been found to be the most realistic model available from an industrial perspective, where the solve times are acceptable for the accuracy of the obtained result. It is appropriate to identify that the EEPA contact model is capable of obtaining results which portray slightly more accurate results in comparison to the developed hybrid model. This however, does come at the price of significantly longer computation times (estimated to be approximately eight times longer than the hybrid model). This becomes much more evident when the quantity of particles in the simulation domain increases, such as the simulation of an industrial transfer chute which can operate up to 12,000 tonnes per hour for iron ore. Additionally, the vast array of parameters which require calibration for the EEPA model make the calibration procedure, as outlined in Section 7.5.2, significantly time consuming.

When the SJKR model (outlined in Section 7.3.1.1) is used for both particle-to-wall and particle-to-particle contacts, the resulting particle flow behaviour results in a stiffer more rigid flow of the particles typically used to represent cohesive powders. Additionally, when the build-up of the bulk material onto a vertically mounted wall liner (representing the hood of a typical transfer chute) is considered, the SJKR fails to replicate these behaviours, as shown in Section

7.6. Similarly, when the Easo liquid bridging model (outlined in Section 7.3.1.3) is used for both particle-to-wall and particle-to-particle contacts, the behaviours exhibited by WSMs are failed to be replicated when particle-to-wall contacts are considered. It is appropriate to identify, that the characteristics of WSMs can be replicated using the Easo liquid bridging model for certain applications. This occurs for applications which only require particle-to-particle contacts to be considered, such as the draw down experimental measurement (outlined in Section 7.5.1.2).

By coupling the SJKR model (outlined in Section 7.3.1.1), for particle-to-wall contact and the Easo liquid bridging model (outlined in Section 7.3.1.3), for particle-to-particle contact, a contact model capable of replicating the behaviours exhibited by WSMs for transfer system applications is created. This is shown in the replication of the build-up of the bulk material onto a vertically mounted wall liner, as shown in Section 7.6. An experimental setup has been constructed (as shown in Section 7.6) to verify the suitability of the hybrid model in replicating the dynamic adhesion of problematic iron ore samples onto a vertically mounted wall liner. Additionally, a series of DEM calibration simulations with systematic parameter variation are conducted to obtain the most accurate set of parameters to replicate the supplied iron ore samples in the simulation domain (as shown in Section 7.5.3). The developed calibration matrices allow for the formation of a parameter database, which can be used for the simulation of on-site applications to optimise plant geometry and other operational parameters. The explanation of the parameters which require systematic variation and the developed calibration procedure are outlined in the succeeding sections.

7.4 DEM CONTACT MODEL INPUT PARAMETERS

Numerical modelling simulations require the calibration of parameters as an essential step for an accurate solution. This is especially found to be the case when DEM is considered. To replicate the behaviours bulk materials show in reality, the sliding and rolling resistance of spherical particles must be considered. These parameters ultimately influence the macroscopic behaviour of non-cohesive bulk materials [146]. By using spherical particle shape representation for this research, a calibration procedure is necessary to replicate the behaviour of the bulk material. During the calibration procedure, the stiffness of the particles typically dictate the required solve time [147, 148]. It is quite common to reduce the stiffness of the particles to improve the efficiency of the simulation solve time. This in effect makes the calibration of sliding and rolling resistance to be of critical importance.

When the additional parameters required for the calibration of cohesive bulk materials are considered, the quantity of simulations and in effect time required for the calibration procedure to be undertaken significantly increase. It is therefore essential to outline the parameters which require implementation into LIGGGHTS® [220] version 3.8.0 for the available cohesion contact models (outlined in Section 7.3.1). The following sections outline the required input parameters and which parameters require calibration using a systematic parameter variation approach. Additionally, the parameters used for the simulations of IOB at 18.5% MC are also outlined in Section 7.4.3.

7.4.1 EEPA CONTACT MODEL INPUT PARAMETERS

During the initial parameter input for the EEPA contact model [212], parameters are loaded into an input script which calls LIGGGHTS® [220] version 3.8.0 to run the simulation. The following parameters are required for implementation prior to the simulation:

- Force overlap relationship power value, n_p, defines if a linear or non-linear model is used;
- Loading spring stiffness, k_1, defines the initial loading stiffness of the particles;
- Unloading spring stiffness, k_2, defines the unloading/reloading stiffness condition of the particles as a ratio of k_1;
- Adhesive force, f_0, defines the constant pull-off force which will be acting between the particles;
- Adhesive surface energy, $\Delta\gamma$, defines the amount of adhesion which will be acting between the particles (holding the particles together);
- Adhesion branch exponent, x, defines the severity of the acting adhesion force following the condition of the peak tensile force that has been obtained;

In addition to the input parameters outlined above, the particle sliding friction and particle rolling friction, are also required as input parameters. When the systematic parameter variation approach for the EEPA contact model [212] is considered, the vast array of parameters required makes this process extremely time consuming. Additionally, when the calibration of WSMs is considered, the identification of a unique parameter setting also proves to be a much more time consuming and computationally expensive exercise. This becomes evident when the parameters required for the developed hybrid model (outline in Section 7.4.2) are considered.

It will be appropriate to identify that the current implementation of the EEPA contact model [212] in the open source software LIGGGHTS® [220] version 3.8.0 is in an unoptimised state which currently take approximately 20% longer than an optimised implementation.

Although the unoptimised version of the EEPA contact model [212] has been used, the required solve time for a simulation is approximately eight times longer than the developed hybrid contact model. This becomes much more significant when the quantity of particles increases for the simulation of an industrial sized materials handling system. For these reasons it has been deemed more appropriate for the use of the developed hybrid contact model for the simulation of WSMs for transfer system applications.

7.4.2 HYBRID CONTACT MODEL INPUT PARAMETERS

During the initial parameter input for the developed hybrid contact model, parameters are loaded into an input script which calls LIGGGHTS® [220] version 3.8.0 to run the simulation. The following parameters are required for implementation prior to the simulation:

- Surficial liquid volume to solids volume, V_{slc}, defines the liquid volume surrounding the particles (measured moisture content is used);
- Surface tension, σ_{ST}, defines the surface tension of the liquid bridge acting between the particles;
- Fluid viscosity, μ_f, defines the viscosity of the fluid in the liquid bridge acting between the particles (assumed to be water i.e. 0.00089 [Pa.s]);
- Contact angle, θ_c, defines the angle of contact formed between the liquid bridge and the particles (assumed to be 60°);
- Adhesion energy density, Ω_{AED}, defines the amount of adhesion which will be acting between the particles and the boundary surfaces (sticking the particles to surfaces);

In addition to the input parameters outlined above, the particle sliding friction and particle rolling friction are also required as input parameters. For the simulation of WSMs, the developed hybrid contact model has been observed to be a more efficient and better representation of industrial applications. This becomes evident when the parameter set which requires iteration and the computational solve times are considered. This can be best determined when the comparison between the hybrid contact model and EEPA contact model [212] are considered.

A systematic parameter variation approach has been utilised for the calibration procedure, outlined in Section 7.5.2 of the developed hybrid contact model. The parameters which require iteration as part of the calibration process for particle-to-particle contacts include the particle sliding friction, particle rolling friction and the surface tension of the liquid bridge. When particle-to-wall contacts are considered, the iteration of the adhesion energy density is required. The parameters which have been used for the simulations undertaken to replicate the behaviours of IOB at 18.5% MC are outlined in the following section.

7.4.3 CALIBRATION INPUT PARAMETERS

The successful selection of a unique parameter set, capable of replicating a range of lab experiments are dictated by the calibration procedure used. These lab experiments must consider a range of materials handling processes, where different flow regimes are used in the aim to replicate industrial processes. For instance, typical lifting cylinder AOR measurements fail to capture the dynamic flow conditions which may be experienced on site in an industrial transfer system. To address these potential drawbacks of DEM, it is essential to calibrate problematic bulk materials with experimental measurements capable of providing flow regimes which can assist in replicating industrial processes. The developed calibration procedure, outlined in Section 7.5.2, uses a range of lab experiments which consider a range of flow regimes. Each of these experiments consider dynamic flow conditions in the aim of replicating problematic bulk material behaviours as they negotiate the materials handling stream.

One of the most debated topics in DEM is the consideration of the particle size range which is simulated. It is unfeasible and almost impossible to undertake any simulation which considers an industrial materials handling system if the real PSD is considered. For instance, if a simple shear box calibration simulation (outlined in Section 7.5.1.1) was undertaken using the real PSD the quantity of particles is far beyond the current capabilities of modern-day computers. This is best explained if IOB was considered where 40 kg of sample would be required to undertake an experimental measurement. In the case where the real PSD of IOB was used to conduct a simple shear box simulation, approximately 427 million particles would be required. This problem becomes much more concerning if a transfer system which operates in excess of 12,000 tonnes per hour required a DEM simulation to be conducted. For these reasons, it is necessary and more appropriate to use either a scalped or scaled PSD for the simulations which are undertaken for the simulations conducted in this research.

The calibration simulations, outlined in Section 7.5.3, have been undertaken using parameters to replicate the behaviours of IOB at 18.5% MC. As determined above, a modified PSD is required to undertake the simulations in a realistic timeframe. A scalped particle diameter has been utilised where the experimental PSD curve for IOB is shown in Figure 7.6. A cut-off range has been set where any particles below this limit are assumed to be 5.6mm, where the

DEM PSD is shown in Figure 7.6. The particle diameter ranges above the set limit use the same values as those which were measured in the lab.

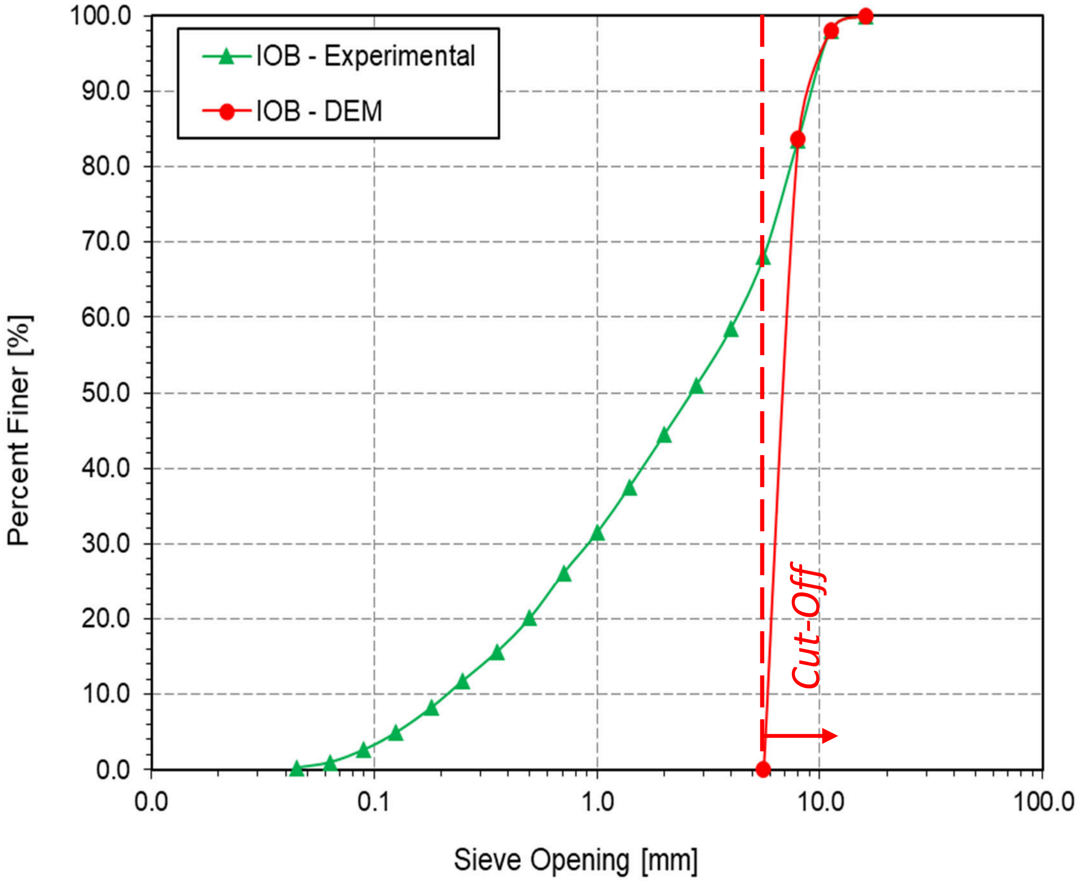

Figure 7.6 – Particle size distribution of IOB showing scalped particle diameter range.

The selection of input parameters requires careful consideration and, in most cases, experimental measurement values are used as input variables. In the case where measured values can be used, these remain constant for all of the simulations undertaken within the scope of this research. For the values which cannot be directly measured with experimental measurements, the calibration of these parameters, using the procedure outlined in Section 7.5.2, is undertaken. A summary of the parameters which are required for the input script which calls LIGGGHTS® [220] version 3.8.0 to undertake the simulations are shown in Table 7.1.

Table 7.1 – DEM Parameters for IOB at 18.5% MC

Input Parameter	*Units*	*Value*
Time Step	[s/step]	9e-6 (≅10% Rayleigh Time)
Coefficient of Restitution (particle-to-particle)	[-]	0.3 (Estimated)
Coefficient of Restitution (particle-to-wall)	[-]	0.4 (Estimated)
Bulk Density	[kg/m^3]	1500
Particle Density	[kg/m^3]	see Section 7.5.2
Poisson's Ratio	[-]	0.3
Young's Modulus	[Pa]	1e8
Minimum Particle Radius	[mm]	2.8
Particle Sliding Friction	[-]	see Table 7.5
Particle Rolling Friction	[-]	see Table 7.5
Wall Friction (Perspex)	[-]	0.32
Wall Friction (Rubber Belt)	[-]	0.55
Wall Friction (Ceramic Wall Liner)	[-]	0.68
Wall Friction (Mild Steel Wall Liner)	[-]	0.65
Adhesion Energy Density	[J/m^3]	see Section 7.5.2
Surficial Liquid Volume	[%]	18.5
Surface Tension	[N/m]	see Table 7.5
Fluid Viscosity	[Pa.s]	8.9e-4
Contact Angle	[°]	60

The determination of the wall friction coefficients and bulk density measurements used for the simulations conducted in this research have been undertaken using the procedures outlined in Sections 2.5.2 and 2.4.6 respectively. It is important to note since the kinematic wall friction angle depends on normal stress, the wall friction is not constant across the range of consolidation stresses. From this, the wall friction coefficients (outlined in Table 7.1) have been determined from an estimation of the consolidation conditions experienced during the conducted experimental measurements. It is also important to identify that the particle-to-wall rolling friction is assumed to be the same as the particle-to-particle rolling friction values.

The timestep and Young's Modulus of the particles have been set to values which are sufficient to run the simulations in a reasonable timeframe. Additionally, these values produce results where the particles in the simulation domain are stable. This is best explained when the particles of the shear box test (outlined in Section 7.5.1.1) are considered, where the resulting mass of particles remain stable once the box has been filled. In the case where a lower Young's Modulus value is used, a pulsing velocity field can be observed. This is attributed to the spherical particles being too soft and the dissipation of energy in the system requiring significantly longer times to achieve steady state.

It is appropriate to identify the density of the particles require to be adjusted depending on the calibrated parameters. This is best explained if a simple shear box test (outlined in Section 7.5.1.1) is considered. For this case a higher number of particles are required to fill the same volume if a lower surface tension (amount of cohesion) is compared to using higher values of surface tension. Due to the dynamic flow regimes of the calibration experiments (outlined in Section 7.5.1), it is essential to match the bulk density between experimental measurements and simulation results. The parameters which require calibration using the procedure outlined in Section 7.5.2 include the particle sliding and particle rolling friction, the surface tension of the liquid bridge and the adhesion energy density for particle-to-wall contacts. The corresponding calibration simulations and the range of values used are outlined in Section 7.5.3.

7.5 DEM CALIBRATION OF WET AND STICKY BULK MATERIALS

Calibration procedures for dry non-cohesive bulk materials exist which typically alter the simulation parameters using a systematic variation of parameter approach [146, 149]. To determine the friction parameters for dry non-cohesive bulk materials there are many calibration experiments which exist. Some of the notable calibration experiments have been identified in Section 7.2. General calibration procedures generally use a single experiment to determine the sliding and rolling friction parameters for dry non-cohesive bulk materials. This results in a multitude of parameter combinations which can replicate the experiment which is being simulated. By only using a single calibration experiment, the selection of a unique parameter combination is extremely difficult to obtain [146]. In the work of Roessler et al. [167] a procedure for the calibration of non-cohesive bulk materials using a range of calibration experiments is considered. This enabled the use of several calibration experiments to be conducted which would then result in several reference values for the calibration. This in turn results in a unique parameter combination. With the determination and correct use of unique parameter settings, users of DEM can have confidence that the selected parameter settings are capable of replicating any materials handling system.

When the calibration of WSMs is considered, new calibration methods must be considered. This is due to the additional adhesion parameters which are required for use in the more complex contact models (as outlined in Section 7.3.1). These additional parameter settings also require calibration in addition to the sliding and rolling resistance. This in turn significantly increases the quantity of simulations and time required for a typical calibration. To undertake the calibration of WSMs using a systematic parameter variation approach, a new method is proposed as shown in Section 7.5.2. To ensure a unique parameter set is obtained, sufficient calibration experiments are essential. The calibration experiments used for the determination of a unique parameter set of IOB at 18.5% MC are outlined in the following section.

7.5.1 CALIBRATION EXPERIMENTS

The calibration of parameters is key to the accuracy of any DEM simulation. When determined correctly, the selected parameter set can represent the physical behaviours which a bulk material shows in practice. It is therefore necessary to undertake experiments to calibrate the parameters identified in Section 7.4. For the DEM simulations conducted within this thesis, a range of calibration experiments have been undertaken on IOB at 18.5% MC. These calibration experiments are undertaken in two streams for particle-to-particle and particle-to-wall contacts. When the more complex particle-to-particle contacts are considered, two calibration experiments have been used. These include shear box tests and draw down tests, where the arching case of the draw down testing is used for validation of the particle-to-particle calibration. For the particle-to-wall contact calibration, two calibration experiments are used. These include the dynamic adhesion inclined plate tests, which represents the spoon of a transfer chute and the dynamic adhesion vertical impact tests, which represents the hood of a transfer chute. Similar to the arching case of the draw down test, the dynamic adhesion vertical impact tests are used as a final validation. The following sections outline each of the calibration experiments. The corresponding results for IOB at 18.5% MC are also included.

7.5.1.1 SHEAR BOX TESTING

Shear box experiments, typically referred to as slump tests, are used to identify the internal strength of a bulk material when no consolidation loads are applied (similar to loose poured bulk density tests outlined in Section 2.4.6.1). A schematic of the shear box testing apparatus is shown in Figure 7.7 and represents a dynamic calibration scenario. The shear box used is constructed from Perspex and has a length, width and height of 300 mm. One of the vertical walls is removable to allow the bulk material to flow (slump) out of the shear box.

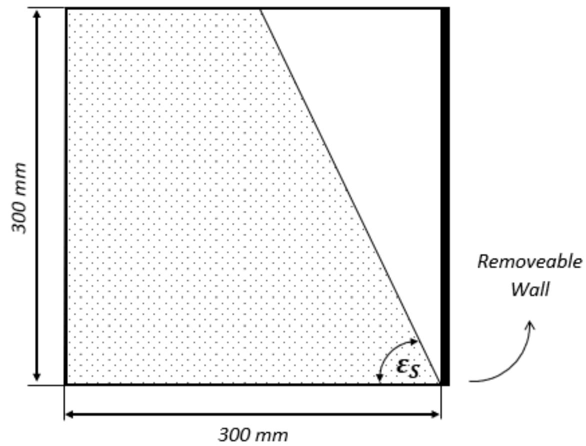

Figure 7.7 – Schematic of shear box testing apparatus.

For the conducted shear box experiments, IOB at 18.5% MC has been tested where approximately 40 kg of sample was required. The iron ore sample was carefully filled to the top of the shear box without adding consolidation to the sample. The iron ore sample was then screed, to result in a known volume of bulk material. After this stage, the flap was rapidly opened, and the iron ore sample was allowed to flow out of the shear box. The residual bulk material in the shear box forms a slope which is typically referred to as the shear angle. Upon completion of each experiment, the residual mass and shear angle, ε_S, are determined and recorded to be used as reference values for the DEM calibration. A summary of the shear box experimental results for IOB at 18.5% MC are summarised in Table 7.2.

Table 7.2 – Shear Box Testing Results for IOB at 18.5% MC

Parameter	*Units*	*Value*
Initial Mass	[kg]	40.3
Residual Mass	[kg]	30.8
Shear Angle	[°]	65.5

7.5.1.2 DRAW DOWN TESTING

To replicate the discharge of a hopper or bin, the draw down test has been developed. The draw down test, as shown in Figure 7.8, consists of an upper and lower box where each box is 500mm high, 500mm wide and 100mm deep. The upper box has a discharge gate (flaps) and an adjustable rectangular opening at the bottom. The discharge gate is rapidly opened (0.3 seconds) and the bulk material sample is allowed to discharge into the lower box. The outflowing bulk material forms a stock pile in the lower box (AOR measurement), while the remaining bulk material forms two slopes in the upper box (shear angle measurement).

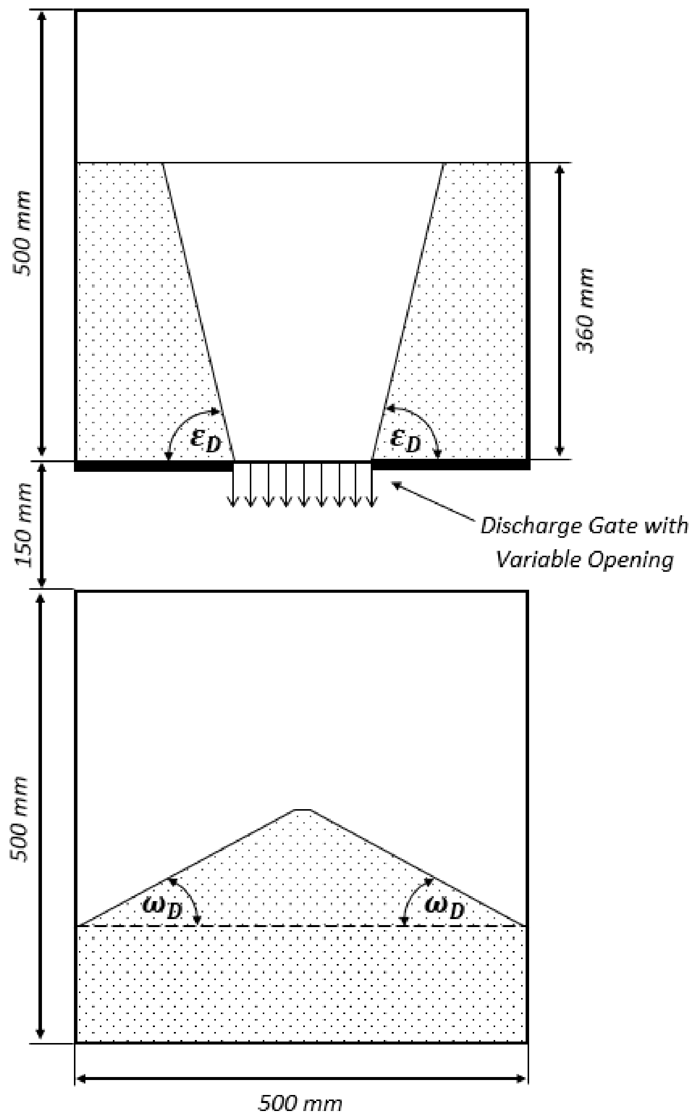

Figure 7.8 – Schematic of draw down testing apparatus.

For the conducted draw down experiments, IOB at 18.5% MC has been tested where approximately 30 kg of sample was required. The iron ore sample was carefully filled into the upper box without adding consolidation to the sample. The iron ore sample was then screed to be level and the height of the material was measured (360 mm). After this stage, the discharge gates were rapidly opened, and the iron ore sample was allowed to flow out of the upper box. The residual bulk material in the lower box forms a stock pile, which is typically referred to as the Angle of Repose (AOR), where the remaining slope angles in the upper box gives the shear angle of the bulk material. Upon completion of each experiment, the residual mass in the lower box, AOR, ω_D, and shear angle, ε_D, are determined and recorded to be used as reference values for the DEM calibration. A summary of the draw down experimental results for IOB at 18.5% MC are summarised in Table 7.3.

Table 7.3 – Draw Down Testing Results for IOB at 18.5% MC

Parameter	*Units*	*Value*	
Initial Mass	[kg]	29.8	29.8
Opening Dimension	[mm]	200	150
Upper Box Sample Height	[mm]	360	360
Residual Mass (Lower Box)	[kg]	14.37	1.96
Angle of Repose	[°]	32.6	N/A
Shear Angle	[°]	80.1	N/A
Regime	N/A	Flowed	Arched

7.5.1.3 DYNAMIC ADHESION INCLINED PLATE TESTING (SPOON CASE)

To replicate the dynamic flow conditions of a bulk material onto the spoon of a transfer chute, the dynamic adhesion inclined plate test (as outlined in Section 6.2) has been undertaken. This calibration test consists of a 450 mm wide belt conveyor situated 1500 mm above a wall liner which allows for varying angles to be investigated. By investigating a range of wall liner angles, the threshold adhesion present in a bulk material sample for particle-to-wall contacts can be determined. A schematic of the dynamic adhesion inclined plate test is shown in Figure 7.9. The residual mass and maximum build-up height perpendicular to the wall liner surface are determined for a range of wall liner angles. The upper (no residual mass) and the lower (highest residual mass) tested wall liner angles are used for the DEM calibration of the AED (outlined in Section 7.3.1.1).

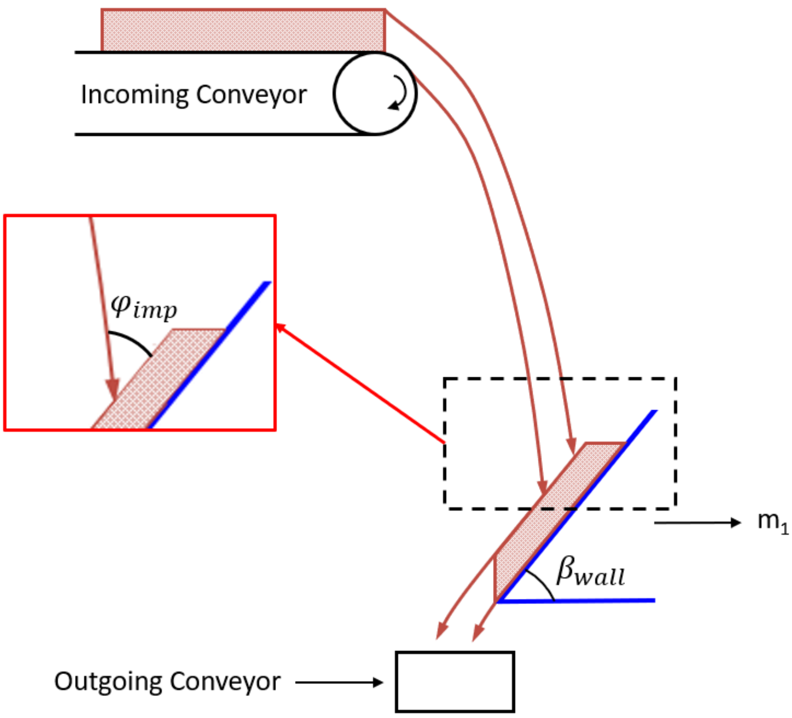

Figure 7.9 – Schematic of dynamic adhesion inclined plate testing apparatus.

For the conducted dynamic adhesion inclined plate experiments, IOB at 18.5% MC has been tested, where a ceramic wall liner has been used. The iron ore sample was loaded onto the conveyors, where the burden profile was calculated during the experiment as the bulk material leaves the head pulley, where a mass flow rate of 6.3 kg/s was measured. This is achieved using a Sony RX10 M3 DSLR camera which is capable of recording up to 1000 frames per second at High Definition quality. This was deemed to be sufficient when the estimated impact velocities were considered. The impact height remained constant at 1500 mm and the belt velocity was also held constant at 0.6 m/s. Upon completion of each experiment, the residual mass which remained on the wall liner, m_1, and the wall liner angle, β_{wall}, are recorded where these values are used as reference values for the DEM calibration. A summary of the dynamic adhesion inclined plate experimental results for IOB at 18.5% MC are summarised in Table 7.4.

Table 7.4 – Dynamic Adhesion Inclined Plate Testing Results for IOB at 18.5% MC

Parameter	*Units*	*Value*	
Wall Liner Angle	[°]	35	60
Drop Height	[mm]	1500	1500
Belt Speed	[m/s]	0.6	0.6
Mass Flow Rate	[kg/s]	6.34	6.34
Burden Width	[mm]	205.6	205.6
Burden Height	[mm]	42.4	42.4
Residual Mass	[kg]	11.3	0.1

7.5.2 CALIBRATION PROCEDURE AND FLOW CHART

The calibration of WSMs can be extremely complex depending on the modelling application which is required to be simulated. This is attributed to the additional adhesion parameters which are required for use in the more complex contact models (as outlined in Section 7.3.1). To reduce this complexity, the developed calibration procedure considers two calibration streams which are undertaken for particle-to-particle and particle-to-wall contacts separately. Due to the vast array of parameters (as outlined in Section 7.4) which require calibration for particle-to-particle contacts, it is appropriate to calibrate these parameters first. The proposed calibration procedure flowchart for particle-to-particle contact is shown in Figure 7.10.

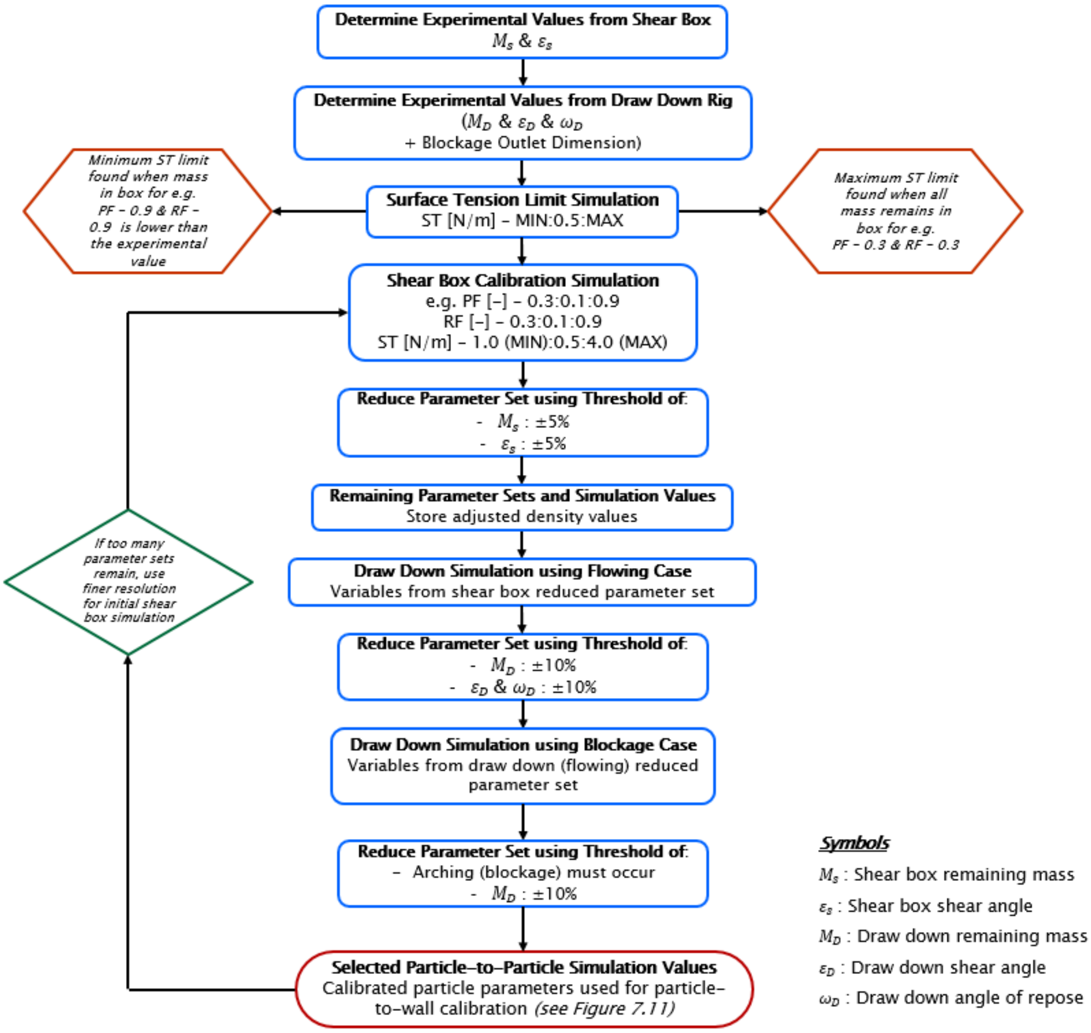

Figure 7.10 – Calibration procedure for particle-to-particle contact.

The calibration experiments required for particle-to-particle calibration of a WSM include shear box testing and draw down testing. Each of these testing apparatuses are outlined in Section 7.5.1 where the corresponding results for IOB at 18.5% MC are also included. The first stage of the particle-to-particle calibration uses the shear box experiment. Once the residual mass and shear angle are determined from the shear box experimental measurements, the minimum and maximum surface tension limits are required. The minimum limit is determined when the mass in the shear box for a particle sliding friction and rolling friction of 0.9, results in a lower value than the experimental value. The maximum limit is determined when all of the particles remain in the shear box for a particle sliding friction and rolling friction of 0.3.

After the surface tension limits are determined, the systematic parameter variation process will begin. This is undertaken by iterating the particle sliding friction, rolling friction and surface tension. The iteration values used for the shear box calibration of IOB at 18.5% MC are shown in Table 7.5. The remaining input variables which have been used for the simulations conducted in this research are outlined in Section 7.4. It will be appropriate to identify when the surface tension of the liquid bridge acting between the particles increases the bulk density of the sample decreases. This is best explained in reference to the shear box overfilling, when compared to the same particle values without additional cohesion. To incorporate this effect into the calibration procedure, the density of the particles in the simulation are adjusted so the volume and mass within the shear box remains constant. It is important to note that the range of particle densities used in this research was approximately 2500 kg/m^3 to 2900 kg/m^3 depending on the value of surface tension acting between the particles.

Table 7.5 – Hybrid Contact Model Parameter Iteration Values

Contact Model Parameter	*Units*	*Parameter Iteration*
Particle Sliding Friction	[-]	0.3 : 0.1 : 0.9
Particle Rolling Friction	[-]	0.3 : 0.1 : 0.9
Surface Tension	[N/m]	1.0 : 0.5 : 3.5

Once the shear box simulations have been completed, a reduction of parameter sets occurs by applying thresholds for the remaining mass and the measured shear angle, ε_S, which are determined from the experimental measurements as outlined in Section 7.5.1.1. The threshold values which have been used for the DEM calibration of IOB at 18.5% MC were set to ±5%. After the reduction of parameters sets has been conducted, the remaining parameter sets are reduced further by simulating the draw down testing apparatus for a flowing case. Upon completion of the draw down calibration simulations, the final reduction of parameter sets occurs by applying thresholds for the remaining mass, the measured shear angle, ε_D, and the measured AOR, ω_D, which are determined from the experimental measurements as outlined in Section 7.5.1.2. To validate the remaining parameters sets and select a unique parameter set for IOB at 18.5% MC, the draw down testing apparatus is simulated for an arching (blockage) case. The resulting simulations are compared to the measured remaining mass, which is determined from the experimental measurements as outlined in Section 7.5.1.2. A summary of the obtained calibration simulation results are outlined in Section 7.5.3.

After a unique parameter set has been selected for the particle-to-particle contacts using the procedure outlined in Figure 7.10, it will be appropriate to calibrate the particle-to-wall contacts using the procedure outlined in Figure 7.11. The calibration experiments required for particle-to-wall calibration of a WSM include the dynamic adhesion inclined plate test (as outlined in Section 6.2). This calibration testing apparatus is outlined in Section 7.5.1.3 where the corresponding results for IOB at 18.5% MC are also included.

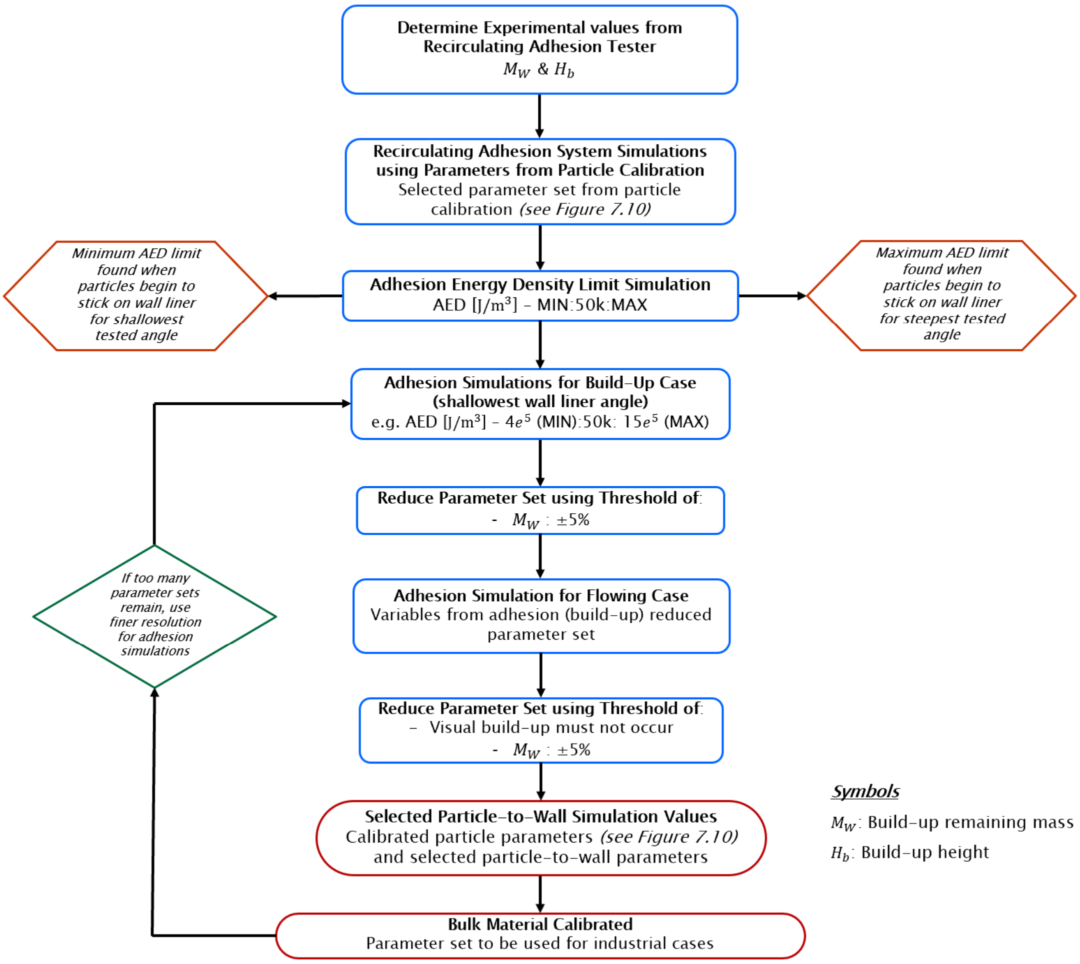

Figure 7.11 – Calibration procedure for particle-to-wall contact.

The first stage of the particle-to-wall calibration requires the residual mass for each of the tested wall liner angles (β_{wall}) to be determined from the dynamic adhesion inclined plate experimental measurements (shown in Table 7.4). Once these residual mass values are determined, the minimum and maximum Adhesion Energy Density (AED) limits are required. The minimum limit is determined when the particles begin to stick to the wall liner for shallowest tested angle. The maximum limit is determined when particles begin to stick on the wall liner for steepest tested angle. The maximum and minimum adhesion energy density thresholds for IOB at 18.5% MC occurred when the AED was $15e^5$ J/m^3 and $4e^5$ J/m^3 respectively. After the AED thresholds are determined, the systematic parameter variation process for particle-to-wall contacts begins by iterating the AED between the determined threshold values. This is conducted for the unique particle-to-particle parameter setting determined in Section 7.5.3. The remaining input variables which have been used for the particle-to-wall calibration simulations conducted in this research are outlined in Section 7.4.

Once the dynamic adhesion inclined plate simulations have been completed, a reduction of the AED parameter set occurs by applying a threshold for the residual mass on the selected (shallowest) wall liner. These residual mass values are determined from the experimental measurements as outlined in Section 7.5.1.3. The threshold values which have been used for the DEM calibration of IOB at 18.5% MC were set to ±10%. A summary of the obtained calibration simulation results are outlined in the following section. To validate the selected parameter set, a further simulation is conducted using a different wall liner angle. Upon the successful selection of a unique parameter set for IOB at 18.5% MC, the final validation for industrial applications will be undertaken as outlined in Section 7.6.

7.5.3 CALIBRATION SIMULATIONS AND MATRICES

To identify if a unique parameter setting can be selected and used to conduct the modelling in Section 7.6, a series of calibration simulations are undertaken using the developed calibration procedure outlined in the previous section. These calibration simulations are conducted for the parameters outlined in Section 7.4.3. The first stage of the calibration simulations require the limits for the amount of surface tension (cohesion) to be identified. This is undertaken using the shear box test (outlined in Section 7.5.1.1) where the threshold and corresponding iteration (calibration) values are shown in Table 7.5. A total of 294 (7 x 7 x 6) simulations are required to undertake the first stage of the calibration procedure.

Once the initial calibration simulations are undertaken, a reduction of parameter sets can occur. The residual mass and the measured shear angle, ε_S, which are determined from the experimental measurements, as outlined in Section 7.5.1.1, are utilised to reduce the parameter sets from the initial shear box simulations. The residual mass results of the shear box simulations can be visualised in the contour plots shown in Figure 7.12 where a limit value of ±5% has been applied. Additionally, the measured shear angle contour plots are shown in Figure 7.13 where a limit value of ±5% has been applied. The following section shows the results of the selected parameter setting which is used for the reminder of the simulations conducted within this research. The selected parameter values are shown in Table 7.6.

Table 7.6 – Hybrid Contact Model Calibrated Parameter Values

Contact Model Parameter	*Units*	*Parameter Value*
Particle Sliding Friction	[-]	0.5
Particle Rolling Friction	[-]	0.3
Surface Tension	[N/m]	3.5

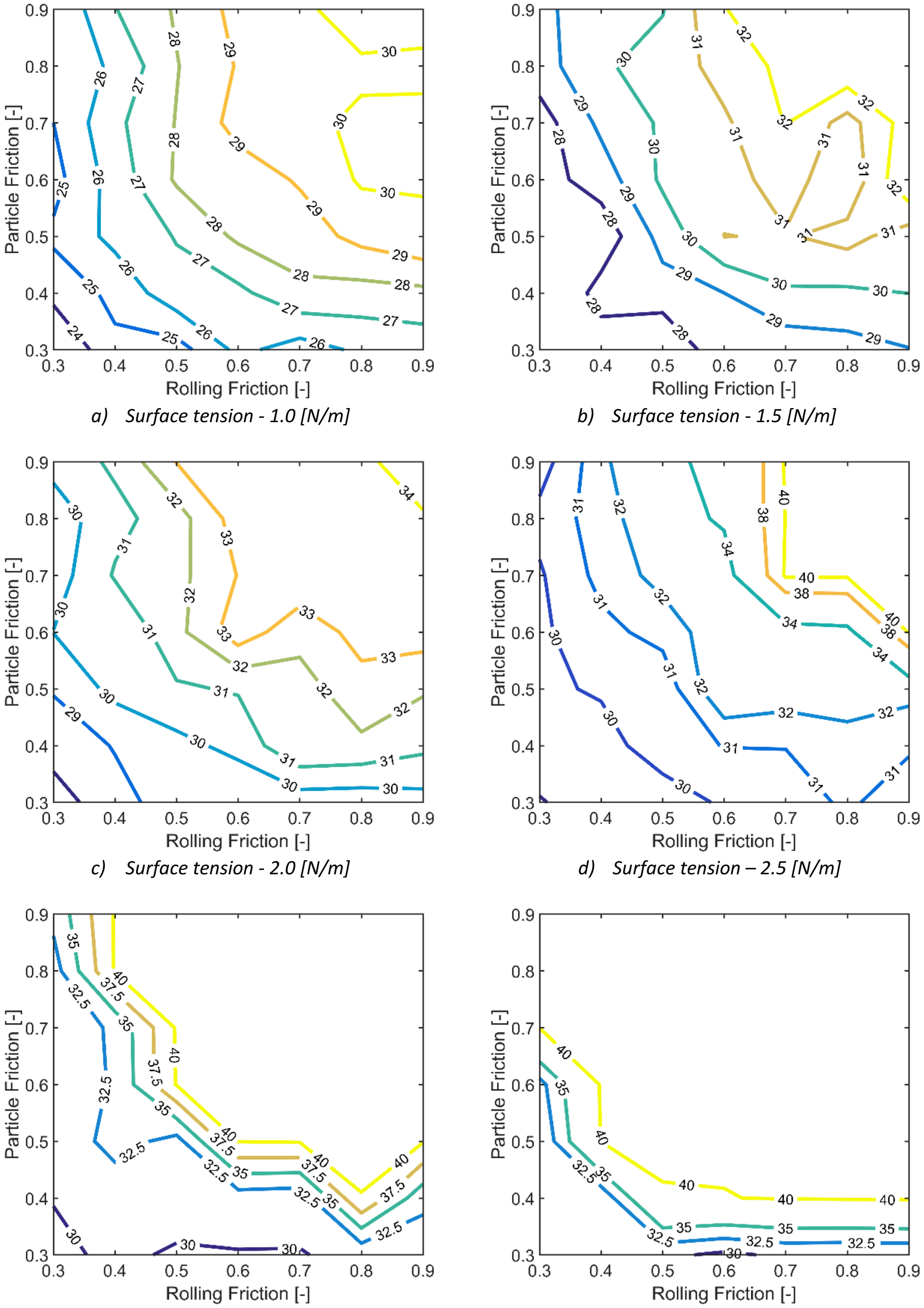

a) *Surface tension - 1.0 [N/m]*
b) *Surface tension - 1.5 [N/m]*
c) *Surface tension - 2.0 [N/m]*
d) *Surface tension – 2.5 [N/m]*
e) *Surface tension - 3.0 [N/m]*
f) *Surface tension – 3.5 [N/m]*

Figure 7.12 – Calibration matrices for shear box simulation residual mass.

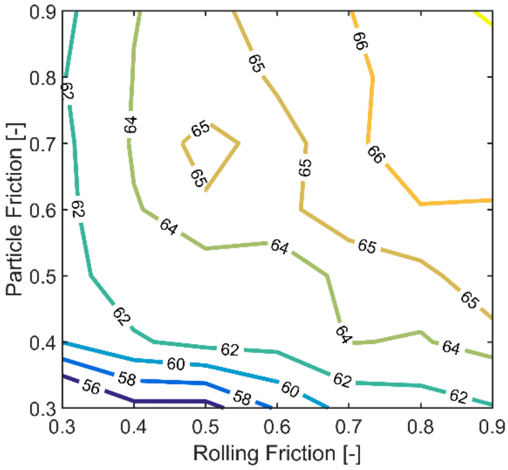

a) Surface tension - 1.0 [N/m]

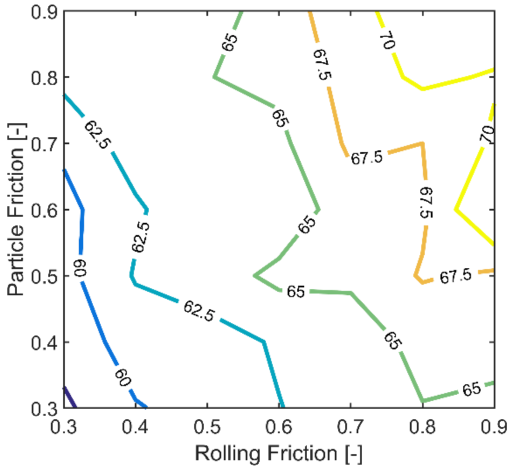

b) Surface tension - 1.5 [N/m]

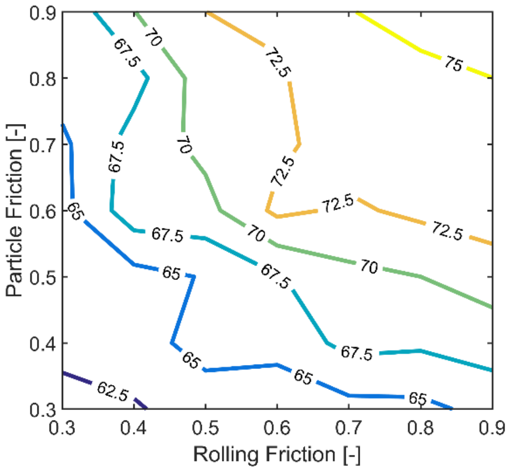

c) Surface tension - 2.0 [N/m]

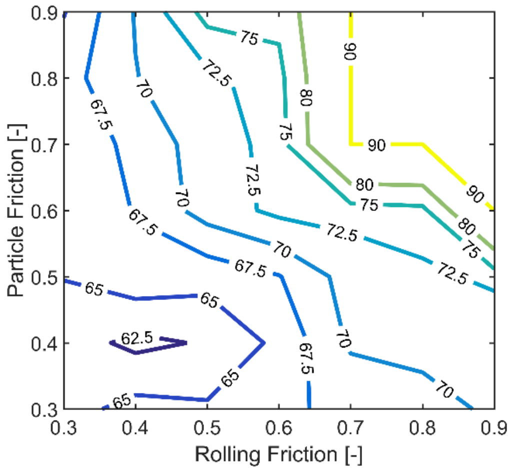

d) Surface tension – 2.5 [N/m]

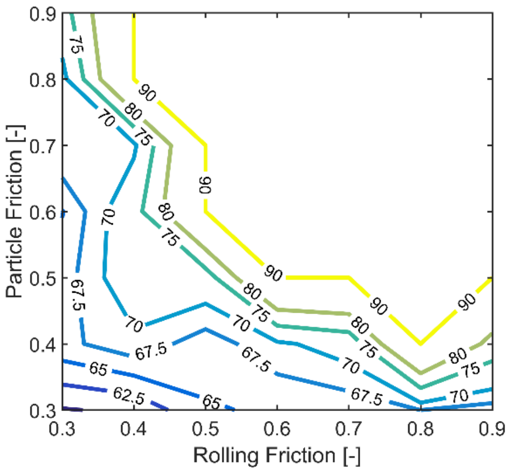

e) Surface tension - 3.0 [N/m]

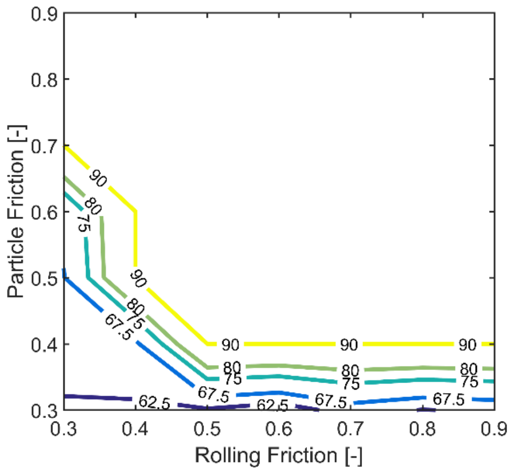

f) Surface tension – 3.5 [N/m]

Figure 7.13 – Calibration matrices for remaining shear angle, ε_S, for shear box simulations.

The comparison between shear box experimental measurements and simulated data for the selected parameter set is shown in Figure 7.14, where the similarities of the measured shear angle can be immediately identified. This becomes evident when the residual mass and measured shear angle are considered.

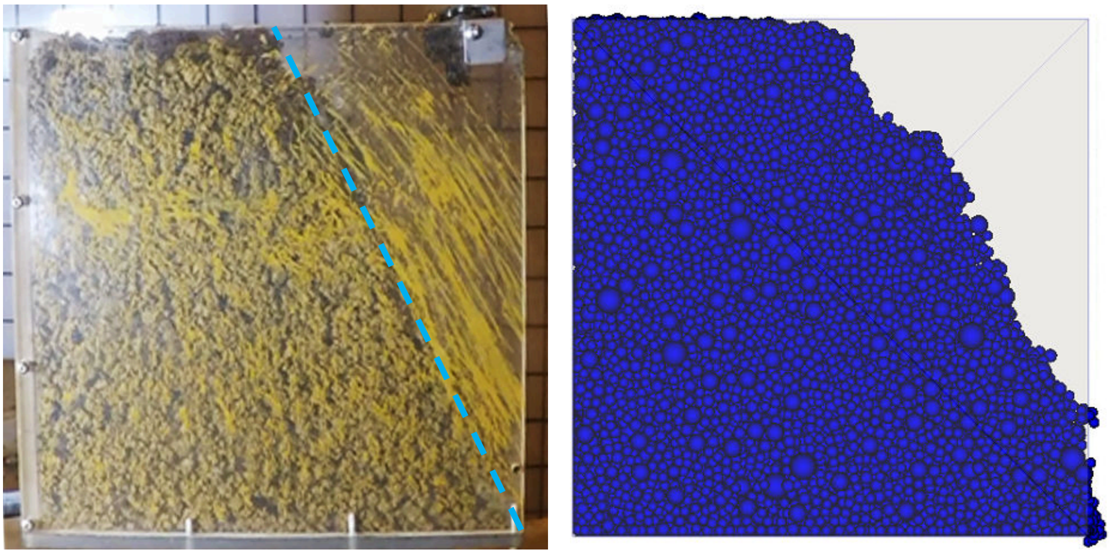

a) *Experimental result* b) *Simulation result*

Figure 7.14 – Comparison between experimental and simulation result for shear box testing.

A summary of the comparison to simulated data and experimental measurement values for the shear box test are shown in Table 7.7. It will be appropriate to identify that the residual mass is a more definitive threshold in comparison to the measured shear angle. This is attributed to the erroneous measurements of the shear angle, which can vary by up to 5°, depending on the interpretation of where the angle should be measured.

Table 7.7 – Shear Box Testing Results Comparison

Reference	*Units*	*Experimental*	*Simulation*	*Deviation*
Residual Mass	[kg]	30.8±0.6	30.2±0.3	-2.0 %
Shear Angle	[°]	65.5±1.9	67.2±1.4	+2.5 %
Bulk Density	[kg/m^3]	1492.6	1589.2	+6.1 %

The second stage of the calibration process utilises the draw down test for a flowing case and can occur once the reduction of parameter sets has been undertaken. The comparison between draw down experimental measurements and simulated data for the selected parameter set is shown in Figure 7.15, where the similarities of the measured shear angle and AOR can be immediately identified. This becomes evident when the residual mass, measured shear angle and measured AOR are considered.

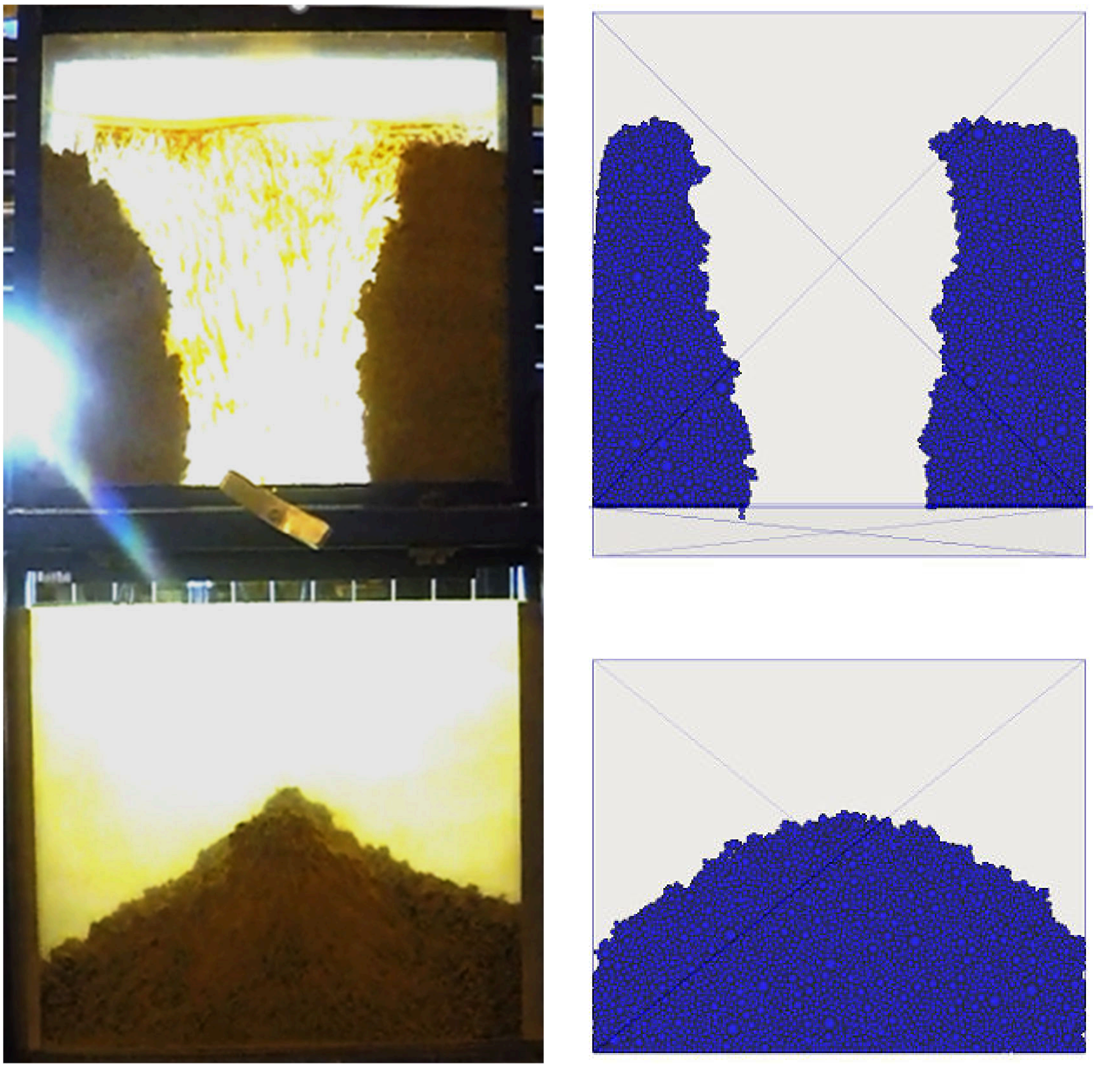

a) Experimental result *b) Simulation result*

Figure 7.15 – Comparison between experimental and simulation result for draw down result (flowing case – 200 mm opening).

A summary of the comparison to simulated data and experimental measurement values for the flowing case of the draw down test are shown in Table 7.8. Similar to the shear box test, it will be appropriate to identify that the residual mass is a more definitive threshold in comparison to the measured shear angle and measured AOR. This is attributed to the erroneous measurements of the shear angle and AOR which can vary by up to 5° depending on the interpretation of where the angle should be measured. It is important to note that the formed AOR for the experimental measurement has a well-defined peak while the simulation has a convex shape that appears glutinous. This can be attributed to the liquid bridge models showing plastic characteristics with lack of stiffness. Additionally, particle shape and particle size may also influence the formed AOR in the simulation result.

Table 7.8 – Draw Down Testing Results Comparison (Flowing Case)

Reference	*Units*	*Experimental*	*Simulation*	*Deviation*
Residual Mass (Lower Box)	[kg]	14.4±0.7	15.6±0.5	+7.6 %
Angle of Repose	[°]	32.6±0.4	34.2±0.6	+4.7 %
Shear Angle	[°]	80.1±1.2	80.3±1.4	+0.2 %
Bulk Density	[kg/m^3]	1655.6	1589.2	-4.2 %

The final stage of the particle-to-particle calibration process utilises the draw down test for an arching (blockage) case. This can occur once the draw down simulations for a flowing case using the reduced parameter sets have been undertaken. The comparison between draw down experimental measurements and simulated data for the selected parameter set is shown in Figure 7.16, where the visual similarities are shown.

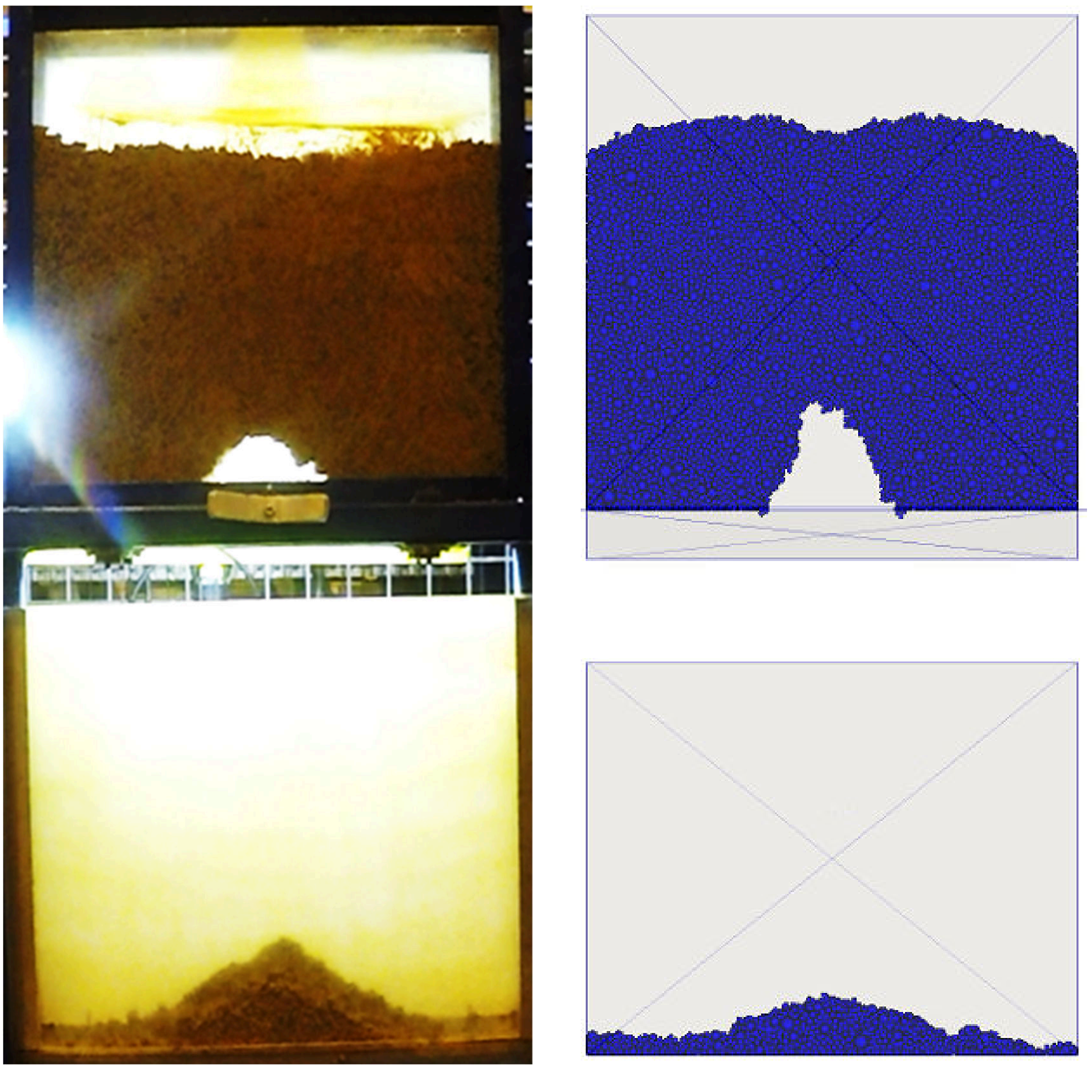

a) Experimental result *b) Simulation result*

Figure 7.16 – Comparison between experimental and simulation result for draw down result (arching case – 150 mm opening).

Since the validation of particle-to-particle calibration utilises an arching (blockage) case, measurements of the shear angle and AOR cannot be undertaken. It is therefore more appropriate to consider the residual mass which is used for the comparison between experimental measurements and simulated data. The residual mass of the simulation was found to be 1.86 kg which resulted in a deviation of -5.4% from the experimental measurement. It is important to note that the minor difference in arch shape observed between the experimental measurement and simulation result (shown in Figure 7.16) can be attributed to the particle shape and size.

The calibration of particle-to-wall contacts utilises the calibration procedure outlined in Figure 7.11. The first stage is to determine the limits for the AED which was determined to range between $15e^5$ J/m^3 and $4e^5$ J/m^3 (as outlined in Section 7.5.2). Once these values are determined, the calibration of particle-to-wall contacts can be undertaken using the dynamic adhesion inclined plate testing apparatus for a build-up case. It is appropriate to identify, the selected parameter set for particle-to-particle contacts, as determined above, is also utilised. The comparison between dynamic adhesion inclined plate experimental measurements and simulated data for the selected parameter set (AED $12e^5$ J/m^3) is shown in Figure 7.17, where the visual similarities of the residual build-up can be identified. This becomes evident when the residual mass, is considered. The residual mass of the simulation was found to be 14.72 kg which resulted in a deviation of -7.9% from the experimental measurement.

a) Experimental result

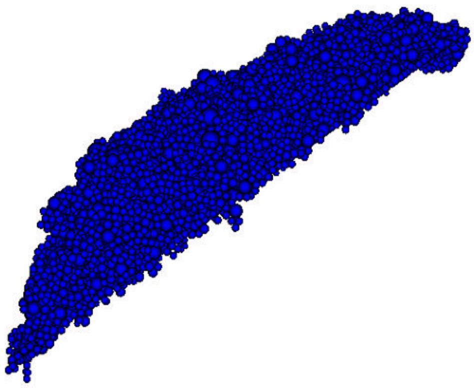

b) Simulation result

Figure 7.17 – Comparison between experimental and simulation residual mass for inclined plate testing (rough welded overlay wall liner at 35°).

It is important to note that although the residual mass may be similar, there are notable differences in the shape/profile of the build-up. This could be attributed to the lack of stiffness/rigidity in the EASO model, wall coefficient of restitution value, wall friction and wall rolling friction values which have been selected. Additionally, the selected particle-to-particle parameters may not be ideal where other combinations of particle friction, rolling friction, and surface tension could result in better a correlation.

Once the calibration of particle-to-wall contacts have been undertaken using the dynamic adhesion inclined plate testing apparatus for a build-up case, a different wall liner angle (no build-up) is considered to validate the chosen AED value. Similar to the build-up case of the dynamic adhesion inclined plate simulations, the selected parameter set for particle-to-particle contacts, as determined above, are also utilised. The comparison between dynamic adhesion inclined plate experimental measurements and simulated data for the selected parameter set (AED $12e^5$ J/m^3) is shown in Figure 7.18, where the visual similarities of no residual build-up are shown. This becomes evident when the residual mass is considered. The residual mass of the simulation was found to be 0.41 kg, which resulted in a deviation of -9.8% from the experimental measurement.

a) Experimental result *b) Simulation result*

Figure 7.18 – Comparison between experimental and simulation residual mass for inclined plate testing (rough welded overlay wall liner at 60°).

With the selection of a unique parameter set which replicates the laboratory calibration experiments, it is essential to validate these settings with a pilot scale testing facility capable of replicating on-site conditions. The parameter settings as outlined above, are utilised to investigate the build-up of a bulk material relative to a vertically mounted wall liner. The verification simulations are outlined in the following section where the comparison between the SJKR and Easo model for both particle-to-particle and particle-to-wall contacts are also investigated.

7.6 NUMERICAL MODELLING VALIDATION

Once a WSM has been calibrated using the procedure outlined in Section 7.5.2, it is essential to verify if a unique parameter set has been identified and selected. This step gives confidence in the developed calibration procedure and whether the procedure is suitable for use in the simulation of on-site applications to optimise plant geometry and other operational parameters. To verify the calibration procedure and the selected parameter set, the build-up of a bulk material relative to a vertically mounted wall liner is investigated. This application would typically be seen within the hood of an industrial transfer chute system.

The build-up of a bulk material against a vertically mounted wall liner can result in the formation of a pseudo chute surface, typically referred to as a *"rhino-horn"* due to its shape, where blockages can occur leading to the downtime of the system. This type of blockage problem has proved to be extremely challenging to model numerically in the past where the build-up of particles in the simulation domain are unable to replicate what would be observed in reality. It is therefore appropriate to model such an application both experimentally and numerically. A significant step forward results if the developed calibration procedure and hybrid contact model are capable of replicating this type of bulk material build-up. The experimental measurements and simulated results using the selected unique parameter set are outlined in the following sections.

7.6.1 DYNAMIC ADHESION VERTICAL IMPACT TESTING (HOOD CASE)

To replicate the dynamic flow conditions of a bulk material onto the hood of a transfer chute, the dynamic adhesion vertical impact test has been developed. This verification test consists of a 450 mm wide belt conveyor with an inclination angle of 10.5° situated 490 mm horizontally from the pulley centreline to a vertically mounted wall liner. The belt velocity is set to 2 m/s to investigate the dynamic conditions of a high-speed incoming bulk material stream. A schematic of the dynamic adhesion vertical impact test is shown in Figure 7.19.

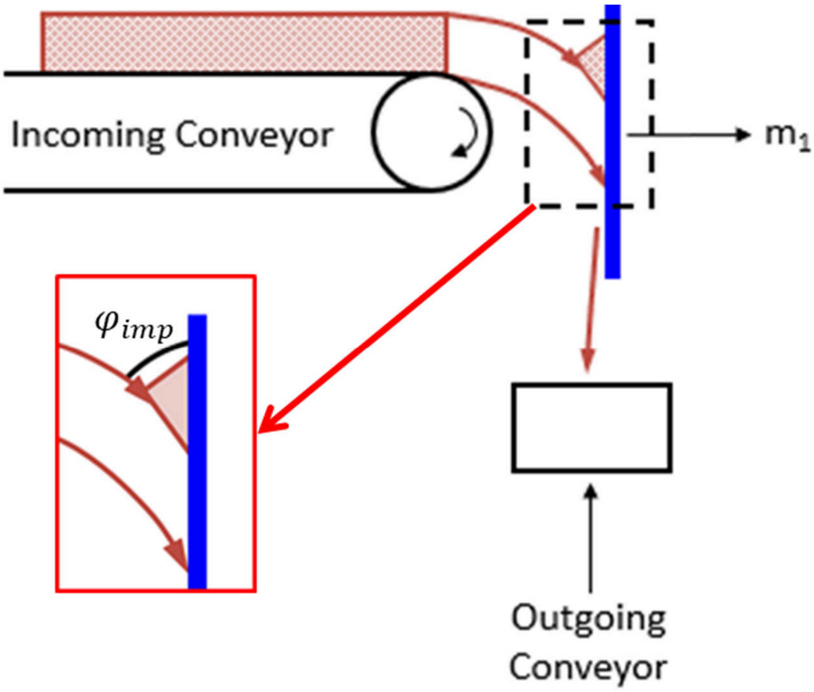

Figure 7.19 – Schematic of dynamic adhesion vertical impact testing apparatus.

For the conducted dynamic adhesion vertical impact experiments, IOB at 18.5% MC has been tested where an approximate mass flow rate of 21.1 kg/s was used. The iron ore sample was loaded onto the conveyors where the burden profile was calculated during the experiment as the bulk material leaves the head pulley. This is achieved using a Sony RX10 M3 DSLR camera where this camera is capable of recording up to 1000 frames per second at High Definition quality. This was deemed to be sufficient when the estimated impact velocities were considered. Upon completion of each experiment, the residual mass which remained on the wall liner, m_1, is recorded where these values are used as reference values for the DEM validation. A summary of the dynamic adhesion vertical impact experimental results for IOB at 18.5% MC are summarised in Table 7.9.

Table 7.9 – Dynamic Adhesion Vertical Impact Testing Results for IOB at 18.5% MC

Parameter	*Units*	*Value*
Horizontal Impact Distance	[mm]	340
Belt Speed	[m/s]	2.0
Mass Flow Rate	[kg/s]	21.1
Burden Width	[mm]	132.8
Burden Height	[mm]	82.9
Maximum Build-Up Height	[mm]	125
Residual Mass	[kg]	2.78
Approximate Angle of Impact	[°]	58

7.6.2 RESULTS AND DISCUSSION

To verify the calibration procedure and the selected parameter set (outlined in Section 7.5.3), the build-up of a bulk material relative to a vertically mounted wall liner is investigated. This type of modelling problem has proved to be extremely challenging to numerically simulate in the past, where the build-up of particles in the simulation domain are unable to replicate what is observed in reality. The flow of the experimental measurement for IOB at 18.5% MC and the calibrated simulation parameter set are shown in Figure 7.20.

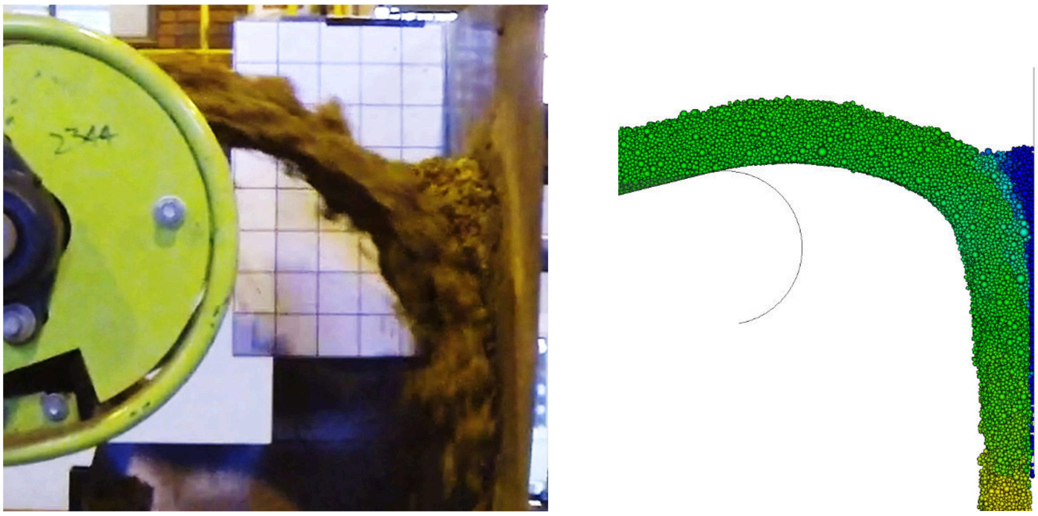

a) Experimental result *b) Simulation result*

Figure 7.20 – Comparison between experimental and simulation burden thickness for vertical impact testing.

When the experimental measurements and simulated data, shown in Figure 7.20, are compared, similarities of the particle flow can be immediately identified. This becomes evident when the formation of the stagnant bulk material zone (blue particles in the simulation result) begins to form. This is also observed within the experimental measurements, shown in Figure 7.20a, where the clarity of the stagnant zone in relation to the incoming bulk material stream represents the formation of a *"rhino-horn"*. It is important to note that differences between the incoming burden thickness can be attributed to differences in bulk density where the values in the DEM simulation may be lower than the experimental values. Upon completion of discharge of the incoming bulk material stream, a residual build-up or *"rhino-horn"* results in the presence of a WSM. The residual build-up of the experimental measurement for IOB at 18.5% MC and the calibrated simulation parameter set are shown in Figure 7.21.

a) Experimental result b) Simulation result

Figure 7.21 – Comparison between experimental and simulation residual mass for vertical impact testing (μ_s=0.5, μ_r=0.3, ST=3.5 N/m, AED=12e^5 J/m^3).

When the experimental measurements and simulated data, shown in Figure 7.21, are compared, similarities of the residual build-up can be immediately identified. This becomes evident when the maximum build-up height and residual mass are considered. A summary of the comparison to simulated data and experimental measurement values are shown in Table 7.10. It is important to note that *"stable"* rhino-horns can take time to form, where the experimental measurement and DEM simulation were undertaken for comparable periods (10 seconds). Differences between the experimental measurement and DEM simulation can be attributed to the internal strength for the EASO model which may lead to limitations when supporting a large amount of self-weight.

Table 7.10 – Dynamic Adhesion Vertical Impact Testing Results Comparison

Reference	*Units*	*Experimental*	*Simulation*	*Deviation*
Maximum Build-Up Height	[mm]	125	99.1	-26.1 %
Residual Mass	[kg]	2.78	2.24	-24.1 %
Approximate Angle of Impact	[°]	57.9	58.5	+1.0 %
Burden Height	[mm]	82.9	81.7	-1.5 %

To understand if the developed hybrid model is the best representation of a WSM it is appropriate to conduct the dynamic adhesion vertical impact test for the SJKR and Easo models in their original forms, i.e. consider particle-to-particle and particle-to-wall contacts. It is important to note that the current implementation of the Easo liquid bridging model does not allow for different parameter values when particle-to-particle and particle-to-wall contacts are considered. This results in the same calibrated parameters for both contacts where the particle-to-wall contacts are not sufficient in *"holding"* a stable rhino-horn.

To consider the SJKR model in its original form, it is appropriate to calibrate the particle-to-particle contacts using the calibration procedure outlined in Section 7.5.2. The selected parameters include; 0.8 as the particle sliding friction, 0.6 as the particle rolling friction and $8e^5$ J/m^3 as the Cohesion Energy Density (CED). A summary of the comparison of simulated data using the SJKR contact model and experimental measurement values for the shear box test are shown in Table 7.11.

Table 7.11 – Shear Box Testing Results Comparison

Reference	*Units*	*Experimental*	*Simulation*	*Deviation*
Residual Mass	[kg]	30.8±0.6	30.3±0.3	-1.7 %
Shear Angle	[°]	65.5±1.9	65.2±1.2	-0.5 %
Bulk Density	[kg/m^3]	1492.6	1589.2	+6.1 %

A summary of the comparison of simulated data using the SJKR contact model and experimental measurement values for the flowing case of the draw down test are shown in Table 7.12. For the validation of particle-to-particle contacts, the draw down test is simulated using the SJKR contact model for an arching (blockage) case. The residual mass of the simulation using the SJKR contact model was found to be 2.03 kg which resulted in a deviation of 3.4% from the experimental measurement.

Table 7.12 – Draw Down Testing Results Comparison (Flowing Case)

Reference	*Units*	*Experimental*	*Simulation*	*Deviation*
Residual Mass (Lower Box)	[kg]	14.4±0.7	15.1±0.5	+5.1 %
Angle of Repose	[°]	32.6±0.4	34.3±0.5	+5.0 %
Shear Angle	[°]	80.1±1.2	82.9±1.3	+3.4 %
Bulk Density	[kg/m^3]	1655.6	1589.2	-4.2 %

Once the calibrated values have been determined for the SJKR contact model for particle-to-particle contacts, the dynamic adhesion vertical impact test simulations can be undertaken. This was also undertaken for the Easo liquid bridging model (for the calibrated parameters) and the EEPA model, where a sensitivity analysis was undertaken to analyse the suitability of the EEPA contact model to numerically model WSMs. It is important to note that the tensile force for the SJKR model decays rapidly in comparison to the Easo model where the adhesion force for the Easo liquid bridging model is large enough with low overlap to replicate the behaviours of WSMs. Additionally, when the SJKR model is considered for internal cohesion, a rigid flow pattern is experienced (replicating a cohesive powder) which fails to hold the shape of the stable rhino-horn. This is attributed to the tensile force of the SJKR model decaying too quickly in comparison to the Easo model (as described above). When the simulated data for all four contact models, shown in Figure 7.22, are compared, it is evident that the developed hybrid contact model is the best representation of a WSM. This is evident with the residual mass and visual comparisons to the experimental measurements are considered. A summary of the residual mass simulated data values for each of the respective contact models are shown in Table 7.13. It is important to note that the EEPA model is capable of replicating this form of modelling problem (shown in Figure 7.22) to some degree however when the computational solve times and the vast array of parameters are considered, this model was deemed to be unpractical for use in industrial cases.

Table 7.13 – Dynamic Adhesion Vertical Impact Testing Contact Model Comparison

Reference	*Units*	*Easo*	*SJKR*	*EEPA*	*Hybrid*
Residual Mass	[kg]	0.35	1.14	2.08	2.24
Deviation	[%]	-694.3	-143.9	-33.7	-24.1

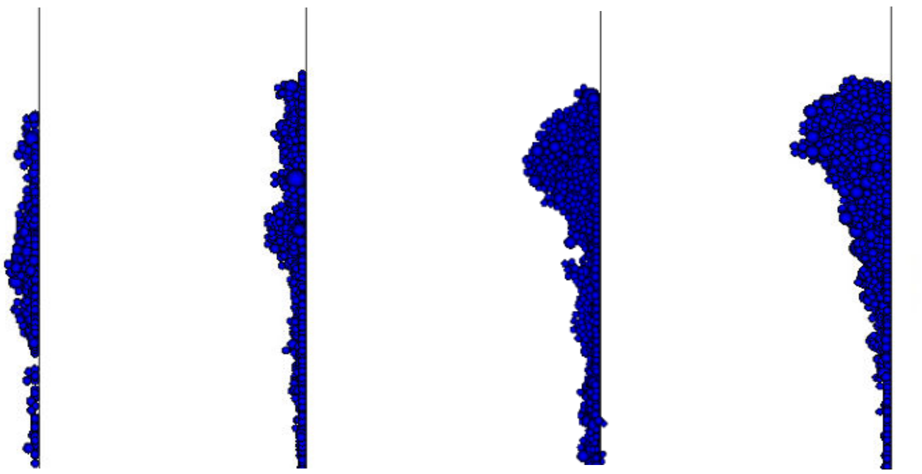

a) Easo model *b) SJKR model* *c) EEPA Model* *d) Hybrid model*

Figure 7.22 – Contact model comparison of residual mass for vertical impact testing.

The comparison of simulated data for the developed hybrid model and experimental measurement values shows good correlation where the calibration procedure outline in Section 7.5 resulted in the identification of a unique parameter setting capable of replicating the behaviours IOB at 18.5% MC shows in the materials handling stream. If the deviation between simulated data and experimental measurement values is considered, the developed hybrid contact model and developed calibration procedure for WSMs is capable of replicating problematic bulk material behaviours. This has been shown throughout all of the simulated cases where different flow regimes have been considered and the resulting deviation has shown very promising results for all of the numerical modelling cases considered.

Although the methodology presented has yielded results which are a significant step forward, it is important to note that considerable research is still required to successfully simulate WSMs into the DEM technique. It is believed that the differences which are evident between the presented experimental measurements and DEM simulation results are mainly attributed to the shape, size and stiffness of the particles. With further advances in computational technologies, it will be feasible to undertake large scale simulations where these parameters are closer to the actual bulk material. Another limitation which should be noted is the potential adhesion acting between the iron ore sample and the Perspex side walls for the draw down testing apparatus. It has been assumed that this adhesion was negligible due to the significantly low consolidation stresses which were present. Further research must therefore be undertaken to investigate the influence of consolidation stresses and the overall size constraints of the draw down testing apparatus. This investigation will allow for the identification of the minimum constraints where the influence of the adhesion has little to no influence on the flow.

7.7 CONCLUSION

This chapter has presented three cohesion contact models capable of replicating problematic bulk material behaviours. The models used include; the Simplified Johnson-Kendall-Roberts (SJKR) model, the Easo Liquid Bridging model and the Edinburgh Elasto-Plastic Adhesion (EEPA) model. Upon initial investigations, it was discovered that two models, the SJKR and Easo liquid bridging models, were unable to replicate the behaviours of bulk material blockages within transfer chute systems, when used in isolation (their original form) for particle-to-particle and particle-to-wall interactions. The EEPA was able to replicate this form of modelling problem to some degree however when the computational solve times and the vast array of parameters are considered, this model was deemed to be unpractical for use in industrial cases.

To model the blockages of transfer chute systems, the coupling of the SJKR and Easo Liquid Bridging models is proposed and consequently used to predict problematic bulk material behaviour. A calibration procedure has been developed and undertaken where the parameters for each cohesion model were discussed in detail (outlined in Section 7.4). A series of calibration simulations with systematic parameter variation were undertaken to define a set of calibration matrices where a unique parameter setting was identified. The developed calibration matrices enabled the formation of a parameter database, which can be used for the simulation of on-site applications to optimise plant geometry and other operational parameters. Finally, numerical modelling validation was undertaken using a lab scale vertical impact testing facility where a good correlation between experimental measurements and simulation results was shown.

CHAPTER EIGHT – APPLICATION TO INDUSTRY, CONCLUSIONS & RECOMMENDATIONS

The following chapter presents a summary of notable findings and key results which have been determined throughout the course of this research thesis. This is undertaken in the form of concluding remarks for each of the respective chapters. Additionally, the implications and benefits to industry are outlined. The future research which should be undertaken as a continuation from this body of work are also outlined.

8.1 APPLICATION TO INDUSTRY

The applications of the work presented within this thesis to the mining industry can be broken down into two key areas. The key areas are those which can be implemented immediately and those which can be used during mine planning strategies. It is appropriate to identify that the mine planning strategies typically result in higher OPEX to implement a solution where a greater risk is associated. For the applications to industry form an immediate standpoint, the use of Discrete Element Modelling (DEM) to numerically model WSMs (outlined in Section 7.5) allows industry to identify problematic materials handling systems and develop strategies which are implemented rapidly increasing efficiency by reducing the downtime of the system. Additionally, when the dynamic transfer system optimisation methodology (outlined in Section 6.4) is considered, protocols can be set in place which also increase the efficiency of any bulk materials handling system. This may be either by changing the properties of the bulk material or changing the geometry of the materials handling equipment. Both methods can be used to predict the potential for problematic behaviours before a WSM enters the materials handling stream.

When mine planning strategies are considered, two key components from this research can be utilised. The first being the use of correctly designed transfer systems which can be undertaken using the methodologies which have been developed in Sections 3.3 and 4.3. The main cause of problematic bulk material behaviours is attributed to the adhesive properties within the bulk material itself. By using the developed methodologies, sufficient transfer systems can be designed and utilised due to the outlined understanding into the mechanisms of adhesion.

The second strategy is the use of systems which effectively reduce the adhesive properties of the bulk material and therefore reduce the likelihood of problematic behaviours occurring. The use of agglomeration (outlined in Chapter 5) has many benefits when problematic bulk material behaviours in the materials handling stream are considered. One of the key ways to reduce the adhesive properties of a bulk material is by *"drying"*. This, however, leads a bulk material to significantly increase the propensity for dust generation. Agglomerating the bulk material within the materials handling stream, results in a novel method to reduce problematic material behaviours (outlined in Section 5.3.2) whilst maintaining the requirements of dust suppression (outlined in Section 5.3.1.3). Each of these methods may result in significant risks to a business from an OPEX viewpoint. However, the increased efficiency and reduction of the materials handling system downtime outweighs this initial risk. This becomes much more evident as the life of the mine increases.

8.2 CONCLUDING REMARKS

The primary aim of the research outlined within this thesis was to provide insight into the behavioural traits WSMs exhibit in the materials handling stream. Emphasis was on transfer systems that typically exhibit rapid induced bulk material blockages. The main areas of research were defined as:

1. The determination of a methodology to explain the dynamic adhesion of problematic bulk materials in transfer systems;
2. To investigate methods for the reduction of adhesive bonds which can allow for the continuation of flow, reducing the likelihood of blockages caused by problematic bulk materials; and
3. Adaption, development and validation of numerical models to be used for the prediction of blockage events prior to entry into the materials handling stream;

The following sections provide a summary of experimental observations and the developed theoretical models which have given a greater insight into the way bulk material adhesion is the dominating factor into rapid induced blockages in the materials handling stream. Additionally, the proposed numerical modelling methodology is summarised and comparisons of simulated data to lab scale experiments are discussed in detail. Following the summary of results obtained within the scope of this thesis, an outline of the relevant and necessary future work which has risen from each of the respective chapters is discussed in Section 8.3.

8.2.1 INDENTIFICATION AND CHARACTERISATION OF PROBLEMATIC BULK MATERIALS

Chapter 2 outlined and discussed the methods used for the identification and characterisation of problematic bulk materials. A brief summary has been presented into the problems that WSMs pose to the materials handling stream. This gave some insight into the key areas where problematic bulk material behaviours may be present in the materials handling stream. It was determined that the existing methods used to determine the physical flow properties of bulk materials lack any direct quantitative measurement technique to the amount of cohesion and/or adhesion present. To overcome this, wall adhesion and inter-particle adhesion tests were developed and undertaken. The flow property and wall lining characterisation tests that were undertaken have been outlined and a summary of key results have also been presented.

The geological regions and typical mineralogy of the supplied iron ore samples has been included to identify the potential handling properties of each sample. The supplied samples included a typical haematite (IOA), a typical problematic sample which contains kaolinitic clays (IOB) and a typical goethite sample (IOC). Each of the supplied iron ore samples exhibited problematic behaviours depending on the moisture content and consolidation regime considered. For rapid induced blockages with transfer systems of the materials handling stream, IOB (18.5% MC) was observed to be the most problematic.

8.2.2 METHODOLOGY FOR COHESION AND ADHESION ANALYSIS

Chapter 3 has presented a revised methodology for the estimation of the cohesion and adhesion of bulk materials determined from the extrapolation of the Instantaneous Yield Locus (IYL). Typical methods used a linear interpolation of the IYL for the estimation of cohesion and adhesion which would in most cases overestimate these values. The revised methodology assumes a parabolic profile which lies tangential to the intersection point of the IYL at the shear stress axis (where the amount of cohesion, τ_o is found) and has its vertex intersecting in the tensile component (negative value) on the normal stress axis. The predicted adhesion values from the presented methodology were compared to experimental test measurements from an inter-particle adhesion tester (shown in Section 2.4.9.2) where good correlation was found. To compare the predicted and measured adhesion values, a mathematical correlation of the pre-consolidation point to the IYL has been presented. This was essential to verify the modified model due to the stress states which are acting in the sample during each of the respective testing regimes.

In addition to the revised methodology for the determination of cohesion and adhesion, a modified Hvorslev surface incorporating the predicted adhesion has been proposed. To explain the modified Hvorslev surface in detail, a yielding theory has also been proposed. This yielding theory considered different flow regimes which occur when the voidage acting between the particles of the family of IYLs of the modified Hvorslev surface and the Wall Yield Locus (WYL) are considered. Three distinct flow regimes were identified when the IYL and WYL are both considered. The first regime occurs when the IYL is greater than the WYL for the full range of consolidation, as shown in Figure 3.9. The second regime occurs when the WYL is greater than the IYL for the full range of consolidation, as shown in Figure 3.10. The final regime can be regarded as a special case and occurs when the WYL and IYL overlap each other and either may be greater depending on the consolidation of the bulk material, as shown in Figure 3.11. It was determined that each of the identified regimes would be possible for the supplied iron ore samples depending on the geometry of the materials handling plant and the properties (moisture content) of the iron ore samples. Finally, the presented yielding theory has also been expanded to consider the flow function and adhesion of the bulk material which expand on the existing theories of Jenike [4] and Roberts [1]. The adhesion of the bulk material is ranked using a similar methodology to that of Jenike [4] and Roberts [1] which can assist in the adequate design of bulk material handling systems.

8.2.3 DYNAMIC ADHESION MODELLING OF PROBLEMATIC BULK MATERIALS

Chapter 4 has given a brief overview of the existing continuum mechanics-based methodologies and explained the current limitations in relation to modelling WSM behaviours from a modelling perspective. When impact plate transfers were considered, the existing methodologies failed to incorporate the build-up of the bulk material into the continuum analysis. This would in most cases fail to identify systems which can be prone to blockages which are caused by WSMs. A theoretical model which considers the build-up onto inclined impact plates is proposed. This model is verified with experimentally measured values which are determined using the inclined plate recirculating system (outlined in Section 6.2).

The developed model determined the height of the bulk material build-up where good correlation between experimental measurements and predicted values was found, as shown in Figure 4.12. From this, the mass of the build-up was determined using a curve fit for the obtained experimental data. The developed model determined the build-up process is bulk material dependent and not significantly influenced by the material of the wall liner (boundary). The critical release angle where an effective build-up height equates to zero was then predicted for an inclined impact plate transfer system. The estimated critical release angle was determined to be approximately 60 degrees for IOB at 18.5% MC (as determined from Figure 4.15). This was found to be similar to the experimental measurement values for all three wall liners, as outlined in Table 6.15.

8.2.4 METHODOLOGY FOR REDUCTION OF ADHESIVE BONDS

Chapter 5 outlines the fundamentals of agglomeration, typically referred to as granulation, where the applications to the materials handling stream were identified. The methods of agglomeration which are used extensively within the steel making industry are outlined and the possible implementation of these systems to the materials handling stream are also proposed. From this, the effects for the reduction of problematic behaviours that WSMs show within the materials handling stream are explored. To quantify the reduction in problematic behaviours and dust generation which can be experienced onsite, a comparison of an agglomerated iron ore sample, investigated using IOB, is compared to the as supplied ROM sample. Two agglomeration samples are considered, one which is formed using the inclined plate recirculating system (outlined in Section 6.2) and one using a granulation drum (used extensively in the steel making industry). This is undertaken for an equivalent moisture content for all samples.

It was observed during the experimental measurements that the agglomerated samples showed a significantly reduced propensity for problematic behaviours when compared to the ROM sample (outlined in Section 5.3.2). Additionally, DEMC tests were undertaken (outlined in Section 5.3.1.3) where the agglomerated samples showed a significantly reduced propensity for dust generation in comparison to the ROM sample. To obtain an idea whether the use of agglomerated particles within the materials handling stream is feasible, the handling characteristics were analysed. This was undertaken by looking at the potential breakage of the agglomerates (analysed in Section 5.3.3.1). Drop tests were undertaken where the agglomerates from the inclined plate recirculating system were *"harder"* than those produced using a granulation drum. This can be attributed to the larger impacts experienced on the inclined plate recirculating system where compaction of the agglomerates occurs. It is appropriate to identify that the study of agglomeration contained within this research only touches the surface into this extremely interesting and well documented field. Although the use of agglomeration is well known within the steel making industry, the benefits to the materials handling stream are not so well known. It is therefore essential that a much more detailed analysis be conducted as outlined in Section 8.3.4.

8.2.5 DYNAMIC ADHESION MEASUREMENT AND TRANSFER SYSTEM OPTIMISATION

Chapter 6 has explained the details of the inclined plate recirculating system and the procedure used to obtain the experimental measurements. The procedure outlined was developed to ensure the experimental measurements would be undertaken in a reproducible manner where confidence in the experimental data resulted. The key experimental measurements are explained in detail where the thresholds for dynamic adhesion in relation to the moisture content of the iron ore samples have also been identified. Additionally, the estimated shape of the iron ore build-up was analysed to give an insight into the severity of the build-up that occurred during the experimental measurements. It was identified that IOB at 18.5% MC was the most problematic of the analysed samples. This was followed closely by IOA at 11.5% MC, which showed that the moisture content can also be a critical parameter to problematic behaviours. By testing IOA for a range of moisture contents, trends were shown that the mineralogical constituents of the sample are not the only consideration leading to problematic behaviours. This was attributed to IOA not having any goethite or kaolinitic clays present. It is important to note, Chapter 2 shows IOB and IOC display the worst flow properties when comparing flow functions (Figure 2.14 to Figure 2.16), wall adhesion measurements (Figure 2.19 to Figure 2.21) and inter-particle adhesion measurements (Figure 2.23 to Figure 2.25) to IOA. However, during the dynamic adhesion testing, it was observed that IOA was worse than IOC for the highest moisture content. From this, further work is required to developing bench scale tests that can measure and quantify the flow properties or attributes that cause build-up and blockage problems in transfer chutes (outlined further in Section 8.3.5).

To identify the threshold moisture contents where blockage problems may become evident for the supplied iron ore samples, a dynamic adhesion classification has been proposed where IOB at 18.5% MC for an impingement angle of 55° was identified as the most problematic for the samples tested. Additionally, the critical release angle where an effective build-up height equates to zero has been identified for transfer chute systems. From this, a design protocol for the reduction of dynamic adhesion was also proposed. Finally, the area’s most prevalent to rapid induced blockages and other related materials handling issues were identified. When the processing stream is considered, transfer chutes, vibrating screens, storage bins, stackers and reclaimers and train load out systems were identified as the *"bottle-necks"* of the materials handling stream. These area's lead to the higher possibility of the downtime of any bulk materials handling system.

8.2.6 NUMERICAL MODELLING OF PROBLEMATIC BULK MATERIALS

Chapter 7 has presented three cohesion contact models capable of replicating problematic bulk material behaviours. The models used include; the Simplified Johnson-Kendall-Roberts (SJKR) model, The Easo Liquid Bridging model and the Edinburgh Elasto-Plastic Adhesion (EEPA) model. Upon initial investigations, it was discovered that two models, the SJKR and Easo liquid bridging models, were unable to replicate the behaviours of bulk material blockages within transfer chute systems. The EEPA was able to replicate this form of modelling problem to some degree however when the computational solve times and the vast array of parameters were considered, this model was deemed to be unpractical for use in industrial cases.

To model the blockages of transfer chute systems, the coupling of the SJKR and Easo Liquid Bridging models was proposed and consequently used to predict problematic bulk material behaviour. A calibration procedure has been developed and undertaken where the parameters for each cohesion model were discussed in detail (outlined in Section 7.4). A series of calibration simulations with systematic parameter variation were undertaken to define a set of calibration matrices where a unique parameter setting was identified. The lab scale experiments which were required as part of the calibration process included the shear box test, the draw down test for particle-to-particle contacts and the inclined plate recirculating test for particle-to-wall contacts. The developed calibration matrices enabled the formation of a parameter database, which can be used for the simulation of on-site applications to optimise plant geometry and other operational parameters.

Upon selection of a unique parameter setting, outlined in Section 7.5.3, numerical modelling validation was undertaken using a lab scale vertical impact testing facility. The build-up of a bulk material against a vertically mounted wall liner can result in the formation of a pseudo chute surface, typically referred to as a *"rhino-horn"* due to its shape, where blockages can occur leading to the downtime of the system. This type of blockage problem has proved to be extremely challenging to model numerically in the past where the build-up of particles in the simulation domain are unable to replicate what would be observed in reality. Simulations were undertaken to determine if the developed hybrid model was capable of replicating the build-up of the iron ore sample in relation to a vertically mounted wall liner. It was deemed appropriate to conduct the dynamic adhesion vertical impact test for the SJKR and Easo models in their original forms, i.e. consider particle-to-particle and particle-to-wall contacts. The comparison between the simulated data for each of the respective models and experimental measurements resulted in the developed hybrid model being the only contact model capable of replicating the build-up of a bulk material against a vertically mounted wall liner. When the hybrid model was considered, a good correlation between experimental measurements and simulation results was shown.

8.3 FUTURE WORK

The research field of bulk material handling will always require further research, in order to maintain and stay ahead with the increasing demand and expansion of the materials handling sector. The following sections provide a summary of relevant and necessary future work which has risen from each of the respective chapters. The author believes extensive research in these following areas is justified.

8.3.1 INDENTIFICATION AND CHARACTERISATION OF PROBLEMATIC BULK MATERIALS

The use of wall adhesion and inter-particle adhesion tests (as outlined in Section 2.3.1) have given an insight into the properties of WSMs. Although a sound correlation of the adhesive characteristics which are found within WSMs was observed, further research must be undertaken. It is in the authors opinion that a larger range of bulk materials must be tested to observe the validity of these testers. Additionally, larger testing rigs should be investigated where the influence of sample and particle size can be analysed. Furthermore, when the wall adhesion tester is considered, different wall lining materials should be investigated. This will be used to analyse the influence of the boundary surface properties acting between the bulk material to wall liner interface.

When the cohesion and internal strength of bulk materials is considered, limitations with Jenike direct shear testers exist. This resulted in some of the tested iron ore samples to be classified as a *"plastic"* material as measurement values were not obtained. One of the testers used for powders which is proposed to be modified on a larger scale is the ring shear tester. Ring shear testers allow for unlimited travel where a much greater range of materials, which cannot be tested using Jenike direct shear testers, are able to have measurements undertaken. Current ring shear testers are not suitable for ROM samples as they are limited to particle top sizes of approximately 1 mm. It is therefore proposed that an analysis using a large ring shear tester be undertaken. This would be used in conjunction with the Jenike direct shear tester where a comparative analysis should be undertaken. It is important to note a large ring shear tester may also experience similar repeatability and irregular plastic deformation when shearing to the Jenike direct shear tester. This may lead to a large ring shear tester to also be limited to a maximum moisture content that can be tested. This will still be an extremely important investigation however, as large ring shear testers will have endless travel which may allow for the measurement of WSMs. Additionally, the investigation of wall friction for both dynamic and static conditions should be investigated using either a large ring shear tester or with a large scale Jenike type wall friction tester. Cutting and preparing annular wall coupons can be difficult with typical liners used in mining making the use of a large scale Jenike type wall friction tester to be the preferred measurement method.

8.3.2 METHODOLOGY FOR COHESION AND ADHESION ANALYSIS

The prediction of the adhesion and cohesion of bulk materials using the developed methodology (outlined in Section 3.3) showed a sound correlation between predicted and measurement values. The measurement values were obtained using an inter-particle adhesion tester (outlined in Section 2.4.9.2). It is in the authors opinion that a larger range of bulk materials must be tested to further observe the validity of the developed model. Additionally, where appropriate measurements of the cohesion should be undertaken. By conducting cohesion measurements, a comparison between predicted and measured values can be undertaken. This will give greater confidence in the validity of the developed model where both the adhesion and cohesion can be considered. This however, will depend on the density of the tested sample where the direct measure of cohesion for dense materials, such as iron ore, is very difficult (outlined in Section 3.3).

The proposed yielding theory (outlined in Section 3.4) considered different flow regimes which occur when the voidage acting between the particles of the family of IYLs of the modified Hvorslev surface and the WYL are considered. A much more detailed study is required, where case studies should be used to identify where each of the three regimes occur in the materials handling stream. Lab scale experiments should be utilised where the geometry is interchangeable to identify each regime for a particular bulk material. This could be undertaken for transfer chutes, storage bins and loading hoppers to identify the thresholds for each regime.

8.3.3 DYNAMIC ADHESION MODELLING OF PROBLEMATIC BULK MATERIALS

The developed model (outlined in Section 4.3.1.2) determined the height of the bulk material build-up where good correlation between experimental measurements and predicted values was found, as shown in Figure 4.12. It is in the authors opinion that a larger range of bulk materials must be tested to further observe the validity of the developed model. Additionally, future work could also include modelling WSMs at higher flow rates and impact velocities to examine how the developed theoretical model will scale up. In this research, the drop height was limited to approximately 1.5 m and conveyor velocities of 2 m/s. Industrial applications typically have conveyor speeds up to 6 m/s and drop heights greater than 15 m, where it is proposed that such parameters be investigated in depth. Currently the prediction of the mass of the build-up is determined using a curve fit for the obtained experimental data. It is proposed that the model be expanded where the prediction of the bulk material build-up mass is calculated analytically without the need to rely solely on experimental inputs, although some experimental parameters may still be required for confidence. Additionally, the influence of the wall lining material should be incorporated into the model where the critical release angles for different wall lining materials can be determined. The presented methodology only considers impact plate transfers. It is therefore essential that other types of transfer systems be considered to check the validity of the developed model.

It was observed during the experimental measurements for the *"rock-box"* transfer that a density profile was evident (outlined in Section 6.3.4.2). It is proposed that the adaption of the developed model be undertaken to suit a *"rock-box"* type transfer. Additionally, an investigation into the density profile should also be undertaken. The density profile was observed to have a denser top layer where a reduction in bulk density with depth from the top resulted. Models exist within soil mechanics which consider the pressure force acting at a point which is attributed to the density of the soil and depth. It is proposed that a similar method be used as a basis to analytically estimate the density profile which is found in the *"rock-box"* type transfer system. Furthermore, this analysis should also be adapted to analyse the density profile for the build-up of the bulk material onto inclined impact plates.

8.3.4 METHODOLOGY FOR REDUCTION OF ADHESIVE BONDS

The study of agglomeration contained within this research only touches the surface into this extremely interesting and well documented field. The use of agglomeration in the materials handling stream is not so well documented, however. It is therefore essential that a much more detailed analysis be conducted. It is in the authors opinion that a larger range of bulk materials must be tested to identify the mineralogical and physical parameters which can lead to natural agglomeration. Additionally, the optimisation of the agglomeration process within the materials handling stream should be undertaken. This would consider existing agglomeration systems where the handling properties should be analysed.

The agglomerated samples showed a significantly reduced propensity for problematic behaviours when compared to the ROM sample (outlined in Section 5.3.2). In addition, DEMC tests were undertaken (outlined in Section 5.3.1.3) where the agglomerated samples showed a significantly reduced propensity for dust generation in comparison to the ROM sample. Significantly more testing is required to further validate these initial observations. Additionally, feasibility studies must be undertaken to identify the financial validity of agglomeration within the materials handling stream.

8.3.5 DYNAMIC ADHESION MEASUREMENT AND TRANSFER SYSTEM OPTIMISATION

To identify the threshold moisture contents where blockage problems may become evident a dynamic adhesion classification has been proposed. From this, the critical release angle where an effective build-up height equates to zero has been identified for transfer chute systems which consider inclined impact plates. It is in the authors opinion that a larger range of bulk materials must be tested to further observe the validity of the proposed classification. Additionally, other types of transfer systems should be considered. These can include curved chute geometries, impacts onto hoods and chutes which have corner (gusset) geometries. It is also appropriate to identify that only low speed trajectories have been considered where it is advised that different belt velocities and impact heights also be investigated.

The area’s most prevalent to rapid induced blockages and other related materials handling issues were identified. When the processing stream is considered, transfer chutes, vibrating screens, storage bins, stackers and reclaimers and train load out systems were identified as the *“bottle-necks”* of the materials handling stream. From this, a design protocol for the reduction of dynamic adhesion was proposed. It is essential that a study be undertaken into the validity of the proposed design protocol. To achieve this, downtime data from site would be required to identify if the reduction of dynamic adhesion is possible. Further work is also required to develop bench scale tests that can measure and quantify the flow properties or attributes that cause build-up and blockage problems in transfer chute systems.

8.3.6 NUMERICAL MODELLING OF PROBLEMATIC BULK MATERIALS

To model the blockages of transfer chute systems, DEM numerical simulations are used. The coupling of the SJKR and Easo Liquid Bridging models (outlined in Section 7.3.1.4) was proposed and consequently used to predict problematic bulk material behaviour. A calibration procedure has been developed for WSMs where a series of calibration simulations with systematic parameter variation were undertaken. It is in the authors opinion, that additional calibration validation is required to give confidence in the calibration procedure for a range of materials handling applications.

Upon selection of a unique parameter setting, outlined in Section 7.5.3, numerical modelling validation was conducted using a lab scale vertical impact testing facility. Simulations were undertaken where it was determined that the developed hybrid model was capable of replicating the build-up of the iron ore sample in relation to a vertically mounted wall liner. It is in the authors opinion that a larger range of bulk materials must be tested to further observe the validity of the hybrid model. Furthermore, it is recommended that simulations are conducted for on-site applications to optimise plant geometry and other operational parameters.

The influence of sample pre-consolidation of the shear box test (outlined in Section 7.5.1.1) has not been examined. It is proposed this type of testing be undertaken to replicate the stress consolidations in transfer chute systems or *"rock-box"* type transfers where the shear surface has consolidation leading to increased bulk density and internal strength (as demonstrated in Section 6.3.4.2). Pre-consolidating the sample will likely increase the shear angle and drained angle of repose in the calibration experiments which may assist to model the cohesive nature of material flow in the inclined plate recirculating system.

When the time required to conduct DEM simulations is considered, the particle stiffness typically dictates the solve time. Additionally, particle diameter will also contribute to the required solve time. Reducing the particle stiffness leads to quicker simulations, however, the stability of the simulation reduces. This is attributed to the increased particle overlap which is found when using *"softer"* particles. It is therefore essential to analyse the particle stiffness and particle diameter to determine their influence on the stability of the simulation and the parameters which are used in the cohesion contact models. Additional future work should also include the investigation of other contact models and influence of particle shape. Furthermore, the use of GPU solvers to investigate large systems and complex contact models, such as the complete JKR or EEPA model, in feasible periods should also be investigated.

REFERENCES

[1] Roberts, A. W., 1998. *Basic Principles of Bulk Solids, Storage, Flow and Handling*. Centre for Bulk Solids and Particulate Technologies. The University of Newcastle, Callaghan, NSW, Australia.

[2] Connelly, D., 2011. *High Clay Ores - A Mineral Processing Nightmare.* The Australian Journal of Mining (AJM). July-August Print Edition. General Magazine Co., Richmond North, Vic, Australia.

[3] Donohue, T. J., Williams, N., Reid, S. C., Chen, B. and Plinke, J., 2019. *Roy Hill: A Case Study on the Path to 100% Reliability.* In: Proceedings ICBMH 2019 - 13th International Conference on Bulk Materials Storage, Handling and Transportation.

[4] Jenike, A. W., 1964. *Storage and Flow of Solids*. Bulletin. No. 123 of the Utah Engineering Experimentation Station, Vol. 53, No. 26:22770. University of Utah, Salt Lake City, United States.

[5] Schulze, D., 2008. *Flow Properties of Powders and Bulk Solids.* Springer – Verlag, Berlin, Germany.

[6] ASTM D 3080, 1998. *Standard Test Method for Direct Shear Test of Soils under Consolidated Drained Conditions.* ASTM International. ASTM International, West Conshohocken, PA 19428-2959, United States.

[7] The Institution of Chemical Engineers, 1989. *Standard Shear Testing Technique for Particulate Solids using the Jenike Shear Cell.* Rugby, England, United Kingdom.

[8] Plinke, J., Prigge, J. D. and Williams, K., 2016. *Development of New Analysis Methods for the Characterization and Classification of Wet and Sticky Ores*. Powder Technology, Vol. 294, pp. 252-258. Elsevier, Amsterdam, Netherlands.

[9] Zwingmann, N., Carter, G., Tezuka, N., Hart, R., Van Riessen, A. and Golovanevskiy, V., 2010. *Impact of Physical Properties on Handling Characteristics of Iron Ore.* In: Proceedings 21st Australian Clay Minerals Conference, Brisbane, Qld, Australia.

[10] Kneeshaw, M., 2003. *Appendix I: Marillana Formation, Channel Deposits in the Marillana Creek Palaeochannel of the Central Hamersley Ranges. Western Australia.* Australian Journal of Earth Sciences, Vol. 50, pp. 685-690.

[11] Harmsworth, R. A., Kneeshaw, M., Morris, R. C., Robinson, C. J. and Shrivastava, P. K., 1990. *BIF-Derived Iron Ores of the Hamersley Province*. In: Hughes, F. E. (Ed.), Geology of the Mineral Deposits of Australia and Papua New Guinea. pp. 617-642. Australian Institute of Mining and Metallurgy Monograph 14.

[12] Stone, M. S., 2004. *Depositional History and Mineralisation of Tertiary Channel Iron Deposits at Yandi, Eastern Pilbara, Australia.* PhD Thesis, School of Earth and Geographical Sciences, The University of Western Australia.

[13] Ramanaidou, E. R., Morris, R. C. and Horwitz, R. C., 2003. *Channel Iron Deposits of the Hamersley Province, Western Australia.* Australian Journal of Earth Sciences, Vol. 50, pp. 669-684.

[14] Kneeshaw, M. and Morris, R. C., 2014. *The Cenozoic Detrital Iron Deposits of the Hamersley Province, Western Australia.* Australian Journal of Earth Sciences, Vol. 61, No. 4, pp. 513-586, (doi:10.1080/08120099.2014.898408).

[15] Stone, M. S., George, A. D., Kneeshaw, M. and Barley, M. E., 2002. *Stratigraphy and Sedimentology Features of the Tertiary Yandi Channel Iron Deposits, Hamersley Province, Western Australia.* In: Proceedings Iron Ore 2002, pp. 137-144. Australasian Institute of Mining and Metallurgy Publication Series 7.

[16] Golder Associates, 2015. *Ecohydrological Conceptualisation of the Marillana Creek Region.* Prepared for BHP Billiton Iron Ore. September 2015. Report No. 137646040-002-R-Rev4.

[17] Arnold, P. C., McLean, A. G. and Roberts, A. W., 1982. *Bulk Solids: Storage, Flow and Handling.* (2nd Ed). The University of Newcastle Research Associates (TUNRA), The University of Newcastle, Callaghan, NSW, Australia.

[18] Johanson, J. R., 1987. *Theory of Bulk Solids Flow – A Historical Perspective.* International Journal of Bulk Solids Storage in Silos, Vol. 3, No. 1, pp. 1-15.

[19] Ashton, A. D., Farley, R., and Valentin, F. H. H., 1964. *An Improved Apparatus for Measuring the Tensile Strength of Powders*. Journal Scientific Instruments, Vol. 41, pp. 763-765. IOP Publishing Limited, Bristol, United Kingdom.

[20] AS 3880, 2017*. Flow Properties of Coal*. Standards Australia International Ltd. Standards Australia, Sydney, NSW.

[21] AS 4156.6, 2000. *Coal Preparation Part 6: Determination of Dust/Moisture Relationship for Coal.* Standards Australia International Ltd. Standards Australia, Sydney, NSW.

[22] Roberts, A. W., Sollie, L. A. and De Silva, S. R., 1993. *The Interaction of Bulk Solid Characteristics and Surface Parameters in Surface and Boundary Friction Measurements.* Tribology International, Vol. 26, No. 5, pp. 335-343.

[23] ISO 4701, 2008. *Iron Ores and Direct Reduction Iron – Determination of Size Distribution by Sieving.* International Organization for Standardization (ISO). October 2008. Reference No. ISO 4701:2008(E).

[24] Soil Survey Staff, 1951. *Soil Survey Manual.* U.S.D.A. Handbook No. 18. U.S. Govern. Printing Office, Washington, D. C., United States.

[25] Tan, K. H., 2005. *Soil Sampling, Preparation, and Analysis.* (2nd Ed). University of Georgia, Greensboro, Georgia. CRC Press, Boca Raton, FL 33487-2742.

[26] Tan, K. H., 2003. *Chemical Processes*. pp. 27-56. In: *Handbook of Processes and Modelling in the Soil-Plant System.* Benbi, D. K. and Nieder, R. (Eds). Food Products Press. The Haworth Reference Press, Inc., Binghamton, NY, United States.

[27] Hurst, V. J. and Pickering, S. M., 1997. *Origin and Classification of Coastal Plain Kaolins. Southeastern USA, and the Role of Groundwater and Microbial Action*. Clays and Clay Minerals, Vol. 45, pp. 274-285.

[28] Ranville, J. F. and Schmiermund, R. L., 1998. *An Overview of Environmental Colloids.* pp. 25-45. In: *Perspectives in Environmental Chemistry*, Macalady, D. L., (Ed). Oxford University Press, New York, NY, United States.

[29] Malvern Instruments, 2007. *Malvern Mastersizer 2000 Essentials MAN0393 Issue 1.0.* Worcestershire WR14 1XZ, United Kingdom.

[30] AS 1289.3.5.1, 2006. *Methods of Testing Soils for Engineering Purposes. Method 3.5.1: Soil Classification Tests – Determination of the Soil Particle Density of a Soil.* Standards Australia International Ltd. Standards Australia, Sydney, NSW.

[31] Thomas, T. R., 1975. *Recent Advances in the Measurement and Analysis of Surface Micro-Geometry.* Wear, Vol. 33, pp. 205-233.

[32] Nowicki, B., 1985. *Multiparameter Representation of Surface Roughness.* Wear, Vol. 102, pp. 161-176.

[33] Ooms, M., 1985. *A Classification of Roughness of Internal Walls.* Report, The University of Newcastle, Callaghan, NSW, Australia.

[34] ASTM D7127 – 17, 2017. *Standard Test Method for Measurement of Surface Roughness of Abrasive Blast Cleaned Metal Surfaces Using a Portable Stylus Instrument.* ASTM International. ASTM International, West Conshohocken, PA 19428-2959, United States.

[35] Finnie, I., 1960. *Erosion of Surfaces by Solid Particles.* Wear, Vol. 3, pp. 87.

[36] Bitter, J. G. A., 1962. *A Study of Erosion Phenomena – Part I.* Wear, Vol. 6, pp. 5-21.

[37] Bitter, J. G. A., 1963. *A Study of Erosion Phenomena – Part II.* Wear, Vol. 6, pp. 169-190.

[38] Tilly, G. P., 1969. *Sand Erosion of Metals and Plastics: A Brief Overview.* Wear, Vol. 14, pp. 241-248.

[39] Tilly, G. P., 1969. *Erosion Caused by Airborne Particles.* Wear, Vol. 14, pp. 63-79.

[40] Wood, C. D. and Espenschade, P. W., 1964. *Mechanisms of Dust Erosion.* In: Proceedings SAE World Congress and Exhibition, SAE Technical Paper 640819. (doi:10.4271/640819).

[41] Goodwin, J. E., Sage, W. and Tilly, G. P., 1969. *A Study of Erosion by Solid Particles.* In: Proceedings of the Institution of Mechanical Engineers, London, United Kingdom, Vol. 184, No. 15, pp. 270-292.

[42] Sage, W. and Tilly, G. P., 1969. *The Significance of Particle Size in Sand Erosion of Small Gas Turbines.* The Aeronautical Journal, Vol. 73, No. 701, pp. 427-428.

[43] Tilly, G. P. and Sage, W., 1970. *The Interaction of Particle and Material Behaviour in Erosion Processes.* Wear, Vol. 16, pp. 429.

[44] Neilson, J. H. and Gilchrist, A., 1968. *Erosion by a Stream of Solid Particles.* Wear, Vol. 11, pp. 111-122.

[45] Hutchings, I. M., 1980. *Some Comments on the Theoretical Treatment of Erosive Particle Impacts.* In: Proceedings 5th International Conference on Erosion by Solid and Liquid Impact, pp. 36.1-36.6.

[46] Engel, P. A., 1977. *Predicting Impact Wear.* Machine Design, May 26, pp. 100-105.

[47] Knoop, F., Peters, C. G. and Emerson, W. B., 1939. *A Sensitive Pyramidal-Diamond Tool for Indentation Measurements*. Journal of Research of the National Bureau of Standards. Vol. 23, No. 1, pp. 39-61. (doi:10.6028/jres.023.022).

[48] ASTM E384, 2012. *E384: Standard Test Method for Knoop and Vickers Hardness of Materials.* ASTM International. ASTM International, West Conshohocken, PA 19428-2959, United States.

[49] Brouwer, P., 2003. *Theory of XRF*. PANalytical B. V., Almelo, The Netherlands. (ISBN: 90-9016758-7).

[50] Wiche, S. J., Keys, S. and Roberts, A. W., 2005. *Abrasion Wear Tester for Bulk Solids Handling Applications.* Wear, Vol. 258, pp. 251-257.

[51] Roberts, A. W., 1989. *Bulk Materials Handling – A Key Discipline of Engineering.* 1989 AGM Michell Award Address, College of Mechanical Engineers, The Institute of Engineers, Australia.

[52] Hering, E., Martin, R. and Stroher, M., 1989. *Physics for Engineers.* VDI-Verlag, Düsseldorf, Germany.

[53] Burbaum, U., 2009. *Adhesion of Cohesive Soils on Material Surfaces of Tunnel Boring Machines.* Darmstadt University of Technology, Institute of Applied Geosciences.

[54] Rumpf, H., 1958. *Principles and Methods of Granulation*. Chemical Engineering and Technology, Vol. 30, No. 3, pp. 144-158.

[55] Essington, M. E., 2003. *Soil and Water Chemistry: A Integrative Approach.* CRC Press, Boca Raton, FL, United States.

[56] Scheffer, F. and Schachtschabel, P., 1998. *Lehrbuch der Bodenkunde.* 14th Ed. Ferdinand Enke Verlag, Stuttgart, Germany.

[57] Habenicht, G., 2006. *Kleben.* Springer Verlag, 5th Ed. Heidelberg, Berlin, Germany.

[58] Jenike, A. W., Elsey, P. J. and Woolley, R. H., 1960. *Flow Properties of Bulk Solids.* In: Proceedings, American Society for Testing Materials, Vol. 60, pp. 1168-1181.

[59] Jenike, A. W., 1961. *Gravity Flow of Bulk Solids.* Bulletin. No. 108 of the Utah Engineering Experimentation Station, Vol. 53, No. 26:22770. University of Utah, Salt Lake City, United States.

[60] Nedderman, R., 1992. *Statics and Kinematics of Granular Materials*. Cambridge, Cambridge University Press. (doi:10.1017/CBO9780511600043).

[61] Rankine, W. M. J., 1857. *On Stability on Loose Earth.* Philosophic Transactions of Royal Society, London, Part I, pp. 9-27.

[62] Coulomb, C. A., 1776. *Essai sur une application des regles des maximis et minimis a quelques problemes de statique, relatifs a l'architecture.* Memoires de Mathematique de l'Academie Royale de Science 7, Paris, France.

[63] Roberts, I., 1882. *Determination of the Vertical and Lateral Pressures of Granular Substances.* In: Proceedings of the Royal Society of London, Vol. 36, pp. 225-240.

[64] Janssen, H. A., 1895. *Tests on Grain Pressure Silos.* Zeitschrift des Vereins Deutscher Ingenieure, Vol. 35, pp. 1045-1049.

[65] Reynolds, O., 1885. *On the Dilatancy of Media Composed of Rigid Particles in Contact.* Philosophical Magazine, Vol. 20, pp. 469-481.

[66] Hvorslev, M. J., 1937. *On the Physical Properties of Distributed Cohesive Soils.* Ingeniorvidensk. Skr. 45.

[67] Roscoe, K. H., Schofield, A. N. and Wroth, C. P., 1958. *On the Yielding of Soils.* Geotechnique, Vol. 8, pp. 22-53.

[68] Ashton, M. D., Cheng, D. C. H., Farley, R. and Valentin, F. H. H., 1965. *Some Investigations into the Strength and Flow Properties of Powders.* In: Proceedings of the British Society of Rheology, University of Nottingham. pp. 206-218.

[69] Orband, J. L. R. and Geldard, D., 1997. *Direct Measurement of Powder Cohesion Using a Torsional Device.* Powder Technology, Vol. 92, pp. 25-33. Elsevier, Amsterdam, Netherlands.

[70] Bateson, I. D., Raven, T. N. and Walker, J. A., 2001. *Rheometer with Axial Resistive Force Measurement.* International Patent Number: US7201040B2, Filed 28 Nov 2001.

[71] Carr, M., Roberts, A. and Wheeler, C., 2018*. A Revised Methodology for Cohesion and Adhesion Analysis of Bulk Materials.* In: Proceedings 9th International Conference for Conveying and Handling of Particulate Solids - CHoPS 2018. London, United Kingdom.

[72] Carr, M., Roberts, A. and Wheeler, C., 2019. *A Revised Methodology for the Determination of Bulk Material Cohesion and Adhesion.* Advanced Powder Technology. *Under review with editor, April 2019.*

[73] Donohue, T. J., 2018. *Private Communication.* TUNRA Bulk Solids Offices, University of Newcastle, Callaghan.

[74] Ooms, M. and Roberts, A. W., 1985. *Significant Influence of Wall Friction in the Gravity Flow of Bulk Solids.* Bulk Solids Handling, Vol. 5, No. 6, pp. 1271-1277.

[75] Roberts, A. W., Ooms, M. and Scott, O. J., 1984. *Surface Friction and Wear in the Storage, Gravity Flow and Handling of Bulk Solids.* In: Proceedings International Conference 'War on Wear', Wear in the Mining and Mineral Extraction Industry, Institute of Mechanical Engineers, Nottingham, pp. 123-134.

[76] Scott, O. J., 1992. *Conveyor Transfer Chute Design, in Modern Concepts in Belt Conveying and Handling Bulk Solids.* The Institute for Bulk Materials Handling Research, University of Newcastle, pp. 11.11-11.13.

[77] Colijn, H. and Conners, P. J., 1972. *Belt Conveyor Transfer Points.* Transactions of the Society of Mining Engineers, AIME, Vol. 252, pp. 204-210.

[78] Roberts, A. W., 2001. *Chute Design Considerations for Feeding and Transfer.* In: Proceedings BELTCON 11, Johannesburg, Republic of South Africa.

[79] Alspaugh, M. A., 2004. *Latest Developments in Belt Conveyor Technology.* In: Proceedings MINExpo 2004, Las Vegas, NV, United States.

[80] Hastie, D. B., 2010. *Belt Conveyor Transfers: Quantifying and Modelling Mechanisms of Particle Flow.* PhD Thesis, University of Wollongong.

[81] Stuart-Dick, D. and Royal, T. A., 1991. *Streamlined Design of Chutes to Handle Bulk Solids.* In: Proceedings Chute Design Conference, Republic of South Africa.

[82] Benjamin, C. W., 1999. *Rapid Design Approach to the Zero-Spillage Transfer Chute.* Australian Bulk Handling Review, Vol. 4, No. 2, pp. 52-58.

[83] Lonie, K., 1989. *The Design of Conveyor Transfer Chutes.* In: Proceedings 3rd International Conference on Bulk Materials Storage, Handling and Transportation, Newcastle, NSW, Australia, pp. 240-244.

[84] Rozentals, J., 1983. *Rational Design of Conveyor Chutes.* In: Proceedings BELTCON 2, Johannesburg, Republic of South Africa.

[85] Huque, S. T., 2004. *Analytical and Numerical Investigations into Belt Conveyor Transfers.* PhD Thesis, University of Wollongong.

[86] Conveyor Equipment Manufacturers Association (CEMA), 2014. *Belt Conveyors for Bulk Materials*, 7th Ed. Naples, Florida, United States.

[87] Low, A. C., Kyle, J. W. and Mechanical Handling Engineers' Association (MHEA), 1986. *Recommended Practice for Troughed Belt Conveyors.* Mechanical Handling Engineers' Association (MHEA), London.

[88] Korzen, Z., 1988. *The Dynamics of Bulk Solids Flow on Impact Plates of Belt Conveyor Systems.* Bulk Solids Handling, Vol. 8, No. 6, pp. 689-697.

[89] Korzen, Z., 1989. *Mechanics of Belt Conveyor Discharge Process as Affected by Air Drag.* Bulk Solids Handling, Vol. 9, No. 3, pp. 289-297.

[90] Booth, E. P. O., 1934. *Trajectories form Conveyors – Method of Calculating Them Corrected.* Engineering and Mining Journal, Vol.135, No.12, pp. 552-554

[91] Golka, K., 1992. *Discharge Trajectories of Bulk Solids.* In: Proceedings 4th International Conference on Bulk Materials Handling and Transportation, Wollongong, NSW, Australia, pp. 497-503.

[92] Golka, K., 1993. *Prediction of the Discharge Trajectories of Bulk Materials.* Bulk Solids Handling, Vol. 13, No. 4, pp. 763-766.

[93] Dunlop, 1982. *Dunlop Industrial Conveyor Manual.*

[94] Goodyear, 1975. *Goodyear Handbook of Conveyor & Elevator Belting.* The Goodyear Tire & Rubber Company, Akron, Ohio, United States.

[95] Roberts, A. W., 1969. *An Investigation of the Gravity Flow of Noncohesive Granular Materials Through Discharge Chutes.* Transactions of the ASME, Journal of Engineering for Industry, Vol. 91, No. 2, pp.373-381.

[96] Roberts, A. W. and Scott, O. J., 1981. *Flow of Bulk Solids through Transfer Chutes of Variable Geometry and Profile.* Bulk Solids Handling, Vol. 1, No. 4, pp. 715-727.

[97] Roberts, A. W., 1967. *The Dynamics of Granular Materials Flow through Curved Chutes.* Mechanical and Chemical Engineering Transactions, Institute of Engineers, Australia, Vol. MC3, No. 2, pp. 216-224.

[98] McBride, B., 1997. *Efficient Transfer Chutes – A Case Study.* In: Proceedings BELTCON 9, International Materials Handling Conference, Midrand, South Africa, pp. 1-7.

[99] McBride, B., 2000. *Curved Transfer Chute – Results of Site Trials and Optimisation.* In: Proceedings International Conference on Powder and Bulk Solids Handling, London, United Kingdom, Professional Engineering Publishing Limited, pp. 411-418.

[100] Page, J., 1991. *Examples of Good and Bad Chute Design.* Chute Design Conference, Johannesburg, South Africa.

[101] Grima, A. and Wypych, P. W., 2010. *Discrete Element Simulation Validation: Impact Plate Transfer Station.* In: Proceedings BulkSolids Europe 2010, Wuerzburg, Germany, pp. 1-17.

[102] Roberts, A. W., 1984. *Vibration of Fine Powders and its Application.* In: Handbook of Powder Science and Technology, M. E. Fayed and L. Otten (Ed.), Van Nostrand Reinhold Company Inc., New York, pp. 181-229.

[103] Roberts, A. W., Ooms, M. and Scott, O. J., 1986. *Influence of Vibrations on the Strength and Boundary Friction Characteristics of Bulk Solids and the Effect on Bin Design and Performance.* Bulk Solids Handling, Vol. 6. No. 1, pp. 161-169.

[104] Roberts, A. W. and Scott, O. J., 1978. *An Investigation into the Effect of Sinusoidal and Random Vibrations on the Strength and Flow Properties of Bulk Solids.* Powder Technology, Vol. 21, pp. 45-53.

[105] Roberts, A. W., Scott, O. J. and Li, K. W., 1979. *The Influence of Mechanical Vibrations on the Flow of Bulk Solids.* In: Proceedings International Conference on Powders and Bulk Solids, Philadelphia, U.W.A., May, 1979.

[106] Roberts, A. W., 1980. *The Effects of Vibration on the Strength and Flow Properties of Bulk Solids in Storage Bin Operation.* In: Proceedings International Conference on Design of Silos for Strength and Flow, University of Lancaster, England, September, 1980.

[107] Capes, C. E., 1980. *Particle Size Enlargement.* Handbook of Powder Technology, Vol. 1. Elsevier, Amsterdam, Netherlands.

[108] Kaminska, J. and Danko, J., 2011. *Analysis of the Granulation Process Mechanism – Stand and Scope of Experimental Investigations.* Metallurgy and Foundry Engineering, Vol. 37 No. 1, pp. 81-87.

[109] Litster, J. D. and Waters, A. G., 1990. *Kinetics of Iron Ore Sinter Feed Granulation.* Powder Technology, Vol. 62, pp. 125-134. Elsevier, Amsterdam, Netherlands.

[110] Pietsch, W. B., 2002. *Agglomeration Processes: Phenomena, Technologies, Equipment.* Wiley-VCH Verlag GmbH, Wienheim, Germany.

[111] Mehos, G. J. and Kozicki, C. M., 2011. *Consider Wet Agglomeration to Improve Powder Flow.* Chemical Engineering Vol. 118, pp. 46-49.

[112] Rumpf, H., 1962. *The Strength of Granules and Agglomerates,* Agglomeration, W. A. Knepper (Ed.), John Wiley, New York, pp. 379-418.

[113] Sochon, R. P. J. and Salman, A. D., 2010. *Particle Growth and Agglomeration Processes.* Chemical Engineering and Chemical Process Technology, Vol. 2, pp. 299-316.

[114] Newitt, D. M. and Conway-Jones, J. M., 1958. *A Contribution to the Theory and Practice of Granulation.* Transactions of the Institute of Chemical Engineering, Vol. 36, pp. 422-442.

[115] Barlow, C. G., 1968. *Granulation of Powders.* Chemical Engineer, Vol. 220, pp. 196-201.

[116] Pietsch, W., Hoffman, E. and Rumpf, H., 1969. *Tensile Strength of Moist Agglomerates.* I and EC Process Design and Development, Vol. 8, No. 1, pp. 58-62.

[117] Rao, P. V. T., 1994. *Agglomeration and Prereduction of Ores.* In: Proceedings 4th Refresher Course on Ferro Alloys. Jamedepur, pp. 1-15.

[118] Kader, A. and Jalil, R., 1998. *In Vitro Release of Theophylline from Poly(Lactic Acid) Sustained-Release Pellets Prepared by Direct Compression.* Drug Development and Industrial Pharmacy, Vol. 24, No. 6, pp. 527-534.

[119] Juslin, L., 1997. *Measurement of Droplet Size Distribution and Spray Angle of Pneumatic Nozzle, and Granule Growth Kinetics and Properties of Lactose, Glucose and Mannitol Granules Made in a Fluidized Bed Granulator.* PhD Thesis, University of Helsinki.

[120] Knop, K. and Lippold, B. C., 1989. *Fluidized Bed Granulation as a Preparation Method for Pellets.* Pharmaceutical Industries, Vol. 51, pp. 302-309.

[121] Wesdyk, R., Joshi, Y. M., Jain, N. B., Morris, K. and Newman, A., 1990. *The Effect of Size and Mass on the Film Thickness of Beads Coated in Fluidized Bed Equipment.* International Journal of Pharmaceutics, Vol. 65, pp. 69-76.

[122] Schaefer, T., 1988. *Equipment for Wet Agglomeration.* Acta Pharmaceutica Suecica, Vol. 25, pp. 205-228.

[123] Kleinebudde, P., Linder, L., 1993. *Experiments with a Twin Screw Extruder using a Single-Step Granulator/Extrusion Process.* International Journal of Pharmaceutics, Vol. 94, pp. 49-58.

[124] Titley, P., 1988. *Agglomeration and Granulation of Powders, Processing and Manufacturing Practice.* Acta Pharmaceutica Suecica, Vol. 25, pp. 267-280.

[125] Gajdos, B., 1984. *Rotary Granulators - Evaluation of Process Technology for Pellet Production using Factorial Design.* Drugs Made in Germany, Vol. 27, pp. 30-36.

[126] Ghebre-Sellassie, I., Gordon, R., Fawzi, M. B. and Nesbitt, R. U., 1985. *Evaluation of a High-Speed Pelletization Process and Equipment.* Drug Development and Industrial Pharmacy, Vol. 11, pp. 1523-1541.

[127] Niskanen, M., 1992. *Powder Layering and Coating in a Centrifugal Granulator: Effect of Binder Solution Concentration, Powder Particle Size and Coating Amount on Pellets Properties*. PhD Thesis, University of Helsinki.

[128] Chamberlin, P. D., 1986. *Agglomeration: Cheap Insurance for Good Recovery when Heap Leaching Gold and Silver Ores*. Mining Engineering, Vol. 38, No. 12, pp. 1105-1109.

[129] Bouffard, S. C., 2005. *Review of Agglomeration Practice and Fundamentals in Heap Leaching.* Journal of Mineral Processing and Extractive Metallurgy Review, Vol. 26, No. 3-4, pp. 233-294.

[130] Ghebre-Sellassie, I., 1989. *Pellets: A General Overview.* Pharmaceutical Pelletization Technology. Marcel Dekker, Inc., New York, USA, Vol. 37, pp. 1-13.

[131] AS 1100.101, 1992. *Technical Drawing – Part 101: General Principles.* Standards Australia International Ltd. Standards Australia, Sydney, NSW.

[132] MATLAB and Statistics Toolbox Release 2016a, The MathWorks, Inc., Natick, Massachusetts, United States.

[133] Rio Tinto, 2013. *Site Visit to Iron Ore Operations in Western Australia.* Rio Tinto Limited, Melbourne, Victoria, Australia.

[134] BHP, 2018. *BHP Approves South Flank Project.* Media News Release (Release Number 07/18).

[135] Clark, R. N., 1999. *Spectroscopy of Rocks and Minerals, and Principles of Spectroscopy.* In Manual of Remote Sensing, Volume 3, Remote Sensing for the Earth Sciences, A.N. Rencz, (Ed.) John Wiley and Sons, New York, pp. 3- 58.

[136] Plinke, J., 2019. *The Integration of Reflectance Spectroscopy and Bulk Flow Characterisation to Evaluate the Handleability of Cohesive Iron Ore.* PhD Thesis, The University of Newcastle, Callaghan, Australia.

[137] Mahesh, S., Jayas, D., Paliwal, J. and White, N., 2010. *Identification of Wheat Classes at Different Moisture Levels using Near-Infrared Hyperspectral Images of Bulk Samples.* Sensing and Instrumentation for Food Quality and Safety, Vol. 5, No. 1, pp. 1-9.

[138] Magendran, T. and Sanjeevi, S., 2011. *Assessing the Grades of Iron Ore of Noamundi, India by Ground Based Hyperspectral Remote Sensing.* International Journal of Earth Sciences and Engineering, Vol. 4, No. 8, pp. 7-16.

[139] Bardet, J. P., 1998. *Introduction to Computational Granular Mechanics.* In: Proceedings Behaviour of Granular Materials, B. Cambou (Ed.), CISM, Italy, pp. 99-169.

[140] Cundall, P. A., 1971. *A Computer Model for Simulating Progressive, Large-Scale Movements in Blocky Rock Systems.* In: Proceedings Symposium International Society Rock Mechanics, Nancy, Vol. 2, No. 8.

[141] Cundall, P. A. and Strack, O. D. L., 1979. *A Discrete Numerical Model for Granular Assemblies.* Geotechnique, Vol. 29, pp. 47-65.

[142] Walton, O. R. and Braun, R. L., 1986. *Stress Calculations for Assemblies of Inelastic Spheres in Uniform Shear.* Acta Mechanica, Vol. 63, pp. 73-86.

[143] Barker, G. C., 1994. *Computer Simulations of Granular Materials.* In: A. Metha (Ed.), Granular Matter: An Interdisciplinary Approach. Springer-Verlag, New York, United States, pp. 35-83.

[144] Campbell, C. S., 1990. *Rapid Granular Flows.* Annual Review of Fluid Mechanics, Vol. 22, pp. 57-92.

[145] Walton, O. R., 1992. *Numerical Simulation of Inelastic Frictional Particle-Particle Interactions.* In: Roco (Ed.), Particulate Two-Phase Flow, Ch. 25, Butterworth-Heinemann, Boston, United States, pp. 884-911.

[146] Wensrich, C. M. and Katterfeld, A., 2012. *Rolling Friction as a Technique for Modelling Particle Shape in DEM.* Powder Technology, Vol. 217, pp. 409-417.

[147] Lommen, S., Schott, D. and Lodewijks, G., 2014. *DEM Speedup: Stiffness Effects on Behaviour of Bulk Material.* Particuology, Vol. 12, pp. 107-112.

[148] Jeschke, H. and Katterfeld, A., 2009. *Computer Simulation of Comminution Processes using the Discrete Element Method.* In: Proceedings Energy, resources, environment, 4th symposium Baumaschinentechnik, Publication Series of the Research Association for Building and Building Material Machines, Dresden, Germany, Vol. 37, pp. 151-160.

[149] Roessler, T. and Katterfeld, A., 2016. *Scalability of Angle of Repose Tests for the Calibration of DEM Parameters.* In: Proceedings ICBMH 2016 - 12th International Conference on Bulk Materials Storage, Handling and Transportation, pp. 201-211.

[150] Benvenuti, L., Kloss, C. and Pirker, S., 2016. *Identification of DEM Simulation Parameters by Artificial Neural Networks and Bulk Experiments.* Powder Technology, Vol. 291, pp. 456-465.

[151] Do, H. Q., Aragon, A. M. and Schott, D. L., 2018. *A Calibration Framework for Discrete Element Model Parameters using Genetic Algorithms.* Advanced Powder Technology, Vol. 29, No. 6, pp. 1393-1403.

[152] Rackl, M. and Hanley, K. J., 2017. *A Methodical Calibration Procedure for Discrete Element Models.* Powder Technology, Vol. 307, pp. 73-83.

[153] Wang, M. and Cao, P., 2017. *Calibrating the Micromechanical Parameters of the PFC 2D(3D) Models using the Improved Simulated Annealing Algorithm*. Mathematical Problems in Engineering, Vol. 2017, pp. 1-11.

[154] Grima, A. P. and Wypych, P. W., 2011. *Discrete Element Simulations of Granular Pile Formation: Method for Calibrating Discrete Element Models.* Engineering Computations, Vol. 28, No. 3, pp. 314-339.

[155] Coetzee, C. J., 2016. *Calibration of the Discrete Element Method and the Effect of Particle Shape.* Powder Technology, Vol. 297, pp. 50-70.

[156] Liu, F., Zhang, J., Li, B. and Chen, J., 2016. *Calibration of Parameters of Wheat Required in Discrete Element Method Simulation Based on Repose Angle of Particle Heap.* Nongye Gongcheng Xuebao/Transactions of the Chinese Society of Agricultural Engineering, Vol. 32, No. 12, pp. 247-253.

[157] Jensen, A., Fraser, K. A. and Laird, G., 2014. *Improving the Precision of Discrete Element Simulations through Calibration Models.* In: Proceedings 13th International LS - DYNA Users Conference, Detroit, Michigan, United States.

[158] Marigo, M. and Stitt, E. H., 2015. *Discrete Element Method (DEM) for Industrial Applications: Comments on Calibration and Validation for the Modelling of Cylindrical Pellets.* KONA Powder and Particle Journal, No. 32, pp. 236-252.

[159] Gröger, T. and Katterfeld, A., 2006. *On the Numerical Calibration of Discrete Element Models for the Simulation of Bulk Solids.* In: Proceedings AIChE Annual Meeting, Conference Proceedings.

[160] Just, S., Toschkoff, G., Funke, A., Djuric, D., Scharrer, G., Khinast, J., Knop, K. and Kleinebudde, P., 2013. *Experimental Analysis of Tablet Properties for Discrete Element Modeling of an Active Coating Process.* AAPS PharmSciTech, Vol. 14, No. 1, pp. 402-411.

[161] Bierwisch, C. S., 2009. *Numerical Simulations of Granular Flow and Filling.* PhD Thesis, The University of Freiburg, Germany.

[162] Weiler, R., Ripp, M., Dau, G. and Ripperger, S., 2009. *Anwendung der Diskrete- Elemente-Methode zur Simulation des Verhaltens von Schüttgütern.* Chemie-Ingenieur- Technik, Vol. 81, No. 6, pp. 749-757.

[163] Zhou, Y. C., Xu, B. H., Yu, A. B. and Zulli, P., 2002. *An Experimental and Numerical Study of the Angle of Repose of Coarse Spheres.* Powder Technology, Vol. 125, No. 1, pp. 45-54.

[164] Rackl, M. and Hanley, K. J., 2017. *A Methodical Calibration Procedure for Discrete Element Models.* Powder Technology, Vol. 307, pp. 73-83.

[165] Ilic, D., 2013. *Bulk Solid Interactions in Belt Conveying Systems.* PhD Thesis, The University of Newcastle, Callaghan, Australia.

[166] Carr, M., Williams, K., Chen, W., Hayter, B., Roberts, A. and Wheeler, C., 2017. *The Dynamic Adhesion of Wet and Sticky Iron Ores onto Impact Plates.* In: Proceedings AusIMM (6th Ed.), Iron Ore 2017 Conference Proceedings. AusIMM: Perth, Australia.

[167] Roessler, T., Richter, C., Katterfeld, A. and Will, F., 2019. *Development of a Standard Calibration Procedure for the DEM Parameters of Cohesionless Bulk Materials – Part I: Solving the Problem of Ambiguous Parameter Combinations.* Powder Technology, Vol. 343, pp. 803-812. (doi:10.1016/j.powtec.2018.11.034).

[168] Chen, W., Roberts, A., Katterfeld, A. and Wheeler, C., 2018. *Modelling the Stability of Iron Ore Bulk Cargoes During Marine Transport.* Powder Technology, Vol. 326, pp. 255-264.

[169] Li, C., Honeyands, T., O'Dea, D. and Moreno-Atanasio, R., 2017. *The Angle of Repose and Size Segregation of Iron Ore Granules: DEM Analysis and Experimental Investigation.* Powder Technology, Vol. 320, pp. 257-272.

[170] Dewicki, G. and Mustoe, G., 2002. *Bulk Material Belt Conveyor Transfer Point Simulation of Material Flow Using DEM.* In: Proceedings 3rd International Conference on Discrete Element Methods, United States.

[171] Donohue, T. J., Ilic, D., Bell, R. and Newman, L., 2010. *The use of DEM in the Design and Analysis of WEARBACK Transfer Chutes.* Australian Bulk Handling Review, No. 11/12, pp. 62-67.

[172] Kessler, F. and Prenner, M., 2009. *DEM – Simulation of Conveyor Transfer Chutes.* FME Transactions, Vol. 37, pp. 185-192.

[173] Nordell, L. K., 1994. *Palabora Installs Curved Transfer Chute in Hard Rock to Minimize Belt Cover Wear.* Bulk Solids Handling, Vol. 14, No. 4, pp. 739-743.

[174] Katterfeld, A., Gröger, T., Hachmann, M. and Becker, G., 2009. *Usage of DEM Simulations for the Development of a New Chute Design in Underground Mining.* In: Proceedings 6th International Conference for Conveying and Handling of Particulate Solids (CHoPS), pp. 90-95.

[175] Katterfeld, A., Gröger, T. and Minkin, A., 2007. *Discrete Element Simulation of Transfer Stations and their Verification.* In: Proceedings 9th International Conference Bulk Materials Storage, Handling and Transportation, Newcastle, NSW, Australia.

[176] Kruse, D. J., 2009. *Chute Designs and Trajectories using the Discrete Element Method.* In: Proceedings BELTCON 15, Boksburg, Republic of South Africa.

[177] Krause, F. and Katterfeld, A., 2004. *Usage of the Discrete Element Method in Conveyor Technologies.* In: Proceedings ICBMH 2004 - 8th International Conference on Bulk Materials Storage, Handling and Transportation, Wollongong, NSW, Australia, pp. 289-293.

[178] Theuerkauf, J., Dhodapkar, S., Manjunath, K., Jacob, K. and Steinmetz, T., 2003. *Applying the Discrete Element Method in Process Engineering.* Chemical Engineering and Technology, Vol. 26, No. 2, pp. 157-162.

[179] Ji, S., Shen, H. H. and Orlando, A., 2006. *Scaling Effect in DEM Simulations of Direct Shear Test.* In: Proceedings 5th World Congress on Particle Technology, Orlando, Florida, United States.

[180] Luding, S., 2006. *Comparison of Ring Shear Cell Simulations in 2D/3D with Experiments.* In: Proceedings 5th World Congress on Particle Technology, Orlando, Florida, United States.

[181] Straub, M., McNamara, S. and Herrmann, H. J., 2007. *Plug Conveying in a Horizontal Tube.* Granular Matter, Vol. 9, No. 1-2, pp. 35-48.

[182] Chu, K. W. and Yu, A. B., 2007. *Numerical Simulation of Complex Particle-Fluid Flows.* Powder Technology, Vol. 179, No. 1, pp. 104-114.

[183] McGlinchey, D., Xiang, J., Cowell, A., Frye, L. and Peukert, W., 2004. *The Prediction of Contact Forces During Dense Phase Pneumatic Conveying.* In: Proceedings ICBMH 2004 - 8th International Conference on Bulk Materials Storage, Handling and Transportation, Wollongong, NSW, Australia, pp. 342-346.

[184] Li, J., Langston, P. A., Webb, C. and Dyakowski, T., 2004. *Flow of Sphero-Disc Particles in Rectangular Hoppers – A DEM and Experimental Comparison in 3D.* Chemical Engineering Science, Vol. 54, No. 24, pp. 5917-5929.

[185] Markauskas, D., 2006. *Discrete Element Modelling of Complex Axisymmetrical Particle Flow.* Mechanika, Vol. 62, No. 6, pp. 32-38.

[186] Balevicius, R., Kacianauskas, R., Mroz, Z. and Sielamowicz, I., 2008. *Discrete-Particle Investigation of Friction Effect in Filling and Unsteady/Steady Discharge in Three-Dimensional Wedge-Shaped Hopper.* Powder Technology, Vol. 187, No. 2, pp. 159-174.

[187] Cleary, P. W., Sinnott, M. D. and Morrison, R. D., 2009. *Separation Performance of Double Deck Banana Screens – Part 2: Quantitative Predictions.* Minerals Engineering, Vol. 22, No. 14, pp. 1230-1244.

[188] Donohue, T. J., Chen, W., Katterfeld, A. and Reid, S., 2017. *Addressing the Challenges Associated with the Modelling of Iron Ore in Vibrating Screens.* In: Proceedings AusIMM (6th Ed.), Iron Ore 2017 Conference Proceedings. AusIMM: Perth, Australia.

[189] Cleary, P. W., Sinnott, M. D. and Morrison, R. D., 2006. *DEM Prediction of Particle Flow and Breakage in Comminution Processes.* In: Proceedings 5th World Congress on Particle Technology, Orlando, Florida, United States.

[190] McBride, A., Govender, I., Powell, M. and Cloete, T., 2004. *Contributions to the Experimental Validation of the Discrete Element Method Applied to Tumbling Mills.* Engineering Computations, Vol. 21, No. 2/3/4, pp. 119-136.

[191] Katterfeld, A., Donohue, T. J. and Ilic D., 2012. *Application of the Discrete Element Method in Mechanical Conveying of Bulk Materials.* In: Proceedings 7th International Conference for Conveying and Handling of Particulate Solids (CHoPS), Friedrichshafen, Germany.

[192] Sadd, M. H., Tai, Q. and Shukla, A., 1993. *Contact Law Effects on Wave Propagation in Particulate Materials using Distinct Element Modelling.* International Journal of Non-Linear Mechanics, Vol. 28, No. 2, pp. 251-265.

[193] Jensen, R. P., Bosscher, P. J., Plesha, M. E. and Edil, T. B., 1999. *DEM Simulation of Granular Media-Structure Interface: Effects of Surface Roughness and Particle Shape.* International Journal for Numerical and Analytical Methods in Geomechanics, Vol. 23, pp. 531-547.

[194] Tsuji, Y., Kawaguchi, T. and Tanaka, T., 1993. *Discrete Particle Simulation of Two-Dimensional Fluidized Bed.* Powder Technology, Vol. 77, pp. 79-87.

[195] Walton, O. R., 1993. *Numerical Simulation of Inclined Chute Rows of Monodisperse, Inelastic, Frictional Spheres.* Mechanics of Materials, Vol. 16, pp. 239-247.

[196] Xu, B. H., 1997. *Numerical Simulation of the Gas-Solid Flow in Fluidized Beds.* PhD Thesis, The University of New South Wales, Sydney, Australia.

[197] Xu, B. H. and Yu, A. B., 1997. *Numerical Simulation of the Gas-Solid Flow in a Fluidised Bed by Combining Discrete Particle Method with Computational Fluid Dynamics.* Chemical Engineering Science, Vol. 52, pp. 2785-2809.

[198] Zhang, X. and Vu-Quoc, L., 2000. *Simulation of Chute Flow of Soybeans Using an Improved Tangential Force-Displacement Model.* Mechanics of Materials, Vol. 32, pp. 115-129.

[199] Lin, X. and Ng, T. T., 1997. *A Three-Dimensional Discrete Element Model using Arrays of Ellipsoids.* Geotechnique, Vol. 47, No. 2, pp. 319-329.

[200] Mustoe, G. G. W. and Miyata, M., 2001. *Material Flow Analysis of Noncircular-Shaped Granular Media Using Discrete Element Method.* Journal of Engineering Mechanics, Vol. 127, No. 10, pp. 1017-1026.

[201] Barr, A., 1981. *Superquadrics and Angle-Preserving Transformations.* IEEE Computer Graphics and Applications, Vol. 1, pp. 11-23.

[202] Mustoe, G. G. W., Miyata, M. and Nakagawa, M., 2000. *Discrete Element Methods for Mechanical Analysis of Systems of General Shaped Bodies.* In: Proceedings of the 5th International Conference on Computational Structures Technology, Leuven, Belgium.

[203] Walton, O. R., 1982. *Explicit Particle Dynamics Model for Granular Materials.* Numerical Methods in Geomechanics, Edmonton, Z. Elsenstein (Ed.), A. A. Balkema, Rotterdam, Vol. 3, pp. 1261-1268.

[204] Walton, O. R., 1982. *Particle-Dynamics Calculations of Shear Flow.* Mechanics of Granular Materials: New Models and Constitutive Relations, In: Proceedings of the U.S./Japan Seminar on New Models and Constitutive Relations in the Mechanics of Granular Materials, Ithaca, New York, J. T. Jenkins and M. Satake (Eds.), Elsevier, Amsterdam, pp. 327-338.

[205] Walton, O. R., Maddix, D. M., Butkovich, T. R. and Heuzé, F. E., 1991. *Redirection of Dynamic Compressive Waves in Materials with Nearly Orthogonal and Random Joint Sets.* Recent Advances in Mechanics of Structured Continua, Vol. 117, pp. 65-73.

[206] Hogue, C., 1998. *Shape Representation and Contact Detection for Discrete Element Simulations of Arbitrary Geometries.* Engineering Computations, Vol. 15, No. 3, pp. 374-390.

[207] Hogue, C. and Newland, D., 1994. *Efficient Computer Simulation of Moving Granular Particles.* Powder Technology, Vol. 78, pp. 51-66.

[208] Potapov, A. and Campbell, C. S., 1998. *A Fast Model for the Simulation of Non-Round Particles.* Granular Matter, Vol. 1, pp. 9-14.

[209] O' Sullivan, C. and Bray, J. D., 2004. *Selecting a Suitable Time Step for Discrete Element Simulations that use the Central Difference Time Integration Scheme.* Engineering Computations, Vol. 21, No. 2/3/4, pp. 278-303. (doi:10.1108/02644400410519794).

[210] Rayleigh, J. W. S., 1885. *On Waves Propagated Along the Plane Surface of an Elastic Solid.* In: Proceedings of the London Mathematical Society, Vol. 1, pp. 4-11. (doi:10.1112/plms/s1-17.1.4).

[211] Thornton, C. and Randall, C. W., 1988. *Applications of Theoretical Contact Mechanics to Solid Particle System Simulation.* Micromechanics of Granular Materials, M. Satake and J. Jenkins (Eds.), Elsevier, Amsterdam, pp. 133–142.

[212] Morrissey, J. P., 2013. *Discrete Element Modelling of Iron Ore Pellets to Include the Effects of Moisture and Fines.* PhD Thesis, The University of Edinburgh, Scotland, United Kingdom.

[213] Cleary, P. W. and Sawley, M. L., 2002. *DEM Modelling of Industrial Granular Flows: 3D Case Studies and the Effect of Particle Shape on Hopper Discharge.* Applied Mathematical Modelling, Vol. 26, No. 2, pp. 89-111.

[214] Ai, J., Chen, J. F., Rotter, J. M. and Ooi, J. Y., 2011. *Assessment of Rolling Resistance Models in Discrete Element Simulations.* Powder Technology, Vol. 206, No. 3, pp. 269-282.

[215] Tsuji, Y., Tanaka, T. and Ishida, T., 1992. *Lagrangian Numerical Simulation of Plug Flow of Cohesionless Particles in a Horizontal Pipe.* Powder Technology, Vol. 71, pp. 239-250.

[216] Hooke, R. 1678. *De Potentia Restitutiva, or of Spring. Explaining the Power of Springing Bodies.* Printed for John Martyn, Printer to the Royal Society, at the Bell in St. Pauls Church-Yard, London, United Kingdom.

[217] Hertz, H., 1882. *Uber die beruhrung fester elastischer korper (On the Contact of Elastic Solids).* Journal für die reine und angewandte Mathematik, Vol. 91, pp. 156-171.

[218] Mindlin, R. D. and Deresiewicz, H., 1953. *Elastic Spheres in Contact Under Varying Oblique Forces.* Journal of Applied Mechanics, Vol. 20, pp. 327-344.

[219] Derakhshani, S. M., Schott, D. L. and Lodewijks, G., 2015. *Micro–Macro Properties of Quartz Sand: Experimental Investigation and DEM Simulation.* Powder Technology, Vol. 269, pp. 127-138.

[220] Kloss, C. and Goniva, C., 2010. *LIGGGHTS – A New Open Source Discrete Element Simulation Software.* In: Proceedings 5th International Conference on Discrete Element Methods, London, United Kingdom, pp. 25-26.

[221] Bradley, R. S., 1932. *The Cohesive Force Between Solid Surfaces and the Surface Energy of Solids.* The London, Edinburgh and Dublin Philosophical Magazine and Journal of Science, Vol. 13 No. 86, pp. 853-862.

[222] Johnson, K. L., Kendall, K. and Roberts, A. D., 1971. *Surface Energy and the Contact of Elastic Solids.* In: Proceedings of the Royal Society of London, Series A: Mathematical and Physical Sciences, Vol. 324, No. 1558, pp. 301-313.

[223] Derjaguin, B. V., Muller, V. M. and Toporov, Y. P., 1975. *Effect of Contact Deformations on the Adhesion of Particles.* Journal of Colloid and Interface Science, Vol. 53, No. 2, pp. 314-326. (doi:10. 1016/0021-9797(75)90018-1).

[224] Muller, V. M., Yushchenko, V. S. and Derjaguin, B. V., 1980. *On the Influence of Molecular Forces on the Deformation of an Elastic Sphere and its Sticking to a Rigid Plane.* Journal of Colloid and Interface Science, Vol. 77, No. 1, pp. 91-101. (doi:10.1016/0021-9797(80)90419-1).

[225] Mitarai, N. and Nori, F., 2006. *Wet Granular Materials*. Advances in Physics, Vol. 55, pp. 1-45. (doi:10.1080/00018730600626065).

[226] Luding, S., 2005. *Anisotropy in Cohesive, Frictional Granular Media.* Journal of Physics: Condensed Matter, Vol. 17, No. 24, pp. 2623-2640. (doi:10.1088/0953-8984/17/24/017).

[227] Luding, S., 2005. *Shear Flow Modeling of Cohesive and Frictional Fine Powder.* Powder Technology, Vol. 158, No. 1-3, pp. 45-50. (doi:10.1016/j.powtec.2005.04.018).

[228] Luding, S., 2006. *About Contact Force-Laws for Cohesive Frictional Materials in 2D and 3D.* In: Proceedings Behavior of Granular Media.

[229] Luding, S., 2007. *Contact Models for Very Loose Granular Materials.* In: Proceedings IUTAM Symposium on Multiscale Problems in Multibody System Contacts, P. Eberhard (Ed.), Chapter 14, Springer Netherlands, pp. 135-150. (doi:10.1007/978-1-4020-5981-0_14).

[230] Luding, S., 2008. *Cohesive, Frictional Powders: Contact Models for Tension.* Granular Matter, Vol. 10, No. 4, pp. 235-246. (doi:10.1007/s10035-008-0099-x).

[231] Walton, O. R. and Johnson, S. M., 2009. *Simulating the Effects of Interparticle Cohesion in Micron-Scale Powders.* In: AIP Conference Proceedings - Powders and Grains 2009: Proceedings of the 6th International Conference on Micromechanics of Granular Media, M. Nakagawa and S. Luding (Eds.), AIP, Golden (Colorado), pp. 897-900. (doi:10.1063/1.3180075).

[232] Thornton, C. and Ning, Z., 1998. *A Theoretical Model for the Stick/Bounce Behaviour of Adhesive, Elastic-Plastic Spheres.* Powder Technology, Vol. 99, No. 2, pp. 154-162. (doi:10.1016/S0032-5910(98)00099-0).

[233] Tomas, J., 2003. *Flow Properties of Cohesive Nanopowders.* China Particuology, Vol. 1, No. 6, pp. 231-241.

[234] Tomas, J., 2003. *Mechanics of Nanoparticle Adhesion - A Continuum Approach.* In: Proceedings Particles on Surfaces 8: Detection, Adhesion and Removal, K. Mittal (Ed.), VSP, pp. 1–47.

[235] Tomas, J., 2004. *Fundamentals of Cohesive Powder Consolidation and Flow.* Granular Matter, Vol. 6, No. 2-3, pp. 75-86. (doi:10.1007/s10035-004-0167-9).

[236] Tomas, J., 2007. *Adhesion of Ultrafine Particles - A Micromechanical Approach.* Chemical Engineering Science, Vol. 62 No. 7, pp. 1997-2010. (doi:10.1016/j.ces.2006.12.055).

[237] Tomas, J., 2007. *Adhesion of Ultrafine Particles - Energy Absorption at Contact.* Chemical Engineering Science, Vol. 62, No. 21, pp. 5925-5939. (doi:10.1016/j.ces.2007.06.036).

[238] Thakur, S. C., Morrissey, J. P., Sun, J., Chen, J. F. and Ooi, J. Y., 2014. *Micromechanical Analysis of Cohesive Granular Materials Using the Discrete Element Method with an Adhesive Elastoplastic Contact Model.* Granular Matter, Vol. 16, pp. 383-400.

[239] Lian, G., Thornton, C. and Adams, M. J., 1993. *A Theoretical Study of the Liquid Bridge Forces Between Two Rigid Spherical Bodies.* Journal of Colloid and Interface Science, Vol. 161, pp. 138-147.

[240] Mikami, T., Kamiya, H. and Horio, M., 1998. *Numerical Simulation of Cohesive Powder Behavior in a Fluidized Bed.* Chemical Engineering Science, Vol. 53, No. 10, pp. 1927-1940. (doi:10.1016/S0009-2509(97)00325-4).

[241] Soulie, F., Cherblanc, F., El Youssoufi, M. S. and Saix, C., 2006. *Influence of Liquid Bridges on the Mechanical Behaviour of Polydisperse Granular Materials.* International Journal for Numerical and Analytical Methods in Geomechanics, Vol. 30, No. 3, pp. 213-228.

[242] Nase, S. T., Vargas, W. L., Abatan, A. A. and Mccarthy, J., 2001. *Discrete Characterization Tools for Wet Granular Media.* Powder Technology, Vol. 116, No. 2-3, pp. 214-223. (doi:10.1016/S0032-5910(00)00398-3).

[243] Rabinovich, Y. I., Esayanur, M. S. and Moudgil, B. M., 2005. *Capillary Forces Between Two Spheres with a Fixed Volume Liquid Bridge: Theory and Experiment.* Particle Engineering Research, University of Florida, Gainesville, FL 32611, United States.

[244] Easo, L. A. and Wassgren, C., 2013. *Comparison of Liquid Bridge Volume Models in DEM Simulations.* In: Proceedings AIChE Annual Meeting, San Francisco, CA, USA.

[245] Roberts, A. D., 1968. *Ph.D. Dissertation.* PhD Thesis, Cambridge University, England.

[246] Kendall, K., 1969. *Ph.D. Dissertation.* PhD Thesis, Cambridge University, England.

[247] CFDEM, 2016. *Gran Cohesion SJKR2 Model* [online]. Available from: <https://www.cfdem.com/media/DEM/docu/gran_cohesion_sjkr2.html> [Accessed: 23 July 2016].

[248] Carr, M. J., Chen, W., Williams, K. and Katterfeld, A., 2016. *Comparative Investigation on Modelling Wet and Sticky Material Behaviours with a Simplified JKR Cohesion Model and Liquid Bridging Cohesion Model in DEM.* In: Proceedings 12th International Conference on Bulk Solids Material Storage, Handling and Transport (ICBMH), Darwin, Australia.

[249] Israelachvili, J. N., 1992. *Intermolecular and Surface Forces.* 2nd Edition, Academic Press: San Diego, CA, United States. (doi:10.1016/C2009-0-21560-1).

[250] CFDEM, 2016. *Gran Cohesion Easo/Capillary/Viscous Model* [online]. Available from: <http://www.cfdem.com/media/DEM/docu/gran_cohesion_easo_capillary_viscous.html> [Accessed: 23 July 2016].